



## Dynamics and control of non-classical electrostriction in doped ceria

**Santucci, Simone**

*Publication date:*  
2020

*Document Version*  
Publisher's PDF, also known as Version of record

[Link back to DTU Orbit](#)

*Citation (APA):*  
Santucci, S. (2020). *Dynamics and control of non-classical electrostriction in doped ceria*. Technical University of Denmark.

---

### General rights

Copyright and moral rights for the publications made accessible in the public portal are retained by the authors and/or other copyright owners and it is a condition of accessing publications that users recognise and abide by the legal requirements associated with these rights.

- Users may download and print one copy of any publication from the public portal for the purpose of private study or research.
- You may not further distribute the material or use it for any profit-making activity or commercial gain
- You may freely distribute the URL identifying the publication in the public portal

If you believe that this document breaches copyright please contact us providing details, and we will remove access to the work immediately and investigate your claim.

# Dynamics and control of non-classical electrostriction in doped ceria

---

Ph.D. Candidate:

**Simone Santucci**

Main supervisor:

**Prof. Vincenzo Esposito**

Co-supervisors:

**Prof. Nini Pryds  
Igor Lubomirsky**



**Section for Functional Oxides (FOX)**

**Department of Energy Conversion and Storage**

**Technical University of Denmark**

Fysikvej, Building 310,

2800 Kgs. Lyngby,

Denmark



# Preface

This thesis gathers the results of three years of work carried out from 14 February 2017 to 14 February 2020 at the Department of Energy Conversion and Storage of the Technical University of Denmark. It is submitted in candidacy for a Philosophiae Doctor degree to the evaluation committee and the Ph.D. school of the Technical University of Denmark. Part of this project was performed at the APE beamline of Elettra synchrotron (Trieste) at Consiglio Nazionale delle Ricerche – Istituto Officina dei Materiali (CNR-IOM) led by scientist Pasquale Orgiani. Professor Vincenzo Esposito and Professor Nini Pryds supervised these three years of work. This research was supported by the Danish Council for Independent Research Technology and Production Sciences for the DFF- Research Project 2 (Grant No. 48293) and the BioWings project funded by the European Union's Horizon 2020, Future and Emerging Technologies (FET) programme (Grant No. 801267).



# Acknowledgment

It has been three years since I came to Denmark and started my PhD. It has been a challenging but beautiful path, and now it is time to express my gratitude to the people that made this experience unforgettable.

First, I would like to thank my supervisor Vincenzo Esposito for his dedicated help and guidance. Vincenzo continuously provided encouragement and was always willing to answer my questions and to discuss my ideas. enthusiastic to assist in any way she could throughout the research project

Thank you also to my supervisor Nini Pryds who was always eager to help me and give me useful suggestions to improve my work.

Together, they not only gave me the opportunity to carry out my PhD study, but they also helped me to grow as a scientist by supporting my ideas and encouraging my curiosity. They did everything possible to allow me to do my job at my best. Thank you!!

Thanks to Igor Lubomirsky for his hospitality at Weizmann institute and for sharing ideas and his opinion in fruitful discussions that taught me a lot.

I would like to thank also Pasquale Orgiani for accepting me in his research group at Elettra synchrotron, where I learned a lot and improved my skills.

Obviously, a lot of other people helped me. Thanks to Simone Sanna, for being both a teacher, colleague and friend. With him, my days spent in the laboratory have been much easier and fun.

I want to extend my gratitude to the other members of my group Haiwu Zhang, Ahsanul Kabir and Jin Han. We shared ideas, helped and encouraged each other. We are a strange but beautiful team.

I wish to thank the assessment committee Jacob Bowen, Andrei Kholkin and Monica Burriel, for taking the time to evaluate my thesis and be part of my defense.



Then, I would express my gratitude to all my friends. During these years, I met a lot of beautiful people from all around the world. Thanks to you, I have memories I will keep for the rest of my life. You are too many, and I do not want to forget someone, but I promise to thank you personally one by one. Finally, a special thanks to Plum.



# Abstract and motivation

Electrostrictive and piezoelectric materials, which change their shape in response to external fields, have critical applications in many different contexts, working as a muscle. Nowadays, electromechanical active materials are used in everyday technology as components of cameras or sound transducer as well as advanced systems such as microelectronics, energy harvesting or ultrasound imaging.

The most diffused electrostrictive materials are Pb-based compounds such as  $\text{Pb}(\text{Mn}_{1/3}\text{Nb}_{2/3})\text{O}_3$  (PMN). Not only they contain lead (Pb), which is highly toxic, but their use has been restricted by the European restriction of hazardous substances directive (RoHS) in 2006. For these reasons, many efforts have been made to find an environmentally friendly alternative as a substitute to current materials.

Recently, bio-compatible defective oxides have been showed to possess high electrostrictive behavior. In particular cerium oxides, i.e. ceria, display a giant electromechanical effect with magnitude comparable or superior to the best State-of-the-Art materials. The electromechanical mechanism in this kind of compounds depends on the oxygen vacancies configuration within the crystal lattice and it differs from classical electrostriction in intensity and dynamics. For this reason, doped ceria is considered a promising candidate for a new generation of “smart” materials.

This project focuses on the mechanism and operation of electrostrictive doped ceria. Thin films are synthesized by PLD technique using several substrates and electrodes. The reliability and mechanical integrity of actuator thin films are enhanced by integration in full ceramic structures and by planar electrodes devices. In order to do this, a sub-nanometer displacement characterization tool is designed and assembled. Then, the electrostrictive effect is mapped depending on the crystal geometry in highly coherent thin films. This not only allows to develop a new interpretation of non-classical electrostriction in doped ceria in terms of atomic displacement but also identifies the optimal distortion condition of the material, resulting in a ten times higher electrostrictive effect. Finally, ultra-thin films coupling with

the substrate is studied by x-ray absorption spectroscopy (XAS), highlighting a strong interfacial electrostriction effect controlled by the inclusion of crystal defects in strained structures.

In general, during this research, both the operative stability and performances of electrostrictive ceria devices has been dramatically improved. Moreover, the underlying mechanism behind the effect has been addressed and explained with a rigorous model, supported by experimental data. Finally, means to control electromechanical response in thin films through crystal orientation and strain manipulation have been showed.

# TABLE OF CONTENTS

---

<b>1</b>	<b>INTRODUCTION .....</b>	<b>1</b>
1.1	ELECTROSTRICTION BASIC EFFECT .....	1
1.2	TECHNOLOGY AND APPLICATION.....	3
1.3	MICROSCOPIC PROPERTIES OF ELECTROSTRICTION.....	5
1.4	MACROSCOPIC PROPERTIES OF ELECTROSTRICTION.....	7
1.4.1	<i>Thermal expansion:</i> .....	7
1.4.2	<i>Mechanical and dielectric properties: Newnham's law</i> .....	8
1.5	MATERIALS .....	8
1.5.1	<i>Linear dielectrics and glasses ceramics</i> .....	9
1.5.2	<i>Perovskites ferroelectrics and relaxor ferroelectrics</i> .....	9
1.5.3	<i>Ferroelectric polymers</i> .....	10
1.6	CERIUM OXIDE .....	11
1.7	ELECTROSTRICTION IN GD-DOPED CERIA .....	13
1.8	MICROSCOPIC MODEL .....	14
1.9	GD-DOPED CERIA THIN FILMS .....	15
1.10	ELECTROSTRICTION IN BULK CGO .....	18
1.11	CGO MEMBRANES.....	20
1.12	THESIS GOAL AND APPROACH.....	23
1.13	THESIS OUTLINE .....	24
1.14	REFERENCES .....	26
<b>2</b>	<b>FABRICATION AND CHARACTERIZATION .....</b>	<b>30</b>
2.1	PULSED LASER DEPOSITION (PLD).....	30
2.1.1	<i>Description of the system (DTU)</i> .....	34
2.1.2	<i>Description of the system (APE beamline, Elettra)</i> .....	35
2.2	STRUCTURAL CHARACTERIZATION BY X-RAY DIFFRACTION: .....	36
2.2.1	<i>Fundamentals</i> .....	36
2.2.2	<i>Theta-2theta scan</i> .....	37
2.2.3	<i>Rocking curve (RC)</i> .....	37
2.2.4	<i>X-ray reflectivity (XRR)</i> .....	38

2.3	ELECTROCHEMICAL CHARACTERIZATION: IMPEDANCE SPECTROSCOPY.....	39
2.4	ELECTROSTRICTION DETECTION SETUP.....	42
2.4.1	<i>Basics and calculations</i> .....	42
2.4.2	<i>Detection system</i> .....	44
2.4.3	<i>Lock-in amplifier</i> .....	46
2.4.4	<i>High voltage and other features</i> .....	47
2.5	X-RAY ABSORPTION SPECTROSCOPY (XAS). ....	48
2.6	REFERENCES.....	51
<b>3</b>	<b>DEVICES PERFORMANCES AND STABILITY, THE ROLE OF ELECTRODES AND MICROSTRUCTURE.....</b>	<b>54</b>
3.1	ELECTRODES AND STABILITY .....	55
3.1.1	<i>Cantilever design and CGO deposition</i> .....	55
3.1.2	<i>Metal electrodes: Ti and Al</i> .....	57
3.1.3	<i>Titanium nitride and gold electrodes</i> .....	59
3.1.4	<i>Electrostriction performances and stress tests</i> .....	61
3.1.5	<i>Ceramic electrodes: LSCF, STN and SRO</i> .....	65
3.2	PLANAR ELECTRODE CONFIGURATION .....	68
3.2.1	<i>Temperature measurements</i> .....	69
3.2.2	<i>Setup requirements</i> .....	70
3.3	GRAIN BOUNDARIES EFFECT ON ELECTROSTRICTION IN BULK CGO.....	71
3.4	REFERENCES.....	76
<b>4</b>	<b>INTRINSIC LATTICE DISTORTION MECHANISM IN HIGHLY COHERENT THIN FILMS.....</b>	<b>79</b>
4.1	HIGHLY COHERENT THIN FILMS .....	80
4.1.1	<i>Electrodes symmetry and <math>M_{12}</math> calculation</i> .....	84
4.1.2	<i>Longitudinal electrostriction effect</i> .....	88
4.1.3	<i>Transverse electrostriction effect</i> .....	89
4.2	MICROSCOPIC MODEL AND DISCUSSION .....	91
4.3	REFERENCES.....	96
<b>5</b>	<b>X-RAY ABSORPTION SPECTROSCOPY IN BULK AND ULTRATHIN FILMS .....</b>	<b>98</b>
5.1	IN-SITU XANES AND BEAMLINES.....	98
5.2	CGO SINGLE CRYSTAL IN-SITU XANES AT LOW TEMPERATURE .....	100
5.2.1	<i>Electrostriction frequency stability in Ca-doped ceria</i> .....	104
5.3	XANES ANALYSIS FOR INTERFACIAL DISLOCATIONS IN HIGHLY ELECTROSTRICTIVE FILMS. ....	107

5.3.1	<i>APE beamline .....</i>	<i>108</i>
5.3.2	<i>Structural characterization .....</i>	<i>108</i>
5.3.3	<i>Electromechanical performances.....</i>	<i>110</i>
5.3.4	<i>X-ray absorption spectroscopy and discussion.....</i>	<i>112</i>
5.3.5	<i>XANES on Nd-YAG laser deposited: Sm-doped ceria. ....</i>	<i>113</i>
5.4	REFERENCES.....	115
<b>6</b>	<b>CONCLUSION AND FUTURE PERSPECTIVE .....</b>	<b>120</b>
	<b>APPENDICES .....</b>	<b>122</b>
A.	LIST OF PAPERS INCLUDED ON THE THESIS .....	122
B.	LIST OF CONFERENCES CONTRIBUTION.....	124
C.	ARTICLES AND MANUSCRIPT.....	125

# LIST OF FIGURES

Figure 1-1: a) Strain quadratic response to an electric field for electrostrictive materials. b) Electrostriction dynamics under an applied AC field, $E=E_0\sin(\omega t)$ .....	3
Figure 1-2: Ion-pair potential respect to the nearest neighbor distance in ionic crystal, $r_0$ is the equilibrium distance between positive and negative ions. ....	6
Figure 1-3: Hydrostatic electrostriction coefficient versus elastic compliance and dielectric constant. Several types of materials are reported. Red line: Newnham's law. Reported with permission from Yavo, N. et al. (2016) Advanced Functional Materials (2016), John Wiley and Sons and Copyright Clearance Center.....	8
Figure 1-4: a) fluorite structure of ceria with the inclusion of one oxygen vacancy. b) fluorite structure organized as sub-cell units centered in Ce cation. c) a single unit with the inclusion of one oxygen vacancy.....	12
Figure 1-5: Scheme of $\text{Ce}_{\text{Ce}}7\text{O}-V\text{O} \bullet\bullet$ unit.. Left: vacancy induced of Ce coordination shell distortion. Right: electric field-induced distortion. ....	15
Figure 1-6: a) Cantilever device. One side is clamped/glued, and the other one is free to move. b) Multilayered structure of the samples: Substrate/bottom electrode/CGO/top electrode. ....	16
Figure 1-7: Relaxation of electrostriction coefficient depending on the frequency in bulk CGO. Ref: [64] .....	19
Figure 1-8: Electromechanical response in CGO bulk for different sintering processes. Saturation is visible in both. Ref: [64]. ....	19
Figure 1-9: a) image of a CGO membrane. b) cross section scheme of the device. Reported with permission from Mishuk et al. Appl. Phys. Lett. <b>110</b> , 142902 (2017) by AIP Publishing and Copyright Clearance Center.....	20
Figure 1-10: Membrane response to squared electric field wave for different temperatures and voltages. Reported with permission from Mishuk et al. Appl. Phys. Lett. <b>110</b> , 142902 (2017) by AIP Publishing and Copyright Clearance Center. ....	21
Figure 2-1: Schematic of a PLD setup and targets carousel.....	30



Figure 2-2: Schematic of the ablation process.....	31
Figure 2-3: plume time evolution depending on pressure and temperature. Reported with permission from Sambri et al., Journal of Applied Physics 104, 053304 (2008), AIP Publishing and Copyright Clearance Center.....	32
Figure 2-4: schematic of thin films microstructure as a function of temperature and pressure. Reported with permission from Infortuna A. et al, Advanced Functional Materials, (2008), John Wiley and Sons and Copyright Clearance Center. ....	34
Figure 2-5: PLD in DTU. Photo of the inside of the main chamber.....	35
Figure 2-6: Photo of the inside of PLD chamber at Elettra. ....	36
Figure 2-7: $\theta$ - $2\theta$ scan mode. a) Diffractometer geometry. b) Diffraction pattern of $\text{CeO}_2$ .....	37
Figure 2-8: Rocking curve (RC) scan mode. a) Diffractometer geometry. b) RC of epitaxial CGO. The grains are parallel and the peak is sharp with $\text{FWHM} = 0.38^\circ$ . c) RC of CGO non-epitaxial CGO. The large $\text{FWHM} = 1.06^\circ$ suggests the presence of mosaic spread of the grains. The pattern was smoothed for clarity.....	38
Figure 2-9: XRR scan mode. a) Dynamics of x-ray penetration and reflection in thin layers. b) Example of XRR pattern of a 17 nm thick CGO film.....	39
Figure 2-10: Schematic representation of a Nyquist plot. ....	40
Figure 2-11: Nyquist plot of CGO bulk samples. ....	41
Figure 2-12: Arrhenius plot of CGO bulk samples. Bulk and grain boundaries contribution are separated. ....	42
Figure 2-13: Cantilever configuration in a sample with planar electrodes. ....	43
Figure 2-14: Michelson interferometer schematics. M1 and M2 are reflecting mirrors. R is a partially reflecting mirror.....	44
Figure 2-15: Vibrometer picture. ....	45
Figure 2-16: Vibrometer measurements in different condition. a) Measurements of oscillating CGO sample with 0.1 frequency, with low noise and drift. b) Static measurement with high environmental noise. c) Static measurement with high drift.....	46

Figure 2-17: Measurement of 1 Hz oscillation amplitude of CGO/YSZ with increasing voltages (at 0.5 Hz) performed with the lock-in amplifier. The displacement values refer to the contribution of 1 Hz oscillation. The frequency chosen is double the electric field frequency because electrostriction vibration depends on the second harmonic. ....	47
Figure 2-18: Schematic of electrostriction experimental setup. ....	48
Figure 2-19: X-ray absorption spectrum example. XANES and EXAFS regions are highlighted. ....	50
Figure 3-1: Schematic of the sample structure. The size can vary slightly. ....	55
Figure 3-2: Structural analysis of CGO deposited on TiN/Si substrate. a) X-ray diffraction. b) SEM cross-section image. ....	56
Figure 3-3: SEM images of Al film grown on CGO. a) top view. b) cross-section ....	58
Figure 3-4: Al coating on CGO film. ....	58
Figure 3-5: SEM images of Ti film grown on CGO. a) top view. b) cross-section and zoom. ....	59
Figure 3-6: $\theta$ -2 $\theta$ scans of CGO thin films. a) CGO deposited on Ti and Al bottom electrodes. b) CGO deposited on TiN, with Au and TiN top electrode ....	60
Figure 3-7: Schematic of TiN based samples. a) Au top electrode: Au/CGO/TiN sample. b) TiN top electrode: TiN/CGO/TiN sample. ....	61
Figure 3-8: SEM images of CGO thin films on TiN/Si substrate. a) Top view of Au top electrode. b) Cross-section of CGO on TiN/Si with Au top electrode. c) top view of TiN top electrode. d) Cross-section of CGO on TiN/Si with TiN top electrode. ....	61
Figure 3-9: Electrostrictive activity with 100 mHz electric field. The frequency of oscillation is reported. 200 mHz and 100 mHz are the first and second harmonic of the applied field, respectively. a) Au/CGO/TiN sample at 25 kV/cm. Left: initial condition. Right: after consecutive measurements. b) TiN/CGO/TiN at 27 kV/cm. Left: initial condition. Right: after consecutive measurements. ....	63
Figure 3-10: Stress-test with a high electric field. a) Au/CGO/TiN sample: (left) oscillation at 25 kV/cm and 71 kV/cm applied field (mechanical failure); (middle) SEM cross-section image of Au/CGO/TiN as deposited; (right) SEM cross-section after the field-induced failure showing the detachment of top electrode. b) TiN/CGO/TiN sample with (left) oscillation at 25 kV/cm and 81 kV/cm applied field. 40 min	

long measurement is displayed; (right) SEM crosses section image after the stress test, TiN electrodes are still intact and perfectly adhered to the CGO film.....	64
Figure 3-11: SEM images of LSCF thin films on STO substrate. a) LSCF top surface. b) Cross-section view. ....	66
Figure 3-12: Photo of CGO sample with LSCF top electrode. Contrast and light adapted to highlight the detachment of electrode. ....	66
Figure 3-13: SEM cross-section image of STN/CGO/SRO/Au heterostructure. A highly coherent structure was achieved as superior stability compared to metal electrodes samples. ....	67
Figure 3-14: Schematic of electrodes configuration. a) Top-bottom geometry. b) Planar geometry. ..	68
Figure 3-15: Thermal measurements of the sample with planar configuration. a) 5 V applied. b) 8V applied.....	69
Figure 3-16: Thermal measurements of the sample with t-b configuration. a) 4.5 V applied. b) 6V applied .....	70
Figure 3-17: SEM images of CGO (or GDC) samples. a) SPS sample. b) Fast firing sample. c) Conventional sample 2.5h. d) Conventional sample 10 h.....	72
Figure 3-18: a) Nyquist plot ( $\rho'$ vs $\rho''$ ) of GDC-SPS and GDC-0.1 h samples. b) Nyquist plot of GDC-10 h and GDC-2.5 h samples. ....	73
Figure 3-19: Electrostriction analysis depending on the electric field and frequency. ....	74
Figure 3-20: Comparative analysis of electrostriction with grain size, grain boundaries resistivity and blocking barrier effect.....	75
Figure 4-1: Schematic of epitaxial relation of CGO and STO. a) Cubic cells of CGO and STO. b) Top view of CGO arrangement on top of (200) oriented STO (gray square). The crystal axis are reported for both the film (black arrows) and substrate (gray arrows). ....	80
Figure 4-2: Structural characterization of (200) oriented CGO on (200) STO. a) $\theta$ -2 $\theta$ scan. b) rocking curve at the (200) peak of CGO. c) SEM Cross section image. ....	81
Figure 4-3: Representation of $\text{NdGaO}_3$ unit cell. The pseudocubic cell is highlighted (green lines). The relation between orthorhombic (o) and pseudocubic (ps) crystal axis are reported. ....	81

Figure 4-4: Schematic of epitaxial relation of CGO and (200) oriented NGO. a) CGO cell with in-plane layer highlighted (dotted lines). b) Top view of the CGO structure on top of (200) oriented NGO. The resulting crystal axis are reported. ....	82
Figure 4-5: Structural properties of (111) oriented CGO on (200) NGO. a) $\theta$ -2 $\theta$ scan. (inset) $\theta$ -2 $\theta$ grazing angle scan performed to exclude substrate peaks. b) Rocking curve at the (111) peak of CGO. c) SEM picture in cross section mode. ....	82
Figure 4-6: Top view of CGO cell on (220) oriented YSZ substrate (gray square). ....	83
Figure 4-7: Structural characterization of CGO on (110) oriented YSZ. a) $\theta$ -2 $\theta$ scan. b) Rocking curve on (110) peak of CGO. c) SEM cross section image. ....	83
Figure 4-8: Electrode configuration depending on crystallographic geometry. a) CGO <sub>(200)</sub> /STO <sub>(200)</sub> sample symmetry. The electrodes are placed parallel to the [011] direction (black arrow). b) CGO <sub>(111)</sub> /NGO <sub>(200)</sub> symmetry with two electrodes configuration. Black arrow: parallel to [0-11]. Red arrow: parallel to [-211]. The two configuration are perpendicular. c) CGO <sub>(110)</sub> /YSZ <sub>(110)</sub> electrodes configuration. Black arrow: parallel to [001]. Red arrow: parallel to [-223] with 45° rotated electrodes. ....	85
Figure 4-9: Substrates contribution to oscillation. a) Displacement of STO <sub>(100)</sub> substrate for 1 Hz electric field. The calculated contribution to the CGO <sub>(100)</sub> /STO <sub>(100)</sub> oscillation is 10%. b) NGO <sub>(100)</sub> substrate at 1 Hz electric field. No contribute was considered as NGO did not show any response to the electric field. c) YSZ <sub>(110)</sub> substrates at 1 Hz electric field. The displacement of YSZ alone is about 50% of the total oscillation of the CGO <sub>(110)</sub> /YSZ <sub>(110)</sub> sample. ....	86
Figure 4-10: Cantilever beam longitudinal and transverse distortion. a) Schematic of the sample. $M_{11}$ is calculated measuring $d$ in a single point. The transverse effect i.e., $M_{12}$ is calculated by multiple measurements along the width of the sample (Y-scan). b) Deformation map of CGO cantilever, for 16 kV/cm applied field and 1 Hz frequency. The distortion takes place both along the length (X-scan) and the width (Y-scan). ....	87
Figure 4-11: Longitudinal electromechanical response of CGO thin films for electric field depending on electric field direction. Stress calculated respect the II harmonic contribution of oscillation @ 1 Hz. a) CGO (110) oriented on YSZ with electric field along [001] axis. b) CGO <sub>(200)</sub> /STO <sub>(200)</sub> sample with	

$E \parallel [011]$ . c)  $\text{CGO}_{(111)}/\text{NGO}_{(100)}$  sample with  $E \parallel [011]$ . d)  $\text{CGO}_{(111)}/\text{NGO}_{(100)}$  sample with  $E \parallel [211]$  diagonal direction. .... 89

Figure 4-12: Displacement Y-scan of CGO thin films with 13 kV/cm applied at 1 Hz. Both in-plane (y) and out-of-plane (z) crystallographic direction perpendicular to  $E$  are considered. a)  $\text{CGO}_{(110)}/\text{YSZ}_{(220)}$  sample with  $E$  perpendicular to  $[110]_z / [110]_y$ . b)  $\text{CGO}_{(200)}/\text{STO}_{(200)}$  sample with  $E \perp [100]_z / [011]_y$ . c)  $\text{CGO}_{(111)}/\text{NGO}_{(100)}$  sample with  $E \perp [111]_z / [211]_y$ . d)  $\text{CGO}_{(111)}/\text{NGO}_{(100)}$  sample.  $E \perp [111]_z / [101]_y$ , the parabolic fit here is not possible as displacement is linear through the width..... 90

Figure 4-13:  $\text{CeO}_2$  structure and oxygen vacancy related neighborhood. a)  $\text{Ce}_{\text{ce}}\text{-}7\text{O-VO} \bullet\bullet$  unit, base of the current model for electrostriction in CGO. Black vector:  $\text{VO} \bullet\bullet$ -  $\text{Ce}_{\text{ce}}$  -  $\text{O}_{\text{O}}$  electro-active triplet with direction of the distortion. Blue vectors: diagonal 6O displacement b) 4-units complex centered on oxygen vacancy linked to four  $\text{Ce}_{\text{ce}}\text{-}7\text{O-VO} \bullet\bullet$  distorted units. Near-empty site oxygen atoms, i.e. 6O, are numbered. Red lines: bonds Ce atoms with oxygen 1 and 2. c) 6O octahedron structure composed of six near-empty site oxygen atoms. New model base structure. .... 92

Figure 4-14: Distortion direction of oxygen ion 2, bonded to Ce cation A and B. Red arrows: displacement vectors  $A2$  and  $B2$  respectively parallel to  $[111]$  and  $[111]$  directions. Black arrow: total displacement vector parallel to  $111 + 111 = [100]$ . It represents the preferential direction of distortion..... 93

Figure 4-15: Octahedron structure with angle between electric field (yellow arrow) and preferred direction (Black arrow). a) Electric field along  $[100]$  direction. b) Electric field along  $[110]$  with an angle of  $45^\circ$ . c)  $E$  to  $[111]$ , with a  $60^\circ$  angle from preferential direction..... 94

Figure 5-1: Picture of sample setup of the experimental hutch, including the cryostat box. Figure adapted from “CLÆSS: The hard X-ray absorption beamline of the ALBA CELLS synchrotron” L. Simonelli et al, © 2016 The Author(s). .... 99

Figure 5-2: Electromechanical properties of 20% Gd-doped ceria single crystal at room temperature for different frequencies. .... 101

Figure 5-3: XANES spectra at Ce L-III edge for different temperatures. “on” and “off” states are reported as well as differential XANES (“on-off”). a) room temperature. b)  $-50^\circ\text{C}$ . c)  $-125^\circ\text{C}$ . d)  $-194^\circ\text{C}$ . e) Diff XANES for CGO-SC at different temperatures. .... 103

Figure 5-4: XANES spectra at the Ce-L <sub>III</sub> edge edge of CDC-5 (CCO 5%) and CDC-15 (CCO 15%) samples. 4 kV/cm electric field is applied during the field on measurements for about 5h.....	106
Figure 5-5: a) $\theta$ - $2\theta$ scans of calcium-doped ceria (CDC) powders and pellets. b) Scanning electron microscopy (SEM) images of the polished cross-section of the CDC pellets. The inset reports the cold-fractural cross-sectional region. The scale bar is 2 $\mu$ m.....	105
Figure 5-6: Structural characterization of 17 nm thin films by XRD. a) $\theta$ - $2\theta$ scans of CGO on NGO, STO and LAO substrates. b) X-ray reflectivity of the samples indicating 17 nm of CGO film thickness. c) Rocking curve of CGO/LAO with FWHM of 0.38°. d) Rocking curve of CGO/NGO with FWHM of 0.17°. e) Rocking curve of CGO/STO smoothed. FWHM = 0.32° .....	109
Figure 5-7: $\theta$ - $2\theta$ scans of 170 nm thick CGO on NGO, STO and LAO substrates with gold top electrodes. ....	110
Figure 5-8: electromechanical performances of a) 17 nm and b) 170 nm thick CGO film deposited on NGO (black), LAO (red) and STO (blue). ....	111
Figure 5-9: XANES of Ce M4 (900 eV) and M5 (882 eV) edges. a) 17 nm and 170 nm CGO/STO. b) 17 nm and 170 nm CGO/NGO. The lower peak intensity of 17 nm samples is not an indication of Ce 3+. c) 17 nm and 170 nm CGO/LAO. The M4 and M5 relative peaks height difference is a 3+ feature.....	112
Figure 5-10: Structural characterization of pure ceria deposited with Nd-YAG laser by PLD. a) $\theta$ - $2\theta$ scan. b) XRR showing a thickness of 34 nm. ....	114
Figure 5-11: XANES spectra of thin films deposited by PLD with Nd-YAG laser. a) Comparison of 20% Gd or Sm doped ceria. b) comparison of 20% and 40% Sm doped thin films.....	115

# LIST OF TABLES

---

Table 1-1: Electrostriction coefficients $M_e$ in thin films, bulk and membranes are reported, including its behavior depending on frequency and temperature. Strain saturation and Joule heating effect are also reported. ....	23
Table 4-1: Longitudinal ( $M_{11}$ ) and transverse ( $M_{12}$ ) electrostriction coefficient of CGO thin films depending on electric field direction and perpendicular orientation. ....	91
Table 5-1: Electrostriction coefficient of SC CGO depending on the frequency of the electric field. ...	101
Table 5-2: Electrostriction longitudinal coefficient ( $M_{33}$ ) of CDC pellets at certain frequencies. ....	106
Table 5-3: Electrostriction coefficient for CGO/STO, CGO/NGO and CGO/LAO for 17 nm and 170 nm thick films. ....	112







# 1 INTRODUCTION

---

In this chapter, the fundamentals of electrostriction effect are presented, including applications and technologies. Also, the principal families of electrostrictor materials such as elastomer and ferroelectrics are described depending on their dielectric and mechanical properties. The electrostriction in cerium oxide is then explained in detail, reporting the current microscopic interpretation of the effect and the results showed up to date, including thin films, bulk and membrane devices.

This introduction is part of the accepted Chapter reported in Appendix A.C *“Electrostrictive Ceramics and their applications”* Simone Santucci, Vincenzo Esposito, included in *“Encyclopedia of Materials: Technical Ceramics and Glasses”*, Elsevier. Editorial board: M. J. Pomeroy, F. Cambier, C. Galassi, S. Hampshire, A. Leriche.

## 1.1 ELECTROSTRICTION BASIC EFFECT

---

Electrostriction is the ability of all insulating or dielectric materials to develop mechanical deformation when subjected to an electric field. The mechanical deformation is a consequence of the polarization of the ions inside the material. When no external electric field is applied, the net charge in insulators is macroscopically zero. However, at the atomic level the crystal is composed of positive (cation) and negative (anion) charged ions. When an electric field is applied through the material, cations and anions rearrange their relative position according to the field. As a consequence, the material develops mechanical deformation. The electrical field-induced strain ( $\lambda$ , dimensionless) is proportional to the applied electric field ( $E$ , [V]) squared or polarization ( $P$ , [Cm<sup>-2</sup>]) squared, which is expressed in tensor notation as:

$$\lambda_{ij} = M_{ijkl} E_k E_l \quad 1.1$$

$$\lambda_{ij} = Q_{ijkl}P_kP_l \quad 1.2$$

where  $M_{ijkl}$  ( $\text{m}^2\text{V}^{-2}$ ) and  $Q_{ijkl}$  ( $\text{m}^4\text{C}^{-2}$ ) are the so-called electrostriction coefficients. These coefficients are elements of a fourth-rank tensor, meaning that electrostriction takes place in all crystal symmetries.<sup>1</sup> The subscripts  $i,j,k,l$  can be abbreviated for materials with isotropic or cubic structures, so it is common to use the Voigt notation<sup>2</sup>:  $M_{ij}$  and  $Q_{ij}$  with  $i,j = 1$  to  $4$ . As a consequence of the dependence of the strain on the electric field squared ( $\propto E_k E_l$ ), the distortion always develops in the same direction, regardless of the sign of  $E$  or  $P$ . Figure 1-1a shows a parabolic field-induced strain in electrostrictive materials. As depicted in Figure 1-1b, if the applied field is oscillating at a frequency  $f$  (the case of AC application), the electrostrictive response would oscillate at twice the frequency  $2f$  ( $2^{\text{nd}}$  harmonic). The strain can develop either as a contraction ( $M, Q < 0$ ) or an expansion ( $M, Q > 0$ ), depending on the type of material. When an object withstands a distortion, it generates a related force or stress  $\sigma$  ( $\text{N}\cdot\text{m}^{-2}$ ) as defined by Hooke's law:

$$\sigma = Y \cdot \lambda \quad 1.3$$

where  $Y$  is Young's modulus, usually given in MPa. Therefore, with the same strain, a softer material with a lower  $Y$  would give rise to higher stress.

Electrostriction coefficients  $M$  and  $Q$  are related to the permittivity properties of the material:

$$M_{ijkl} = Q_{ijkl}\{\epsilon_0(\epsilon_r - 1)\}^2 \quad 1.4$$

with  $\epsilon_0$  being the vacuum permittivity and  $\epsilon_r$  being the dielectric constant of the material. The use of the coefficients depends on the type of material. For high permittivity dielectrics that can show nonlinear polarization or strain-field hysteresis,  $Q$  is usually preferred. It is worth noticing that for the same  $Q$  value, materials with a larger  $\epsilon_r$  show a larger strain. Since the electrostriction originates from a fundamental interaction common in all materials such as ferroelectric ceramics and polymers, it can vary considerably in both magnitude and dynamics, depending on the physical properties of the material. Consequently, electrostriction coefficients range across several order of magnitude depending on the material itself, with a  $Q$  from  $10^{-3} \text{ m}^4\text{C}^{-2}$  for ferroelectrics such as PLZT to  $10^3 \text{ m}^4\text{C}^{-2}$  in polyurethane films.<sup>2</sup> Furthermore, while most of the electrostrictors such as linear dielectrics, ceramics

and perovskites develop a positive strain (expansion), fluorites and polymers can have the opposite behavior<sup>1</sup>.

For materials that are also piezoelectric, the electrostrictive and piezoelectric effects sum up, resulting in a general electromechanical effect which can be written as:

$$\lambda_{ij} = g_{kij}P_k + Q_{ijkl}P_kP_l \quad 1.5$$

where  $g_{kij}$  (C/m<sup>-2</sup>) is the piezoelectric coefficient. Electrostriction can be considered as a second-order contribution of the general electromechanical coupling. Usually, the electrostrictive effect is smaller than the linear contribution by several orders of magnitude <sup>1,3,4</sup>. Electrostrictive materials however, show desirable characteristics such as low hysteresis in the polarization-strain loop and no remnant strain, making them more attractive for high accuracy applications.<sup>1,5,6</sup>

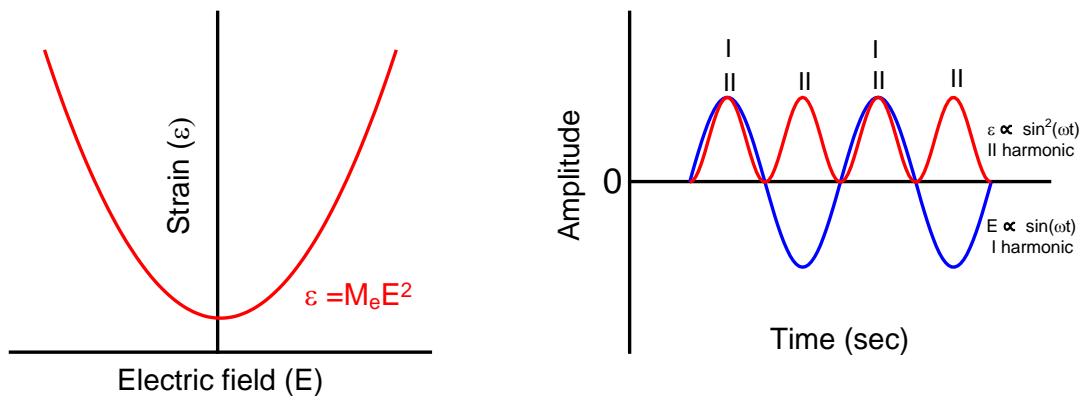


Figure 1-1: a) Strain quadratic response to an electric field for electrostrictive materials. b) Electrostriction dynamics under an applied AC field,  $E=E_0\sin(\omega t)$ .

## 1.2 TECHNOLOGY AND APPLICATION

The ability of electrostrictors to convert an electric signal to mechanical distortion has been used extensively in transducing technologies.<sup>7-11</sup> In particular, an actuator is a transducer whose function is to displace an object, working as an electrostrictive motor. Actuators are used in devices that need an electrical/mechanical signal conversion such as ink-jet printer heads, micro-pumps and noise

cancellation systems. A proper actuator should provide a significant displacement with a minimal electric field. Additionally, the performances should be stable and reproducible, allowing fine control of the actuating process. The average strain of a standard actuator is in the order of magnitude of 0.1%<sup>12</sup>. This value can be amplified in specifically engineered devices such as multilayered actuators<sup>13</sup>, or flextensional actuators (CYMBALs)<sup>9</sup>. Transducers can also be used in ultrasound imaging and sensors for diagnostic and sonar devices<sup>6,9</sup>. An electrostrictive ultrasound device can convert electrical signal in mechanical vibration, generating ultra-acoustic waves with extreme accuracy.

Piezoelectric transducers usually have higher performances. However, electrostrictors have many advantages over piezoelectrics due to the features of specific materials or the absence of remnant polarization<sup>1,14</sup>. Such advantages include high accuracy of the strain-field response (no hysteresis or remnant strain), low creep or aging effects and high-speed response ( $<10$  ms)<sup>2</sup>. Also, they can perform at high temperature and frequency<sup>1</sup>. Such features are useful in optical systems, namely interferometric dilatometers or deformable mirrors, in which high displacement accuracy is necessary<sup>15</sup>.

In recent years, electrostrictor materials have been frequently used in miniaturized devices known as micro-electromechanical systems (MEMS).<sup>5,13</sup> MEMS have many fields of application, such as robotics<sup>16</sup>, micro-motors and electronics<sup>17</sup>, biomedical devices<sup>6,18</sup>. There are several reasons one would choose electrostrictors over piezoelectrics for MEMS. Within small-sized devices, the electric field increases significantly, and the quadratic effect becomes the main contributor in the electromechanical activity. This effect has been observed in amorphous silica glass ( $10^{-21} \text{ m}^2\text{V}^{-2}$ )<sup>4</sup>. In thin films with a thickness lower than 100 Å, electrostriction strain is higher than piezoelectric contribution.<sup>2</sup> This effect can be exploited in the design of materials with a zero-electromechanical coefficient, useful in devices potentially damaged by electric fields<sup>1</sup>. In MEMS, the electro-active materials are introduced as thin films, coupled with substrates, usually Si<sup>19</sup>. Therefore, mechanical and chemical compatibility with other compounds is an essential factor when developing real applications. Piezoelectrics are hard to integrate into these devices, due to the high temperature processes<sup>20</sup>, the need for poling<sup>21</sup>, as well as the diffusion effects for lead-based piezoelectrics<sup>22</sup>.

Both piezoelectric and electrostrictive materials have a limited role in pure medical application, as the best performing materials are toxic, lead-based (PZT, PMN). Indeed, these materials have been banned by the RoHS compliant of 2006 <sup>23</sup>, due to environmental awareness. For this reason, in recent years many efforts have been made to find lead-free alternatives.

Half of the global market of actuators is focused in MEMS applications, followed by phone and digital cameras or lenses, fuel injectors and ink cartridges <sup>12</sup>.

## 1.3 MICROSCOPIC PROPERTIES OF ELECTROSTRICTION

---

The ions of a material shift from their original position when it is polarized with an electric field, causing a mechanical strain. The relative displacement of positive and negative ions should erase each other, and the net strain should be null. The energy required to compress an ion-pair ( $U_c$ ) is usually much higher than the energy needed to enlarge it ( $U_e$ ). <sup>1,24</sup> This can be clearly seen from the ion-pair potential with respect to the equilibrium position showed in Figure 1-2. Consequently, the polarization usually increases the ion-pair bond length and result in a positive electrostriction coefficient. However, for some materials, such as defective fluorites, polarization shrinks the ion-pair, causing a negative electrostriction coefficient. <sup>2,3</sup>

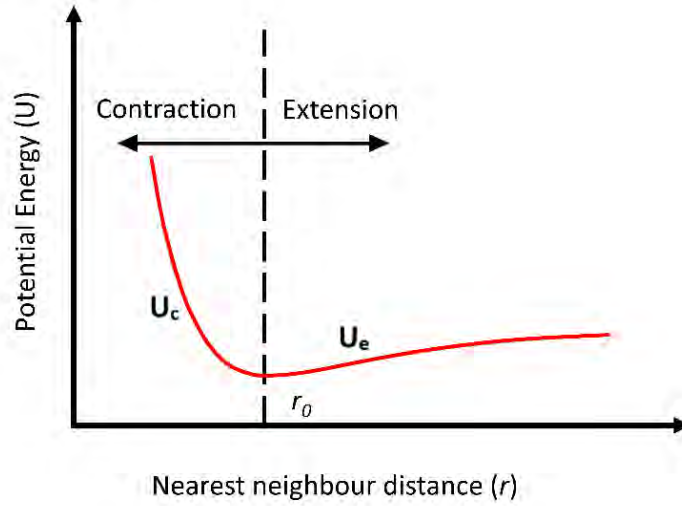


Figure 1-2: Ion-pair potential respect to the nearest neighbor distance in ionic crystal,  $r_0$  is the equilibrium distance between positive and negative ions.

Considering a rigid model of  $+q$  and  $-q$  charged ions, the potential energy function can be described as<sup>1,25,26</sup>:

$$\Delta U = U(r) - U(r_0) = f(r - r_0)^2 - g(r - r_0)^3 \quad 1.6$$

where  $r$  is the relative distance of positive and negative ions and  $r_0$  is the equilibrium position. The harmonic and anharmonic contributions of the energy are represented by  $f$  and  $g$ , respectively. Under an electric field, the strain and polarization can be calculated:<sup>1,25,26</sup>

$$\lambda_1 = \left( \frac{3gq^2}{4f^3r_0^3} \right) E_1^2 \quad 1.7$$

$$P_1 = \left( \frac{q^2}{4fr_0^3} \right) E_1 \quad 1.8$$

As well as the electrostriction coefficient:

$$Q_{11} = \frac{12gr_0^5}{fq^2} \quad 1.9$$

$g/f$  represents the ratio between anharmonic and harmonic energy contribution to the overall ion-pair potential. Therefore, a high anharmonic component corresponds to a high electrostriction coefficient.

$f$  and  $g$  are associated with the material's microscopic properties such as ionic radius and charge, crystal structure and symmetry. Consequently, compounds with similar microscopic environment show similar electrostriction magnitudes.<sup>1–3,26–29</sup>

## 1.4 MACROSCOPIC PROPERTIES OF ELECTROSTRICTION

---

### 1.4.1 Thermal expansion:

In order to describe materials with different anisotropic properties, it is useful to define the hydrostatic electrostriction coefficient  $Q_h$ , as the variation of electrical susceptibility with applied hydrostatic pressure. For isotropic or cubic materials<sup>30</sup>,  $Q_h$  can be written as:

$$Q_h = 0.5 \left( \frac{d\chi}{dp} \right) \approx Q_{11} + 2Q_{12} \quad 1.10$$

where  $Q_{11}$  and  $Q_{12}$  are the longitudinal and transverse electrostriction coefficients, respectively. Newnham investigated various materials and found an empirical relationship between macroscopic physical properties and electrostriction coefficients.<sup>1,2,5</sup> Both the electrostriction and thermal expansion originate from ion-pair potential anharmonicity.<sup>5</sup> The thermal expansion coefficient can, in fact, be written as:

$$\alpha = \frac{3gk_b}{4f^2r_0} \quad 1.11$$

with  $k_b$  being the Boltzmann's constant and  $r_0$  being cation-anion distance at equilibrium. Similarly to electrostriction, thermal expansion coefficient  $\alpha$  is zero when the anharmonic factor  $g$  is 0. Based on Newnham results<sup>2</sup>:

$$\alpha = 4.2 \cdot 10^{-5} Q_h^{0.5} \quad 1.12$$

Thermal expansion and  $Q_h$  are thus related, as both are related to the ion's anharmonic potential.



## 1.4.2 Mechanical and dielectric properties: Newnham's law

Newnham also reported a relationship between  $Q_h$  and elastic/dielectric effects. As a result, the vast majority of electrostrictive materials follow an empirical relationship <sup>2</sup>:

$$|Q_h| \approx 2.37 \cdot \left( \frac{S}{\epsilon_r \epsilon_0} \right)^{0.59} \quad 1.13$$

where  $S$  is the elastic constant, which is equal to the inverse of Young's modulus. Figure 1-3 shows that the logarithm of the electrostriction coefficient depends almost linearly on  $\log(S/\epsilon_0 \epsilon)^{30}$ . Most of the materials follow this relationship, even if they show very different properties.

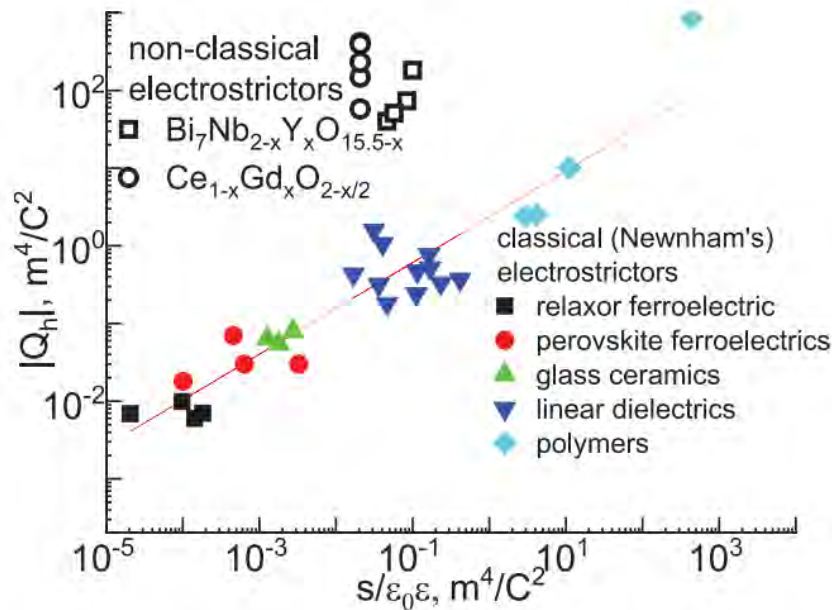


Figure 1-3: Hydrostatic electrostriction coefficient versus elastic compliance and dielectric constant. Several types of materials are reported. Red line: Newnham's law. Reported with permission from Yavo, N. et al. (2016) *Advanced Functional Materials* (20016), John Wiley and Sons and Copyright Clearance Center.

## 1.5 MATERIALS

The plot shown in Figure 1-3 is split into four areas to highlight the different families of materials. The center of the plot (blue triangles) represents materials with high stiffness but low dielectric constant

such as linear dielectrics and glasses ceramics. The left side includes highly dielectric materials such as ferroelectrics (red circles) and relaxors (black squares). On the right side, there are polymers (light blue rhombi), which have low permittivity and low stiffness. On the top, defective oxides are reported as empty circles and squares. These compounds share the same mechanical and electric properties with linear dielectrics. However, they do not follow Newnham's law and show two orders of magnitude higher electrostriction.

### 1.5.1 Linear dielectrics and glasses ceramics

Linear dielectrics are materials whose polarization depends linearly on the electric field. They can be single crystals, glasses or ceramics.<sup>1,2,4</sup> These materials usually have a low dielectric constant ( $\epsilon < 10$ ) and their Young's modulus is around  $Y \approx 10^2$  GPa. Some examples are  $\text{CaF}_2$  single crystal or AlN and ceramics, with  $Q_h = 0.47$  and  $0.3 \text{ m}^4\text{C}^{-2}$  respectively.<sup>2,4</sup> Some ceramics, such as  $\text{BaBi}_2\text{Nb}_2\text{O}_9$  reach high permittivity:  $\epsilon \approx 400$ <sup>31</sup> and  $Q_h = 0.038 \text{ C}^2\text{m}^{-4}$ .<sup>1</sup>

### 1.5.2 Perovskites ferroelectrics and relaxor ferroelectrics

Ferroelectrics are materials with domains that are microscopically polarized in random directions. Like piezoelectrics, it is possible to pole ferroelectrics to enhance their performances. Poling process in fact, aligns the individual dipoles to the high electric field applied, macroscopically observed as domain-wall motion, resulting in a stronger response during operation. Perovskite ferroelectrics show higher dielectric constant with respect to linear dielectrics such as  $\text{SrTiO}_3$  ( $\epsilon = 450$ ),  $\text{PbTiO}_3$  ( $\epsilon = 270$ ) and  $\text{BaTiO}_3$  ( $\epsilon = 1070$ ) but similar Young's modulus<sup>2</sup>. The electrostriction coefficients are in the range of  $Q \approx 0.04 \text{ m}^4\text{C}^{-2}$ .<sup>1,2</sup>

Relaxor is a family of ferroelectrics with peculiar properties such as a gradual phase transition between ferroelectric and paraelectric phase<sup>32,33</sup>. Also, they show a high dielectric constant ( $\epsilon \approx 10^3$ ) that depends strongly on both temperature and frequency<sup>15,32–36</sup>. Relaxor ferroelectrics are generally lead-based perovskites with  $\text{Pb}(\text{B}_1\text{B}_2)\text{O}_3$  structure, where  $\text{B}_1$  and  $\text{B}_2$  are two different ions *i.e.* Na, K. These compounds are frequently used as piezoelectric, but they also possess high electrostriction coefficient. The interest of research and industry started in the '80 thanks to the first electrostrictive relaxors:

$\text{Pb}(\text{Mg}_{1/3}\text{Nb}_{2/3})\text{O}_3$  (PMN),  $\text{Pb}(\text{Zn}_{1/3}\text{Nb}_{2/3})\text{O}_3$  (PZN) and  $\text{Pb}(\text{La}_{0.09}\text{Zr}_{0.65}\text{Ti}_{0.35})\text{O}_3$  (PLZT) were studied thanks to the promising performances, with a strain up to 0.3%.<sup>6, 1,5,6,35,37</sup> The electrostriction coefficients are about  $Q_h = 0.002 \text{ m}^4\text{C}^{-2}$  and  $M = 2 \cdot 10^{-18} \text{ m}^2\text{V}^{-2}$  for PMN.<sup>3</sup> Lead-based piezoelectric and electrostrictors are used in most of transducer and actuator devices<sup>12</sup> in which a combination of massive displacement and high mechanical reliability is needed.<sup>13</sup> Moreover, most of the relaxors are also piezoelectric, and it is possible to combine the two effects.<sup>6</sup> As mentioned before, many efforts have been made to introduce lead-free electromechanical materials, and some relaxor alternatives examples are bismuth or niobium based systems.<sup>12</sup>

### 1.5.3 Ferroelectric polymers

Ferroelectric polymers such as polyvinylidene fluoride (PVDF) and its copolymers, shows drastically different mechanical properties with respect to ceramics and glasses. Polymers are flexible, with a low density and small Young's modulus ( $\approx 10^3 \text{ MPa}$ ). They also display a low dielectric constant ( $\epsilon \approx 10$ ).<sup>2</sup> Under an electric field, polymers deploy considerable strain on the order of 0.25%, giving rise to electrostriction coefficients around  $Q_h \approx 2 \text{ m}^4\text{C}^{-2}$ . Polymers properties include frequency dependent field-induced strain and high Maxwell stress contribution (35-50%)<sup>2</sup>. In terms of displacement, polymers are comparable with the best relaxor electrostrictors (PMN, PZT)<sup>4</sup>. However, polymers do not generate high stress because of the small Young's modulus, making them difficult to integrate into force related applications. Nonetheless, they are cheap, and they comply with complex shapes and surfaces. Polymers are frequently used in composite technology coupled with electromechanical ceramics.<sup>35</sup> The properties of the devices are usually engineered to the specific application, and the connectivity between the two materials has a significant role. Composites materials offer advantages in sonar and medical ultrasonic imaging.<sup>35</sup>

## 1.6 CERIUM OXIDE

Cerium oxide, i.e.  $\text{CeO}_2$ , commonly known as ceria, is a ceramic oxide with cubic fluorite structure (Figure 1-4a). This material is commonly used as three-way-catalyst and as an electrolyte in solid oxide fuel cells (SOFC), due to its high ionic conductivity at intermediate temperatures (500-600°C).<sup>38–40</sup>

Besides these major applications, ceria is also used as an oxygen sensor,<sup>39</sup> a pollutant chemical trap (CO or NO storage)<sup>41</sup> and in water splitting at high temperatures (thermal splitting).<sup>42</sup> In low dimensional structures,  $\text{CeO}_2$  thin films are promising candidates for miniaturized SOFC<sup>43</sup> and memristors<sup>44</sup>. Also, in heterojunctions<sup>45</sup> or superlattices<sup>46</sup> it is possible to increase ceria's ionic conductivity through strain lattice control. Moreover,  $\text{CeO}_2$  is a refractory material and can be coupled with several technological components without any chemical barrier layers.<sup>47</sup>

The key features of ceria are actually linked to the oxidation state of Ce cation, which can switch between 3+ and 4+, depending on the oxygen partial pressure.<sup>39,41,48</sup> This is essential in the catalytic process as well for the oxygen storage<sup>38–40</sup>, as a change of the oxidation state produce a release or trapping of an oxygen atom.

When ceria is set in a reducing environment ( $p_{\text{O}_2} \approx 2.5 \times 10^{-3}$  atm)<sup>49</sup> and high temperatures (1200 °C),<sup>41</sup> oxygen ions leave the lattice, and the material acquires non-stoichiometric features, with the formula:  $\text{CeO}_{2-\delta}$ . This process can be reversed in a high oxygen partial pressure environment. The reaction, written in Kroger-Vink notation, is:



where  $V_O^{\bullet\bullet}$  is a +2 charged oxygen vacancy,  $O_O^{\times}$  is a neutral oxygen atom in its site in the lattice,  $e'$  is an electron in the conduction band and  $1/2O_2(g)$  is half oxygen molecule in the gas phase. This process introduces a large amount of vacancies in the lattice and increases the ionic conductivity of ceria. The electrons formed are localized on Ce cation as a consequence of the reduction  $\text{Ce}^{4+} \rightarrow \text{Ce}^{3+}$ . At high temperatures, the electrons have enough thermal energy to activate the hopping process (*quasi-free*

electrons or small polarons), which contributes to the overall conductivity of ceria, i.e. making it a mixed ionic-electronic conductor (MIEC).<sup>50</sup>

The amount of vacancies increases by substitutional doping with aliovalent cations such as  $\text{Sm}^{3+}$ ,  $\text{Gd}^{3+}$ ,  $\text{Ca}^{2+}$ ,  $\text{Y}^{3+}$ . Gd is mostly used as acceptor dopant, and the effect can be described as:

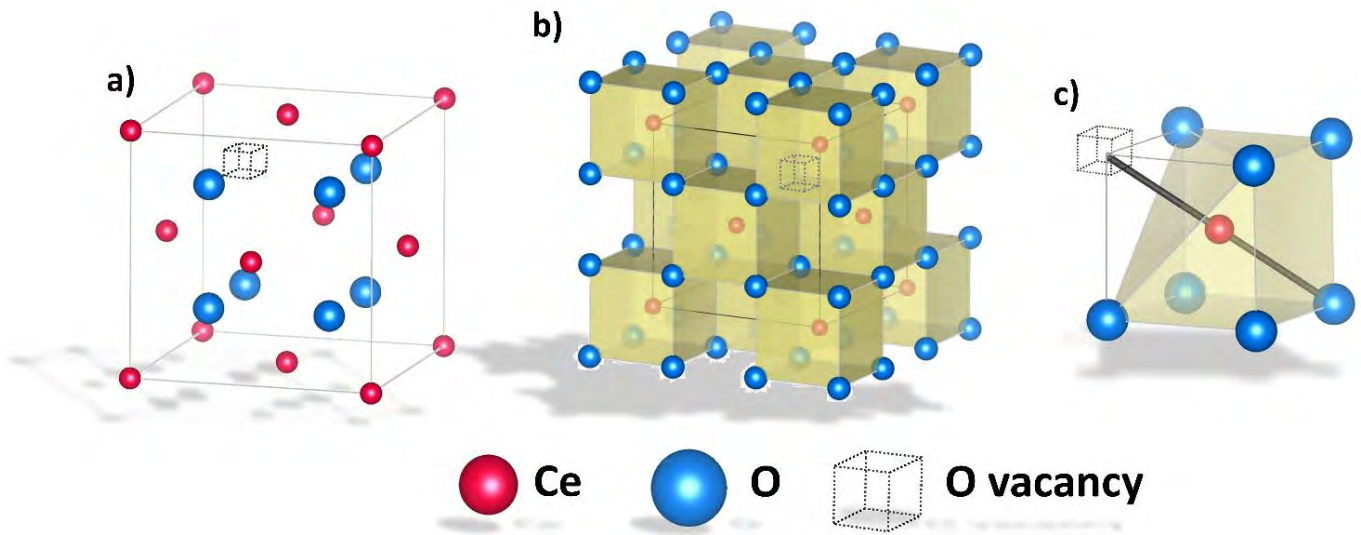
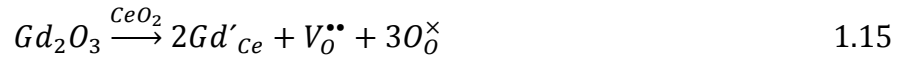


Figure 1-4: a) fluorite structure of ceria with the inclusion of one oxygen vacancy. b) fluorite structure organized as sub-cell units centered in Ce cation. c) a single unit with the inclusion of one oxygen vacancy.

3+ ion doping generates extrinsic vacancies in the lattice, independently from oxygen partial pressure. Also, the process does not generate electrons. The ceria lattice can withstand a high amount of vacancies and dopant. In particular, a large concentration of defects is achievable with 20 mol % Gd doping, resulting in 5% of oxygen sites to be empty.<sup>51</sup> Figure 1-4 shows the lattice structure of ceria with the inclusion of an oxygen vacancy. The fluorite lattice can also be represented by Ce first coordination shells as depicted in Figure 1-4b. Figure 1-4c shows a single coordination cell unit with the inclusion of one oxygen vacancy. The stability limit of the *Fm-3m* fluorite phase is within 20 and 25 mol % Gd doping. For higher values, ceria turns abruptly into *Ia-3* double-fluorite.<sup>51</sup>

## 1.7 ELECTROSTRICTION IN GD-DOPED CERIA

---

The interesting properties of doped ceria extend to its electromechanical features. Starting from 2012 in fact, several works from Igor Lubomirsky's team at the Weizmann Institute of Science reported promising results on particularly high electrostriction in  $\text{Ce}_{0.8}\text{Gd}_{0.2}\text{O}_{1.9}$  (CGO) <sup>52–56</sup>.

CGO's elastic and dielectric properties are similar to other linear dielectrics such as  $\text{CaF}_2$ : the permittivity is stable at low temperatures, with a value of  $\epsilon \approx 28$  from 1 Hz to 1 MHz<sup>57</sup> and with Young's modulus of  $Y = 200$  GPa.<sup>57</sup> However, CGO does not follow the trend expected by Newnham's law (Figure 1-3) and it shows an electrostrictive coefficient of  $Q_h \approx 10^2 \text{ m}^4\text{C}^{-2}$  that is two orders of magnitude higher than similar materials.<sup>30</sup> Additionally, the electromechanical response shows a very high-stress saturation point, with values exceeding 500 MPa.<sup>52</sup> Piezoelectric materials, on the other hand, do not show such high distortion and have a relatively small saturation point<sup>52</sup>. The discovery of the so-called 'giant electrostriction' in CGO makes this class of materials promising as a new generation of electromechanical materials. In addition to the high performances, ceria compounds are environmentally friendly and biocompatible, allowing the use in health applications.<sup>58</sup>

The extraordinary performances of CGO suggest that a mechanism different from classical electrostriction is in play, and many efforts have been made to disclose its origins. The effect is attributed to lattice distortion in the vicinity of oxygen vacancies, in particular close to  $V_{\text{O}}^{\bullet\bullet}$ -Ce pairs. When the electric field is applied, the local geometry rearranges, yielding electrostriction. <sup>52,54,59</sup>

In this thesis, the progress of non-classical electrostriction in Gd-doped ceria research is presented including microscopic explanation, performances and properties in different structures such as thin films, bulk and membranes. For materials with low and stable dielectric constant such as CGO,  $M$  coefficient is preferred over  $Q$ , as it depends only on the applied field. In the following, the electrostriction coefficient will be reported only as  $M$ .

## 1.8 MICROSCOPIC MODEL

---

From the first work, the electromechanical behavior of CGO has been attributed to local distortion in the vicinity of oxygen vacancies.<sup>52</sup> To better understand this mechanism, several studies utilizing X-ray absorption spectroscopy (XAS) have been conducted.<sup>52,54,59</sup> *In-situ* experiments compare measurements in standard condition with measurements under an applied electric field. When using energies close to *L-III* absorption edge of Ce, it is possible to obtain information about Ce's chemical state and surroundings. For the details of XAS technique and results, see sections 2.5 and 5.

The model proposed in literature considers the first coordination cell of a Ce cation composed of seven oxygen atoms and one oxygen vacancy (Figure 1-4c). Let us call this object a  $Ce_{ce}-7O-V_O^{\bullet\bullet}$  unit. The presence of the oxygen vacancy causes an overall deformation of the cell. Figure 1-5 shows the reorganization of the ions in detail. The  $Ce_{ce}-V_O^{\bullet\bullet}$  and  $O-Ce_{ce}$  pairs along the diagonal withstand an increasing on the bond length, while the other six oxygen atoms shift in a position closer to the cation. Previous analysis confirms this interpretation.<sup>51,54,60</sup> In fact, XAS measurements report that Gd-doped ceria presents a decreased average in  $O-Ce_{ce}$  bond length with respect to pure ceria ( $l=2.22$  Å for CGO and  $l=2.34$  Å for  $CeO_2$ ). On the other hand, the  $V_O^{\bullet\bullet}-Ce$  distance increased ( $l=2.62$  Å).<sup>44</sup> The deviation from cubic symmetry causes local elastic field and asymmetric charge distribution. In the presence of the electric field, extended x-ray absorption fine structure (EXAFS) results<sup>54</sup> reported redistribution of the average bond length of Ce-O pairs ( $l=2.33$  Å) that reacquire a cubic structure.<sup>54</sup> In this condition, the distorted CGO cell comes back towards a fully cubic structure. As depicted in Figure 1-5, the electric field induces shrinkage of  $O-Ce_{ce}-V_O^{\bullet\bullet}$  diagonal and an expansion of the remaining  $Ce_{ce}-O$  pairs.

The main electroactive component is represented by the triplet  $O-Ce_{ce}-V_O^{\bullet\bullet}$ . When the electric field is parallel or antiparallel to the diagonal, the distortion of the single cell is at its maximum.<sup>54</sup> In previous work, this concept has been generalized, claiming that an electric field along with [111] direction of the film results in the best performances.<sup>52,54,61</sup> One noticeable effect which is opposite to the effect in classic piezoelectrics, is that in this condition the material shrinks in the direction parallel to the electric field, and expands perpendicularly.

Further findings showed that the Gd does not participate actively on electrostriction effect, as no change in bond length was detected.<sup>52,54</sup> Moreover, it was reported that oxygen vacancies are mostly placed in Ce vicinity, as the defect association energy disfavors large dopants such as Gd.<sup>60</sup> However, Gd doping is still needed so that a large amount of oxygen vacancies is introduced in the lattice, and therefore electrostriction is triggered. Pure ceria in fact, does not display high electromechanical effects, though a small activity was detected for highly defective  $\text{CeO}_{2-\delta}$ .<sup>54</sup>

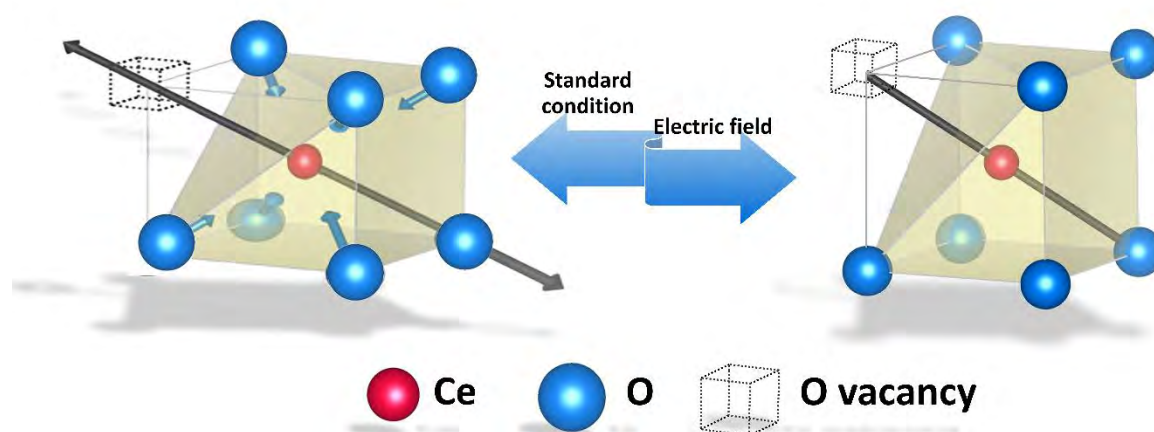


Figure 1-5: Scheme of  $\text{Ce}_{\text{Ce}}\text{-7O-V}_\text{O}^{**}$  unit.. Left: vacancy induced of Ce coordination shell distortion. Right: electric field-induced distortion.

## 1.9 GD-DOPED CERIA THIN FILMS

The earliest results were obtained in polycrystalline Gd doped ceria thin films deposited on Si or glass substrates.<sup>52,53,61,62</sup> These works were mostly carried out on vibrating cantilever, with a multilayered structure of the type Si/bottom electrode/CGO/top electrode. Figure 1-6 shows the cantilever device and the cross-section with the different layers. The electrodes are usually metals: Al, Ti or Cr. *Lubomirsky et al.* reported for the first time a high electrostriction coefficient of  $M = 6.47 \cdot 10^{-18} \text{ m}^2\text{V}^{-2}$ ,<sup>52</sup> while the expected value calculated from Newnham's law is  $\approx 10^{-20} \text{ m}^2\text{V}^{-2}$ . Such discovery represented a breakthrough in the field of electrostrictive materials, as it suggests a new, still unknown mechanism.



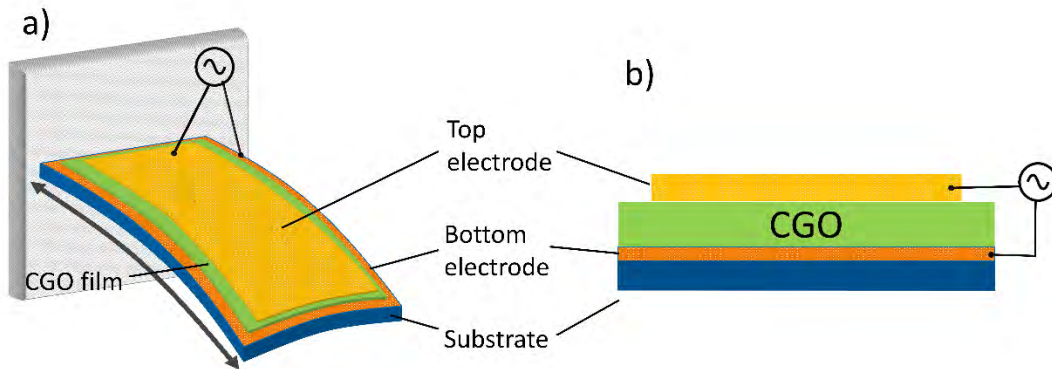


Figure 1-6: a) Cantilever device. One side is clamped/glued, and the other one is free to move. b) Multilayered structure of the samples: Substrate/bottom electrode/CGO/top electrode.

Prolonged electric stress at 45 kV/cm, increases the response of the film from 5 MPa to 20 MPa, with a consequence saturation <sup>52</sup>. Although this behavior might seem similar to the poling effect in ferroelectrics, this mechanism is different as a voltage of opposite polarity does not reduce the response and so it is attributed to defect rearrangement. Moreover, measurements at high temperature (150 °C) decreased the responses of about 50% <sup>52</sup>.

While stable under 100 Hz, the performances dropped quickly for higher frequencies <sup>53</sup>, which is considered a major concern in an application point of view. In fact, many of the commercial devices operate in the range of kHz-MHz in fields such as ultrasound imaging <sup>11</sup>. It is possible to exploit the cantilever mechanical resonance within a narrow window of frequencies, increasing the electromechanical response <sup>53</sup>. However, cantilevers with length in the range of 10 mm resonate at relatively low frequencies  $\approx 100\text{-}300\text{ Hz}$ <sup>53</sup>. For shorter cantilevers, the resonant frequency increases. Additionally, the resonating amplitude decreases by a few orders of magnitude for harmonics next to the first one, making the measurements difficult.<sup>53,62</sup>

Paul Muralt's team of Ecole Polytechnique Fédérale de Lausanne (EPFL) also worked on CGO thin films, reporting an extensive view of the operational condition and challenges <sup>61</sup>. Even though they obtained a slightly lower electrostriction coefficient ( $M=0.9 \cdot 10^{-18}\text{ m}^2\text{V}^{-2}$ ),<sup>61</sup> they confirmed the high-frequency reduction of performances.

The electrodes (Al, Cr and Pt) were shown to have a serious impact on the efficiency and stability of the samples. The bottom metallic electrode in fact, influences the microstructure of the film above<sup>61</sup>. CGO grown on Al showed the highest (111) texturing and fine grains, as well as the best performances. For this reason, an ordered (111) microstructure is thought to promote the electrostriction effect. Metallic electrodes however show frequently pinholes as a consequence of the top-bottom electrodes configuration, and often the samples are damaged by Joule heating.<sup>61</sup>

The CGO thin films reported are deposited at room or low temperatures<sup>52,53,61</sup>. An annealing process is not necessary<sup>61</sup>, as RT deposited films displayed high electrostrictive performances,

Varying the Gd-dopant amount seems to influence the electromechanical activity.<sup>54</sup> Gd in fact, introduces in ceria lattice oxygen vacancies. As electrostriction in CGO is related with vacancies, a higher amount of Gd increases the electromechanical response, up to  $15.5 \cdot 10^{-18} \text{ m}^2\text{V}^{-2}$  for 33 *mol %* CGO.<sup>54</sup> Nonetheless, this result is not clear, as successive works on 10 *mol %* CGO bulk showed a higher response than in 20 *mol %*, suggesting that not only the amount of vacancies determine the magnitude of electrostriction effect. Additionally, between 20 and 25% of Gd doping,  $\text{CeO}_2$  turns progressively  $\text{Ce}_2\text{O}_3$ <sup>51</sup>. Therefore, the interpretation of the effect for doping close to the phase transition is still unexplored. Undoped ceria ( $\text{CeO}_{1.96}$  and  $\text{CeO}_{1.99}$ ) showed a small electrostriction effect as well, strengthening the hypothesis that vacancies are the key point on the effect.<sup>51</sup>

Despite several operative challenges, CGO thin films showed high performances as well as promising advantages. With an electrostrictive coefficient up to  $15.5 \cdot 10^{-18} \text{ m}^2\text{V}^{-2}$ , CGO can be deposited on cheap and common substrates (Si, glass) and electrodes (Al, Ti, Cr, Pt). Processes like poling and annealing are not necessary. Diffusion barriers are unnecessary as well. Depending on the cantilever length, mechanical resonance can be exploited for higher performances, even if the kHz range remains unreachable. Other limitations include the stability of the device, detaching of the electrodes and Joule heating.

## 1.10 ELECTROSTRICTION IN BULK CGO

---

Electrostriction in bulk was first described in 10 mol% Gd-doped ceria by Yavo *et al.*<sup>63</sup> Bulk analysis brings several possibilities to understand the electrostrictive behavior of ceria better. In bulk, specific features can in fact influence the electrostriction effect, such as grain size, grain boundaries, strain saturation and density<sup>39</sup>. The development of thick devices is an essential point in application-focused research, as several actuator devices are made of bulk materials (multilayered actuators, CYMBALS)<sup>9</sup>.

In this first work, ceramic pellets of a few millimetres thickness were produced with different processes condition. By varying the temperature and its gradient during sintering, it was possible to control the grain size<sup>63</sup>. The electrostrictive analysis confirmed that CGO shrank along with the electric field and expanded in the out-of-plane direction, as expected from the microscopic model<sup>54</sup>. Once more, the electromechanical response in bulk decreased for low frequencies. In particular, it is possible to describe the relationship between the electrostriction coefficient and frequency as a non-ideal Debye function:

$$M_{33}(f) = \frac{M_{33}^0}{\sqrt{(\tau \cdot f)^{2+\alpha} + 1}} + M_{33}^\infty \quad 1.16$$

where  $M_{33}^0$  and  $M_{33}^\infty$  are electrostrictive coefficients for low and high frequencies respectively, and  $\tau$  is the relaxation time. The quantity  $\alpha=-0.3-1.3$  is the non-ideality factor that suggests a wide distribution of relaxation times of part of the material. These findings indicate that electrostriction in CGO is a slow driven process in which the electroactive complexes reorganize with different timing, probably due to a large rearrangement of atomic clusters. Figure 1-7 shows the typical M behavior as a function of frequency in bulk samples<sup>64</sup>.

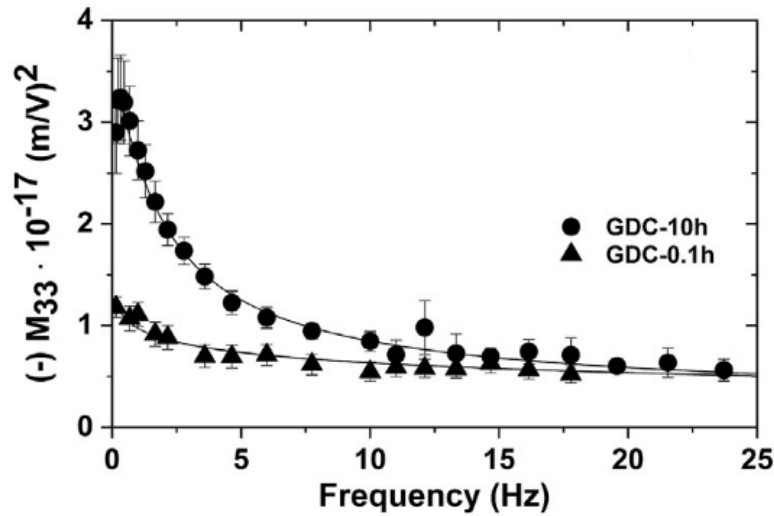


Figure 1-7: Relaxation of electrostriction coefficient depending on the frequency in bulk CGO. Ref: [64]

Besides the new insight into the dynamics of distortion, the experiment on CGO bulk showed high electrostriction coefficients  $M_{33}^0 \approx (2-20) \cdot 10^{-17} \text{ m}^2\text{V}^{-2}$  for low frequencies (0.1-1 Hz)<sup>63</sup>. Interestingly, the mechanical strain displayed saturation at low electric fields ( $\approx 2.5 \text{ kV/cm}$ ), while in thin films this effect is absent even for higher fields up to  $60 \text{ kV/cm}$  at  $0.1 \text{ Hz}$ .<sup>52</sup> Figure 1-8 shows an example of electromechanical response on CGO bulk<sup>64</sup>. As the electromechanical properties in thin films are not affected by the grain size, the reason for the scattered performances and saturation was attributed to the grain boundaries. In bulk materials in fact, they behave as charge traps and provide a non-uniform voltage distribution<sup>63,64</sup>.

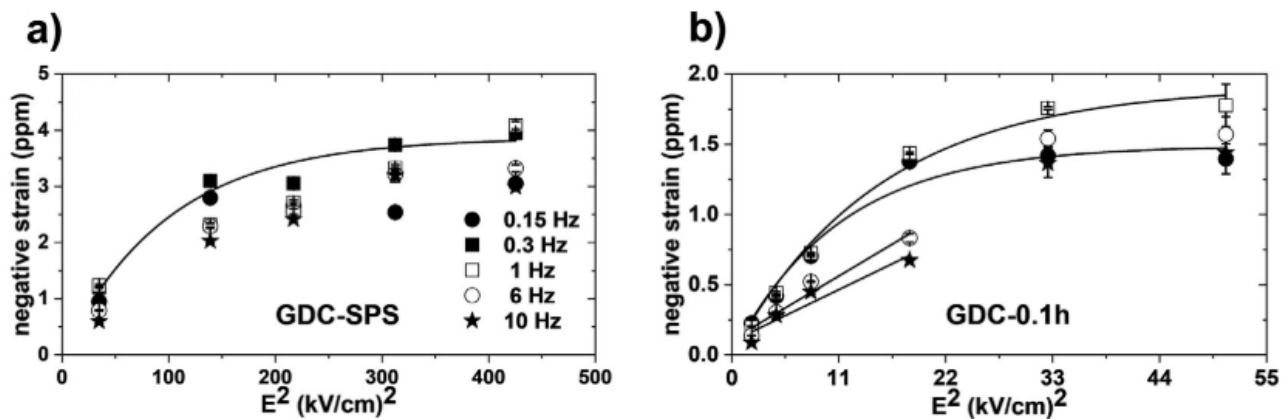


Figure 1-8: Electromechanical response in CGO bulk for different sintering processes. Saturation is visible in both. Ref: [64].

It is worth to notice that giant electrostriction was also reported in bulk (Y, Nb)-stabilized  $\delta\text{-Bi}_2\text{O}_3$ .<sup>30</sup> As visible in Figure 1-3, bismuth oxides show an electrostriction coefficient similar to the one of CGO. However, it did not display frequency relaxation or strain saturation. The choice to study this material is not random;  $\delta\text{-Bi}_2\text{O}_3$  present a fluorite structure and can accommodate a large amount of vacancies exactly like CGO. Following this method, Y-stabilized  $\text{ZrO}_2$  (YSZ) pellets were also measured. YSZ is also a defective oxide with fluorite structure, but it did not show any electromechanical effect.

Overall, bulk CGO presents fascinating properties and a generally high electrostriction coefficient. The saturation effect and non-ideal-Debye relaxation help to understand the dynamics of the effect as a slow-kinetic complex lattice rearrangement. In addition, tuning the configuration of grain boundaries enhances the electrostrictive response by limiting ionic migration. However, several technologic difficulties have been presented, such as decreased performances at high frequencies.

## 1.11 CGO MEMBRANES

As devices in the form of membranes are used in different fields as pumps or acoustic wave generators, several works report the development of free-standing 20% CGO.<sup>55,56,65</sup>

The fabrication method consists of sequential deposition on a Si substrate of the bottom metallic electrode and CGO film, followed by a top electrode (sandwiched configuration). The substrate is then

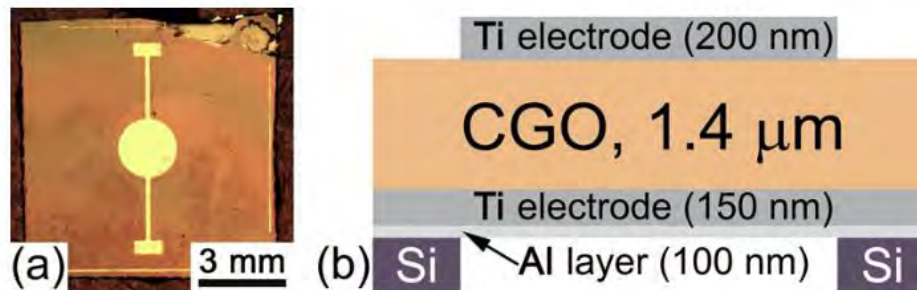


Figure 1-9: a) image of a CGO membrane. b) cross section scheme of the device. Reported with permission from Mishuk et al. *Appl. Phys. Lett.* **110**, 142902 (2017) by AIP Publishing and Copyright Clearance Center.

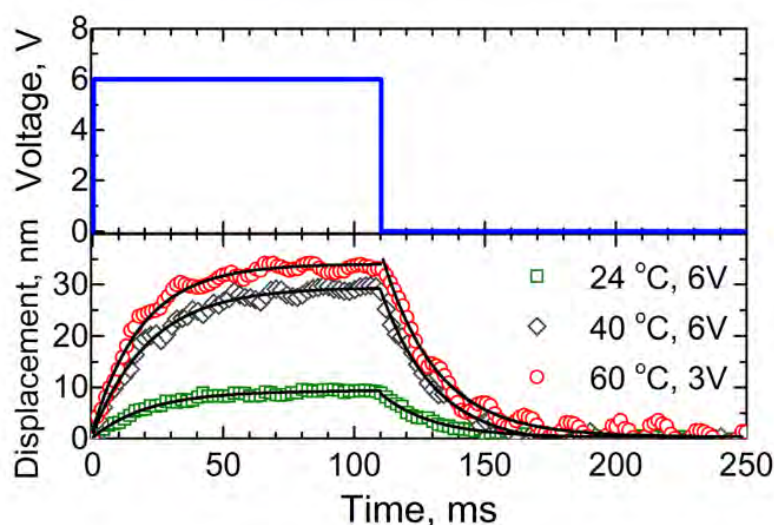


Figure 1-10: Membrane response to squared electric field wave for different temperatures and voltages. Reported with permission from Mishuk et al. *Appl. Phys. Lett.* **110**, 142902 (2017) by AIP Publishing and Copyright Clearance Center.

removed by reactive ion etch (RIE)<sup>55</sup>, leaving the structure in a self-supported state (Figure 1-9). The devices obtained had roughly 2 mm diameters.<sup>55,56,65</sup> Due to the residual of film strain, the CGO membranes show a buckled surface, which can be removed by an annealing process before substrate etching. The fabrication process resulted in being reliable. It was reported that close to 100% of the produced devices were functioning.<sup>55</sup>

As for bulk and thin films, the electromechanical responses decreased with the increase of frequency, suggesting once more a typical slow-kinetic process which is characteristic of the material rather than the device. In general, CGO membranes electrostriction coefficient is similar to the supported thin film counterpart ( $M = 4\text{--}5 \cdot 10^{-18} \text{ m}^2\text{V}^{-2}$ )<sup>55,65</sup>, but with a vertical displacement for 40 kV/cm and low frequencies within (0.1-10Hz) up to 500 nm as a result of the absence of the substrate.<sup>55</sup> Due to the slow process, a slight hysteresis was found occasionally.<sup>65</sup> Such high distortion is easy to detect and allows the performance of detailed measurements on the reaction and relaxation time of membranes subjected to squared waves (on-off states). At low frequencies, the characteristic time (20 ms) is independent of the amplitude of electric field and sample temperature (Figure 1-10), but it is not clear if thermal expansion contributes in this effect.<sup>65</sup> As a matter of fact, membranes frequently display Joule heating because of film cracks as a consequence of high displacement<sup>65</sup>. At high frequencies in

particular, the overall displacement effect was attributed to thermal expansion. It was reported that under 66 kV/cm and  $f > 100$  Hz, the temperature at the center of the membrane increased by 8 K.<sup>55</sup>

The electromechanical response as a function of temperature has been measured up to 60°C, showing a progressive increase in the performances, although the effect has been attributed to Schottky barrier at the electrode-film interface<sup>65</sup>.

As for thin films, the choice of electrodes is a key factor in the overall performances and stability<sup>61</sup>. Up to now, only metallic electrodes have been used. Al, Ni and Cr in particular, were reported to seriously hinder electrostrictive properties, making it impossible to evaluate any activity.<sup>55</sup> Ti in the other hand allowed a clean and measurable response.<sup>55</sup> This result is explained by the low contact resistance at Ti-CGO interface that was in the order of k $\Omega$ , while for the other metals it resulted in three orders of magnitude higher. If the applied field is oscillating, membranes sometimes show a double harmonic oscillation that is two vibration modes which depend on the first and the second harmonics of the field. The reason is mainly attributed to the different properties of top and bottom electrodes, such as microstructure quality, mechanical evolution under electrical stress, but also to chemo-mechanical process at the Ti-film interface.<sup>55,56</sup>

In summary, free-standing fabrication methods are well suited for Gd-doped ceria films and allow the production of large membranes (up to 2 mm) with a thickness of around 2  $\mu\text{m}$ . These devices show performances similar to thin films while having much higher displacement with no sign of saturation, due to the self-supported structure. Besides the well-known limitations in the high-frequency area, membranes seem to suffer from stability problems. Al, Ni and Cr electrodes in fact nullify electromechanical response. Ti in the other hand generates a double harmonic oscillation that suggests operative malfunctioning of top-bottom electrodes pair and chemo-mechanical process at the film interfaces<sup>55</sup>. Finally, Joule heating has a serious contribution to the overall performances, and it is the first effect at high frequencies<sup>55</sup>.

Table 1-1: Electrostriction coefficients  $M_e$  in thin films, bulk and membranes are reported, including its behavior depending on frequency and temperature. Strain saturation and Joule heating effect are also reported.

Electrostriction in:	$M_e$ ( $\text{m}^2\text{V}^{-2}$ )	Frequency	Temperature	Saturation	Joule heating
<b>Thin films</b> <sup>52-54</sup>	$(6-15) \cdot 10^{-18}$	Decreases	decreases	No	At high electric field
<b>Bulk</b> <sup>63</sup>	$(0.2-20) \cdot 10^{-17}$	Decreases	No data	After 2 kV/cm	No
<b>Membranes</b> <sup>55,56,65</sup>	$(4-5) \cdot 10^{-18}$	decreases	Increases (electrode effect)	no	At high frequencies

To summarize the main properties of each device, Table 1-1 shows the values of the electrostriction coefficient for thin films, bulk and membranes, including the relationship with the principal influencing factor. Bulk materials are less subjected to instabilities such as joule heating and electrodes blocking barrier when compared to the thin films. However, bulk materials present saturation early. Moreover, the complex microstructure has to be taken into account. The main problems of thin films are Joule heating and the coupling with the electrodes.

## 1.12 THESIS GOAL AND APPROACH

In this thesis an extended view of electrostriction mechanism and performances in different structures are given, but also several challenges are reported.

From an application point of view, full stability is still not obtained, since poor electrodes compatibility and thermal expansion hinder performances and cause mechanical failure. Extensive work is necessary to find the best configuration for working and reliable devices.

Moreover, identifying the essential factors that contribute to electrostriction is fundamental to understand the mechanism better, and also to achieve control of the electrostriction properties of the material.



This Ph.D. project aims to identify a methodology to stabilize and tailor the electrostrictive properties of Gd-doped ceria in thin films and to understand the essential mechanism in relation to microstructure and oxygen vacancies configuration.

This research includes:

- Design of an experimental setup for electromechanical measurements, suitable for both thin films and bulk materials' characterization.
- Development of stable electrostrictive thin films, including coupling with electrodes and configuration of the device.
- New insight into the mechanism, by means of electrostriction geometric analysis.
- Enhance of the performances through microstructure and strain control.

## 1.13 THESIS OUTLINE

---

After this first introductory section, five chapters will follow describing the theory, methods, and results of the Ph.D. project.

Chapter 2 will describe the techniques used for the fabrication and characterization of CGO thin films as well as the theory for data analysis. The first section presents the pulsed laser deposition (PLD) as the principal thin films fabrication method. Then, the sub-nanoscale experimental setup designed for electromechanical analysis is described in detail as well as other techniques such as X-ray diffraction (XRD) and X-ray absorption spectroscopy (XAS).

Chapter 3 focuses on the cantilever device stability and mechanical enhancement. The thin film/electrodes coupling issue are discussed and addressed. Furthermore, an alternative configuration is presented and examined as a solution for Joule heating problem. Then, the final section briefly describes the influence of grain boundaries in bulk CGO electrostrictive properties.

Chapter 4 gives an extensive analysis of the microstructure influence on electrostriction geometry and performance. The first section focuses on the fabrication method of CGO epitaxial thin film with

different crystal orientation. Then, the relationship between the control of the electric field direction and the resulting properties are addressed. As a consequence of asymmetries found in electrostrictive behavior, a microscopic model of electrostriction atomic distortion is proposed.

The chapter 5 is about the enhancement of electrostriction in low dimensional strained thin films and vacancies inclusion by defect creation. This analysis was performed using XANES. Then, high frequency and low temperatures electrostrictive behavior of bulk ceria are studied with the support of XAS measurements.

Chapter 6 includes then conclusive remarks and suggestions for future work.

## 1.14 REFERENCES

---

- <sup>1</sup> F. Li, L. Jin, Z. Xu, and S. Zhang, Appl. Phys. Rev. **1**, (2014).
- <sup>2</sup> R.E. Newnham, V. Sundar, R. Yimnirun, J. Su, and Q.M. Zhang, J. Phys. Chem. B **101**, 10141 (1997).
- <sup>3</sup> R.E.N. V. Sundar, J.-F. Li, D. Viehland, Mater. Res. Bull. **31**, 555 (1996).
- <sup>4</sup> R. Yimnirun, P.J. Moses, R.E. Newnham, and R.J. Meyer, J. Electroceramics **8**, 87 (2002).
- <sup>5</sup> K. Uchino, S. Nomura, L.E. Cross, R.E. Newnham, and S.J. Jang, J. Mater. Sci. **16**, 569 (1981).
- <sup>6</sup> G.H. Haertling, J. Am. Ceram. Soc. **82**, 797 (1999).
- <sup>7</sup> S.H. Baek, J. Park, D.M. Kim., V.A. Aksyuk, and R.R. Das, Science (80-. ). **334**, 958 (2011).
- <sup>8</sup> N.N.G. Jones T.B., *Electromechanics and MEMS* (Cambridge University Press, 2013).
- <sup>9</sup> R.J. Meyer, A. Dogan, C. Yoon, S.M. Pilgrim, and R.E. Newnham, Sensors Actuators, A Phys. **87**, 157 (2001).
- <sup>10</sup> F. Restagno, J. Crassous, E. Charlaix, and M. Monchanin, Meas. Sci. Technol. **12**, 16 (2001).
- <sup>11</sup> K. Martin, B. Lindsey, J. Ma, M. Lee, S. Li, F. Foster, X. Jiang, and P. Dayton, Sensors **14**, 20825 (2014).
- <sup>12</sup> W. Jo, R. Dittmer, M. Acosta, J. Zang, C. Groh, E. Sapper, K. Wang, and J. Rödel, J. Electroceramics **29**, 71 (2012).
- <sup>13</sup> K. Uchino, J Electroceram **20**, 301 (2008).
- <sup>14</sup> D. Damjanovic, *Hysteresis in Piezoelectric and Ferroelectric Materials* (2005).
- <sup>15</sup> L.E. Cross, Ferroelectrics **76**, 241 (1987).
- <sup>16</sup> J. Paulo Davim, *Mechatronics and Manufacturing Engineering* (Woodhead Publishing Limited, 2012).
- <sup>17</sup> P. Muralt, J. Micromechanics Microengineering **10**, 136 (2000).
- <sup>18</sup> E. Pengwang, K. Rabenorosoa, M. Rakotondrabe, and N. Andreff, Micromachines **7**, 1 (2016).

- <sup>19</sup> D. Isarakorn, A. Sambri, P. Janphuang, D. Briand, and S. Gariglio, J. Micromechanics Microengineering Ep. **20**, (2010).
- <sup>20</sup> P. Muralt, Integr. Ferroelectr. **17**, 297 (1997).
- <sup>21</sup> V. V. Shvartsman, A.L. Kholkin, M. Tyunina, and J. Levoska, Appl. Phys. Lett. **86**, 222907 (2005).
- <sup>22</sup> R.A. Dorey and R.W. Whatmore, J. Electroceramics **19** (2004).
- <sup>23</sup> [https://ec.europa.eu/environment/waste/rohs\\_eee/legis\\_rohs1\\_en.htm](https://ec.europa.eu/environment/waste/rohs_eee/legis_rohs1_en.htm)
- <sup>24</sup> C. Kittel, *Introduction to Solid State Physics* (John Wiley & Sons, Inc., 2005).
- <sup>25</sup> K. Uchino, S. Nomura, K. Vedam, R.E. Newnham, and L.E. Cross, Phys. Rev. B **29**, 6921 (1984).
- <sup>26</sup> V. Sundar and R.E. Newnham, Mater. Res. Bull. **31**, 545 (1996).
- <sup>27</sup> T. Yamada, J. Appl. Phys. **43**, 328 (1972).
- <sup>28</sup> J.J. Wang, F.Y. Meng, X.Q. Ma, M.X. Xu, and L.Q. Chen, J. Appl. Phys. **108**, (2010).
- <sup>29</sup> A.W. Warner, M. Onoe, and G.A. Coquin, J. Acoust. Soc. Am. **42**, 1223 (1967).
- <sup>30</sup> N. Yavo, A.D. Smith, O. Yeheskel, S. Cohen, R. Korobko, E. Wachtel, P.R. Slater, and I. Lubomirsky, Adv. Funct. Mater. **26**, 1138 (2016).
- <sup>31</sup> M.A.Æ.Z. Ujma and Æ.M. Pawe, 5317 (2006).
- <sup>32</sup> W. Yang, F. Fang, and D.N. Fang, Compr. Struct. Integr. **2**, 645 (2003).
- <sup>33</sup> A.A. Bokov and Z.G. Ye, J. Mater. Sci. **41**, 31 (2006).
- <sup>34</sup> A. You, M.A.Y. Be, and I. In, Appl. Phys. Lett. **95**, 1 (2009).
- <sup>35</sup> A.J. Moulson and J.M. Herbert, Wiley 339 (2003).
- <sup>36</sup> Heywang W., K. Lubitz, and W. Wersing, *Piezoelectricity* (2008).
- <sup>37</sup> G.H. Blackwoodt and M.A. Ealey, Smart Mater. Struct. **2**, 124 (1993).

- <sup>38</sup> J.L.M. Rupp and L.J. Gauckler, *Solid State Ionics* **177**, 2513 (2006).
- <sup>39</sup> V. Esposito and E. Traversa, *J. Am. Ceram. Soc.* **91**, 1037 (2008).
- <sup>40</sup> E. Gourba, P. Briois, A. Ringuedé, M. Cassir, and A. Billard, *J. Solid State Electrochem.* **8**, 633 (2004).
- <sup>41</sup> M. Melchionna and P. Fornasiero, *Mater. Today* **17**, 349 (2014).
- <sup>42</sup> V. Esposito, D.W. Ni, S. Sanna, F. Gualandris, and N. Pryds, *RSC Adv.* **7**, 13784 (2017).
- <sup>43</sup> N. Pryds and V. Esposito, *J. Electroceramics* **38**, 1 (2017).
- <sup>44</sup> A. Younis, D. Chu, X. Lin, J. Yi, F. Dang, and S. Li, *ACS Appl. Mater. Interfaces* **5**, 2249 (2013).
- <sup>45</sup> M.C. Göbel, G. Gregori, and J. Maier, *Phys. Chem. Chem. Phys.* **13**, 10940 (2011).
- <sup>46</sup> S. Sanna, V. Esposito, A. Tebano, S. Licoccia, E. Traversa, and G. Balestrino, *Small* **6**, 1863 (2010).
- <sup>47</sup> S. Santucci, H. Zhang, S. Sanna, N. Pryds, and V. Esposito, *APL Mater.* **7**, 071104 (2019).
- <sup>48</sup> R. Schmitt, J. Spring, R. Korobko, and J.L.M. Rupp, *ACS Nano* **11**, 8881 (2017).
- <sup>49</sup> S. Ackermann and A. Steinfeld, *J. Phys. Chem* 5216–5225 (2014).
- <sup>50</sup> S.R. Bishop, T.S. Stefanik, and H.L. Tuller, *Phys. Chem. Chem. Phys.* **13**, 10165 (2011).
- <sup>51</sup> A. Kossoy, Q. Wang, R. Korobko, V. Grover, Y. Feldman, E. Wachtel, A.K. Tyagi, A.I. Frenkel, and I. Lubomirsky, *Phys. Rev. B* **87**, 054101 (2013).
- <sup>52</sup> R. Korobko, A. Patlolla, A. Kossoy, E. Wachtel, H.L. Tuller, A.I. Frenkel, and I. Lubomirsky, *Adv. Mater.* **24**, 5857 (2012).
- <sup>53</sup> R. Korobko, E. Wachtel, and I. Lubomirsky, *Sensors Actuators, A Phys.* **201**, 73 (2013).
- <sup>54</sup> R. Korobko, A. Lerner, Y. Li, E. Wachtel, A.I. Frenkel, and I. Lubomirsky, *Appl. Phys. Lett.* **106**, 042904 (2015).
- <sup>55</sup> E. Mishuk, E. Makagon, E. Wachtel, S.R. Cohen, R. Popovitz-Biro, and I. Lubomirsky, *Sensors Actuators, A Phys.* **264**, 333 (2017).

- <sup>56</sup> E. Mishuk, A.D. Ushakov, S.R. Cohen, V.Y. Shur, A.L. Kholkin, and I. Lubomirsky, *Solid State Ionics* **327**, 47 (2018).
- <sup>57</sup> V. Shelukhin, I. Zon, E. Wachtel, Y. Feldman, and I. Lubomirsky, *Solid State Ionics* **211**, 12 (2012).
- <sup>58</sup> C. Sun, H. Li, and L. Chen, *Energy Environ. Sci.* **5**, 8475 (2012).
- <sup>59</sup> Y. Li, O. Kraynis, J. Kas, T.C. Weng, D. Sokaras, R. Zacharowicz, I. Lubomirsky, and A.I. Frenkel, *AIP Adv.* **6**, (2016).
- <sup>60</sup> A. Kossoy, A.I. Frenkel, Q. Wang, E. Wachtel, and I. Lubomirsky, *Adv. Mater.* **22**, 1659 (2010).
- <sup>61</sup> M. Hadad, H. Ashraf, G. Mohanty, C. Sandu, and P. Murali, *Acta Mater.* **118**, 1 (2016).
- <sup>62</sup> A.D. Ushakov, N. Yavo, E. Mishuk, I. Lubomirsky, V.Y. Shur, and A.L. Kholkin, *KnE Mater. Sci.* **1**, 177 (2016).
- <sup>63</sup> N. Yavo, O. Yeheskel, E. Wachtel, D. Ehre, A.I. Frenkel, and I. Lubomirsky, *Acta Mater.* **144**, 411 (2018).
- <sup>64</sup> A. Kabir, S. Santucci, N. Van Nong, M. Varenik, I. Lubomirsky, R. Nigon, P. Murali, and V. Esposito, *Acta Mater.* **174**, 53 (2019).
- <sup>65</sup> A.D. Ushakov, E. Mishuk, E. Makagon, D.O. Alikin, A.A. Esin, I.S. Baturin, A. Tselev, V.Y. Shur, I. Lubomirsky, and A.L. Kholkin, *Appl. Phys. Lett.* **110**, 142902 (2017).

## 2 FABRICATION AND CHARACTERIZATION

In this chapter, I present the details of the experimental characterization and the tools used in this research, including the samples' deposition method, the electromechanical characterization setups as well as the structural analyzation techniques, *i.e.* X-ray absorption spectroscopy which was used for in-depth material chemical and microscopic properties.

### 2.1 PULSED LASER DEPOSITION (PLD)

PLD is a physical vapor deposition technique, in which a high power laser hits a target and vaporizes the material that is deposited as a thin films<sup>1</sup>. Figure 2-1 schematically shows a PLD setup. The growth is carried out in high vacuum conditions (in the range of  $10^{-8}$  mbar), often with a background gas flux such as  $O_2$  and  $N_2$ . The most used laser sources are KrF excimer laser for ultra-violet (UV) wavelengths and

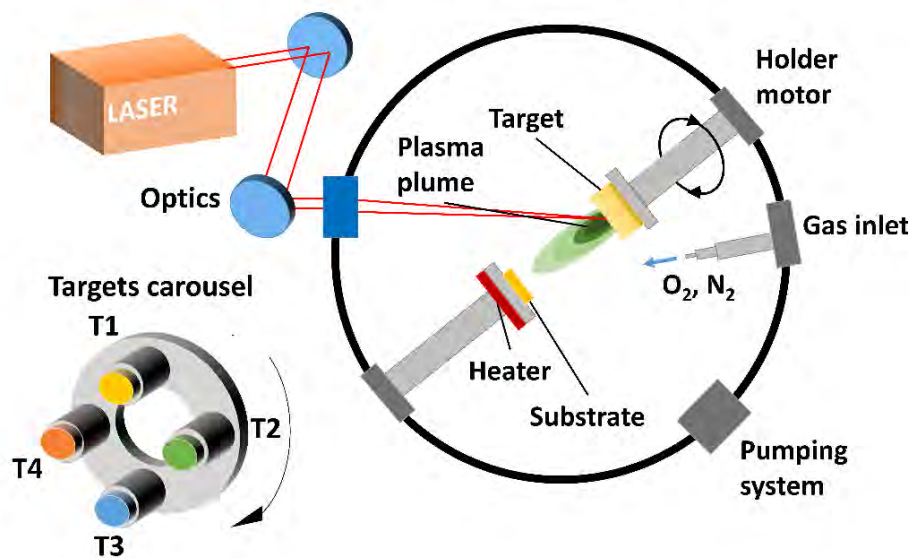


Figure 2-1: Schematic of a PLD setup and targets carousel.

Nd:YAG laser for infrared (IR). Short pulses with high fluency ( $J/cm^2$ ) hit a target of the material to be deposited, creating a plasma plume which propagates towards the substrate. As a result, atoms, ions

and clusters are ejected from the target in the form of a “plasma plume”. The “plasma plume” consists of species such as ions, electrons and radicals all ejected from the target and directed towards the substrate. Due to the high energy of the laser, When these species arrive at the substrate, the film grows with dynamics that depend on several factors such as laser energy, gas pressure, temperature and substrate-target distances. PLD has significant benefits including preservation of stoichiometry of complex oxide systems<sup>2</sup> and control of the growth on a monolayer resolution, i.e. allows depositing extremely thin layers with just a unit cell or even sub-unit cell of thickness<sup>3,4</sup>. Consequently, PLD is particularly suitable for ultra-thin films<sup>5,6</sup>, buffer layers<sup>7,8</sup>. By varying the targets during the deposition (carousel in Figure 2-1, multilayers or heterostructures structures can be fabricated<sup>9–11</sup>. PLD setups can be coupled with many in-situ techniques that allows surface, chemical and thickness characterization, e.g. Some examples are X-ray photoemission spectroscopy (XPS)<sup>12,13</sup>, reflection high/low energy electron diffraction (RHEED-LEED)<sup>12,14</sup> and scanning tunneling microscopy (STM)<sup>14</sup>.

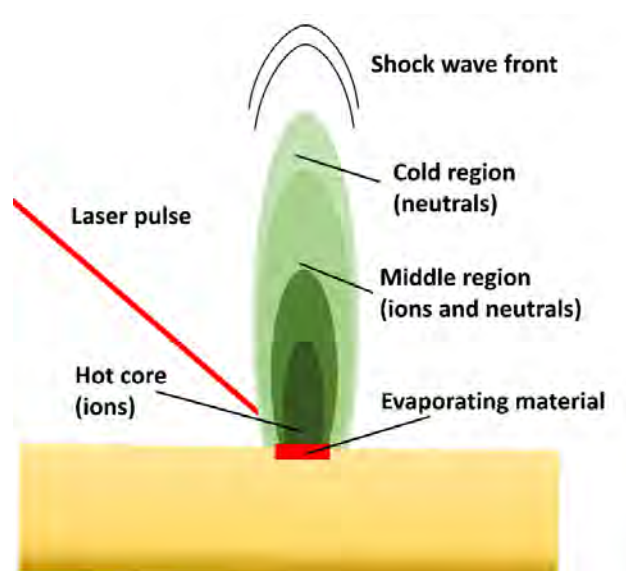


Figure 2-2: Schematic of the ablation process.

Two steps can summarize the PLD process: plume formation and dynamics, and film growth at the substrate.

The plume formation takes place when a pulsed laser beam causes a rapid removal of material from a target. When the laser light (photons) hits the target, the photons are converted first into electronic excitations and then into thermal and chemical energy. If the energy absorbed by the atoms in the targets is larger than their binding energy ( $E_{\text{abs}} > E_{\text{b}}$ ), ions leave the target with a kinetic



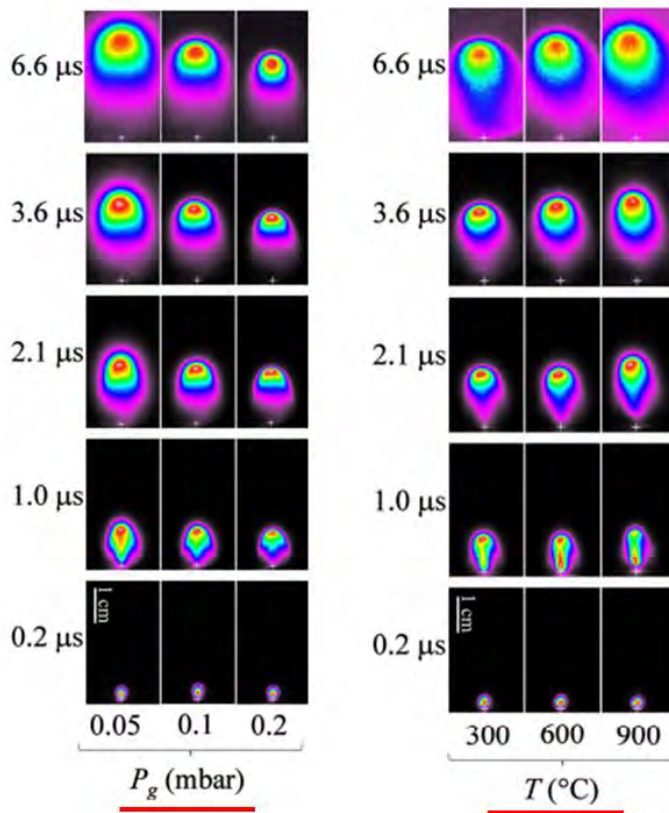


Figure 2-3: plume time evolution depending on pressure and temperature. Reported with permission from Sambri et al., *Journal of Applied Physics* 104, 053304 (2008), AIP Publishing and Copyright Clearance Center.

energy  $E_{\text{kin}} = E_{\text{abs}} - E_b > 0$ <sup>1</sup>. If the energy is too small, the laser simply heats the material. Figure 2-2 shows the ablation process and the composition of the plume: a hot core at the target and progressively colder regions<sup>1</sup>. The plume dynamics are dependant on the environmental parameters such as temperature and pressure<sup>1,15–17</sup>, as depicted in Figure 2-3<sup>15</sup>. For high temperatures, the propagation of the ions occurs faster, and the background gas resistance reduces<sup>15</sup>. High pressure on the other hand, slows down the high energy ions due to scattering, thus reduces the deposition rate. When the flux of background gas is high, the plume will be smaller and its propagation speed will be slower<sup>15</sup>.

When the species ejected from the target hit the substrates, they can stick to the surface (adatoms) and start the growing process. The growth is usually not in thermodynamic equilibrium condition<sup>1</sup>. The limited surface available and the supersaturation of the species during laser pulses cause a large nucleation rate. Consequently, different growth modes can occur and are dominated by kinetic effects<sup>1</sup>.

The diffusion coefficient  $D_s$  is an essential kinetic parameter as it describes the average distance of adatoms before being trapped (free path). The simplest case to define the diffusion coefficient is when the deposited material is the same as the substrate (homoepitaxial growth):

$$D_s = \nu a^2 \exp\left(-\frac{E_a}{k_b T}\right) \quad 2.1$$

$E_a$  is the activation diffusion energy,  $\nu$  is the jump attempt frequency and  $a$  the jump distance. The temperature is the only parameter that can be controlled experimentally. The consequent free path is defined as:

$$l_D = \sqrt{D_s \tau} \quad 2.2$$

where  $\tau$  is the time before the re-evaporation of the atom from the surface. High substrate temperature allows the particles to rearrange in a condition closer to thermodynamic equilibrium. High background gas pressure can modify the growth dynamics as it is needed to provide the correct stoichiometry from the target. Three modes of growth are possible: step-flow, layer-by-layer and 3D island growth.

In the step-flow growth, the steps along the substrate surface in which the atoms nucleate at the step edges. In the layer-by-layer growth, the deposited material creates islands that grow across the surface until they come into contact. This process is called coalescence. The islands expand until the single layer is completed and another one is started. Finally, in the 3D island growth, in which the material can nucleate on top of existing islands.

The growing mode can significantly influence the overall microstructure of the film. Let us considering CGO and YSZ as an example. *Infortuna et al.* studied their microstructure and crystallinity depending on pressure and temperature in PLD thin films on Si substrates<sup>18</sup>. Figure 2-4 shows the microstructure of the films obtained for different combinations of parameters. Generally, the microstructure is columnar with vertical grain boundaries. At low pressures, the films are dense (A), and for high temperatures (B) they are highly coherent with big grains. At high pressures and temperature (C), the columns present several pits as the films grow in the 3D growth mode. If the temperature is low (D), the film results of amorphous like structure.

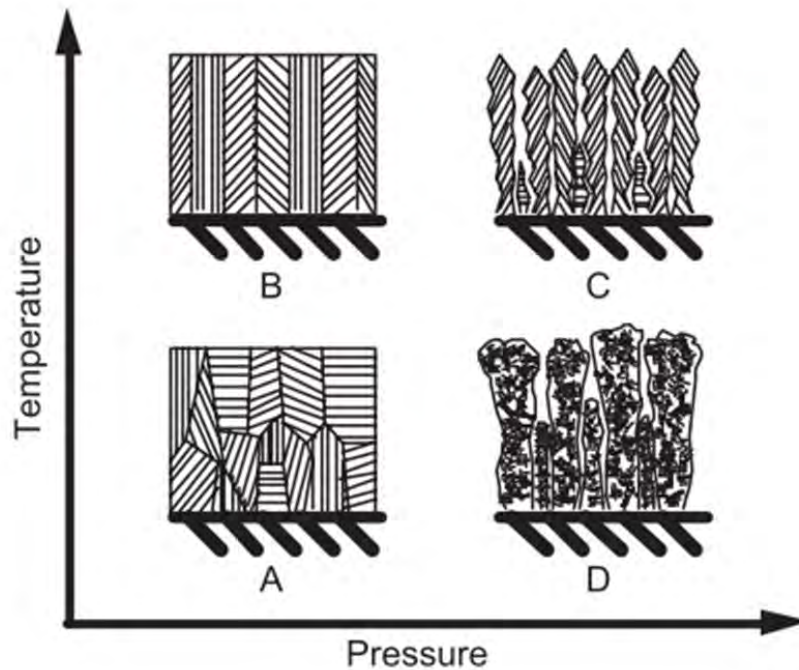


Figure 2-4: schematic of thin films microstructure as a function of temperature and pressure. Reported with permission from Infortuna A. et al, *Advanced Functional Materials*, (2008), John Wiley and Sons and Copyright Clearance Center.

### 2.1.1 Description of the system (DTU)

The PLD used in this project is a SURFAC Lab system, which is composed by a load lock chamber, in which the substrates are introduced in the vacuum environment, and the main chamber that is always in high vacuum condition ( $10^{-8}$  mbar). A vacuum valve separates the two chambers, and allows the transfer of the samples when low pressure is achieved in the load lock. The target to substrate distance is kept constant, at about 72 mm. The substrate is heated by Pt coils up to 700 °C. The targets are placed in a four-site carousel. Oxygen and nitrogen pressure can be varied in the range of  $10^{-2}$ - $10^{-4}$  mbar. Figure 2-5 shows a picture of the inside of the main chamber. The KrF excimer laser is used (Lambda physics COMPex) with a wavelength of 248 nm and an energy variable between 100-300 mJ. The condition used in the present experiments is usually 120 mJ and 10-20 Hz. For these values, the average deposition rate found is around  $0.06 \text{ Å/pulse}$ . The system is fully automated and controlled by Labview software.

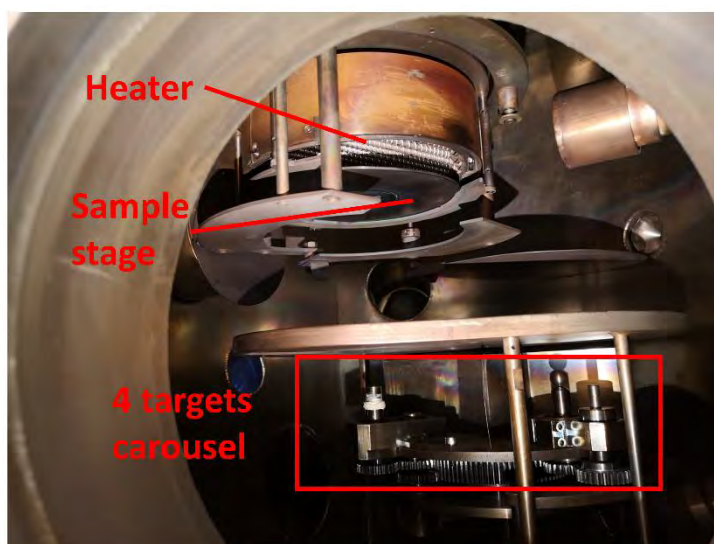


Figure 2-5: PLD in DTU. Photo of the inside of the main chamber..

### 2.1.2 Description of the system (APE beamline, Elettra)

PLD system used at Elettra, synchrotron APE beamline (Italy), is part of a bigger system connected to the synchrotron beamline. The samples are placed in a high vacuum system ( $10^{-9}$  mbar) in a small load lock chamber. Then, they are transferred from a distribution chamber to different characterization tools, such as x-ray absorption spectroscopy (XAS), Angle-resolved photoemission spectroscopy (ARPES), low-energy electron diffraction (LEED), and Scanning tunnelling microscope (STM). This allows the transfer of the PLD grown samples without breaking the vacuum. In the PLD chamber, the samples are placed on a stage. A light bulb is used as a heater (current up to 8-9 A), and it is placed on the back of the sample holder. The temperature can be increased up to  $\approx 750$  °C, and oxygen or nitrogen can be used as background gas. Figure 2-6 exhibits a photo of the inside of the chamber. The PLD facility is equipped with two lasers: a KrF excimer laser (same model of DTU) and a Nd:YAG laser with 1064 nm and with a fixed energy of 700 mJ.

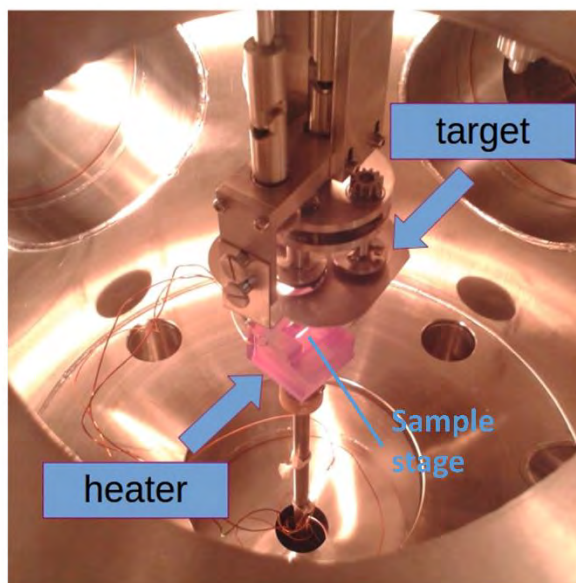


Figure 2-6: Photo of the inside of PLD chamber at Elettra.

## 2.2 STRUCTURAL CHARACTERIZATION BY X-RAY DIFFRACTION:

### 2.2.1 Fundamentals

The X-ray diffraction (XRD) is a technique in which a beam of X-rays hits a sample, and it is scattered with angles that depend on the crystallographic structure of the material <sup>19,20</sup>. The resulting diffraction pattern gives lots of crystallographic information, such as crystal/amorphous phases balance, lattice parameter and face orientation. This technique can be applied for many kind of compounds from thin films to powder and glasses, but also for polymers and biological materials.

X-ray diffraction is based on the fundamental effect of wave interference. When a beam of x-rays with a single wavelength  $\lambda$  hits a crystal with a periodic lattice, the radiation is scattered by every plane of the material causing constructive interference at certain angles determined by the Bragg's law:

$$2d \cdot \sin\theta = n\lambda \quad 2.3$$

where  $d$  is the interplane distance, and  $n$  an integer number representing the order of reflection.  $d$  is linked to the lattice constant through the Miller indices ( $h\ k\ l$ ), depending on the crystal structure. In cubic symmetries:

$$d_{hkl} = \frac{c}{\sqrt{h^2 + k^2 + l^2}} \quad 2.4$$

where  $c$  is the lattice parameter of the crystal. In other words, by measuring the angles of diffraction it is possible to know the crystal lattice and the orientation of the samples.

### 2.2.2 Theta-2theta scan

Theta-2theta is a scan mode, in which an X-ray source is stationary and directed to a sample. The sample stage moves by the  $\theta$  angle and the detector moves by  $2\cdot\theta$ . Figure 2-7a exhibits the geometry in a Bragg Brentano setup. The resulting diffraction pattern shows Bragg reflections that are reported at  $2\theta$  positions. Besides lattice parameters and  $(h\ k\ l)$  indices, it is possible to obtain information about grain size and phase from the shape and intensity of the peaks. As an example, in Figure 2-7b a typical  $\theta$ - $2\theta$  scan of  $\text{CeO}_2$  is shown.

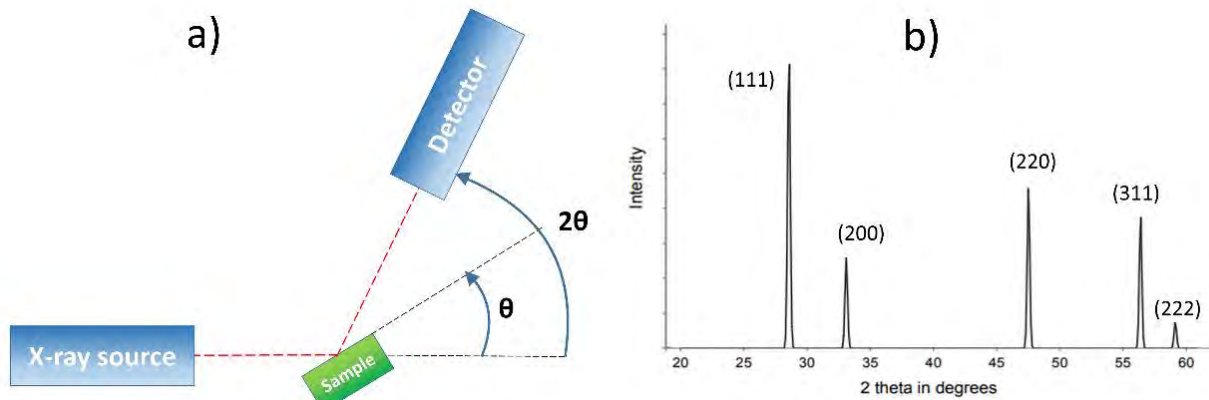


Figure 2-7:  $\theta$ - $2\theta$  scan mode. a) Diffractometer geometry. b) Diffraction pattern of  $\text{CeO}_2$ .

### 2.2.3 Rocking curve (RC)

Rocking curve scans give information about the quality of a crystal. In this mode, the detector is fixed at  $2\theta$  Bragg reflection. The X-ray source performs the scan around the  $\theta$  angle (also referred to as  $\omega$  incident angle). The diffractometer geometry is reported in Figure 2-8. If the planes are perfectly parallel, the resulting peak is sharp, and it has a small full width half maximum (FWHM) value. Defects like mosaic spreads and dislocation broaden the peak, increasing the FWHM. The epitaxial quality of



the films is evaluated by comparing the FWHM values of substrates and deposited material. Epitaxial and non-epitaxial CGO rocking curves are reported as an example in Figure 2-8b,c.

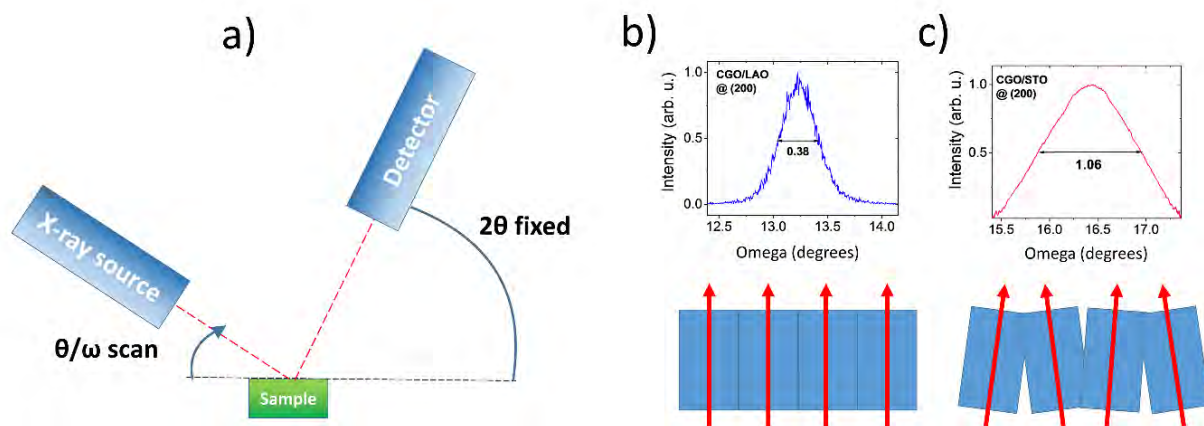


Figure 2-8: Rocking curve (RC) scan mode. a) Diffractometer geometry. b) RC of epitaxial CGO. The grains are parallel and the peak is sharp with FWHM= 0.38°. c) RC of CGO non-epitaxial CGO. The large FWHM= 1.06° suggests the presence of mosaic spread of the grains. The pattern was smoothed for clarity.

## 2.2.4 X-ray reflectivity (XRR)

X-ray reflectivity (XRR) is a non-destructive technique used to measure the thickness of thin films or multilayers/heterostructures. In this mode, the x-ray source scans in the proximity of the surface critical reflection angle. The X-ray penetration depth in such conditions is a few nanometers since the XRD beam is arriving at a very shallow angle. At every interface where the electron density of the material changes, a part of the X-ray beam is reflected back. Figure 2-9a displays an example of the dynamics of reflection for two interfaces. The interference of the reflected portions creates an oscillation with a width that depends on the distance between the two interfaces or the thickness of the thin film. Figure 2-9b shows an example of a reflectivity pattern of a 17 nm thick sample of CGO. This technique is also used to evaluate the surface roughness of thin films and the thickness ratio in a superlattice<sup>5,21,22</sup>.

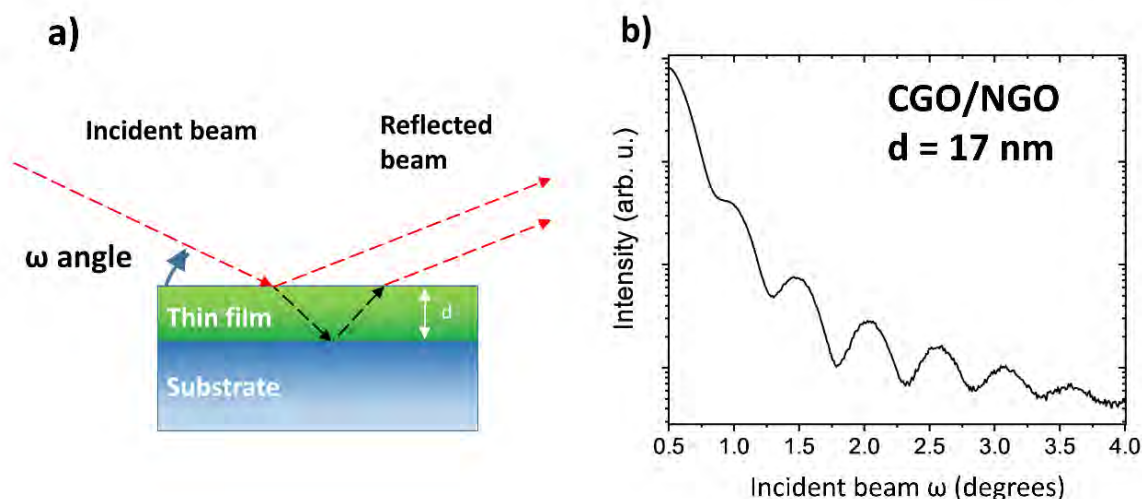


Figure 2-9: XRR scan mode. a) Dynamics of x-ray penetration and reflection in thin layers. b) Example of XRR pattern of a 17 nm thick CGO film.

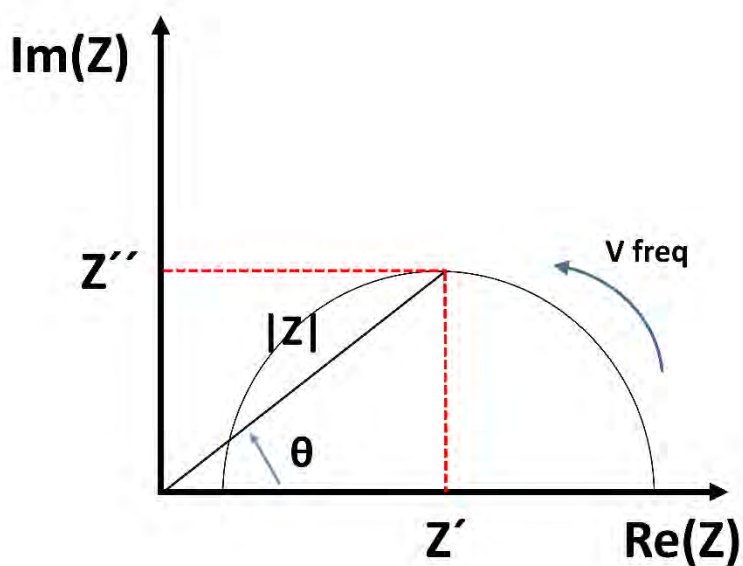
## 2.3 ELECTROCHEMICAL CHARACTERIZATION: IMPEDANCE SPECTROSCOPY

Impedance spectroscopy (IS) is a technique used to characterize the conduction properties of materials and the dynamics at the electrode interfaces<sup>23</sup>. This technique gives information about the type of conduction (ionic, electronic, mixed), the activation energy of the carriers, the capacitance, inductance and resistance depending on frequency, temperature or gas environment. IS is used to study the ionic properties of electrochemical materials (both solids and liquids) and systems. For the characterization of ionic conductivity in solid-state materials, the main approach is to apply a small oscillating voltage (with an amplitude generally in the range of 0.05-0.2 V) across a sample with electrodes in a wide frequency range (from MHz to mHz) and to measure the real and imaginary parts of the impedance, linked to resistance and capacitance, respectively. Several microscopic processes determine the response of the solid-state ionic materials such as ionic and electronic conduction, polarization effects, reduction or oxidation processes and interface charge transfers.<sup>23</sup> In oxygen defective metal oxides,



such as cerium oxide, grain boundaries blocking effects, oxygen vacancy migration at high temperatures and microstructure features can be analyzed by IS <sup>7,24,25</sup>.

A typical way to visualize the impedance of ionic materials is via the “Nyquist plot”. The impedance, which can be written as  $Z(\omega) = Z' + jZ''$ , is a vector quantity, and it is usually plotted using polar



coordinates, where  $Re(Z) \equiv Z' = |Z|\cos\theta$  and  $Im(Z) \equiv Z'' = |Z|\sin\theta$ , as depicted in Figure 2-10. The angle theta is the phase angle:

$$\theta = \tan^{-1}(Z''/Z') \quad 2.5$$

And the modulus is:

$$|Z| = \sqrt{(Z')^2 + (Z'')^2} \quad 2.6$$

In impedance spectroscopy, the oscillating voltage  $V = V_0 \cdot \sin(\omega t)$  is applied at several frequencies (up to

Figure 2-10: Schematic representation of a Nyquist plot.

MHz), and each ( $Z'$ - $Z''$ ) point is plotted in the so-called Nyquist plot (schematic in Figure 2-10). The interpretation of impedance data is carried out by comparing the data with the response of equivalent circuit models. The right model has to match the experimental impedance, with a composition of electrical elements (R, C, L) that realistically represent the physical and chemical processes in the sample. When studying ionic materials, each element in the circuit, such as resistors and capacitors, must be associated to electrochemical processes occurring in the material, such as ionic migration, material's polarization, ion-electron charge transfer at the electrolyte/electrodes interface and electrodes polarization <sup>23</sup>. Real cells have several processes, the response of which can overlap in impedance spectroscopy measurements, occur in real cells. Therefore the deconvolution of the different contribution can become complicated Figure 2-11 shows a Nyquist plot for bulk CGO samples with Au-Ag mixture electrodes <sup>26</sup>.

When fixing the frequency, it is possible to measure the conductivity (inverse of resistance) depending on the temperature. This is useful in ionic conductors that are thermally activated, and their conduction is described as:

$$\sigma = \sigma_0 \cdot \exp\left(-\frac{E_a}{k_b T}\right) \quad 2.7$$

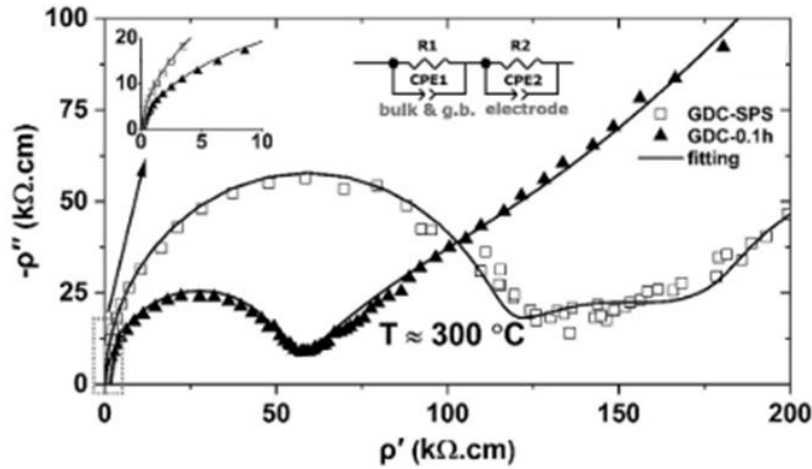


Figure 2-11: Nyquist plot of CGO bulk samples.

where  $\sigma_0$  is the pre-exponential factor and  $E_a$  the activation energy of the charge carrier/s.  $E_a$  describes the energy required for the system to evolve towards an equilibrium state or in other words, the energy needed to activate carriers. Experimentally  $E_a$  is determined by the slope of the logarithm of the conductivity  $\log \sigma$  versus the inverse of a temperature  $1000/T$  in the so-called Arrhenius plot. It is also possible to report each contribution in the Nyquist plot i.e. bulk and grain boundaries separately. Figure 2-12 shows an example of the Arrhenius plot for CGO pellets as reported in ref <sup>26</sup>.

To perform the impedance spectroscopy measurements a Solartron 1260 (UK) was used. The applied AC voltage had a frequency range of 0.01 Hz to 1 MHz with an amplitude of 100 mV.

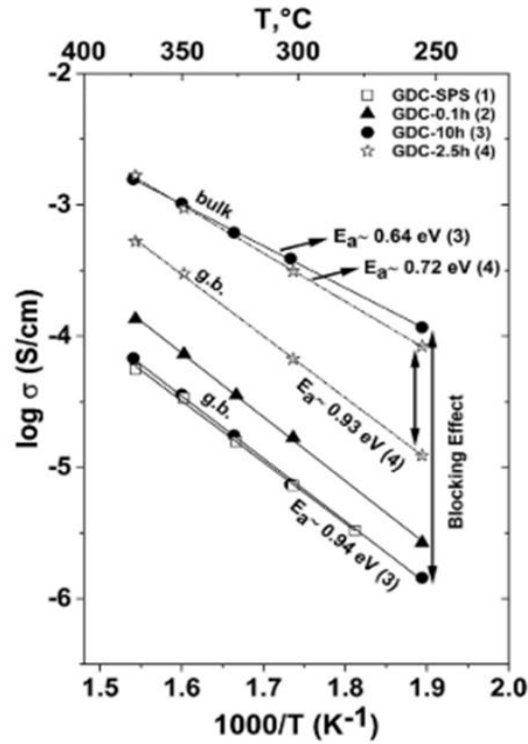


Figure 2-12: Arrhenius plot of CGO bulk samples. Bulk and grain boundaries contribution are separated.

## 2.4 ELECTROSTRICTION DETECTION SETUP

### 2.4.1 Basics and calculations

The first step of this PhD project was to design and build an effective experimental setup for the characterization of electrostriction, possibly suitable for both thin films and bulk pellets. The description of both instruments and calculations is given in this section.

The primary function of the designed setup is to induce oscillating vibrations in an electroactive sample and to be able to measure such oscillation. From the amplitude of the response, the material electrostriction coefficient of the material can be determined.

When using thin films configuration, a substrate with the size around 5x5 mm, 0.1 mm thick and a coating of electroactive CGO are used. Electrodes are fabricated by PLD or sputtering, with sandwiched geometry or planar electrodes configuration. The sample is fixed to a base, with one end of the sample

clamped and the other end free to move. Figure 2-13 shows the configuration of a sample with planar electrodes.

By applying an electric field, the sample vibrates with a particular amplitude  $d$ . When the displacement  $d$  is much smaller than the length of the sample  $L$  (i.e.,  $d \ll L$ ), the curvature  $\Delta k$  ( $\text{m}^{-1}$ ) is defined as:

$$\Delta k = \frac{2d}{L^2} \quad 2.8$$

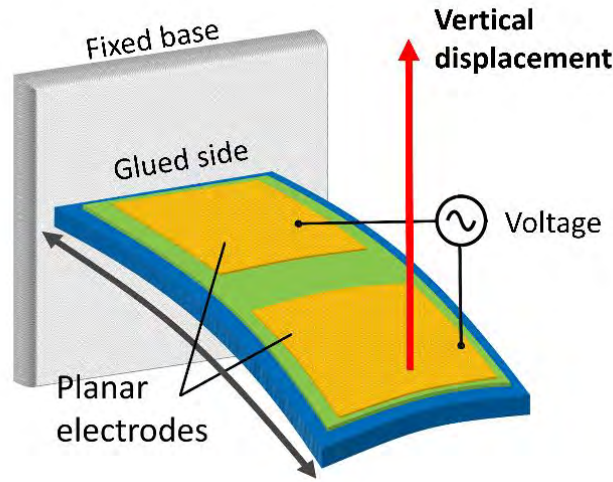


Figure 2-13: Cantilever configuration in a sample with planar electrodes.

The curvature develops when there is a residual stress  $\Delta\sigma$  in the film lattice. In films with thickness  $t_f$  very small compared to the substrate  $t_s$  ( $t_f \ll t_s$ ), the value of the stress is calculable with the Stoney formula

$$\Delta\sigma = \frac{Y_s}{1 - \nu_s} \frac{t_s^2}{6t_f} \Delta k \quad 2.9$$

where  $Y_s$  is Young's modulus of the substrates (MPa) and  $\nu_s$  the Poisson ratio. Finally, the field electrostriction coefficient  $M_e$  can be determined through the constitutive equation:

$$\Delta\sigma = Y_f \cdot M_e \cdot E^2 \quad 2.10$$

where  $Y_f$  is Young's modulus (MPa) of the film and  $E$  is the applied electric field (V). If the information about the size and mechanical properties of the film and substrate is already known, the electrostriction coefficient can be calculated just by measuring the displacement amplitude of the cantilever when an electric field with intensity  $E$  is applied.

## 2.4.2 Detection system

Measuring the electrostriction oscillation is a challenging operation. The displacement caused by the electromechanical activity of CGO is in the order of magnitude between 10 nm and 0.1 nm. Therefore, extremely high precision displacement sensors, such as capacitive<sup>27</sup> or photonic<sup>28</sup> sensors, atomic force microscope<sup>29,30</sup>, CCD tracking<sup>31</sup>, are needed. Laser interferometers in particular<sup>32,33</sup>, are suitable instruments to detect small displacement down to ~pm range, with oscillation frequency from static to few MHz.

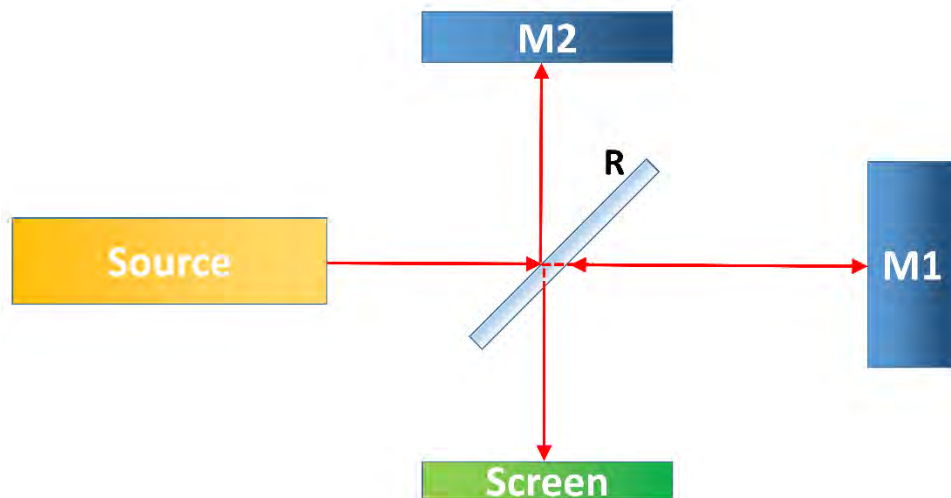


Figure 2-14: Michelson interferometer schematics. M1 and M2 are reflecting mirrors. R is a partially reflecting mirror.

Most of the laser interferometers are built on the principle of “Michelson interferometers”. Figure 2-14 shows a schematic of this type of interferometer. Coherent light beams are obtained by splitting the source laser beam with a

partially reflecting mirror (R). The resulting waves are reflected of mirrors M1 and M2 and are directed to a screen where they create interference fringes as a result of the superimposition principle. The number of fringes depends on the different path lengths of the reflected and the transmitted beams.

Accurate displacement measurements can be performed by moving one of the reflecting mirrors and counting the fringes that move by a reference point.

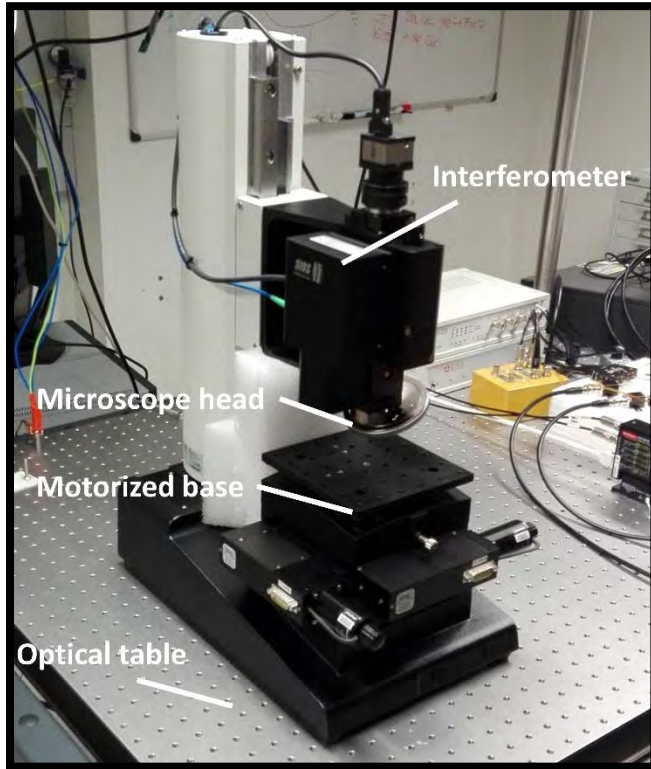


Figure 2-15: Vibrometer picture.

To carry out nano-displacement measurements, I used a SIOS Nano vibration analyzer NA series, consisting of a modified Michelson interferometer with plane-mirror reflector and integrated microscope (Figure 2-15). The light source is a He-Ne laser that produces a beam with a 632.8 nm wavelength. The instrument resolution is 5 pm from 0 to 5 MHz oscillation frequency. The diameter of the laser spot is about 6  $\mu\text{m}$  which allows surface displacement mapping. The sample is mounted on a motorized stage that can move on the X-Y plane with a range of 50x50 mm and can rotate with two degrees of freedom. The instrument is placed on top of an optical table to minimize the

environmental vibration to the minimum. The measurement outputs available are both digital (USB connected) and analog ( $\pm 3\text{V}$  output with resolution  $\approx 0.2\text{ nm}$ ).

The sample vertical displacement is measured at the free end of the cantilever while an oscillating electric field is applied by an Aim-TTI TGP 3100 function generator. As electrostriction often demonstrated to reduce with the frequency, the voltage is usually applied at  $f = 0.1$  to 1 Hz. The surface hit by the laser has to be as reflective as possible since a higher amount of reflected beam would give rise to more accurate measurements. Figure 2-16 illustrates three examples of measurement. All of the measurements are displayed after a smoothing process is applied to the data, which is needed to exclude laser high frequency interferences. Figure 2-16a shows an example of a clean measurement of a CGO/Si sample oscillation with an applied field. In some cases, the quality of detection is reduced by

environmental noise, coming from external vibration, low amount of reflected laser beam or mechanical drift of some component of the setup. Figure 2-16b,c display measurements of a static surface with high environmental noise and high drift, respectively. As a result, the actual measurements resolution is reduced to the 5-10 nm range.

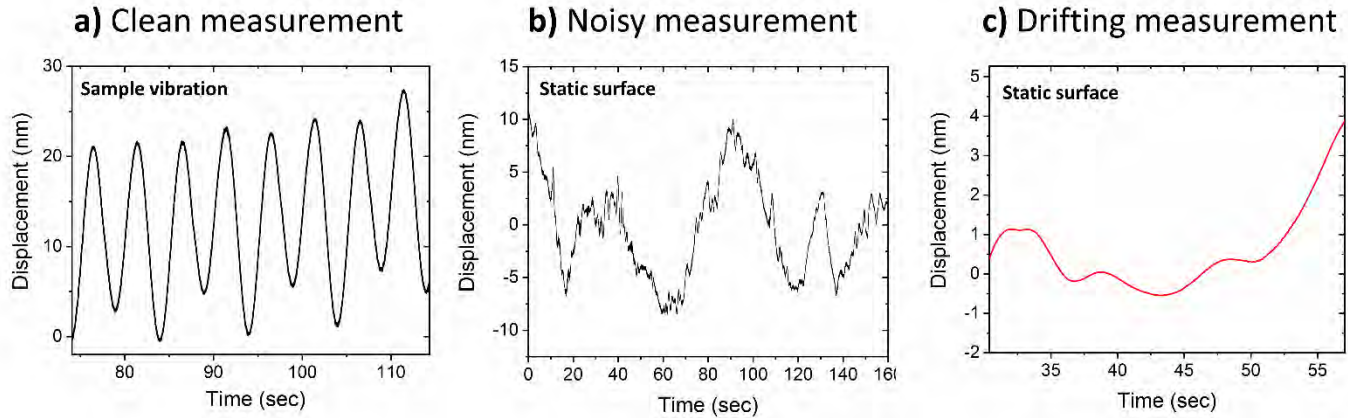


Figure 2-16: Vibrometer measurements in different condition. a) Measurements of oscillating CGO sample with 0.1 frequency, with low noise and drift. b) Static measurement with high environmental noise. c) Static measurement with high drift.

### 2.4.3 Lock-in amplifier

In order to improve the resolution of the measurements, a lock-in amplifier model 7230 General Purpose DSP was connected to the analogic output of the interferometer. A lock-in amplifier is an instrument that extracts a waveform with a specific frequency from a noisy signal. This kind of instruments is widely used for signal analysis. In brief, they operate on the original signal multiplying it with a reference one and integrating over time. As a result, it is possible to single out the component of the signal with the chosen frequency even if the noise is orders of magnitude higher. The output is a DC signal proportional to the amplitude of the oscillating wave.

In our setup, the lock-in amplifier is connected to a USB data acquisition (DAQ) device. A Labview program has been made to control and manage the data. Then, the signal is converted from mV to nm by the instrument's conversion factor reported in the datasheet provided by the manufacturer. As a result, the precision of the measurements was improved significantly. However, precision is frequency-dependent. For signals with  $f < 3$  Hz or  $f > 100$  Hz, the achieved resolution goes down to 0.2 nm, allowing the detection of rather small oscillations. In order to detect electrostriction oscillation, the chosen



frequency has to be twice the frequency of the applied field. Figure 2-17 shows the measurement performed on a CGO/YSZ sample for voltages from 0 to 3 V. The magnitude of the oscillation at the selected frequency is measured continuously and displayed as a function of time. The sampling frequency is usually between 100 to 1000 Hz, and the measurement time is 5 minutes. The values measured (100 values/sec for 5 minutes) are averaged to obtain an accurate evaluation of oscillation. The implementation of a lock-in amplifier brings several improvements to the setup besides increasing the resolution. The external drift is canceled from the analysis automatically because it is a static effect. However, this process is sensible to only one frequency per measurement. Therefore, one-time events, static contribution or double harmonic oscillations are not detectable with this technique.

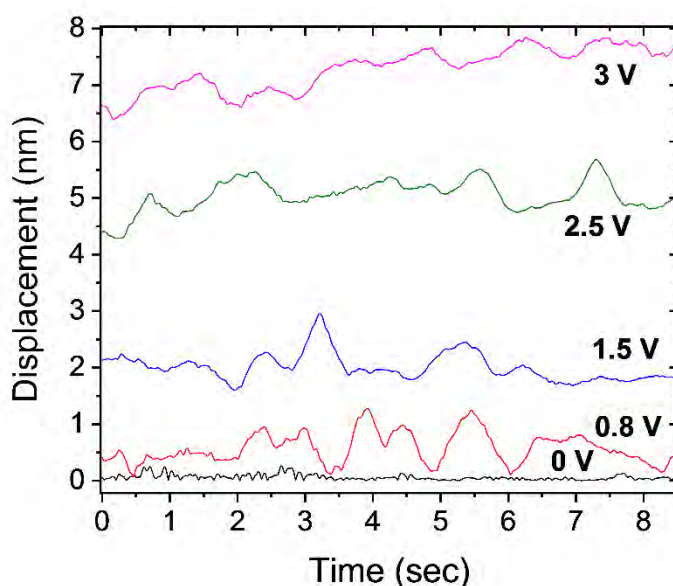


Figure 2-17: Measurement of 1 Hz oscillation amplitude of CGO/YSZ with increasing voltages (at 0.5 Hz) performed with the lock-in amplifier. The displacement values refer to the contribution of 1 Hz oscillation. The frequency chosen is double the electric field frequency because electrostriction vibration depends on the second harmonic.

#### 2.4.4 High voltage and other features

In order to apply high voltage signals, a Trek 2200 amplifier was added to the function generator, allowing to reach high voltages up to 2 kV. This makes possible to generate high electric fields to induce large displacements, e.g. in thick samples or thin films with distant lateral electrodes (i.e bulk pellets or thin films with planar electrodes). The voltage and current monitors are connected to Labview software,



and it is possible to track any voltage drops or shortcuts. Finally, a FLIR SC5000 thermal camera is used to detect if the thermal expansion effect takes place.

To summarize, a nano-vibration setup has been developed, with a resolution of 0.2 nm and voltage up to 2 kV, for oscillations with frequency from 0 to 5 MHz. The developed software allows to keep track of the voltage and current in real-time, and the thermal effect is also monitored. The motorized sample base makes it possible to obtain X-Y mapping. The setup is suitable for several types of samples, such as thin films, bulk, and membranes. Figure 2-18 shows a schematic of the experimental setup.

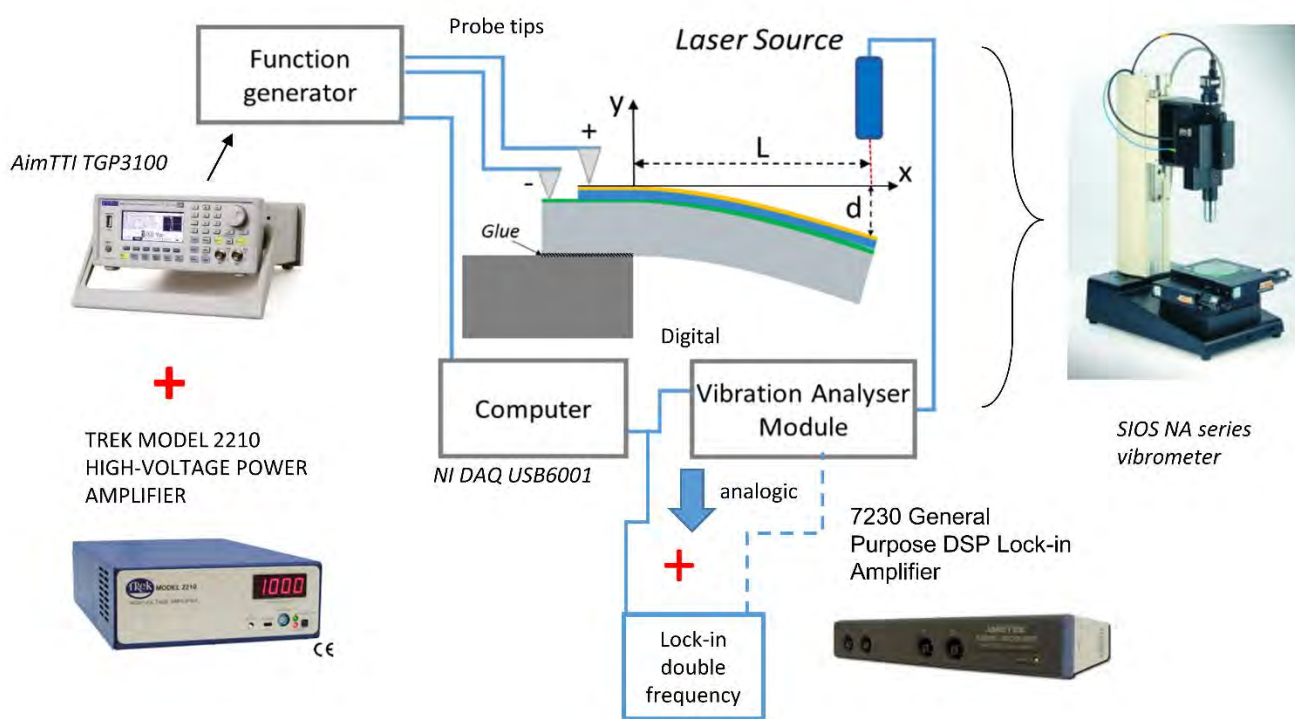


Figure 2-18: Schematic of electrostriction experimental setup.

## 2.5 X-RAY ABSORPTION SPECTROSCOPY (XAS).

(XAS) is a local analysis technique based on the optical absorption of a specific element inside a material. At the right energies, the interaction of X-rays with matter causes the absorption of a photon from an

electron at the inner shells of the atom<sup>34–36</sup>. If the energy absorbed is higher than the binding energy, the electron unbounds with kinetic energy:

$$E_k = h\nu - E_b \quad 2.11$$

where  $h\nu$  is the energy of the photon and  $E_b$  is the binding energy. Each element has well defined binding energies, and it is therefore necessary to choose a value of X-ray energy close to this value<sup>34–36</sup>. This energy is called “edge”. Every electron bound state has an edge labeled by a letter K, L, M that depends on the principal quantum number  $n=1,2,3$  respectively, and by a number corresponding to the angular quantum number  $l$ . For example, a transition from the  $2p_{3/2}$  state is called  $L_3$ <sup>34–36</sup>. The edge energies lie within 100 eV and 200 keV, depending on the element and the edge. When the photon energy is lower than the binding energy, the selected element does not absorb any radiation. At energies close to an edge however, the absorption coefficient value has a series of discontinuities which appear in the form of peaks. Every peak represents the promotion of a core electron. The main peak is the promotion to the continuum, while some “pre-peaks” indicate that the electrons move to unoccupied bound states of the atom. For this reason, XAS is an element and edge selective, allowing the study of a single element in complex compounds<sup>34–36</sup>.

XAS can be divided into two different analysis: X-ray absorption near-edge spectroscopy (XANES) and extended X-ray absorption fine structure (EXAFS)<sup>34–36</sup>. Figure 2-19 shows an example of an absorption spectrum with the two regions divided. XANES includes the pre-edge and edge regions of the absorption spectra with an energy range of about 50 eV. It provides information about oxidation state, coordination number and geometry<sup>31,37–39</sup>. EXAFS includes the region after the main edge. At these energies, the electron ejected from the atom withstands back-scattering from neighbor atoms, and consequently a self-interference effect is observed. This creates oscillations in the absorption that can give information about the chemical and structural surrounding (coordination number, lattice symmetry, bond distortion). EXAFS allows quantitative analysis through Fourier transform, and it is possible to calculate the distribution of bond lengths of the surrounding<sup>37,40,41</sup>.

We performed *in-situ* EXAFS at BL22 – CLÆSS beamline of Alba synchrotron in Barcelona and SuperXAS beamline at PSI (Villigen). The samples were measured prior to and during the application of an electric

field. The measurements were carried out at Ce  $L_3$  edge. The goal is to analyze the changing in the EXAFS spectra due to lattice distortion caused by electrostriction. Low-temperature measurements were also performed in the same condition in a CGO bulk single-crystal sample. At APE beamline of Elettra synchrotron (Trieste), XANES experiments are performed at Ce  $M_4$  and  $M_5$  edges. The measurements are carried out in films with different thickness and with either compressive, tensile or no strain. For XAS analysis of CGO, see Chapter 5.

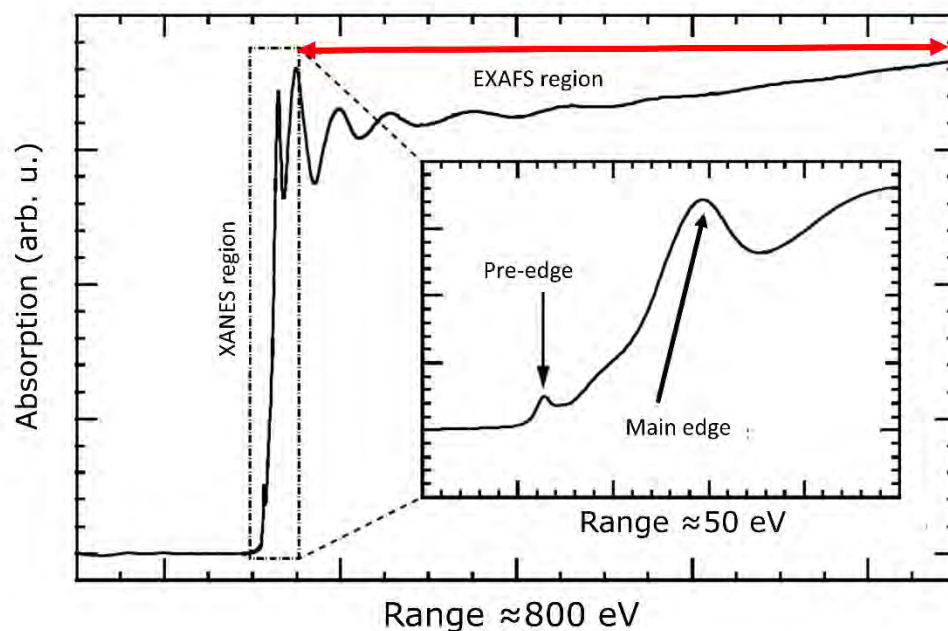


Figure 2-19: X-ray absorption spectrum example. XANES and EXAFS regions are highlighted.

## 2.6 REFERENCES

---

- <sup>1</sup> R. Eason, *Pulsed Laser Deposition of Thin Films* (2007).
- <sup>2</sup> A. Schatz, D. Pantel, and T. Hanemann, *J. Appl. Phys.* **114**502, (2017).
- <sup>3</sup> D. Reisinger, B. Blass, J. Klein, J.B. Philipp, M. Schonecke, A. Erb, L. Alff, and R. Gross, *Appl. Phys. A Mater. Sci. Process.* **77**, 619 (2003).
- <sup>4</sup> M. Matvejeff, T. Chikyow, and M. Lippmaa, *J. Cryst. Growth* **311**, 1201 (2009).
- <sup>5</sup> Y. Shi, S.C. Lee, M. Monti, C. Wang, Z.A. Feng, W.D. Nix, M.F. Toney, R. Sinclair, and W.C. Chueh, *ACS Nano* **10**, 9938 (2016).
- <sup>6</sup> C. Balaji Gopal, M. García-Melchor, S.C. Lee, Y. Shi, A. Shavorskiy, M. Monti, Z. Guan, R. Sinclair, H. Bluhm, A. Vojvodic, and W.C. Chueh, *Nat. Commun.* **8**, (2017).
- <sup>7</sup> S. Sanna, V. Esposito, D. Pergolesi, A. Orsini, A. Tebano, S. Licoccia, G. Balestrino, and E. Traversa, *Adv. Funct. Mater.* **19**, 1713 (2009).
- <sup>8</sup> A. Chopra, M. Bayraktar, M. Nijland, J.E. Ten Elshof, F. Bijkerk, and G. Rijnders, *Sci. Rep.* **7**, 1 (2017).
- <sup>9</sup> C.M. Wang, S. Azad, V. Shutthanandan, D.E. McCready, C.H.F. Peden, L. Saraf, and S. Thevuthasan, *Acta Mater.* **53**, 1921 (2005).
- <sup>10</sup> S. Sanna, V. Esposito, M. Christensen, and N. Pryds, *APL Mater.* **4**, 2 (2016).
- <sup>11</sup> L. Dos Santos-Gómez, S. Sanna, P. Norby, N. Pryds, E.R. Losilla, D. Marrero-López, and V. Esposito, *Nanoscale* **11**, 2916 (2019).
- <sup>12</sup> M. Yoshimoto, H. Nagata, T. Tsukahara, and H. Koinuma, *Jpn. J. Appl. Phys.* **29**, L1199 (1990).
- <sup>13</sup> N. Yang, P. Orgiani, E. Di Bartolomeo, V. Foglietti, P. Torelli, A. V. Ievlev, G. Rossi, S. Licoccia, G. Balestrino, S. V. Kalinin, and C. Aruta, *J. Phys. Chem. C* **121**, 8841 (2017).
- <sup>14</sup> J. Shin, S. V. Kalinin, H.N. Lee, H.M. Christen, R.G. Moore, E.W. Plummer, and A.P. Baddorf, *Surf. Sci.* **581**, 118 (2005).
- <sup>15</sup> A. Sambri, S. Amoruso, X. Wang, F.M. Granozio, and R. Bruzzese, *J. Appl. Phys.* **104**, (2008).
- <sup>16</sup> M. Capitelli, A. Casavola, G. Colonna, and A. De Giacomo, *Spectrochim. Acta - Part B At. Spectrosc.* **59**, 271 (2004).
- <sup>17</sup> M.S. Dawood, A. Hamdan, and J. Margot, *AIP Adv.* **5**, (2015).
- <sup>18</sup> A. Infortuna, A.S. Harvey, and L.J. Gauckler, *Adv. Funct. Mater.* **18**, 127 (2008).
- <sup>19</sup> D. Ketih Bowen and B.K. Tanner, *High Resolution X-Ray Diffractometry and Topography* (2005).

- <sup>20</sup> Y. Waseda, E. Matsubara, and K. Shinoda, *X-Ray Diffraction Crystallography* (2011).
- <sup>21</sup> P. Patsalas and S. Logothetidis, **989**, (2005).
- <sup>22</sup> C. Sacco, A. Galdi, F. Romeo, N. Coppola, P. Orgiani, H.I. Wei, B.H. Goodge, L.F. Kourkoutis, K. Shen, D.G. Schlom, and L. Maritato, *J. Phys. D. Appl. Phys.* **52**, 135303 (2019).
- <sup>23</sup> E. Barsoukov and J.R. Macdonald, *Impedance Spectroscopy Theory, Experiment, and Applications* (2005).
- <sup>24</sup> V. Esposito and E. Traversa, *J. Am. Ceram. Soc.* **91**, 1037 (2008).
- <sup>25</sup> E. Gourba, P. Briois, A. Ringuedé, M. Cassir, and A. Billard, *J. Solid State Electrochem.* **8**, 633 (2004).
- <sup>26</sup> A. Kabir, S. Santucci, N. Van Nong, M. Varenik, I. Lubomirsky, R. Nigon, P. Mural, and V. Esposito, *Acta Mater.* **174**, 53 (2019).
- <sup>27</sup> N. Yavo, A.D. Smith, O. Yeheskel, S. Cohen, R. Korobko, E. Wachtel, P.R. Slater, and I. Lubomirsky, *Adv. Funct. Mater.* **26**, 1138 (2016).
- <sup>28</sup> M. Hadad, H. Ashraf, G. Mohanty, C. Sandu, and P. Mural, *Acta Mater.* **118**, 1 (2016).
- <sup>29</sup> D.Q. Shi, M. Ionescu, J. McKinnon, and S.X. Dou, *Phys. C Supercond. Its Appl.* **356**, 304 (2001).
- <sup>30</sup> I.K. Bdikin, J.A. Pérez, I. Coondoo, A.M.R. Senos, P.Q. Mantas, and A.L. Kholkin, *J. Appl. Phys.* **110**, 0 (2011).
- <sup>31</sup> R. Korobko, A. Patlolla, A. Kosoy, E. Wachtel, H.L. Tuller, A.I. Frenkel, and I. Lubomirsky, *Adv. Mater.* **24**, 5857 (2012).
- <sup>32</sup> A.D. Ushakov, N. Yavo, E. Mishuk, I. Lubomirsky, V.Y. Shur, and A.L. Kholkin, *KnE Mater. Sci.* **1**, 177 (2016).
- <sup>33</sup> A.L. Kholkin, C. Wüthrich, D. V. Taylor, and N. Setter, *Rev. Sci. Instrum.* **67**, 1935 (1996).
- <sup>34</sup> J.A. van Bokhoven and C. Lamberti, *X-Ray Absorption and X-Ray Emission Spectroscopy: Theory and Applications* (2015).
- <sup>35</sup> C.S. Schnorr and M.C. Ridgway, *X-Ray Absorption Spectroscopy of Semiconductors* (2015).
- <sup>36</sup> B.K. Teo and D.C. Joy, *EXAFS Spectroscopy: Techniques and Applications* (1981).
- <sup>37</sup> G. Silversmit, H. Poelman, V. Balcaen, P.M. Heynderickx, M. Olea, S. Nikitenko, W. Bras, P.F. Smet, D. Poelman, R. De Gryse, M.F. Reniers, and G.B. Marin, *J. Phys. Chem. Solids* **70**, 1274 (2009).
- <sup>38</sup> S.O. Kucheyev, B.J. Clapsaddle, Y.M. Wang, T. Van Buuren, and A. V. Hamza, *Phys. Rev. B - Condens. Matter Mater. Phys.* **76**, 1 (2007).
- <sup>39</sup> A.M. Shahin, F. Grandjean, G.J. Long, and T.P. Schuman, *Chem. Mater.* **17**, 315 (2005).
- <sup>40</sup> O. Müller, M. Nachtegaal, J. Just, D. Lützenkirchen-Hecht, and R. Frahm, *J. Synchrotron Radiat.* **23**,

260 (2016).

<sup>41</sup> Q. Kong, F. Baudalet, J. Han, S. Chagnot, L. Barthe, J. Headspith, R. Goldsbrough, F.E. Picca, and O. Spalla, *Sci. Rep.* **2**, 1 (2012).

# 3 DEVICES PERFORMANCES AND STABILITY, THE ROLE OF ELECTRODES AND MICROSTRUCTURE.

---

In this chapter, the stability and the structure of electrostrictive CGO based devices are addressed. For practical applications, it is fundamentally important to design devices with good performance and facile integration. However, many factors could obstacle the characterization of thin films, such as faulty electrodes or substrates, pinholes or conductive paths, impurity oxide formation at the interface or grain boundaries, etc. In particular, several challenges involving stability, chemical compatibility and microstructure-properties are interlinked. This is especially reported for the state-of-the-art lead-based piezoelectric which, for thin film technology, requires several processing steps <sup>1,2</sup>. Despite such challenges, the integration of ceria based thin films into the silicon-based actuators resolve in facile methods with clarity of criteria and handy solutions.

Here, some representative examples of the strategies we took for integrations of ceria thin films electrostrictors into reliable devices are presented. This is especially described on samples with cantilever and the electrodes used. The quality of CGO film, as well as crystallographic properties and electromechanical activity are characterized. Moreover, metal and ceramic electrodes are compared in terms of performances and stability under stress.

A new planar electrode configuration is presented, which makes it possible to avoid the shortcut problem found for thin films with top-bottom electrodes. The reliability of Thin polycrystalline films have often a columnar microstructure <sup>3</sup>. Consequently, when the electrodes are placed parallel to the surface, the electric field interacts with vertical grain boundaries <sup>4</sup>. Therefore, accurate analysis of electrostriction depending on grains and boundaries morphology is needed.

Bulk CGO samples with specific microstructures are fabricated with different synthesis methods and synthesis parameters<sup>5</sup> (e.g., sintering temperature, sintering time). The electrostriction of such samples were characterized and the role of different grain boundary configurations are investigated.

## 3.1 ELECTRODES AND STABILITY

### 3.1.1 Cantilever design and CGO deposition.

Sample design is an important matter when it comes to characterizing electromechanical response of thin films because the field-induced strain can be very small (comparable to background noise). Cantilever shaped samples however, is shown to be an optimal solution, as the strain developed along the length of the cantilever is significantly amplified<sup>6-9</sup>. In particular, the vertical displacement of the cantilever depends on the length squared. With a non-contact detection system, it is possible to

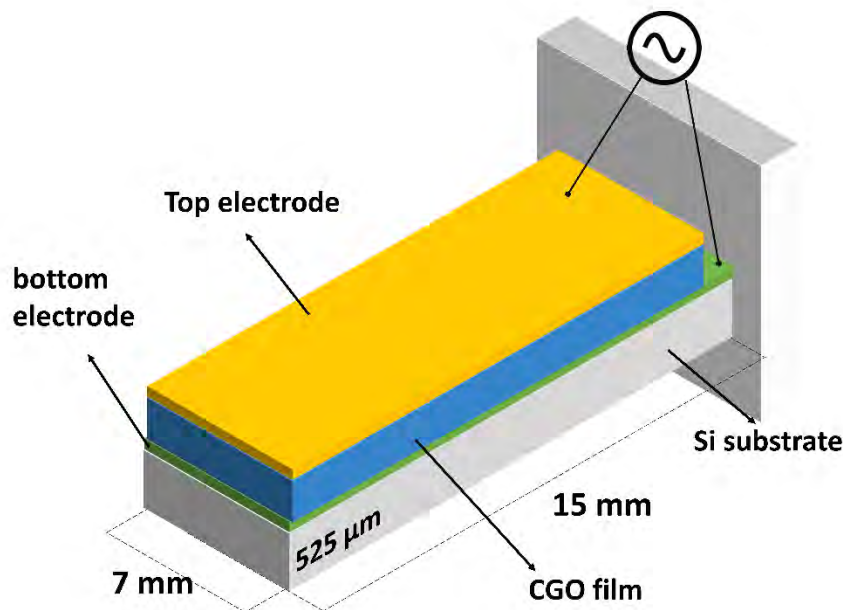


Figure 3-1: Schematic of the sample structure. The size can vary slightly.



measure the curvature of the samples and then calculate the lattice strain or electrostriction coefficient, as mentioned in Chapter 2.4.

Figure 3-1 shows the standard design of a cantilever sample with a size of 7 mm x 15 mm. The substrate is a Si wafer 525  $\mu\text{m}$  thick and (100) oriented. The film of  $\text{Ce}_{0.8}\text{Gd}_{0.2}\text{O}_{1.9}$  is sandwiched between two metal electrodes in a top/bottom configuration.

CGO thin films are deposited by PLD using a  $\text{Ce}_{0.8}\text{Gd}_{0.2}\text{O}_{1.9}$  target fabricated from powder by uniaxial cold- pressing at 140 MPa and then sintered at 1723 K for 10 h. A high pure fluorite phase was observed for the as prepared targets. The laser frequency is set at 10-20 Hz and the energy at 200 mJ, with 3 J/cm<sup>2</sup> fluence. For the deposition of polycrystalline films, the deposition temperature is set to be 400 °C and the oxygen partial pressure in the chamber is set to be  $10^{-3}$  mbar. Several studies show high temperature and low pressure are important factors to obtain a dense film and ensure mechanical continuity <sup>3,10-12</sup>. As reported by Infantina *et al.*<sup>3</sup>, for oxygen partial pressure higher than  $P_{\text{O}_2} = 5 \cdot 10^{-2}$  mbar, clusters form in the plume and they land on the substrate resulting in a porous and disordered microstructure. Also, at low temperatures, amorphous CGO films form.

Figure 3-2 shows an example of structural characterization of CGO deposited on Si substrate. The  $\theta$ -2 $\theta$  scan indicates a polycrystalline sample with (111) orientation. As depicted in Figure 3-2b the

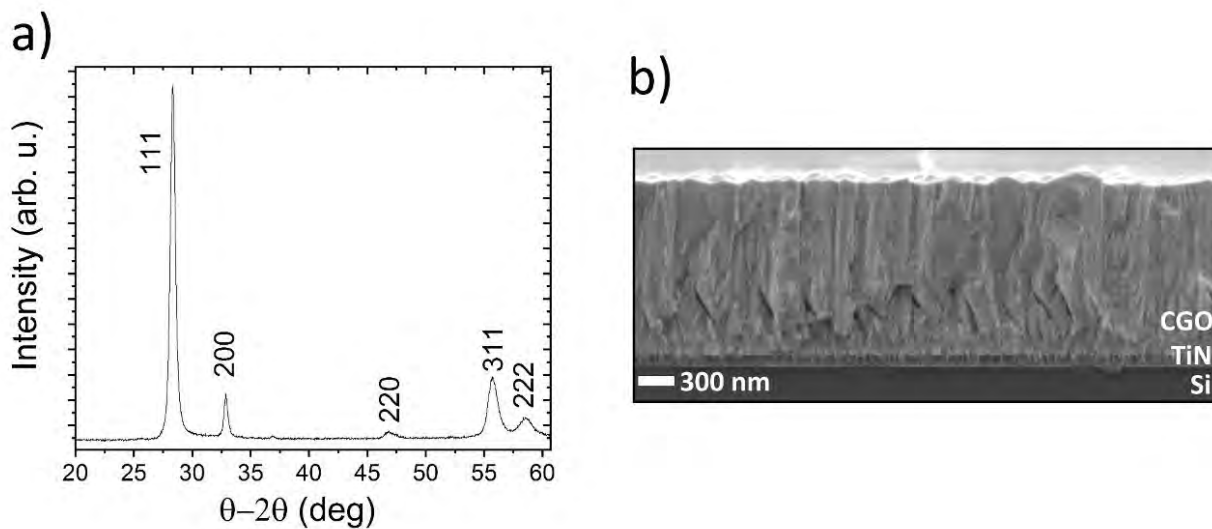


Figure 3-2: Structural analysis of CGO deposited on TiN/Si substrate. a) X-ray diffraction. b) SEM cross-section image.

microstructure appears columnar and dense. CGO is a refractory material and does not need post-process or chemical barriers to avoid diffusion or reaction with other compounds<sup>12,13</sup>. Therefore, it shows easy integration with a wide variety of materials such as Si, glass and perovskite single crystals<sup>10,12-14</sup>.

### 3.1.2 Metal electrodes: Ti and Al.

The choice of the electrodes is a significant factor for the functioning of the cantilever. M. Hadad *et al.* report electromechanical activity in CGO thin films with different metal electrodes (Cr, Pt and Al), highlighting a noticeable difference in performances<sup>15</sup>, resulting in electrostriction coefficient ranging from  $0.4 \cdot 10^{-19} \text{ m}^2\text{V}^{-2}$  for Pt, to  $5.4 \cdot 10^{-19} \text{ m}^2\text{V}^{-2}$  for Al. Oxide formation at the film/electrode interface are also reported. Ushakov *et al.*<sup>16,17</sup> and Mishuk *et al.*<sup>18</sup> report similar issues including corrosion of electrodes and Joule heating in both CGO thin films and membranes.

The initial design includes Ti or Al electrodes. Metal electrodes are often used due to their high conductivity and accessibility<sup>19</sup>. These materials can be deposited with a PLD system. However the excimer laser does not constitute the proper laser source<sup>20</sup>. At UV wavelengths in fact, the metals reflection coefficient is around 50-90%, and therefore the ablation rate would be drastically reduced<sup>20</sup>. On the other hand, sputtering deposition technique is a suitable tool for the deposition of pure metals<sup>19,21</sup>. Therefore, Ti and Al electrodes were deposited by DC sputtering at room temperature and base pressure is  $< 10^{-6}$  mTorr. The deposition were carried out with Ar flow with a pressure of  $10^{-3}$  mTorr.

We have though observed some possible disadvantages of using metal/CGO/metal structure. Figure 3-3 shows SEM images of CGO film with Al top electrode. Though evident defect on the microstructure are not visible from the top surface (Figure 3-3a), the cross-section in Figure 3-3b highlights irregular adhesion of the top film and rough surface. Moreover, the free surface of Al electrodes displays severe corrosion visible to the naked eye after a few days from the deposition (Figure 3-4), making any electromechanical test impossible.

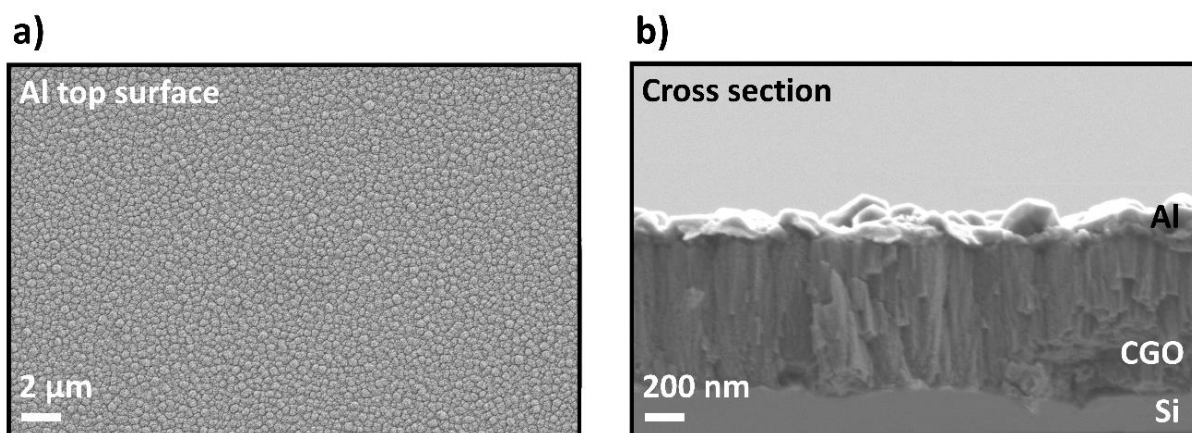


Figure 3-3: SEM images of Al film grown on CGO. a) top view. b) cross-section

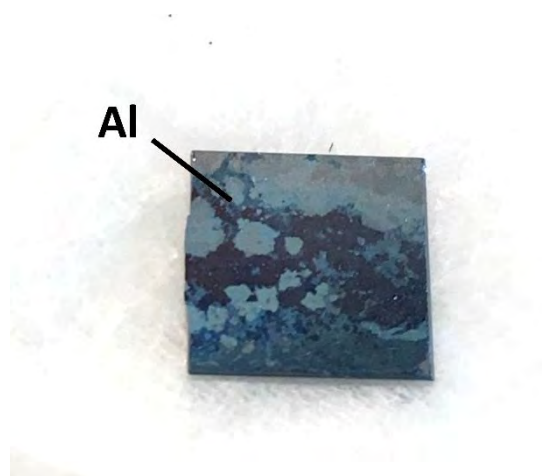


Figure 3-4: Al coating on CGO film.

Figure 3-5 shows SEM images for Ti top electrode. In this case, several flaws are visible from both top view and cross-section pictures. The poor adhesion resulted in bubbles and cracks across the surface. This can be caused by the low-temperature condition during metal sputtering or contamination of CGO surface when breaking the vacuum after the film deposition.

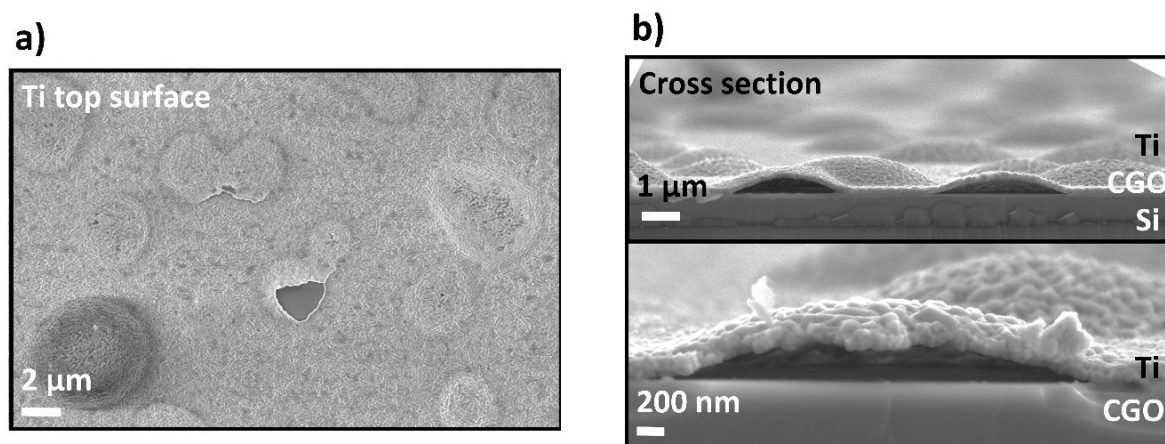


Figure 3-5: SEM images of Ti film grown on CGO. a) top view. b) cross-section and zoom.

When used as bottom electrodes, Al and Ti films affect the CGO crystal quality due to the poor adhesion of the ceramic-metallic interface. This can lead to the formation of pinholes and consequent shortcut of the sample. This constitutes the most severe problem in thin films with metal electrodes, where most of these films ( $\approx 90\%$ ) were shorted as deposited. Ti and Al bottom electrodes also affect the crystallographic properties of CGO top film. Polycrystalline CGO tends to grow with a dominating (111) orientation<sup>15</sup>. Figure 3-6a show  $\theta$ - $2\theta$  scan of CGO grown on Al and Ti metals electrodes. Here, CGO shows a mixture of several textures in a similar amount.

### 3.1.3 Titanium nitride and gold electrodes.

TiN is an excellent candidate as electrode as it shows high conductivity (200 S/cm at RT) and chemical stability<sup>22,23</sup>. TiN in fact, is a well-established material in Si-based applications as electrode and barrier to avoid diffusion or chemical interaction between two materials, but also as gate and Schottky barrier contact<sup>24-27</sup>. Therefore, it is expected to prevent oxide formation at the electrode/film interface<sup>22,23</sup>.

In order to evaluate performances and mechanical stability of the device, TiN electrodes are evaluated by means of electrostrictive long-time and high electric field performances. The results of using TiN electrodes are also compared to Au electrodes sample. Gold is chemically stable material and provides

excellent conduction. Also, it does not show detachment as Ti and Al do. The samples depicted in Figure 3-7, includes bottom TiN electrodes.

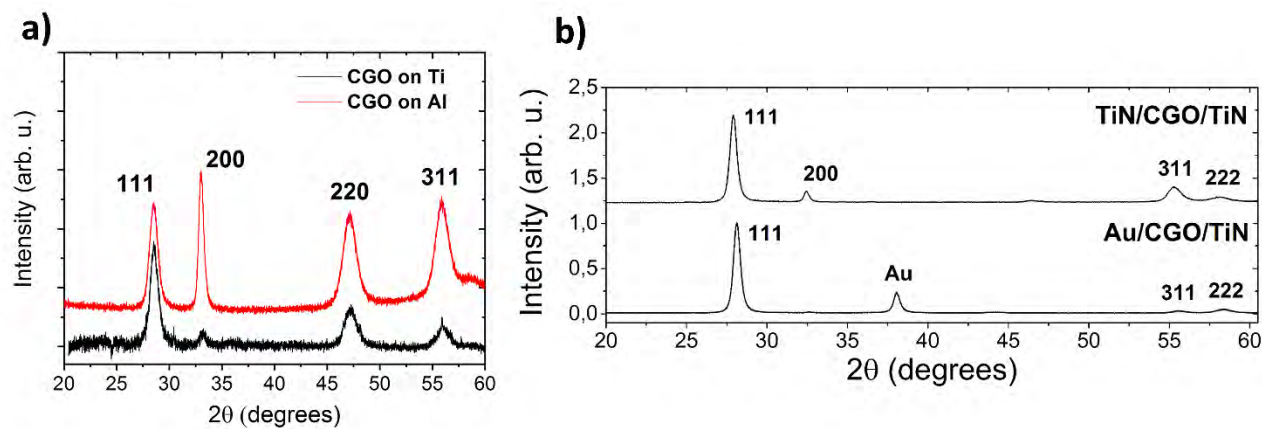


Figure 3-6:  $\theta$ - $2\theta$  scans of CGO thin films. a) CGO deposited on Ti and Al bottom electrodes. b) CGO deposited on TiN, with Au and TiN top electrode

TiN top electrode was grown by PLD at 600 °C with nitrogen flow at  $10^{-3}$  mbar using a TiN target supplied by CRM material. Such high temperature is necessary to deposit conductive films<sup>28</sup>, while the  $N_2$  flow is needed to transport the correct stoichiometry to the substrate<sup>28</sup>. The laser frequency is 20 Hz with 200 mJ energy and 3 J/cm<sup>2</sup> fluence. TiN deposition is challenging, as oxygen impurities oxygen impurities can remain in the vacuum chamber and affect the film quality<sup>28</sup>. For this reason, background pressure  $< 10^{-7}$  mbar is recommended<sup>28</sup>. Au is sputtered with a Bal-Tec SCD 005 coater at room temperature.

The as-deposited top electrodes show good adhesion with CGO as visible in Figure 3-8. CGO films show a dense columnar microstructure, with no sign of evident flaws at the interface with the electrodes. Figure 3-6b show the XRD  $\theta$ - $2\theta$  of CGO thin films grown on the TiN/Si substrate. The films are highly textured with a preferred (111) orientation, and no additional phases are detected, demonstrating high crystallographic order in CGO films if compared to metal bottom electrodes.

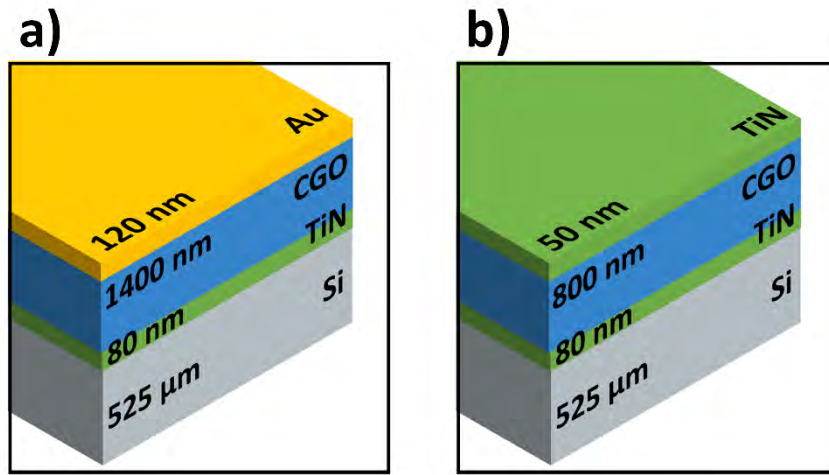


Figure 3-7: Schematic of TiN based samples. a) Au top electrode: Au/CGO/TiN sample. b) TiN top electrode: TiN/CGO/TiN sample.

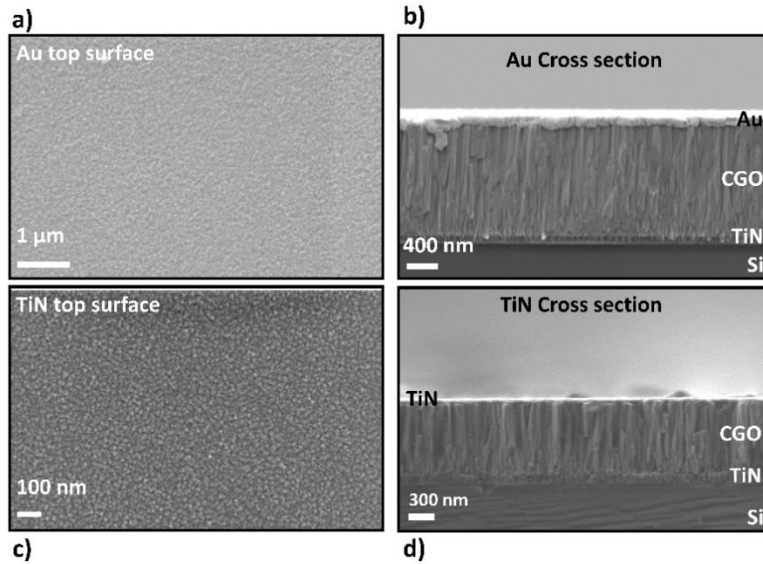


Figure 3-8: SEM images of CGO thin films on TiN/Si substrate. a) Top view of Au top electrode. b) Cross-section of CGO on TiN/Si with Au top electrode. c) top view of TiN top electrode. d) Cross-section of CGO on TiN/Si with TiN top electrode.

### 3.1.4 Electrostriction performances and stress tests.

For the electrostriction performances analysis, the vertical displacement at the free tip of the cantilever is measured as described in Chapter 2.4, while an alternating electric field is applied at a frequency of  $f_e=100$  MHz. TiN/CGO/TiN and Au/CGO/TiN samples both show electrostrictive response, with a similar



coefficient:  $M_{13} = 2.3 \pm 0.3 \cdot 10^{-18} \text{ m}^2\text{V}^{-2}$  and  $M_{13} = 1.5 \pm 0.2 \cdot 10^{-18} \text{ m}^2\text{V}^{-2}$  respectively. The stress detected consist of a compression in the direction parallel to the electric field. Moreover, the oscillation is found to be a second harmonic of the electric field frequency, in consistence with the previous works<sup>8</sup>.

One should be careful with the interpretation the results. Maxwell stress tensor and thermal expansion, in particular, can affect electrostriction evaluation, leading to false results. Both effects depend on the squared of the electric field and its second harmonic<sup>28</sup>. Maxwell tensor represents the stress due to the electrostatic attraction of two electrodes with parallel faces and, in static field condition, is described as  $\sigma_{ij}$ :

$$\sigma_{ij} = \varepsilon_0 E_i E_j - \frac{1}{2} \varepsilon_0 E^2 \delta_{ij} \quad 3.1$$

$\varepsilon_0$  is the vacuum permittivity and  $\delta_{ij}$  is the Kronecker's delta that is 1 if  $i = j$  and 0 if  $i \neq j$ . The tensor contribution is noticeable in polymers<sup>28</sup>, but for hard materials such as CGO it is usually negligible<sup>29</sup>. The vibration of the cantilever measured in our experiments is due to the in-plane stress induced by perpendicular electric field *i.e.*  $\sigma_{13}$ . In this geometry, the Maxwell tensor is zero<sup>28</sup>. The temperature increase is monitored experimentally using a thermal camera. No heating was detected.

Figure 3-9 exhibits the response of the samples in the initial and final state of the experiment. Both Au/CGO/TiN and TiN/CGO/TiN display oscillation. As reported in literature<sup>7</sup>, the vibration observed depends on the second harmonic of the applied field, and the compressive stress develops in the direction parallel to the electric field. After five minutes measuring time, Au/CGO/TiN displays a decreasing in the performances (Figure 3-9a, right side). Moreover, the oscillation shows an additional contribution that depends on the first harmonic of the electric field (100 mHz). A double harmonic oscillation should take place when both a static ( $E_{DC}$ ) and alternating ( $E_{AC}$ ) electric fields are applied. When it happens, the resulting stress is proportional to both first and second harmonics:

$$\sigma \propto \{E_{ac} \cos(\omega t) + E_{dc}\}^2 = E_{dc}^2 + \frac{E_{ac}^2}{2} + 2E_{ac}E_{dc} \cos(\omega t) + \frac{E_{ac}^2}{2} \cos(2\omega t) \quad 3.2$$

With  $\omega = 2\pi f$ . As this behavior raises during the experiment, it can be ascribed to an evolution of the system, in particular to the creation of an internal bias representing the static term  $E_{DC}$  in the equation.

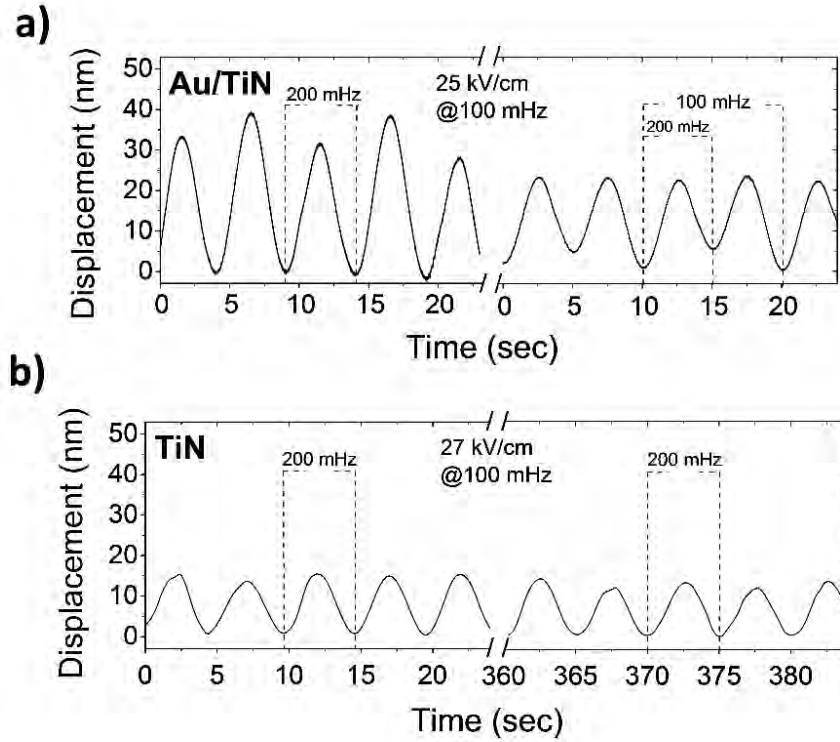


Figure 3-9: Electrostrictive activity with 100 mHz electric field. The frequency of oscillation is reported. 200 mHz and 100 mHz are the first and second harmonic of the applied field, respectively. a) Au/CGO/TiN sample at 25 kV/cm. Left: initial condition. Right: after consecutive measurements. b) TiN/CGO/TiN at 27 kV/cm. Left: initial condition. Right: after consecutive measurements.

The structural reason for both double harmonic oscillation and reduced performances can be attributed to a decreasing of the electrode quality due to poor adhesion, hindered conductivity and/or polarization effect at the interface. TiN/CGO/TiN sample, on the other hand, displays stable performances with no



sign of undesired effects, confirming the good quality of both top and bottom TiN electrodes and their coupling with CGO film.

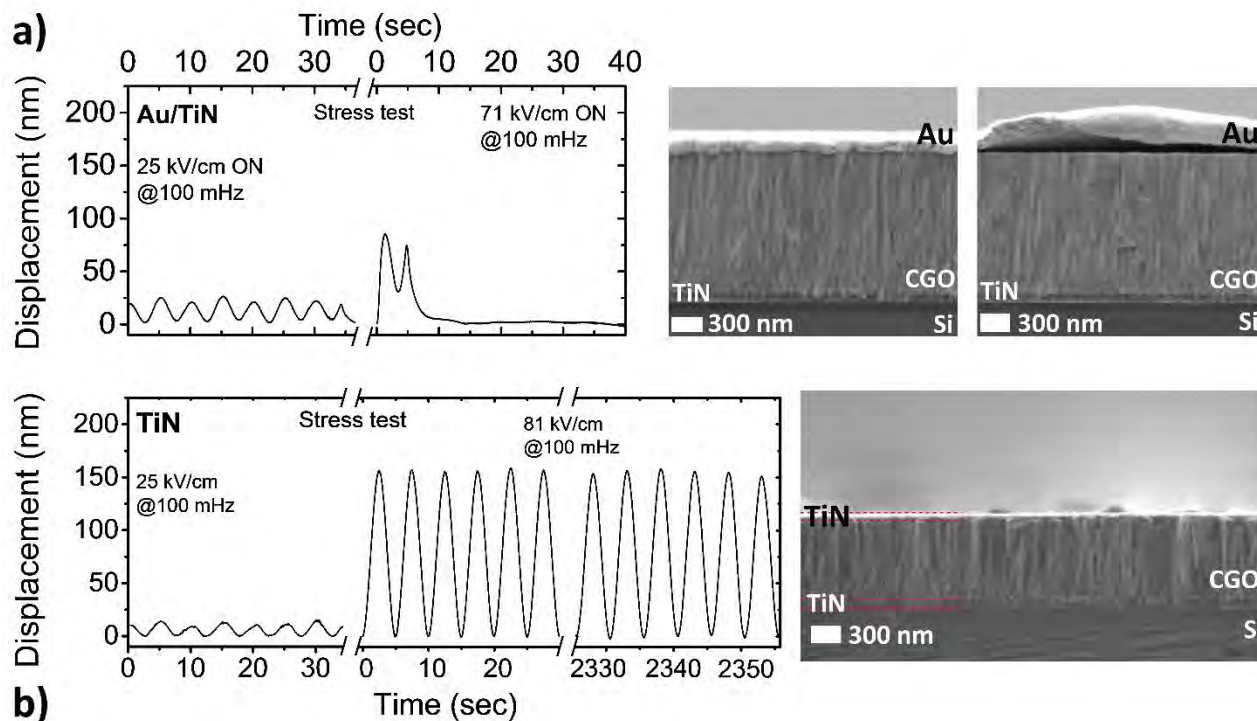


Figure 3-10: Stress-test with a high electric field. a) Au/CGO/TiN sample: (left) oscillation at 25 kV/cm and 71 kV/cm applied field (mechanical failure); (middle) SEM cross-section image of Au/CGO/TiN as deposited; (right) SEM cross-section after the field-induced failure showing the detachment of top electrode. b) TiN/CGO/TiN sample with (left) oscillation at 25 kV/cm and 81 kV/cm applied field. 40 min long measurement is displayed; (right) SEM cross section image after the stress test, TiN electrodes are still intact and perfectly adhered to the CGO film.

Figure 3-10 shows the stress test at high electric field for both samples. Upon increasing the field from 25 kV/cm to 71 kV/cm, Au/CGO/TiN displays a high oscillation amplitude which disappears rapidly. The resistance increased from 10 k $\Omega$  to 100-200 M $\Omega$  and did not restore with the time. The mechanical failure of the sample is attributed to the failure of the electrodes, as in line with the previous stress test. Figure 3-10a (middle) shows the SEM cross-section of an as-deposited Au/CGO/TiN structure, in which is visible the adhesion of Au electrode. Figure 3-10a (right) instead, shows the postmortem of the sample: a severe detachment of the top electrode is clearly visible, while CGO film does not show any apparent flaws as well as the CGO/TiN interface.

On the other hand, CGO film does not display any apparent flaws as well as the CGO/TiN interface. Figure 3-10b reports oscillations of the ceramic sample at 81 kV/cm over applying 40 minutes electric field, continuously. Again, TiN/CGO/TiN do not show any sign of degradation in the performances or failure. After this test, cross-section SEM is performed, and no flaws are detected in the whole structure. These tests demonstrate exceptional integrity of CGO/TiN structure due to mechanical and electrical stability. This finding demonstrate that TiN/CGO structured thin films represent a promising candidate for the development of Si-based application in the field of electromechanical technologies.

This work has been published as: “Enhanced electro-mechanical coupling of TiN/Ce<sub>0.8</sub>Gd<sub>0.2</sub>O<sub>1.9</sub> thin film electrostrictor”, S. Santucci, H. Zhang, S. Sanna, N. Pryds, V. Esposito (2019), *APL Materials*, 7(7), p. 071104., reported in Appendix A.C.

### 3.1.5 Ceramic electrodes: LSCF, STN and SRO.

We further investigated other ceramic perovskites as electrodes. Qualitative tests have been performed on microstructure, conductivity and stability of La<sub>x</sub>Sr<sub>1-x</sub>Co<sub>1-y</sub>Fe<sub>y</sub>O<sub>3</sub> (LSCF), Nb-doped SrTiO<sub>3</sub> (STN) and SrRuO<sub>3</sub> (SRO).

La<sub>0.58</sub>Sr<sub>0.4</sub>Co<sub>0.2</sub>Fe<sub>0.8</sub>O<sub>3-δ</sub> (LSCF) is a well-known perovskite used in solid oxide fuel cells (SOFCs) as cathode<sup>30–33</sup>. Being a mixed conductor, LSCF has high conductivity at temperatures around 300–700 °C. However, at room temperature, it still possesses a resistivity of about  $\rho \approx 10^{-2} \Omega \cdot cm$ <sup>32,33</sup>, with the exact value depends on the level of the composition, defect chemistry, etc<sup>33,34</sup>. LSCF thin films are deposited by PLD at 10 Hz frequency and a fluence of 4 J/cm<sup>2</sup>. The temperature is set at 600 °C<sup>30</sup>. P<sub>O2</sub> is set at 10<sup>-2</sup> mbar. Such high pressure guarantees a dense microstructure, maintaining the correct stoichiometry of the material<sup>30</sup>. The resulting films were conductive with spread values  $\rho \approx 10^{-1}/10^{-2} \Omega \cdot cm$ . Figure 3-11 illustrates SEM of the microstructure of LSCF on STO. The thin films display a dense and continuous microstructure with no sign of detachment. LSCF however, demonstrates a quick degradation process soon after the deposition. After some hours, the in-plane resistance of the thin film increases to MΩ on an area of 0.25 cm<sup>2</sup>, probably caused by insulating phase formation at the interface. Moreover, after a

couple of days, delamination visible by the naked eye of top LSCF takes place (Figure 3-12). For these reasons, LSCF is excluded from further analysis.

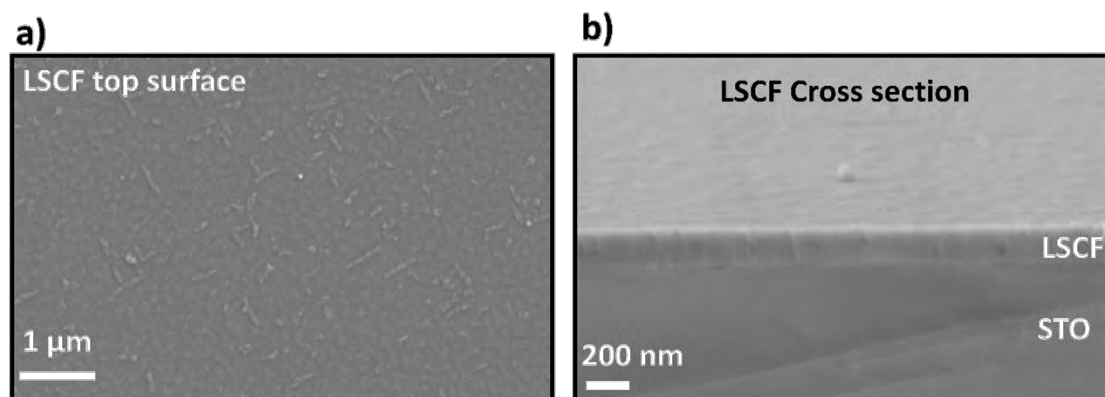


Figure 3-11: SEM images of LSCF thin films on STO substrate. a) LSCF top surface. b) Cross-section view.

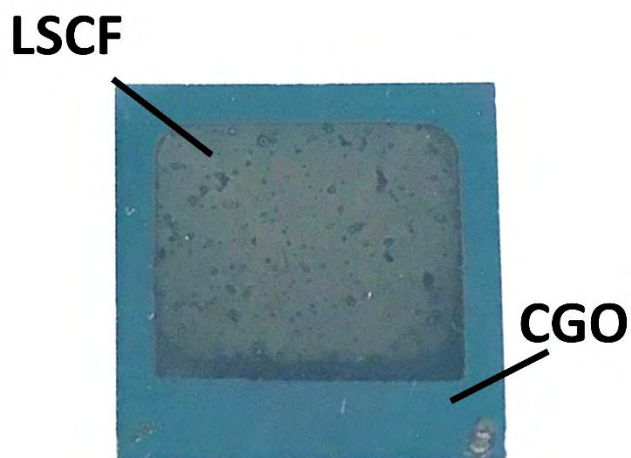


Figure 3-12: Photo of CGO sample with LSCF top electrode. Contrast and light adapted to highlight the detachment of electrode.

When doped with Nb, STO becomes conductive (n-type), and it can be used as electrode<sup>35,36</sup>. As electrode, 1.4 mol% Nb-doped SrTiO<sub>3</sub> (STN) showed excellent properties. Indeed, STN single crystals are commercially available and can be directly used as substrate as well as bottom electrode. We use commercial STN (200) oriented single crystal from Crystech. The substrates had a measured resistivity

of  $\rho = 1 \cdot 10^{-3} \Omega \cdot \text{cm}$ . STO and STN both allow highly coherent CGO films since the lattice parameters are similar. For XRD results and microstructure properties, see Chapter 4.1.

Alternatively,  $\text{SrRuO}_3$  (SRO) is also used. SRO is a conductive perovskite used as an electrode in a wide range of structure due to the high conductivity and chemical stability<sup>36–39</sup>. SRO can grow epitaxially on several substrates such as STO, LAO, YSZ and Si<sup>36,40</sup>. SRO thin films were deposited on CGO films by PLD at 700 °C temperature. This high temperature is necessary, as the resistivity increases dramatically for  $T < 700$  °C<sup>41</sup>. Also, high quality crystal growth<sup>40</sup> is ensured by high oxygen partial pressure, set at  $10^{-1}$  mbar. The resistivity measured is in the range of  $\rho = 4.99 \cdot 10^{-3} \Omega \cdot \text{cm}$ , comparable with literature<sup>36,41</sup>. In contrast, films deposited at  $P_{\text{O}_2} = 10^{-3}$  mbar showed  $\rho = 3.00 \cdot 10^{-2} \Omega \cdot \text{cm}$ . The laser frequency is at 10 Hz and fluency at  $4 \text{ J/cm}^2$ .

As an electrode, SRO demonstrates excellent reliability with no delamination after time or voltage stress. Qualitatively, it endured the operative electric field. In order to ensure constant voltage distribution across the in-plane electrode surface, a 40-50 nm sputtered Au coating is used as current collector on top of the SRO. With high electric fields, Au coating can detach, but the SRO is not damaged. Consequently the sample can usually be used again. Figure 3-13 shows the structure for highly coherent thin film sample using STN as substrate and bottom electrode and SRO/Au as top electrodes.

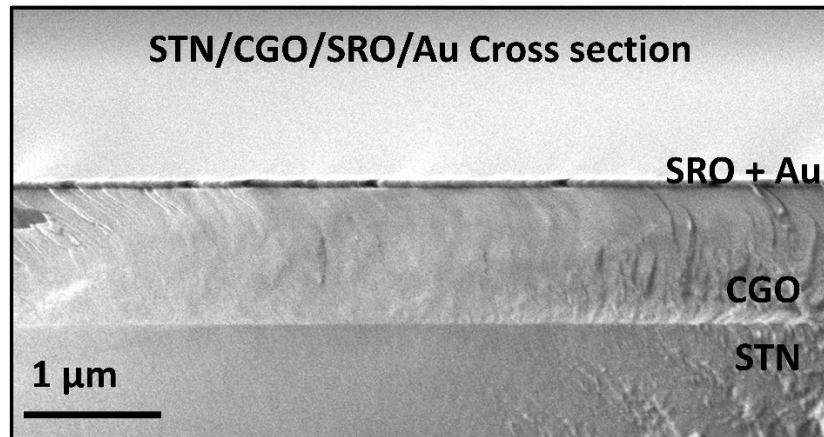


Figure 3-13: SEM cross-section image of STN/CGO/SRO/Au heterostructure. A highly coherent structure was achieved as superior stability compared to metal electrodes samples.

## 3.2 PLANAR ELECTRODE CONFIGURATION

Despite the optimization of mechanical stability and electrodes performances, shortcut is a severe problem often occurring on samples with a top-bottom electrode configuration. As a matter of fact, crystal defects, particulates, substrate imperfection can cause pinholes through CGO film and create conductive paths. The distance between the electrodes (around  $1\ \mu\text{m}$ ) is small if compared to the in-plane area. Consequently, the probability of having pinholes is high. In shorted samples, the applied field through the material is dramatically reduced. Therefore, the electrostriction effect is no more detectable. One way to overcome this problem is to deposit films with high thickness while keeping the electrode as thin as possible. However, the fraction of shorted sample results still very high, around 80%. In addition, reducing the area of the cantilever helps to decrease the probability of pinhole. However, the cantilever oscillation depends on the squared of the length (Chapter 2.4). As a result, small cantilevers develop low displacement, difficult to detect.

This issue cannot be solved easily but can be bypassed with a different electrodes configuration. Here, an alternative planar geometry with both the electrodes placed on the surface of CGO, at a distance of 300-500  $\mu\text{m}$ , was used. Figure 3-14 shows the two configurations. The planar geometry (Figure 3-14b) ensures high resistance as a consequence of the distance between the electrodes.

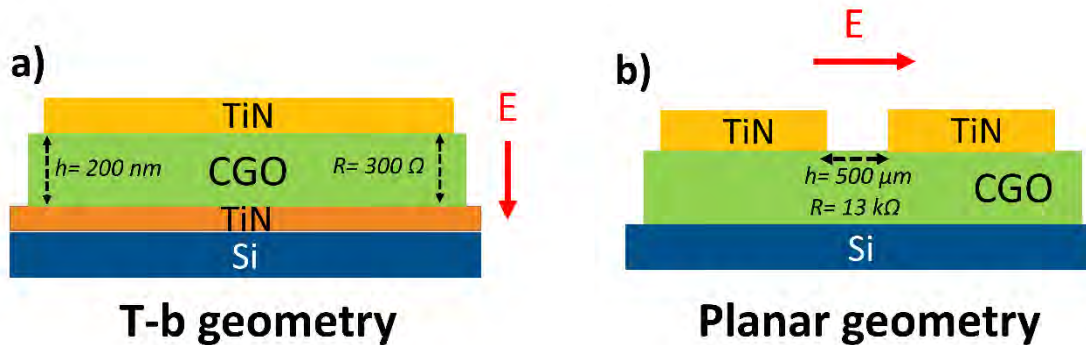


Figure 3-14: Schematic of electrodes configuration. a) Top-bottom geometry. b) Planar geometry.

Planar configuration brings even further advantages. In this configuration, CGO film can be grown epitaxial on various substrates such as NGO and STO perovskites<sup>10,43</sup>, without the bottom electrode affecting the film microstructure. By changing the position of the electrodes with respect to the CGO



in-plane orientation, it is possible to study electrostriction in different crystallographic directions. For the electromechanical performances of planar electrodes configuration, see Chapter 4.

### 3.2.1 Temperature measurements.

To compare top-bottom (t-b) and planar symmetries electrical integrity, we perform thermal measurements under an applied voltage. A temperature increase is an issue derived from low resistance, which leads to Joule heating when voltage is applied. The samples used are depicted in Figure 3-14a,b. The top-bottom (t-b) and planar geometry samples have a resistance of 300  $\Omega$  and 13 k $\Omega$  for, respectively. The samples with top surface electrodes usually have a resistance in the range of  $10^6 \Omega$ . A low resistance sample has been chosen to highlight the possible thermal increasing. The voltage applied is in the form of square waves, with a frequency of 200 mHz. The contacts are made with Ag paste. During the thermal camera scan, accurate thermal measurements are taken on several single points on the sample surface and then averaged.

Figure 3-15 shows the temperature spectrum for the sample with surface electrodes. For both 5 V and 8 V applied voltage, the temperature increase is below the resolution of the instrument. A slightly hotter region is found on the Ag paste.

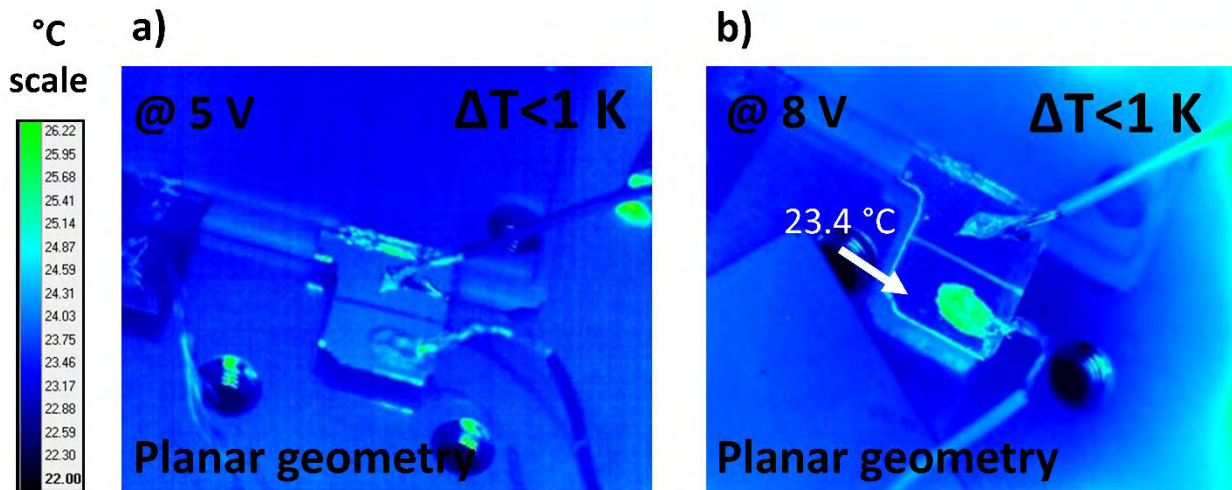


Figure 3-15: Thermal measurements of the sample with planar configuration. a) 5 V applied. b) 8V applied

Figure 3-16, on the other hand, displays the result for the sample in the t-b configuration. When applying 4.5 V, no temperature increase is detected. At 6 V however, the thermal camera detects 26 °C corresponding to an increase of  $\Delta T = 2.4$  K across the sample surface, above all around the top electrode. The Ag paste is again found to be hotter than the rest of the sample, with a temperature of 28 °C.

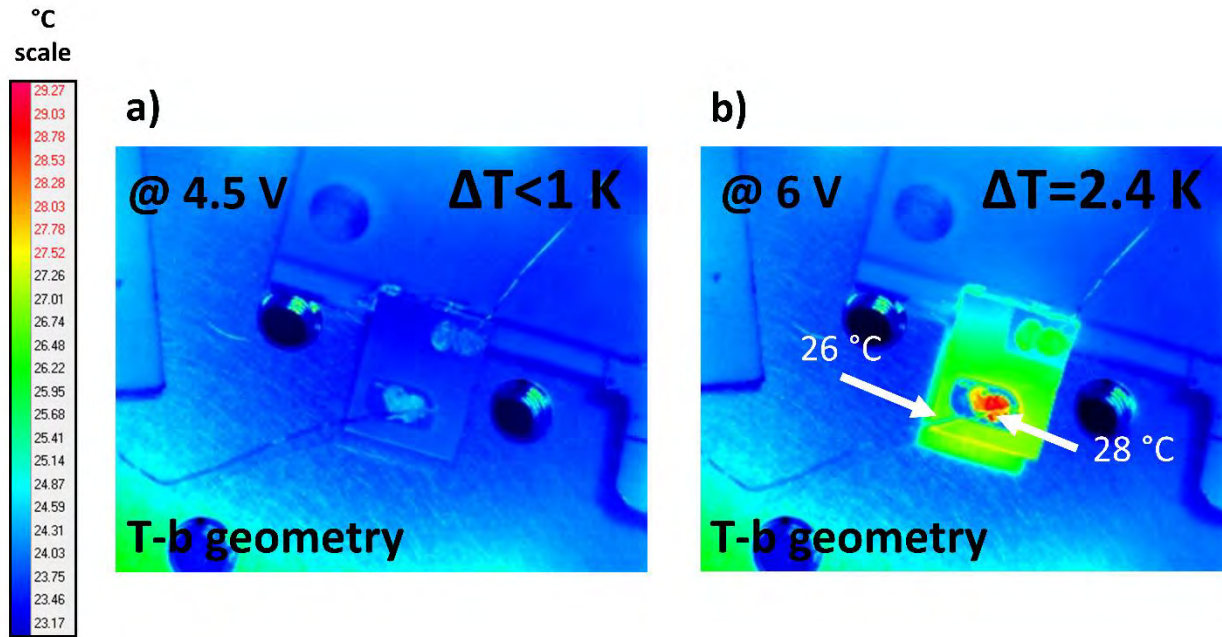


Figure 3-16: Thermal measurements of the sample with t-b configuration. a) 4.5 V applied. b) 6V applied

Overall, planar geometry has proved to be a reliable alternative to top-bottom configuration. To enhance the device, we use a shadow mask of  $\text{Al}_2\text{O}_3$  with a gap of 500  $\mu\text{m}$  provided by Lasertech A/S. The electrodes have an area of 4  $\text{mm}^2$  each. Most of the samples developed have high resistance ( $R > 1 \text{ M}\Omega$ ). Also, arm probes with Tungsten needle tip are used as contacts instead Ag paste to avoid increasing of the temperature. These probes are not recommended in top-bottom samples, as the tip can penetrate the layers and cause shortcut.

### 3.2.2 Setup requirements.

Planar structured samples require some new requirements from our setup. In planar geometry the only electromechanically active part of CGO is the area between the electrodes, which is 500  $\mu\text{m}$  long. Residual electromechanical effects of CGO film of other parts of the sample are not considered in

measurements. Consequently, the electrostrictive oscillation amplitude reduces drastically. In order to detect such small displacement, we need to use a lock-in amplifier. This instrument extracts from a noisy signal an oscillating wave with a specific frequency and amplitude with extremely high precision. In our setup, this allows measurements down to the sub-nanometer range. In particular, the background noise at 1-3 Hz frequency is about 0.2 nm, meaning that oscillation with higher amplitude can be measured. As the distance between the electrodes is significant, high voltage sources are needed to reach intense electric fields. We use a voltage amplifier Trek 2200, coupled with the wave generator, to reach such fields. To have an electric field high enough to trigger the electrostriction effect, we needed to apply a typical voltage around 100-200 V.

In polycrystalline films, the CGO microstructure is columnar with vertical grain boundaries. In the planar electrode configuration, the electric field is applied horizontally. Consequently, the contribution of grain boundaries affects the overall electrostriction process<sup>19</sup>. In order to clarify the effect of grain blocking barriers on the electrostrictive process we will focus in the following on electromechanical performance dependency of microstructure.

### 3.3 GRAIN BOUNDARIES EFFECT ON ELECTROSTRICTION IN BULK CGO.

---

The effect of oxygen defects ion-blocking barriers on electrostriction is investigated. A study of the bulk CGO pellets with different grain boundary (g.b.) morphology and grain size were studied. The study has been published as *“Effect of oxygen defects blocking barriers on gadolinium doped ceria (GDC) electro-chemo-mechanical properties”* Kabir A., Santucci S., Nong N. V., Varenik M., Lubomirsky I., Nigon R., Mural P., Esposito V. (2019), *Acta Materialia*. Elsevier Ltd, 174, pp. 53–60.

In polycrystalline ion conductors such as CGO, the grain boundaries are areas of disordered phases *i.e.* dopant- vacancies associations <sup>43–45</sup>, and voltage drop layers <sup>19</sup>. Ionic migration is significantly hindered at the grain boundaries <sup>43,46–48</sup>. Moreover, solute segregation, phase transformation, nano-domain formation, porosity also introduce vast ion-blocking effect. All of these effects are also assumed to block



the electrostriction effect as well <sup>19</sup>. This work aims to study the oxygen defects configuration influence on electrostriction.

The microstructure of bulk materials can be controlled by process parameters such as sintering temperature and time. When the dopant amount is fixed, the solute drag mechanism can be controlled by sintering conditions and can create specific grain boundaries configuration <sup>4</sup>. 10 mol% CGO polycrystalline samples have been sintered by conventional, fast firing and field-assisted (SPS) methods to produce different oxygen vacancies configuration.

The conventional samples are uniaxially cold pressed at 300 MPa for 30 seconds and then sintered at 1450 °C in air for 10 h or for 2.5 h. Field-assisted spark plasma sintering (SPS) was used at pressure  $<6 \cdot 10^{-6}$  Torr, at 980 °C and uniaxial pressure of 70 MPa for 5 minutes. The samples were post-annealed to avoid reduction at 700 °C for 1 h. Finally, a fast-fired sample was made by consolidating the powders by SPS at 900 °C and then sintered at 1450 °C for 0.1 h, with a rapid heating and cooling rate of 20°C/min.

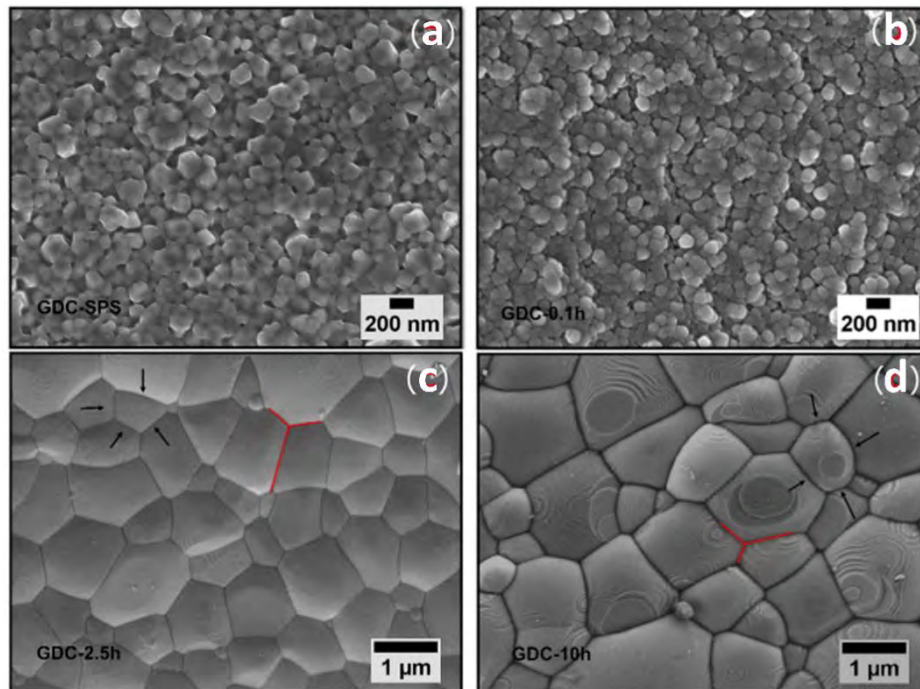


Figure 3-17: SEM images of CGO (or GDC) samples. a) SPS sample. b) Fast firing sample. c) Conventional sample 2.5h. d) Conventional sample 10 h.

Figure 3-17 shows the microstructure image of the resulting samples by SEM. SPS and fast-firing samples (GDC-SPS and GDC-0.1h) display small average grain size, around 150-200 nm, with a homogenous distribution. On the other hand, conventional sintered samples (GDC-2.5h and GDC-10h) possess bigger grains,  $2.0 \pm 0.3 \mu\text{m}$  and  $1.5 \pm 0.2 \mu\text{m}$ , respectively.

The electrical properties at the grain boundaries can be described through their blocking factor  $\alpha_{gb}$ . It is defined as the ratio of g.b. resistance ( $R_{gb}$ ) and total resistance:

$$\alpha_{gb} = \frac{R_{gb}}{R_{gb} + R_g} \quad 3.3$$

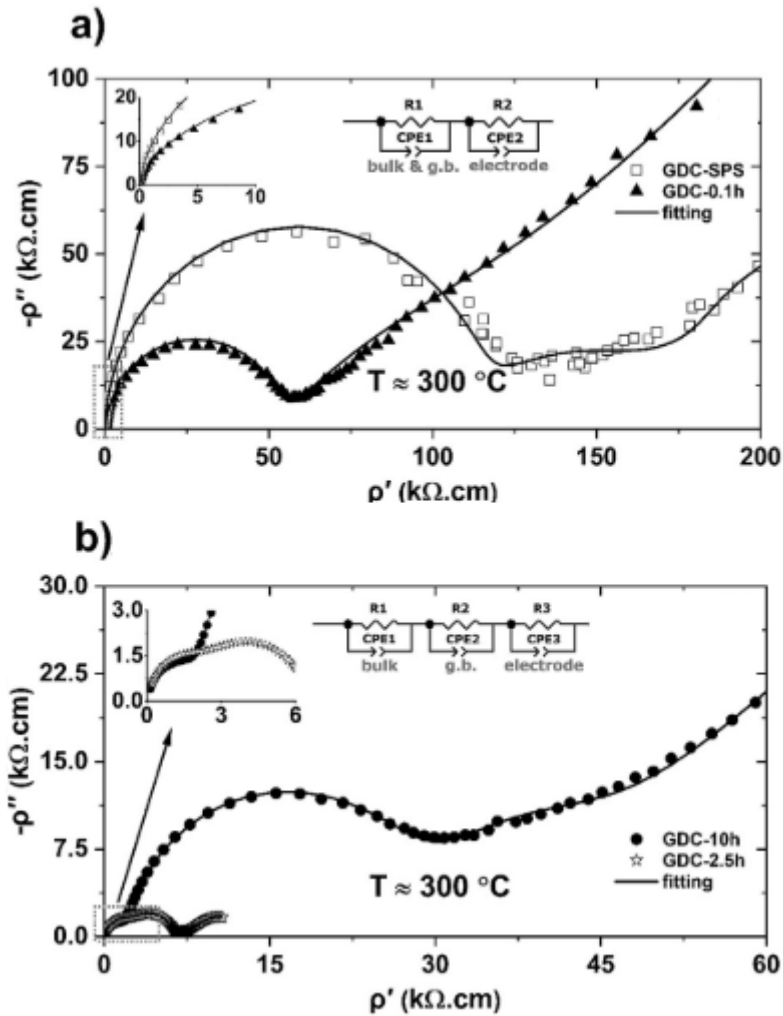


Figure 3-18: a) Nyquist plot ( $\rho'$  vs  $\rho''$ ) of GDC-SPS and GDC-0.1 h samples. b) Nyquist plot of GDC-10 h and GDC-2.5 h samples.

High blocking factor means that grain boundaries possess high oxygen trapping behavior and vacancy clustering, and therefore gives information about the morphology. Impedance spectroscopy analysis (Figure 3-18) shows that, despite having samples with similar density and same dopant concentration, the grain boundaries blocking factor results to be quite different, as a consequence of distinctive configuration of oxygen vacancies. The blocking factor attributed to the grain boundaries results high on GDC-SPS, with a value near 1, meaning that most of the overall resistance of the sample is due to g.b. Then

conventional samples GDC-10h and GDC-2.5h show  $\alpha_{gb} = 0.9$  and  $0.65$  respectively, with GDC-0.1h having an intermediate value.

Figure 3-19 exhibits the in-plane strain as a function of the squared in-plane electric field:  $\lambda_{33}$ . All the samples demonstrate negative strain and oscillation depending on the second harmonic of the electric field, as expected from literature<sup>7</sup>. For electric fields with low frequency, the samples display strain saturation. On the other hand, at high frequencies, the strain developed decreases. As a reference, we consider 1 Hz relative electrostriction coefficient: GDC-10h demonstrates the highest performances with an electrostriction coefficient of  $M_{33} = 2.8 \cdot 10^{-17} \text{ m}^2/\text{V}^2$ , followed by GDC-0.1h with  $M_{33} = 1.0 \cdot 10^{-17} \text{ m}^2/\text{V}^2$ . Then, GDC-SPS and GDC-2.5h displayed low coefficients:  $M_{33} = 0.4 \cdot 10^{-17} \text{ m}^2/\text{V}^2$  and  $M_{33} = 0.6 \cdot 10^{-17} \text{ m}^2/\text{V}^2$  respectively.

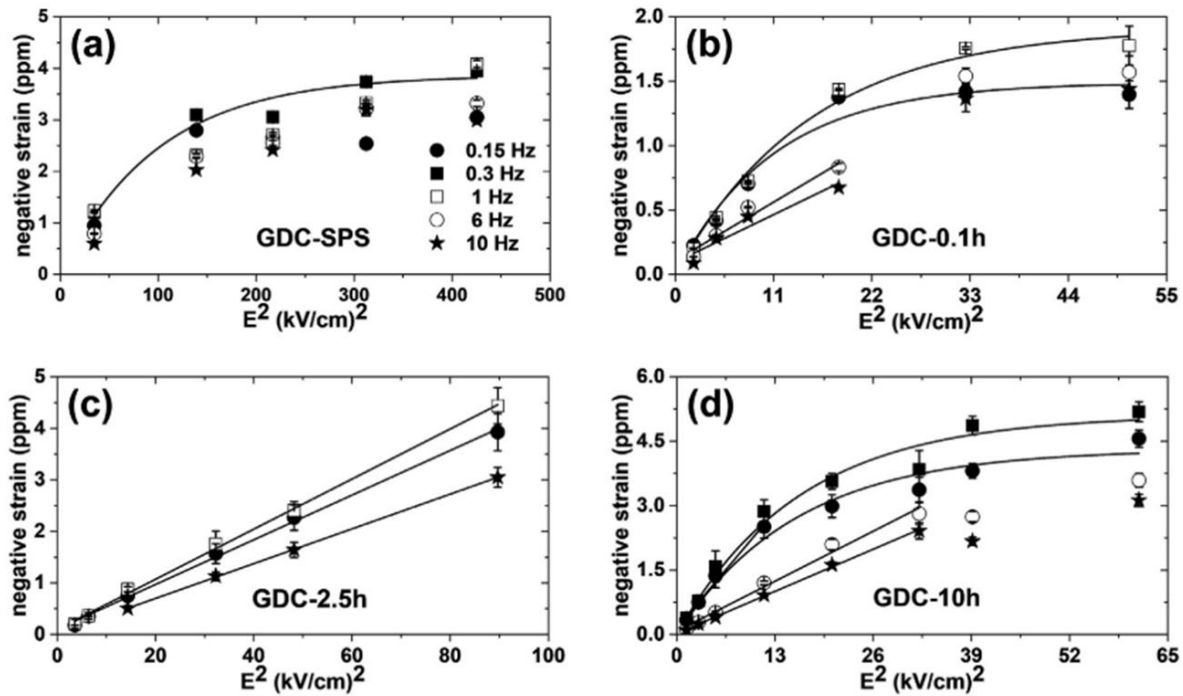


Figure 3-19: Electrostriction analysis depending on the electric field and frequency.

From these results, it can be concluded that electrostriction does not depend on the grain size, microstructure or dopant amount: GDC-10 and GDC-2.5 have same Gd amount and similar microstructure, but they also displayed different electromechanical activity. On the other hand, grain

boundaries blocking factor increase with the electrostriction coefficient. This trend then stops when  $\alpha_{gb}$  is close to 1 (“super blocking” g.b.), and the electromechanical activity is reduced drastically. The comparison of the electrostriction effect with grain size, grain boundaries resistivity and blocking barrier effect is visible in Figure 3-20.

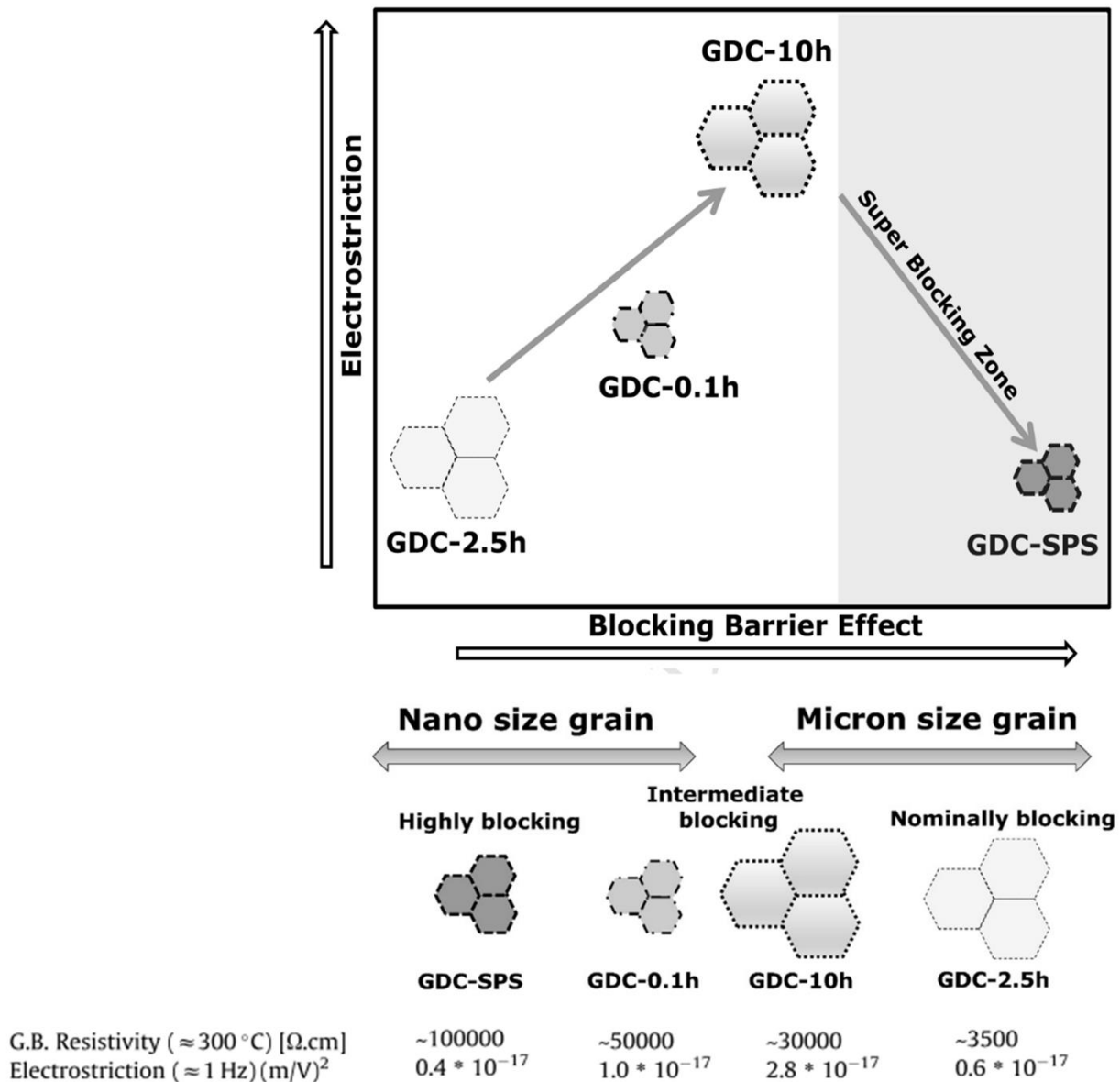


Figure 3-20: Comparative analysis of electrostriction with grain size, grain boundaries resistivity and blocking barrier effect.

## 3.4 REFERENCES

---

- <sup>1</sup> P. Muralt, J. Micromechanics Microengineering **10**, 136 (2000).
- <sup>2</sup> P. Muralt, Integr. Ferroelectr. **17**, 297 (1997).
- <sup>3</sup> A. Infortuna, A.S. Harvey, and L.J. Gauckler, Adv. Funct. Mater. **18**, 127 (2008).
- <sup>4</sup> E. Wachtel, A.I. Frenkel, and I. Lubomirsky, Adv. Mater. **30**, 1 (2018).
- <sup>5</sup> V. Esposito and E. Traversa, J. Am. Ceram. Soc. **91**, 1037 (2008).
- <sup>6</sup> A. Mazzalai, D. Balma, N. Chidambaram, R. Matloub, and P. Muralt, J. Microelectromechanical Syst. **24**, 831 (2015).
- <sup>7</sup> M. Chekchaki, V. Lazarus, and J. Frelat, J. Appl. Mech. **78**, 011008 (2011).
- <sup>8</sup> R. Korobko, A. Patlolla, A. Kossoy, E. Wachtel, H.L. Tuller, A.I. Frenkel, and I. Lubomirsky, Adv. Mater. **24**, 5857 (2012).
- <sup>9</sup> R. Korobko, E. Wachtel, and I. Lubomirsky, Sensors Actuators, A Phys. **201**, 73 (2013).
- <sup>10</sup> S. Sanna, V. Esposito, D. Pergolesi, A. Orsini, A. Tebano, S. Licocchia, G. Balestrino, and E. Traversa, Adv. Funct. Mater. **19**, 1713 (2009).
- <sup>11</sup> J. Schou, Appl. Surf. Sci. **255**, 5191 (2009).
- <sup>12</sup> N. Pryds, K. Rodrigo, S. Linderöth, and J. Schou, Appl. Surf. Sci. **255**, 5232 (2009).
- <sup>13</sup> A. Bieberle-Hütter, J.L. Hertz, and H.L. Tuller, Acta Mater. **56**, 177 (2008).
- <sup>14</sup> V. Esposito, D.W. Ni, S. Sanna, F. Gualandris, and N. Pryds, RSC Adv. **7**, 13784 (2017).
- <sup>15</sup> M. Hadad, H. Ashraf, G. Mohanty, C. Sandu, and P. Muralt, Acta Mater. **118**, 1 (2016).
- <sup>16</sup> A.D. Ushakov, N. Yavo, E. Mishuk, I. Lubomirsky, V.Y. Shur, and A.L. Kholkin, KnE Mater. Sci. **1**, 177 (2016).
- <sup>17</sup> A.D. Ushakov, E. Mishuk, E. Makagon, D.O. Alikin, A.A. Esin, I.S. Baturin, A. Tselev, V.Y. Shur, I. Lubomirsky, and A.L. Kholkin, Appl. Phys. Lett. **110**, 142902 (2017).
- <sup>18</sup> E. Mishuk, E. Makagon, E. Wachtel, S.R. Cohen, R. Popovitz-Biro, and I. Lubomirsky, Sensors Actuators, A Phys. **264**, 333 (2017).
- <sup>19</sup> V. V. Felmetzger and M.K. Mikhov, 2012 IEEE Int. Freq. Control Symp. IFCS 2012, Proc. 406 (2012).
- <sup>20</sup> R. Eason, *Pulsed Laser Deposition of Thin Films* (2007).
- <sup>21</sup> A.H. Simon, *Sputter Processing* (Elsevier Inc., 2018).

- <sup>22</sup> J.E. Sundgren, *Thin Solid Films* **128**, 21 (1985).
- <sup>23</sup> N.K. Ponon, D.J.R. Appleby, E. Arac, P.J. King, S. Ganti, K.S.K. Kwa, and A.O. Neill, *Thin Solid Films* **578**, 31 (2015).
- <sup>24</sup> R.H. Dauskardt, M. Lane, Q. Ma, and N. Krishna, **61**, 141 (1998).
- <sup>25</sup> M.C. Lemme, J.K. Efavi, T. Mollenhauer, M. Schmidt, H.D.B. Gottlob, T. Wahlbrink, and H. Kurz, **83**, 1551 (2006).
- <sup>26</sup> M. Lukosius, C. Walczyk, M. Fraschke, D. Wolansky, H. Richter, and C. Wenger, *Thin Solid Films* **518**, 4380 (2010).
- <sup>27</sup> C.N. Kirchner, H. Hallmeier, R. Szargan, T. Raschke, and C. Radehaus, *Electroanalysis* **19**, 1023 (2007).
- <sup>28</sup> R. Chowdhury, R.D. Vispute, K. Jagannadham, and J. Narayan, *J. Mater. Res.* **11**, 1458 (1996).
- <sup>29</sup> Y.M. Shkel and D.J. Klingenberg, *J. Appl. Phys.* **80**, 4566 (1996).
- <sup>30</sup> L. Liu and P. Sharma, *J. Mech. Phys. Solids* **112**, 1 (2018).
- <sup>31</sup> P. Plonczak, A. Bieberle-Hutter, M. Søggaard, T. Ryll, J. Martynczuk, P.V. Hendriksen, and L.J. Gauckler, *Adv. Funct. Mater.* **21**, 2764 (2011).
- <sup>32</sup> D.Z. De Florio, R. Muccillo, V. Esposito, E. Di Bartolomeo, and E. Traversa, *J. Electrochem. Soc.* **152**, 88 (2005).
- <sup>33</sup> M. Lubini, E. Chinarro, B. Moreno, V.C. De Sousa, A.K. Alves, and C.P. Bergmann, *J. Phys. Chem. C* **120**, 64 (2016).
- <sup>34</sup> P. Plonczak, M. Søggaard, A. Bieberle-Hütter, P.V. Hendriksen, and L.J. Gauckler, *J. Electrochem. Soc.* **159**, B471 (2012).
- <sup>35</sup> R. Schmitt, J. Spring, R. Korobko, and J.L.M. Rupp, *ACS Nano* **11**, 8881 (2017).
- <sup>36</sup> V. Foglietti, N. Yang, C. Aruta, P. Orgiani, F. Di Pietrantonio, D. Cannatà, M. Benetti, and G. Balestrino, *J. Phys. Chem. C* **121**, 23406 (2017).
- <sup>37</sup> A. Ito, H. Masumoto, and T. Goto, *Mater. Trans.* **48**, 227 (2007).
- <sup>38</sup> J.-P.P. Maria, S. Trolrier-McKinstry, D.G. Schlom, M.E. Hawley, and G.W. Brown, *J. Appl. Phys.* **83**, 4373 (1998).
- <sup>39</sup> A.J. Hartmann, M. Neilson, R.N. Lamb, K. Watanabe, and J.F. Scott, *Appl. Phys. A Mater. Sci. Process.* **70**, 239 (2000).
- <sup>40</sup> X.D. Wu, S.R. Foltyn, R.C. Dye, Y. Coulter, and R.E. Muenchausen, *Appl. Phys. Lett.* **62**, 2434 (1993).
- <sup>41</sup> T. Higuchi, Y. Chen, J. Koike, S. Iwashita, M. Ishida, and T. Shimoda, *Japanese J. Appl. Physics, Part 1 Regul. Pap. Short Notes Rev. Pap.* **41**, 6867 (2002).

- <sup>42</sup> N.D. Zakharov, K.M. Satlyalakshmi, G. Koren, and D. Hesse, *J. Mater. Res.* **14**, (1999).
- <sup>43</sup> L. Chen, C.L. Chen, D.X. Huang, Y. Lin, X. Chen, and A.J. Jacobson, *Solid State Ionics* **175**, 103 (2004).
- <sup>44</sup> L. Sun, D. Marrocchelli, and B. Yildiz, *Nat. Commun.* **6**, 1 (2015).
- <sup>45</sup> Y. Lei, Y. Ito, N.D. Browning, and T.J. Mazanec, *J. Am. Ceram. Soc.* **85**, 2359 (2002).
- <sup>46</sup> S. Kim, P. Jain, H.J. Avila-Paredes, A. Thron, K. Van Benthem, and S. Sen, *J. Mater. Chem.* **20**, 3855 (2010).
- <sup>47</sup> K. Mohan Kant, V. Esposito, and N. Pryds, *Appl. Phys. Lett.* **100**, (2012).
- <sup>48</sup> Y.L. Kuo, C. Lee, Y.S. Chen, and H. Liang, *Solid State Ionics* **180**, 1421 (2009).
- <sup>49</sup> H.J. Avila-Paredes, K. Choi, C.T. Chen, and S. Kim, *J. Mater. Chem.* **19**, 4837 (2009).

# 4 INTRINSIC LATTICE DISTORTION MECHANISM IN HIGHLY COHERENT THIN FILMS.

---

As shown in Chapter 3.3, the grain boundaries' blocking effect is a significant factor in determining the electromechanical performances. To better understand the intrinsic lattice distortion mechanism, a geometric analysis of CGO electromechanical properties is crucial. XAS analysis confirmed the theoretical model described in Chapter 1.8, which attribute the effect to a single-cell distortion and a strong interaction along  $\langle 111 \rangle$  crystallographic direction (the single-cell model) <sup>1-3</sup>. However in thin films, only the transverse out-of-plane effect, *i.e.*  $M_{13}$ , has been studied to date, with the electric field parallel to  $\langle 111 \rangle$  crystallographic direction of the crystal <sup>1,4-6</sup>. This is also the case for XAS studies <sup>2,3</sup>. Detailed information about anisotropy, distortion preferential direction and longitudinal-transverse effect relationship are still missing. Therefore, an extensive geometric analysis of electrostriction could shed new light on the atomistic mechanisms.

This chapter reports a characterization of the electrostriction effect of CGO films with various geometric configurations. To do this, grain boundaries free films are deposited with different orientations, with planar electrode configuration. With different crystallographic directions and different geometries of electrodes, it is possible to characterize both longitudinal ( $M_{11}$ ) and transverse effect ( $M_{12}$ ). Based on these results, a new geometric model of electrostriction is proposed and compared with the current single-cell model <sup>1-3</sup>. More importantly, it is demonstrated that through controlling of CGO film orientation, the electrostriction coefficient could be improved by one order of magnitude.



## 4.1 HIGHLY COHERENT THIN FILMS

CGO exhibits a good lattice match with  $\text{SrTiO}_3$  (STO) <sup>7,8</sup>, Y-stabilized  $\text{ZrO}_2$  (YSZ) <sup>8,9</sup> and  $\text{NdGaO}_3$  (NGO) <sup>8,10</sup>, which allows CGO films to grow epitaxial, with a low degree of structural defects <sup>7</sup>.

In this work, 1  $\mu\text{m}$  thick CGO films were deposited on STO, YSZ and NGO substrates. The deposition was carried out at 600 °C and  $10^{-3}$   $\text{P}_{\text{O}_2}$ , with a laser frequency of 10 Hz and 3  $\text{J}/\text{cm}^2$ . Such high temperature promotes crystallization of the material <sup>11</sup> by providing the deposited particles enough energy to arrange in the lowest energy configuration (Chapter 2.1). The substrates used are commercial (200) oriented STO, (100) oriented NGO and (110) oriented YSZ with dimension of 5×5  $\text{mm}^2$  and 0.1 mm in thickness. (100)-, (111)-, and (110)-oriented CGO films are deposited and characterized systematically.

Figure 4-1 shows a schematic illustration of the epitaxial relationship between a (200) oriented STO substrate and the CGO film <sup>7,8</sup>. CGO grows in (200) textured, with the cubic axes rotated by 45° with respect to the substrate lattice. The STO and CGO have a cell parameter of 3.91 Å and 5.42 Å, respectively. The basal diagonal of STO is 5.53 Å, and it matches CGO lattice constant. Consequently, the film arranges on the substrate as depicted in Figure 4-1b, with  $\langle 110 \rangle_{\text{CGO}}$  directions parallel to the

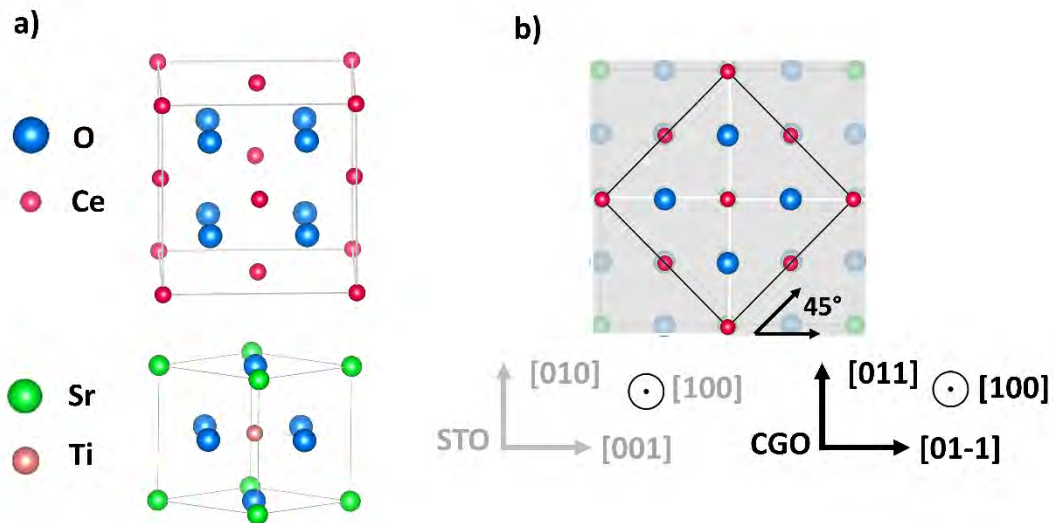


Figure 4-1: Schematic of epitaxial relation of CGO and STO. a) Cubic cells of CGO and STO. b) Top view of CGO arrangement on top of (200) oriented STO (gray square). The crystal axis are reported for both the film (black arrows) and substrate (gray arrows).

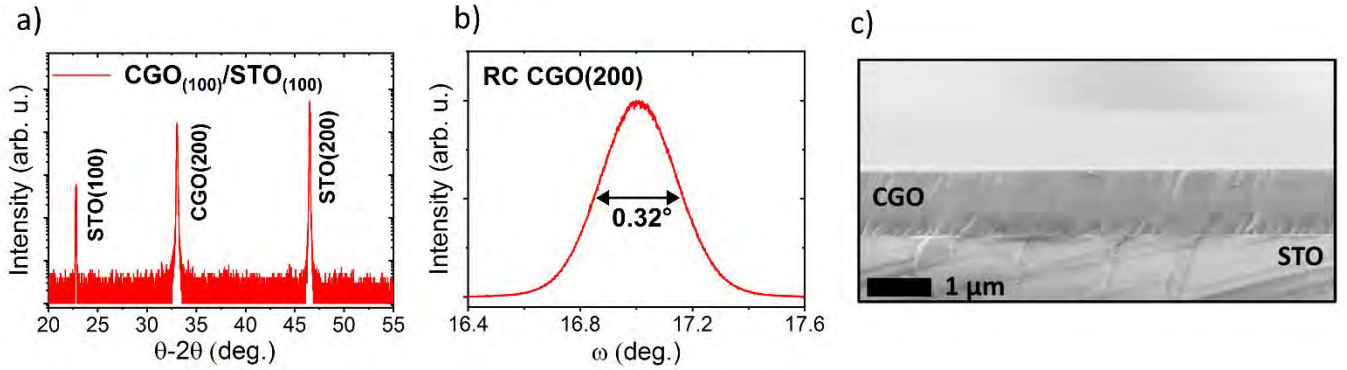


Figure 4-2: Structural characterization of (200) oriented CGO on (200) STO. a)  $\theta$ - $2\theta$  scan. b) rocking curve at the (200) peak of CGO. c) SEM Cross section image.

$\langle 100 \rangle_{\text{STO}}$ . Figure 4-1b also exhibits the crystallographic axis of both the substrate (gray arrows) and film (black arrows).

Figure 4-2 illustrates the structural characterization of CGO deposited on (200) oriented STO. As visible in  $\theta$ - $2\theta$  scan, the film grows with a single orientation (200). The rocking curve (RC) scan demonstrates

a narrow peak with a FWHM of 0.32°. Such low value indicates a highly coherent crystal, with a low amount of crystal defects. The SEM cross-section image shows dense and uniform microstructure.

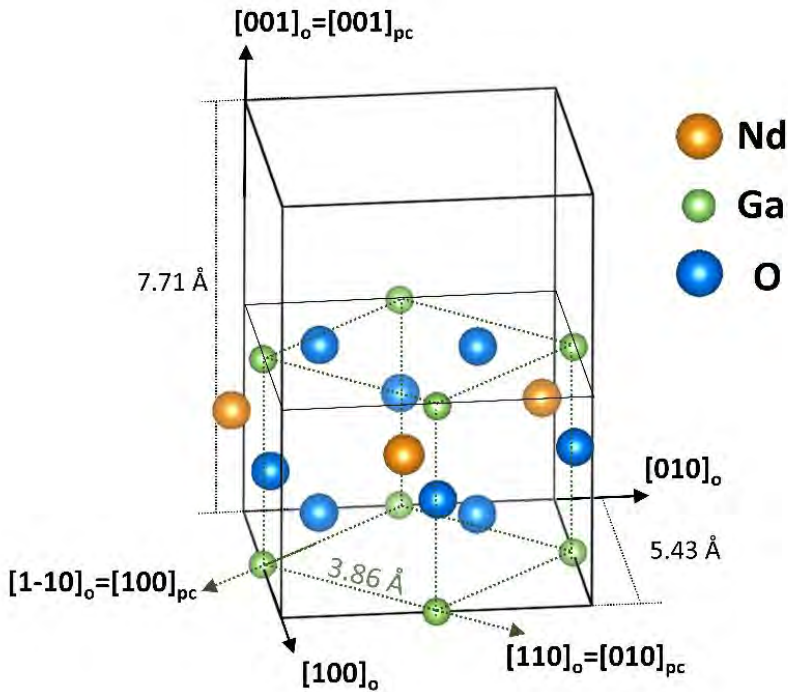


Figure 4-3: Representation of NdGaO<sub>3</sub> unit cell. The pseudocubic cell is highlighted (green lines). The relation between orthorhombic (o) and pseudocubic (ps) crystal axis are reported.

NGO is a perovskite with an orthorhombic cell, as depicted in Figure 4-3 and with parameters  $a = 5.428 \text{ \AA}$ ,  $b = 5.498 \text{ \AA}$ , and  $c = 7.708 \text{ \AA}$ <sup>12</sup>. The structure can be viewed as a pseudocubic cell, with lattice parameter  $a \approx 3.86 \text{ \AA}$ . The  $[100]_{ps}$ ,  $[010]_{ps}$  and  $[001]_{ps}$  crystallographic

axis of the pseudocubic cell correspond to the  $[1-10]_o$ ,  $[110]_o$  and  $[001]_o$  of the orthorhombic one, respectively. Considering an NGO substrate with  $(200)_o$  orientation, a good crystallographic match is given by  $(111)$  face of CGO ( $\Delta a/a = 0.2\%$ ).

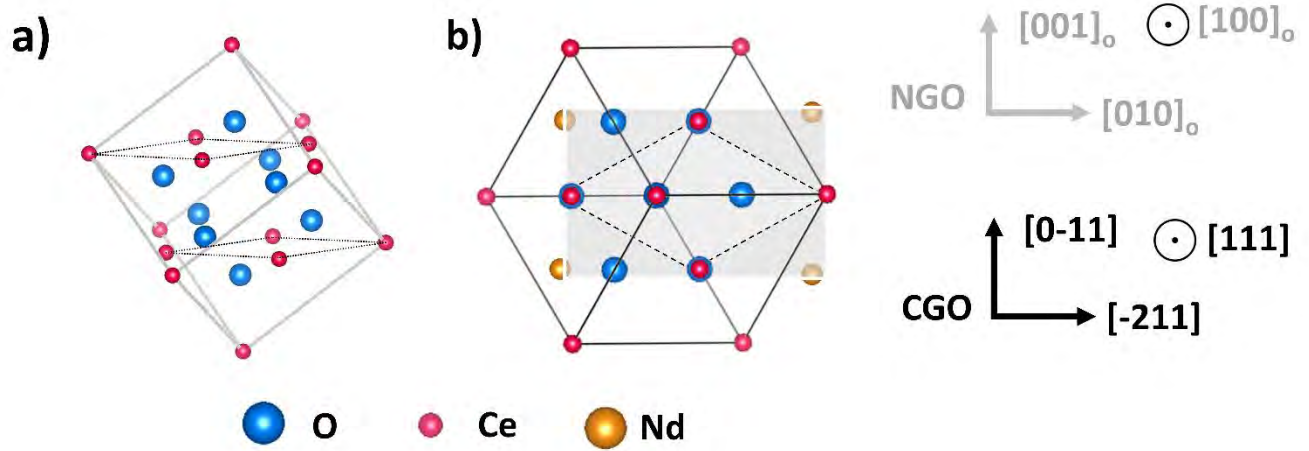


Figure 4-4: Schematic of epitaxial relation of CGO and  $(200)$  oriented NGO. a) CGO cell with in-plane layer highlighted (dotted lines). b) Top view of the CGO structure on top of  $(200)$  oriented NGO. The resulting crystal axes are reported.

Figure 4-4 shows the epitaxial relation between CGO cell and NGO  $(200)$  substrate. The film in-plane layers are highlighted in Figure 4-4a, while Figure 4-4b illustrates the top view of the CGO cell on the substrate. The film in-plane layer arranges along with NGO pseudocubic structure (gray rectangle) with horizontal axis  $[0-11]_{\text{CGO}}$  and  $[-211]_{\text{CGO}}$ , and out-of-plane orientation along  $[111]_{\text{CGO}}$  direction.

Figure 4-5 reports the structural characterization of CGO film grown on NGO  $(200)$ . The  $\theta$ - $2\theta$  scans are taken both in standard and low incident angle mode. NGO and CGO  $(200)$  peak in fact overlap at  $33^\circ$ .

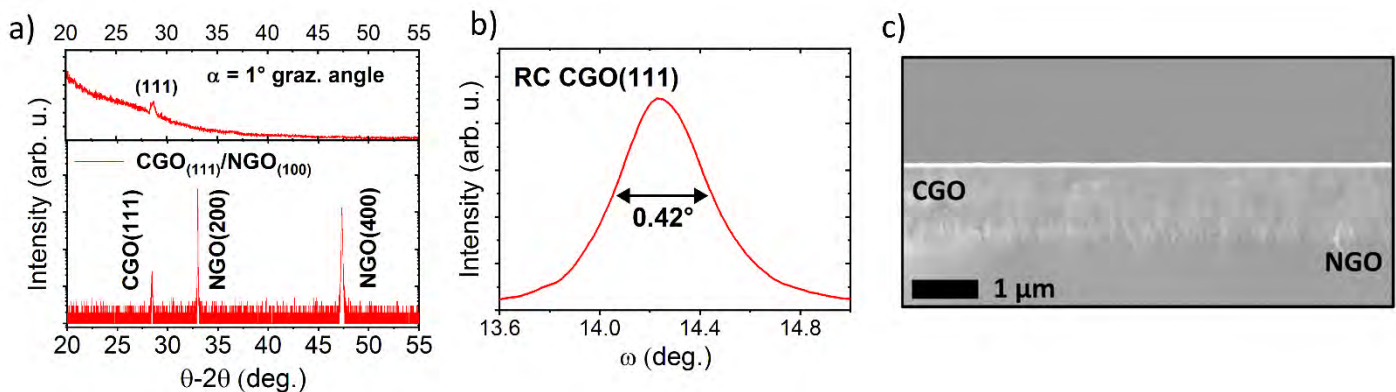


Figure 4-5: Structural properties of  $(111)$  oriented CGO on  $(200)$  NGO. a)  $\theta$ - $2\theta$  scan. (inset)  $\theta$ - $2\theta$  grazing angle scan performed to exclude substrate peaks. b) Rocking curve at the  $(111)$  peak of CGO. c) SEM picture in cross section mode.

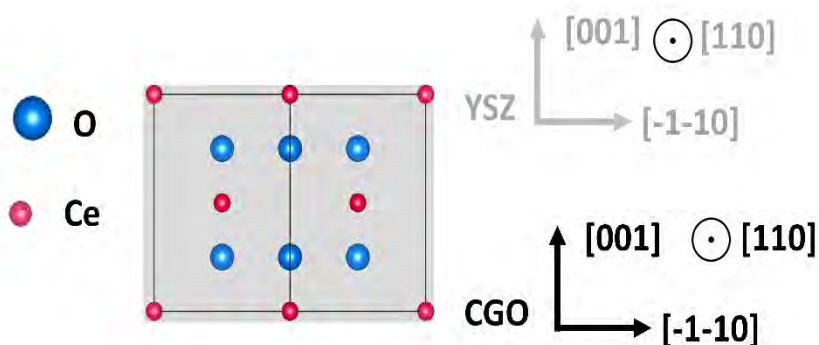


Figure 4-6: Top view of CGO cell on (220) oriented YSZ substrate (gray square).

The grazing angle scan (Figure 4-5a, inset) allows to exclude the contribution of the substrate and confirm the single orientation of CGO film. The analysis indicates a single (111) CGO orientation of CGO. Figure 4-5b shows the rocking curve scan on (111) peak of CGO with an FWHM value of  $0.42^\circ$ , indicating a high crystallinity of the film. Figure 4-5c exhibits the cross-section SEM image. The microstructure appears continuous and homogenous.

YSZ has a fluorite structure like CGO, but with a smaller lattice parameter<sup>8,9</sup>. Figure 4-6 is a depiction of the epitaxial relation between (110) oriented YSZ and CGO. The basal diagonals of both YSZ and CGO align, and the resulting film is (110) as well.. The structural characterization is depicted in Figure 4-7. A gold-sputtered electrode is included on the structure. As for the other samples, CGO shows a single (110) orientation and a FWHM of  $0.33^\circ$  (Figure 4-7b). The microstructure of the film is dense and without flaws.

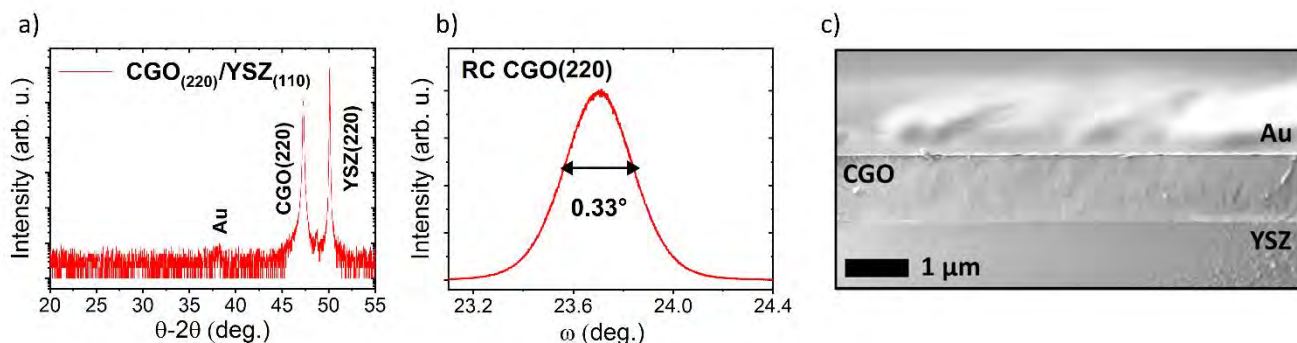


Figure 4-7: Structural characterization of CGO on (110) oriented YSZ. a)  $\theta$ - $2\theta$  scan. b) Rocking curve on (110) peak of CGO. c) SEM cross section image.

Overall, epitaxial CGO films grown with different orientations are obtained. By choosing suitable substrates CGO<sub>111</sub>/NGO<sub>200</sub>, CGO<sub>200</sub>/STO<sub>200</sub> and CGO<sub>110</sub>/YSZ<sub>220</sub> samples are obtained. Thanks to the Orientation controlled electrostriction. different geometries of the films, it is possible to study the electrostriction effect along the in-plane crystallographic axis of CGO. To do this, we applied planar electrodes with specific symmetries.

#### 4.1.1 Electrodes symmetry and $M_{12}$ calculation.

Depending on the in-plane crystallographic axis of CGO films, it is possible to apply the electric field through a specific crystallographic direction by placing the electrodes parallel to them. In order to evaluate the geometric contributions of electrostriction, several crystallographic directions are tested on the samples described in the previous section.

Figure 4-8 illustrates the electrode configuration of the samples, with respect to the crystallographic orientation of the film. CGO<sub>200</sub>/STO<sub>200</sub> (Figure 4-8a) has the electrodes placed along [011] direction (black arrow). CGO<sub>111</sub>/NGO<sub>200</sub> presents two electrodes configuration: along to [0-11] (black arrow) and [-211] (red arrow) directions (Figure 4-8b), which are perpendicular to each other. CGO<sub>110</sub>/YSZ<sub>220</sub> shows two possible configurations (Figure 4-8c) as well: along [011] (black arrow) and [-223] (red arrow). The second configuration has been made by placing the electrodes 45° rotated and then cutting the squared substrate to obtain a rectangular cantilever.



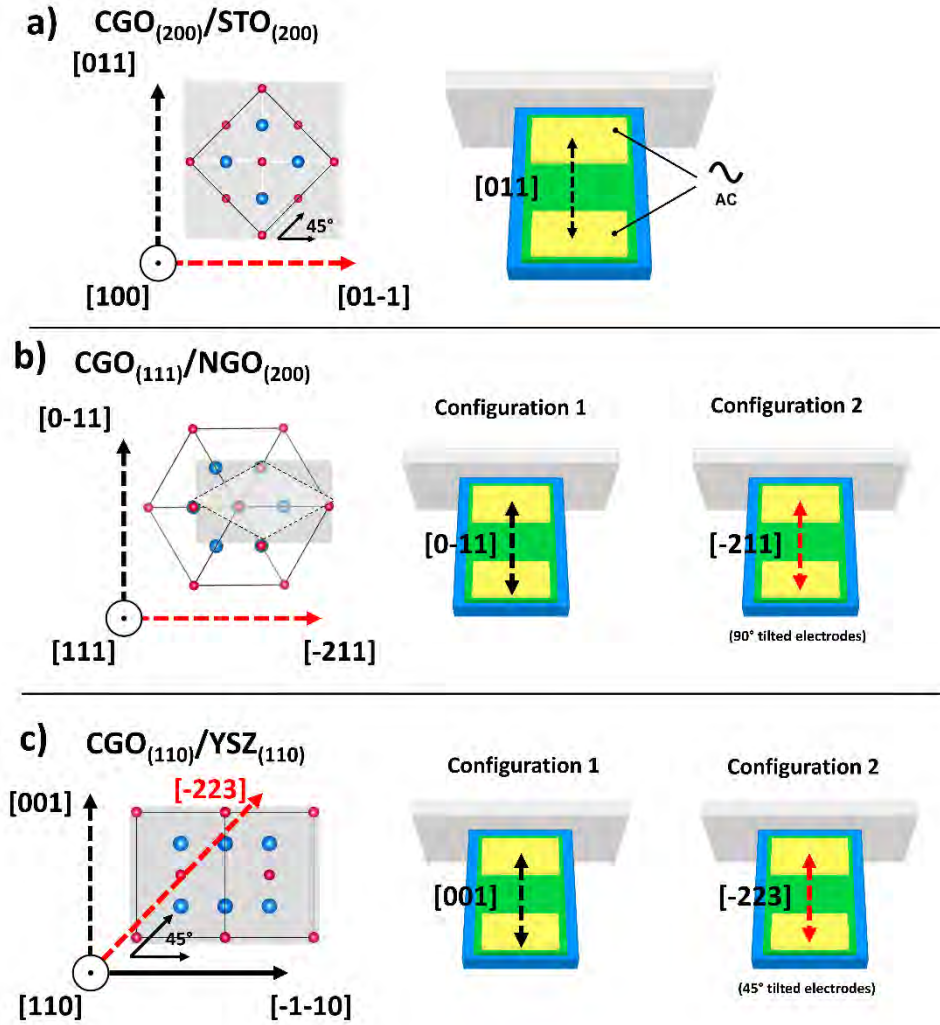


Figure 4-8: Electrode configuration depending on crystallographic geometry. a)  $\text{CGO}_{(200)}/\text{STO}_{(200)}$  sample symmetry. The electrodes are placed parallel to the  $[011]$  direction (black arrow). b)  $\text{CGO}_{(111)}/\text{NGO}_{(200)}$  symmetry with two electrodes configuration. Black arrow: parallel to  $[0-11]$ . Red arrow: parallel to  $[-211]$ . The two configuration are perpendicular. c)  $\text{CGO}_{(110)}/\text{YSZ}_{(110)}$  electrodes configuration. Black arrow: parallel to  $[001]$ . Red arrow: parallel to  $[-223]$  with 45° rotated electrodes.

Planar electrode configuration allows to measure the  $M_{11}$  component of electrostriction coefficient matrix. The electric field applied to the samples is considered to be constant along the vertical direction of the CGO film as the thickness of the sample is small compared to the in-plane area. This approximation is standard in planar impedance spectroscopy experiments<sup>7,13–15</sup>. The typical oscillation in this configuration is too low to be measured using only the interferometer, and the use of a lock-in amplifier is necessary (Chapter 2.4.3). Despite the extreme accuracy, the lock-in reports only the amplitude of the oscillation, not the direction. Consequently, it is not possible to distinguish if the strain

developed is tensile or compressive. It is then assumed that stress develops as a contraction parallel to the electric field and as an extension perpendicularly, as expected from the current model.

The planar electrode geometry introduces an issue during electromechanical experiments. When the voltage is applied, film and substrates act roughly like two in parallel resistors. This can possibly bring unwanted effects related to the interaction of substrate and electric fields such as Maxwell tensor or thermal expansion. In order to ensure the reliability of the measurements, it is crucial to evaluate the substrate contribution. Besides monitoring temperature, voltage and current, a cantilever test is performed on substrates alone, with the same electrodes configuration and method for full samples. The values of stress, displacement and electrostriction coefficient for CGO samples are reported after subtracting the substrate contribution. Figure 4-9 shows the results for STO, NGO and YSZ substrates. The first two did not exhibit obvious effects, while YSZ demonstrates oscillations that are in line with the electrostriction effect. YSZ is a material sharing many properties with CGO. They both are highly defective oxide with fluorite structure, and a similar lattice constant. Moreover, both possess high ionic conductivity. This measurement strengthens the hypothesis that defective oxides are electromechanically active. During the main experiment, the current flowing is always below the resolution of DAQ 6001 i.e.,  $\approx 3 \mu\text{A}$ , and no heating is observed.

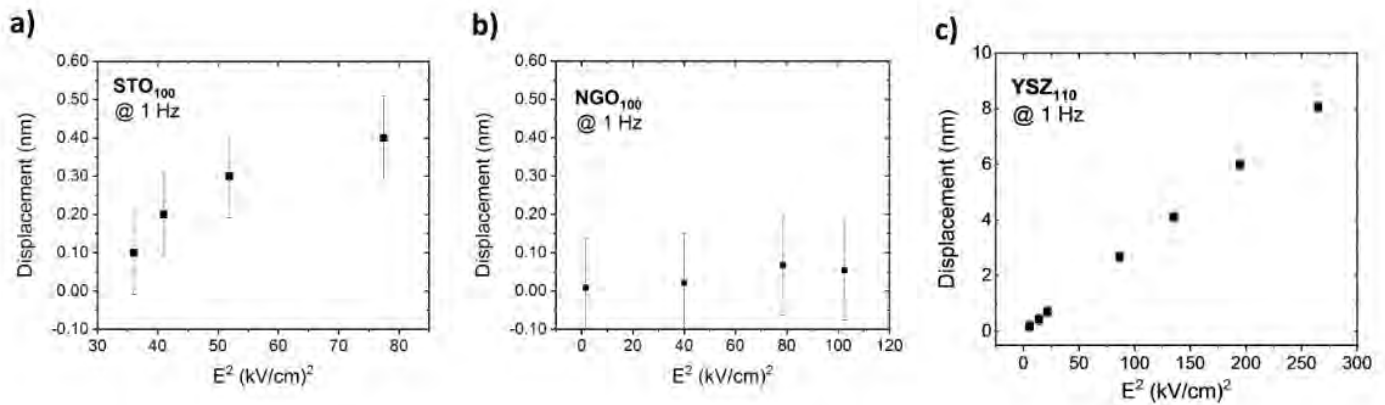


Figure 4-9: Substrates contribution to oscillation. a) Displacement of  $\text{STO}_{(100)}$  substrate for 1 Hz electric field. The calculated contribution to the  $\text{CGO}_{(100)}/\text{STO}_{(100)}$  oscillation is 10%. b)  $\text{NGO}_{(100)}$  substrate at 1 Hz electric field. No contribute was considered as NGO did not show any response to the electric field. c)  $\text{YSZ}_{(110)}$  substrates at 1 Hz electric field. The displacement of YSZ alone is about 50% of the total oscillation of the  $\text{CGO}_{(110)}/\text{YSZ}_{(110)}$  sample.

In addition to the longitudinal effect  $M_{11}$ , our setup makes the measurement of the in-plane shear coefficient ( $M_{12}$ ) also possible. According to the current interpretation of electrostriction, the distortion

should develop both in the perpendicular and parallel directions with respect to the electric field. However, no experimental results has been reported so far.

In order to measure the transverse  $M_{12}$  coefficient, the vertical displacement of the cantilever is measured along the width (Y-scan), with the same electric field amplitude. Figure 4-10 illustrates a schematic deformation map of cantilever displacement along X and Y directions. The transverse effect along the Y direction exhibits a parabolic profile. In order to calculate  $M_{12}$ , the Y-scan points are fitted with a second-order polynomial equation. The curvature is calculated with the following equation:

$$\Delta k = \frac{2a}{(1 + (2ay + b)^2)^{3/2}} \quad 4.1$$

with  $d = ay^2 + by + c$ .  $y$  is the width position and  $d$  is the vertical displacement. The lowest curvature radius in the parabola is considered. The induced stress value is then calculated with Stoney formula and the rest of the procedure described in Chapter 2.4.1, eventually  $M_{12}$  can be obtained. Such measurements confirm that the strain develops both parallel and perpendicular with respect to the electric field.

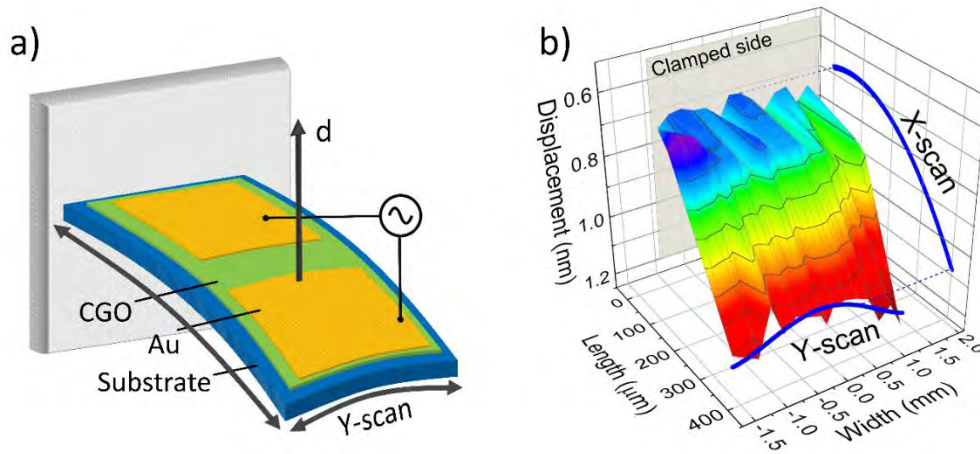


Figure 4-10: Cantilever beam longitudinal and transverse distortion. a) Schematic of the sample.  $M_{11}$  is calculated measuring  $d$  in a single point. The transverse effect i.e.,  $M_{12}$  is calculated by multiple measurements along the width of the sample (Y-scan). b) Deformation map of CGO cantilever, for 16 kV/cm applied field and 1 Hz frequency. The distortion takes place both along the length (X-scan) and the width (Y-scan).



### 4.1.2 Longitudinal electrostriction effect

Figure 4-11 shows the longitudinal electromechanical response of CGO thin films. The stress developed is proportional to the electric field ( $\vec{E}$ ) squared, applied at 1 Hz of frequency. Saturation is not detected for any of the samples. Figure 4-11a illustrates the performances of CGO<sub>(110)</sub>/YSZ<sub>(110)</sub> with the electric field along [001] direction. This sample displays the highest electrostriction coefficient of the set, with the value of  $M_{11} = 4.93 \cdot 10^{-17} \text{ m}^2 \text{V}^{-2}$ . Figure 4-11b,c report the response of CGO<sub>(100)</sub>/STO<sub>(100)</sub> and CGO<sub>(111)</sub>/NGO<sub>(100)</sub>. For both samples, the electric field is applied along [110] direction. In this case, the electrostriction coefficient is found to be reduced to  $M_{11} = 2.22 \cdot 10^{-17} \text{ m}^2 \text{V}^{-2}$  and  $M_{11} = 3.50 \cdot 10^{-18} \text{ m}^2 \text{V}^{-2}$ . CGO<sub>(111)</sub>/NGO<sub>(100)</sub> then, shows the lowest electrostriction when the field is applied along [-211] direction, with an  $M_{11} = 2.03 \cdot 10^{-18} \text{ m}^2 \text{V}^{-2}$ . Finally, measurements on CGO<sub>(110)</sub>/YSZ<sub>(110)</sub> with  $\vec{E}$  parallel to [-223] show no apparent oscillation (results not shown here). The signal, in this case, is comparable with background noise and the electrostriction coefficient is  $M_{11} = <6.72 \cdot 10^{-19} \text{ m}^2 \text{V}^{-2}$ .

According to the current interpretation of electrostriction<sup>1-3</sup>, the maximum electrostriction coefficient should be observed when an electric field is applied along the crosswise direction, i.e. <111>, which is parallel to the electromechanically active triplet  $O\text{-Ce}_{ce}\text{-}V_O^{\bullet\bullet}$ . However, our results demonstrated that, electric fields along [001] induce the highest electrostriction coefficient, followed by [110] and then by [111].

## Longitudinal $M_{11}$

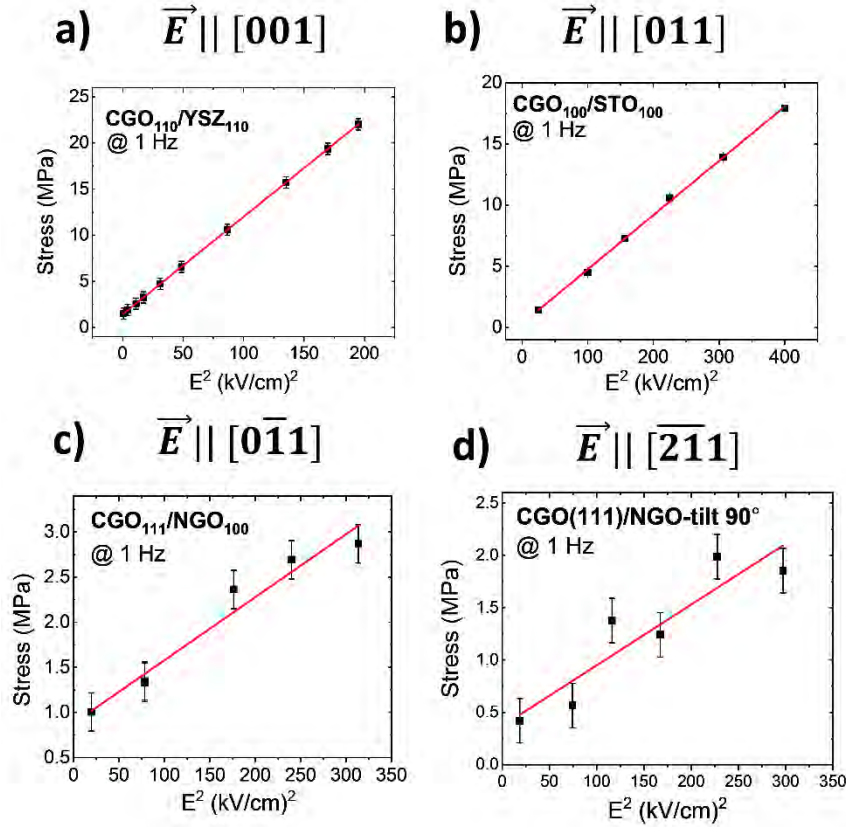


Figure 4-11: Longitudinal electromechanical response of CGO thin films for electric field depending on electric field direction. Stress calculated respect the II harmonic contribution of oscillation @ 1 Hz. a) CGO (110) oriented on YSZ with electric field along [001] axis. b) CGO<sub>(200)</sub>/STO<sub>(200)</sub> sample with  $\vec{E} \parallel [011]$ . c) CGO<sub>(111)</sub>/NGO<sub>(100)</sub> sample with  $\vec{E} \parallel [0\bar{1}1]$ . d) CGO<sub>(111)</sub>/NGO<sub>(100)</sub> sample with  $\vec{E} \parallel [\bar{2}11]$  diagonal direction.

### 4.1.3 Transverse electrostriction effect

Figure 4-12 reports the displacement Y-scans for  $M_{12}$  analysis. The measurements are taken with 13 kV/cm applied field at the frequency of 1 Hz. The shear electrostriction coefficient  $M_{12}$  describes the electromechanical activity along the direction perpendicular to the electric field. As the electrostriction transverse effect takes place along both in- and out- of plane directions, the crystal distortion is considered in terms of vertical (z) and lateral directions (y).

Figure 4-12a presents the Y-scan of  $\text{CGO}_{(110)}/\text{YSZ}_{(110)}$  vertical displacement with a polynomial fit. The electrostriction coefficient is  $M_{12} = 0.26 \cdot 10^{-17} \text{ m}^2\text{V}^{-2}$  for electric field perpendicular to  $[110]_z / [-1-10]_y$  directions. In  $\text{CGO}_{(100)}/\text{STO}_{(100)}$  the electrostriction coefficient is  $M_{12} = 0.79 \cdot 10^{-17} \text{ m}^2\text{V}^{-2}$  along  $[100]_z / [0-11]_y$  as depicted in Figure 4-12b. Interestingly,  $\text{CGO}_{(100)}/\text{STO}_{(100)}$  shows the highest transverse coefficient  $M_{12}$  of the set, but not the highest  $M_{11}$ . Figure 4-12c, reports  $\text{CGO}_{(111)}/\text{NGO}_{(100)}$  sample with  $M_{12} =$

### Transverse $M_{12}$

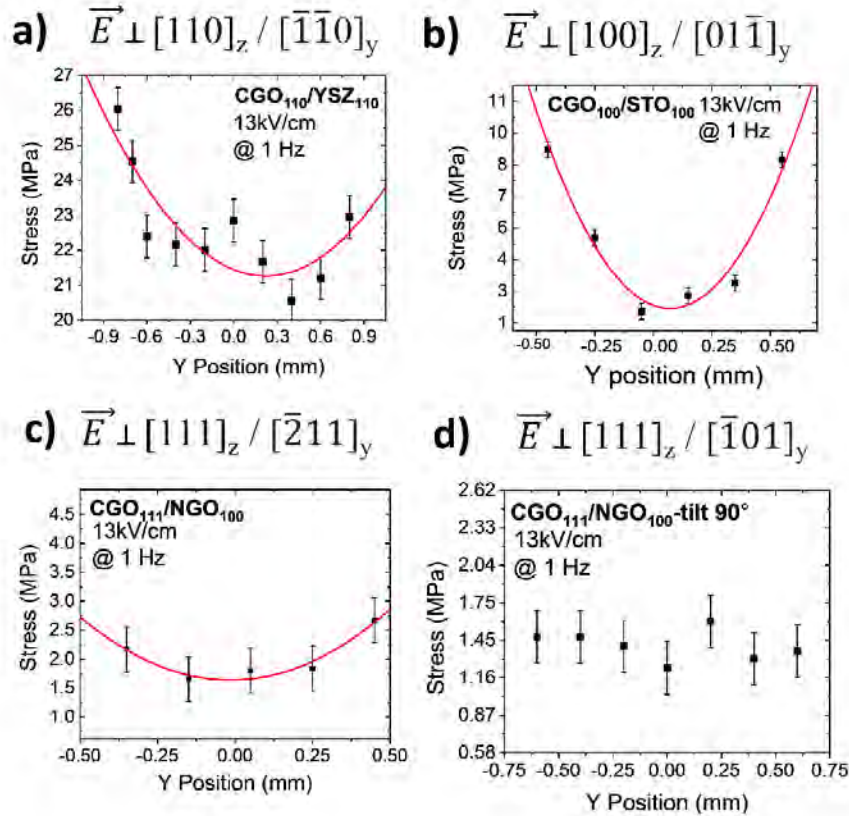


Figure 4-12: Displacement Y-scan of CGO thin films with 13 kV/cm applied at 1 Hz. Both in-plane ( $y$ ) and out-of-plane ( $z$ ) crystallographic direction perpendicular to  $\vec{E}$  are considered. a)  $\text{CGO}_{(110)}/\text{YSZ}_{(220)}$  sample with  $\vec{E}$  perpendicular to  $[110]_z / [\bar{1}\bar{1}0]_y$ . b)  $\text{CGO}_{(200)}/\text{STO}_{(200)}$  sample with  $\vec{E} \perp [100]_z / [01\bar{1}]_y$ . c)  $\text{CGO}_{(111)}/\text{NGO}_{(100)}$  sample with  $\vec{E} \perp [111]_z / [\bar{2}11]_y$ . d)  $\text{CGO}_{(111)}/\text{NGO}_{(100)}$  sample.  $\vec{E} \perp [111]_z / [\bar{1}01]_y$ , the parabolic fit here is not possible as displacement is linear through the width.

$1.9 \cdot 10^{-18}$  for  $[111]_z / [-211]_y$  directions. Finally, along  $[111]_z / [-101]_y$  perpendicular directions,  $\text{CGO}_{(111)}/\text{NGO}_{(100)}$  do not provide any clear profile. The displacement is roughly the same, and it is not possible to calculate the electrostriction coefficient.  $\text{CGO}_{(110)}/\text{YSZ}_{(110)}$  with  $45^\circ$  rotated electrodes also

do not show any activity. All the results are summarized in Table 4-1. It can be seen that these results differ again from the expectation of the single-cell model<sup>1-3</sup> and will be discussed in the next section.

Table 4-1: Longitudinal ( $M_{11}$ ) and transverse ( $M_{12}$ ) electrostriction coefficient of CGO thin films depending on electric field direction and perpendicular orientation.

	ORIENTATION $\parallel \vec{E}$	LONGITUDINAL $M_{11} (m^2/V^2)$	ORIENTATION $\perp \vec{E}$	SHEAR $M_{12} (m^2/V^2)$
CGO <sub>110</sub> /YSZ <sub>110</sub>	[001]	$4.93 \cdot 10^{-17}$	<sup>a)</sup> [110] <sub>z</sub> / [-1-10] <sub>y</sub>	$0.26 \cdot 10^{-17}$
CGO <sub>100</sub> /STO <sub>100</sub>	[011]	$2.22 \cdot 10^{-17}$	[100] <sub>z</sub> / [01-1] <sub>y</sub>	$0.79 \cdot 10^{-17}$
CGO <sub>111</sub> /NGO <sub>100</sub>	[0-11]	$3.50 \cdot 10^{-18}$	[111] <sub>z</sub> / [-211] <sub>y</sub>	$1.9 \cdot 10^{-18}$
CGO <sub>111</sub> /NGO <sub>100</sub> *	[-211]	$2.03 \cdot 10^{-18}$	[111] <sub>z</sub> / [-101] <sub>y</sub>	//
CGO <sub>110</sub> /YSZ <sub>110</sub> **	[-223]	$<6.72 \cdot 10^{-19}$	[110] <sub>z</sub> / [-33-4] <sub>y</sub>	//

\*90° tilted. \*\*45° tilted

## 4.2 MICROSCOPIC MODEL AND DISCUSSION

The experimental results deviate from the explanation provided in the literature about the CGO electrostriction mechanism<sup>1-3</sup> and suggest that the current model cannot explain the effect thoroughly. Therefore, a new interpretation is proposed to describe of electrostriction in terms of atomic distortion, based on our experimental results. This new model is an “extension” of the previous one, so it is not in contrast with previous findings. Moreover, it is supported by our experimental data.

As shown in Figure 4-13a, the single-cell based model<sup>1-3</sup> considers one single CeO<sub>2</sub> as the base of local structure rearrangement. However, neglecting the rest of  $V_O^{\bullet\bullet}$  neighborhood limits the effectiveness of the model. As a matter of fact, oxygen atoms in CGO lattice have a coordination number of 4. Consequently, a single vacancy is part of four cells. The interpretation of the electrostriction effect proposed includes the whole surrounding of an oxygen vacancy, as depicted in Figure 4-13b. The six numbered particles represent the oxygen ions (6O) closest to the  $V_O^{\bullet\bullet}$  site, which represents the center of elastic field and charge distribution anomaly. Besides, each of these oxygen atoms is bonded with two Ce cations. For these reasons, when a field is applied, the 6O group is expected to withstand higher

induced distortion. Figure 4-13 shows the structure composed by the 6O as a regular octahedron centered in  $V_O^{**}$  site. In the model presented here I describe the distortion of the  $6O-V_O^{**}$  structure, considering the oxygen ions far from the vacancy as secondary effect.

We already know that considering one unit cell, the preferential displacement of the oxygen is along  $[111]$  direction because the Ce-O bond chain is diagonal. This is true also in the octahedron model. However, in this case, two forces are applied simultaneously to each oxygen ion.

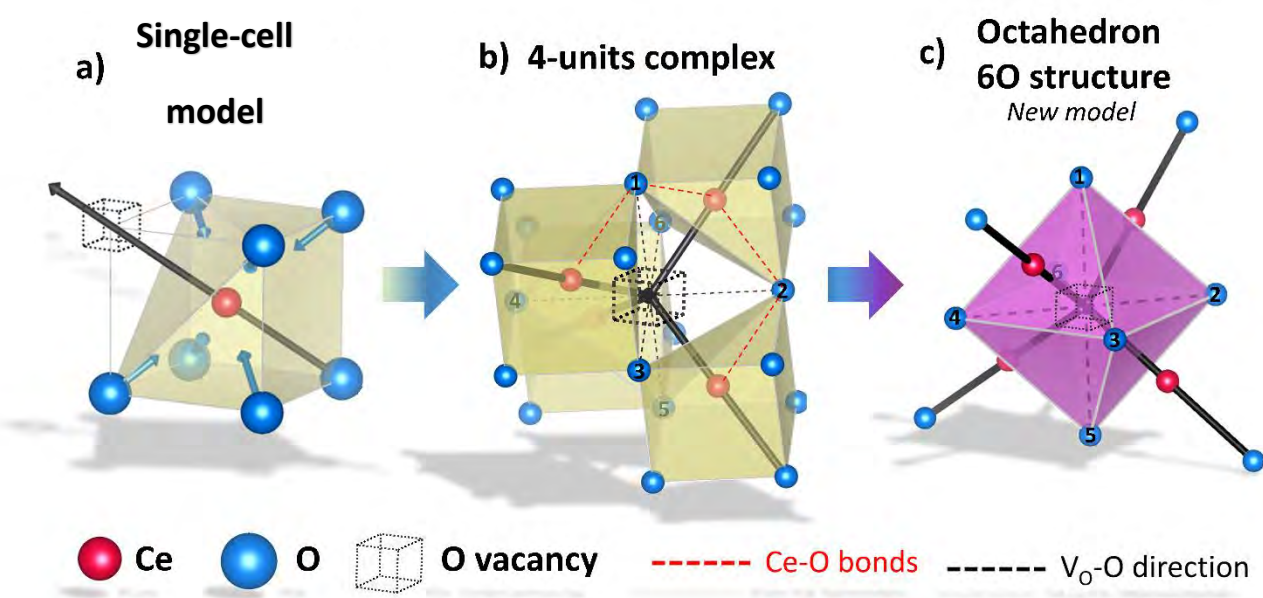


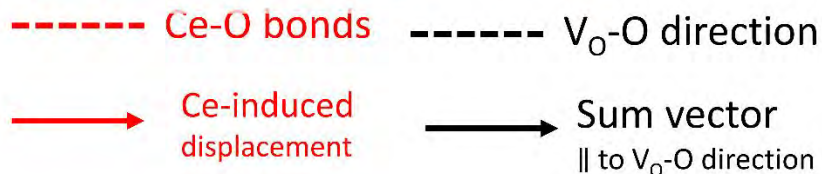
Figure 4-13:  $CeO_2$  structure and oxygen vacancy related neighborhood. a)  $Ce_{ce}-7O-V_O^{**}$  unit, base of the current model for electrostriction in CGO. Black vector:  $V_O^{**}-Ce_{ce}-O_O$  electro-active triplet with direction of the distortion. Blue vectors: diagonal 6O displacement b) 4-units complex centered on oxygen vacancy linked to four  $Ce_{ce}-7O-V_O^{**}$  distorted units. Near-empty site oxygen atoms, i.e. 6O, are numbered. Red lines: bonds Ce atoms with oxygen 1 and 2. c) 6O octahedron structure composed of six near-empty site oxygen atoms. New model base structure.

Single unit distortion

$$\overrightarrow{A2} = [1\bar{1}\bar{1}]$$

$$\overrightarrow{B2} = [111]$$

Final preferential direction

$$\overrightarrow{V_02} = [100]$$




A similar model describes the electrostriction distortion in  $\text{ABO}_3$  perovskites, where oxygen atoms form an octahedron structure centered on the B-ion<sup>16–18</sup>. Moreover, perovskites share the same directional

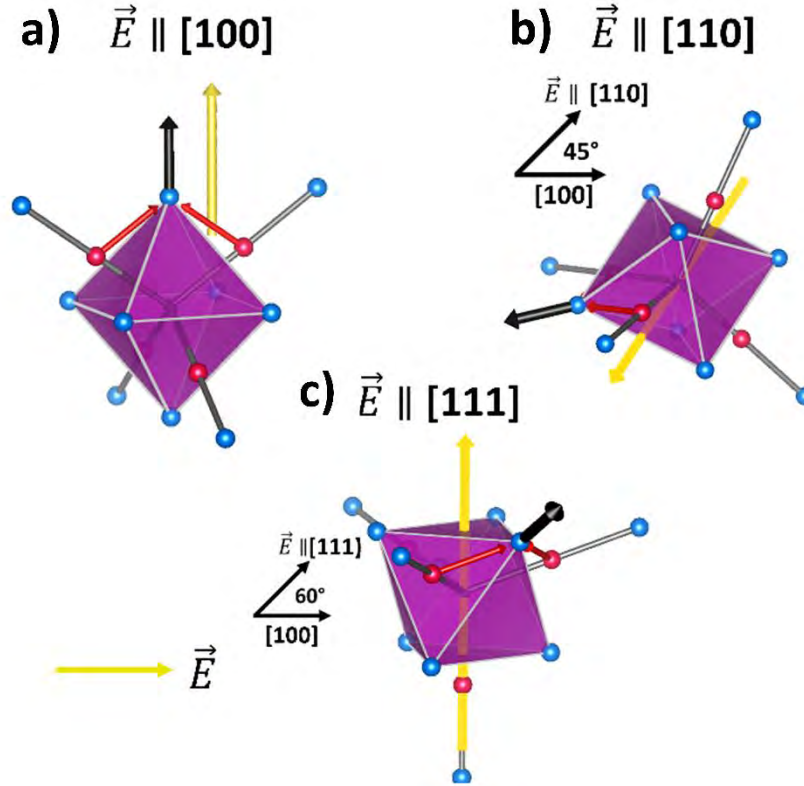


Figure 4-15: Octahedron structure with angle between electric field (yellow arrow) and preferred direction (Black arrow). a) Electric field along  $[100]$  direction. b) Electric field along  $[110]$  with an angle of  $45^\circ$ . c)  $E$  to  $[111]$ , with a  $60^\circ$  angle from preferential direction..

mechanism, with high distortion along  $\langle 100 \rangle$ <sup>17,18</sup>. In comparison, displacement parallel to  $\langle 110 \rangle$  directions results in an overall counteracting of the surrounding, decreasing the electromechanical effect. The distortion is even weaker along  $\langle 111 \rangle$  directions<sup>17,18</sup>. Considering the stress developed by each cell to be different, asymmetric effects can take place in the form of a transverse contribution of oxygen atoms distortion.

This kind of behavior has been already shown in  $\text{BaTiO}_3$  as well as PMN-xPT ( $x = 0.32, 0.27, 0.28$ )<sup>17,18</sup>, but also in other ionic compounds with an oxygen octahedron structure such as  $\text{LiNbO}_3$ ,  $\text{LiTaO}_3$ ,  $\text{KNbO}_3$ ,  $\text{Ba}_2\text{NaNb}_5\text{O}_{15}$ <sup>19,20</sup>. This suggests that this kind of anisotropy is related to the oxygen octahedron system<sup>21</sup>. CGO electrostrictive behavior shares similarities with these materials because of the oxygen octahedron structure mentioned.

Interestingly, the experimental results are in qualitative accordance with the microscopic model presented here: the longitudinal electrostriction effect follows the trend expected with maximum electrostriction coefficient with field along [001] direction, followed by [011] and [0-11] having intermediate performances. Even if not part of the  $\langle 111 \rangle$  family, the diagonal [-211] and [-223] directions show the lowest activity.

In all the samples,  $M_{12}$  shows values considerably lower but, considering the couples of both the in-plane and out-of-plane perpendicular directions, they agree with the model. CGO<sub>100</sub>/STO<sub>100</sub> shows lower  $M_{11}$  compared to CGO<sub>110</sub>/YSZ<sub>110</sub> sample, but higher  $M_{12}$ . This is because the longitudinal effect in CGO<sub>100</sub>/STO<sub>100</sub> takes place along [011], while in CGO<sub>110</sub>/YSZ<sub>110</sub> is along [100]. On the other hand, the transverse effect in CGO<sub>100</sub>/STO<sub>100</sub> is the highest because it takes place along the couple  $[100]_z / [01-1]_y$  that includes one preferred direction. Lower coefficients follow along  $[110]_z / [-1-10]_y$  and then  $[111]_z / [-211]_y$ . Remarkably, the electrostriction coefficient in CGO<sub>(100)</sub>/STO<sub>(100)</sub> and CGO<sub>(111)</sub>/NGO<sub>(100)</sub> samples is quite different despite having the field applied along with directions of the same family. The reason can be ascribed to the different transverse effect, that is higher for CGO<sub>(100)</sub>/STO<sub>(100)</sub>.

In order to fully understand the lattice distortion dynamics in CGO, further investigations are needed. EXAFS has been demonstrated to be a powerful tool and also DFT could help to simulate atomic displacement in the complex described. However, the model presented here is a big step forward, as it provides a more in-depth knowledge of the mechanism of electrostriction in CGO and gives a way to enhance electrostriction activity through control of crystallographic orientation.



## 4.3 REFERENCES

---

- <sup>1</sup> R. Korobko, A. Patlolla, A. Kossoy, E. Wachtel, H.L. Tuller, A.I. Frenkel, and I. Lubomirsky, *Adv. Mater.* **24**, 5857 (2012).
- <sup>2</sup> R. Korobko, A. Lerner, Y. Li, E. Wachtel, A.I. Frenkel, and I. Lubomirsky, *Appl. Phys. Lett.* **106**, 042904 (2015).
- <sup>3</sup> Y. Li, O. Kraynis, J. Kas, T.C. Weng, D. Sokaras, R. Zacharowicz, I. Lubomirsky, and A.I. Frenkel, *AIP Adv.* **6**, (2016).
- <sup>4</sup> M. Hadad, H. Ashraf, G. Mohanty, C. Sandu, and P. Muralt, *Acta Mater.* **118**, 1 (2016).
- <sup>5</sup> R. Korobko, E. Wachtel, and I. Lubomirsky, *Sensors Actuators, A Phys.* **201**, 73 (2013).
- <sup>6</sup> A.D. Ushakov, N. Yavo, E. Mishuk, I. Lubomirsky, V.Y. Shur, and A.L. Kholkin, *KnE Mater. Sci.* **1**, 177 (2016).
- <sup>7</sup> S. Sanna, V. Esposito, D. Pergolesi, A. Orsini, A. Tebano, S. Licocchia, G. Balestrino, and E. Traversa, *Adv. Funct. Mater.* **19**, 1713 (2009).
- <sup>8</sup> S. Sanna, V. Esposito, A. Tebano, S. Licocchia, E. Traversa, and G. Balestrino, *Small* **6**, 1863 (2010).
- <sup>9</sup> R. Sinclair, S.C. Lee, Y. Shi, and W.C. Chueh, *Ultramicroscopy* **175**, 25 (2017).
- <sup>10</sup> L. Chen, C.L. Chen, D.X. Huang, Y. Lin, X. Chen, and A.J. Jacobson, *Solid State Ionics* **175**, 103 (2004).
- <sup>11</sup> A. Infortuna, A.S. Harvey, and L.J. Gauckler, *Adv. Funct. Mater.* **18**, 127 (2008).
- <sup>12</sup> A. Biswas, C.H. Yang, R. Ramesh, and Y.H. Jeong, *Prog. Surf. Sci.* **92**, 117 (2017).
- <sup>13</sup> K. Rodrigo, S. Heiroth, M. Lundberg, N. Bonanos, K. Mohan Kant, N. Pryds, L. Theil Kuhn, V. Esposito, S. Linderroth, J. Schou, and T. Lippert, *Appl. Phys. A Mater. Sci. Process.* **101**, 601 (2010).
- <sup>14</sup> A. Bieberle-Hütter, J.L. Hertz, and H.L. Tuller, *Acta Mater.* **56**, 177 (2008).
- <sup>15</sup> I. Kosacki, T. Suzuki, V. Petrovsky, and H.U. Anderson, *Solid State Ionics* **136–137**, 1225 (2000).
- <sup>16</sup> K. Uchino, S. Nomura, L.E. Cross, R.E. Newnham, and S.J. Jang, *J. Mater. Sci.* **16**, 569 (1981).
- <sup>17</sup> F. Li, L. Jin, Z. Xu, and S. Zhang, *Appl. Phys. Rev.* **1**, (2014).

- <sup>18</sup> F. Li, L. Jin, Z. Xu, D. Wang, and S. Zhang, Appl. Phys. Lett. **102**, (2013).
- <sup>19</sup> R.E.N. V. Sundar, J.-F. Li, D. Viehland, Mater. Res. Bull. **31**, 555 (1996).
- <sup>20</sup> L. Liang, Y.L. Li, S.Y. Hu, L.Q. Chen, and G.H. Lu, J. Appl. Phys. **108**, (2010).
- <sup>21</sup> T. Yamada, J. Appl. Phys. **43**, 328 (1972).

# 5 X-RAY ABSORPTION SPECTROSCOPY IN BULK AND ULTRATHIN FILMS

---

In this chapter, the results from synchrotron x-ray absorption spectroscopy near edge spectroscopy (XANES) are reported. The structure of this chapter contains the following: (1) *in situ* Differential XANES method description, (2) DiffXANES analysis of Gd-doped ceria single crystal is presented for temperatures ranging from RT to -194 °C. These results are part of the ongoing and unpublished work: “Low temperature *in-situ* EXAFS on electrostrictor doped ceria” Simone Santucci, Ahsanul Kabir, Haiwu Zhang, Jin Kyu Han, Simone Sanna, Nini Pryds, Vincenzo Esposito. (3) The results from DiffXANES in ceria pellets with different Ca doping concentration, which are summarized as part of the work currently under preparation: “Steady Electrostriction Properties in Calcium Doped Cerium Oxide” Ahsanul Kabir, Simone Santucci, Karl Tor Sune Thyden, Maxim Varenik, Igor Lubomirsky, Eugenio Paris, Vincenzo Esposito. (4) Standard XANES to characterize the valence state of Ce cation in ultrathin CGO films, comparing the results to electrostriction performances. These findings constitute the unpublished results on: “Interfacial electromechanical effect tuned by strain in Gd-doped ceria thin films”, Simone Santucci, Haiwu Zhang, Sandeep Chavuladi, Simone Sanna, Pasquale Orgiani, Nini Pryds, Vincenzo Esposito, to be submitted and included in Appendix A.C.

## 5.1 IN-SITU XANES AND BEAMLINES

---

In this section, the results of *in-situ* experiments performed at CLÆSS beamline <sup>1</sup> in ALBA synchrotron (Barcelona) and SuperXAS beamline <sup>2</sup> at PSI (Villigen) are presented <sup>3,4</sup>. The measurements are taken with the sample at rest (“off” state) and during a static ( $E_{DC}$ ) electric field applied (“on” state). The DiffXANES is then obtained by subtracting the “on” and “off” states. The differential spectrum gives

information about the local evolution of the chemical environment of Ce caused by the external electric field. Previous works reported DiffXAS as a tool to evaluate the distortion mechanism of lattice, allowing to formulate the first microscopic model<sup>5-7</sup>.

CLÆSS is a beamline dedicated to x-ray absorption spectroscopy (XAS) techniques<sup>3</sup>. The experiment is performed at the Ce L-III edge ( $\approx 5,7$  keV) in fluorescence mode, using Si (111) double crystal monochromator resulting in a flux of  $10^{12}$  photons/sec and beam size of  $200 \times 200 \mu\text{m}^2$ . The acquisition is made through a multi-channel SDD, which allows up to six spectra for each measurement. The results presented here are a merge of  $\approx 15$ -20 acquisitions, each performed with all six canals available. The spectra are then normalized with Athena software<sup>8,9</sup>. The sample setup is a liquid nitrogen cryostat (LN<sub>2</sub>-cryo) at low vacuum pressure ( $\approx 10^{-3}$  mbar) to maintain the x-ray beam intensity. The cryostat can

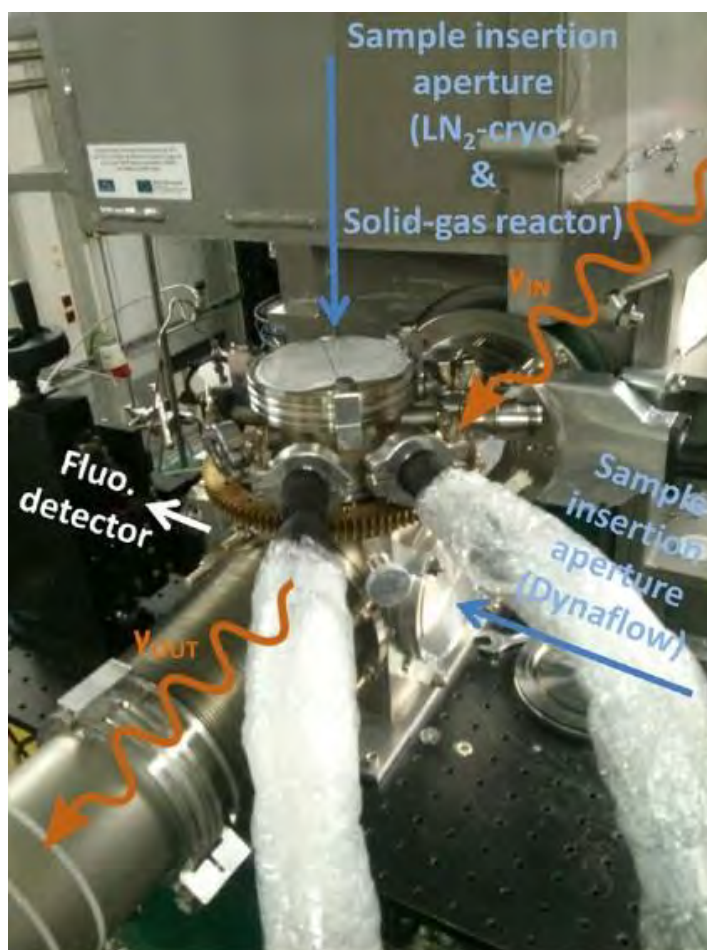


Figure 5-1: Picture of sample setup of the experimental hutch, including the cryostat box. Figure adapted from "CLÆSS: The hard X-ray absorption beamline of the ALBA CELLS synchrotron" L. Simonelli et al, © 2016 The Author(s).

reach  $-194\text{ }^{\circ}\text{C}$  through liquid nitrogen cooling passing through the holder of the sample. In low-temperature measurements, a stabilization time of 30 minutes has been considered as well as the estimation of temperature reported by the beamline<sup>10</sup>. The sample contacts are made at the electrodes with small Cu plates. The static field is applied with a function generator and voltage amplifier (described in Chapter 2.4). The cables are introduced in the cryostat through a vacuum valve, with BHV contact on the outside and solder contact inside. Figure 5-1 shows a picture of the experimental setup with the cryostat fixed in the beamline. A static electric field was applied to the samples during “on” state measurements.

SuperXAS beamline, is suitable for high energy XAS. The beam energy range is  $4.5 - 35\text{ keV}$ , with a flux on the sample of  $10^{12}\text{ ph/sec}$ . The spot size is from  $100 \times 100\text{ }\mu\text{m}^2$  to  $5 \times 0.5\text{ mm}^2$ . The beamline allows in-situ measurements and QuickEXAFS for high frequency scans<sup>4,11</sup>. The measurement and data analysis method mentioned before also apply to these data.

## 5.2 CGO SINGLE CRYSTAL IN-SITU XANES AT LOW TEMPERATURE

---

Temperature dependent electrostriction properties have been rarely reported and the few results on thin films demonstrate a decrease of performances with increasing of the temperatures in the range of  $60\text{-}150\text{ }^{\circ}\text{C}$ <sup>5,12,13</sup>.

In this section, we report DiffXANES results for 20% Gd-doped ceria single crystal (CGO-SC) from room temperature to  $-194\text{ }^{\circ}\text{C}$ . CGO-SC is utilized to avoid low-temperature substrate-induced stress and grain boundaries influence, which presented in thin films and polycrystals. The single-crystal sample was provided by the group of Martin Lerch at the Berlin University of Technology and was grown using a skull melting technique, as reported in their works together with structural characterization<sup>14–18</sup>. The

sample is a square with 4 mm size and 0.7 mm thickness. Gold electrodes are placed on the two main faces and then contacted to the Cu plates.

Before the XANES experiment, we evaluate the electrostrictive behavior of the sample. Figure 5-2 reports the strain [part per million] developed as function of the applied field for several frequencies.

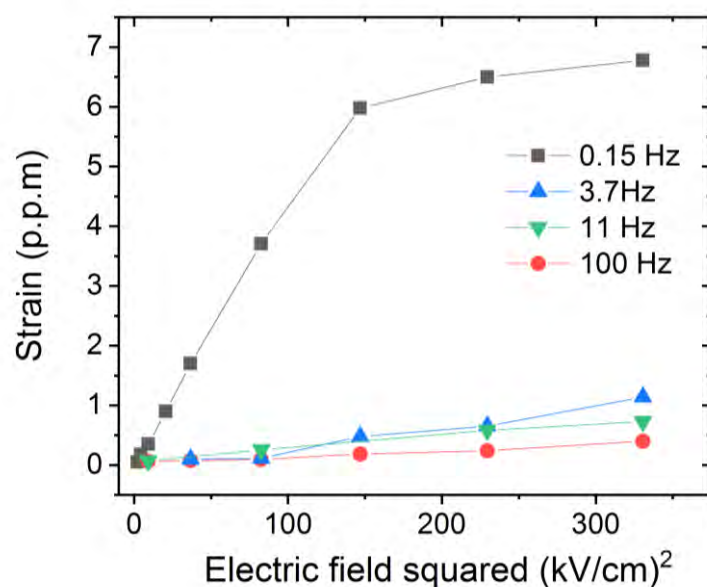


Figure 5-2: Electromechanical properties of 20% Gd-doped ceria single crystal at room temperature for different frequencies.

CGO-SC sample displays an electrostriction coefficient  $M_{33} = 3.88 \cdot 10^{-18} \text{ (m}^2\text{V}^{-2}\text{)}$  at 0.15 Hz applied field. However,  $M_{33}$  drops quickly by increasing the electric field frequency (e.g. 3.7, 11 and 100 Hz), as reported in Table 5-3.

Table 5-1: Electrostriction coefficient of SC CGO depending on the frequency of the electric field.

frequency (Hz)	0.15	3.7	11	100
$M_{33} \cdot 10^{-18} \text{ (m}^2\text{V}^{-2}\text{)}$	3.88	0.27	0.39	0.21

Figure 5-3 displays the XANES and DiffXANES spectra from RT to -194 °C. During the “on” state, static 11 kV/cm are applied to the sample. The measurements started at room temperature, and then are repeated every -75 °C.

Figure 5-3e reports a comparison of the DiffXANES spectra. Depending the temperature, two trends are visible in different position. In the area corresponding to the main twin peaks at  $\approx 5730$ - $5740$  eV, the DiffXANES spectrum displays an upward trend with reducing the temperature. The increase of the edge peaks indicates an increment of the corresponding transition  $2p_{3/2} \rightarrow 5d$ <sup>19</sup>, and denotes higher ionic behavior<sup>5-7</sup>. In particular, the “on-off” difference increases at the edge from -1% at RT to +8% at -194 °C. Previous works reports high DiffXANES values as a result of high lattice distortion caused by electric field<sup>5-7</sup>.

Interestingly, an opposite trend is visible at the pre-peak at  $\approx 5723$  eV. The “on-off” difference decreases from nearly 0% at RT to -2% at -194°C. This pre-peak feature corresponds to  $2p_{3/2} \rightarrow 4f$  transition, as an effect of  $4f$  and  $5d$  orbital hybridization<sup>20,21</sup>. Therefore, at low temperature  $4f$ - $5d$  hybridization appears to be blocked by the external electric field, while seems to be negligible at room temperature.

Low temperatures demonstrate to affect the bond properties of Ce in presence of electric field. Cryogenic condition promotes crystal distortion and ionic behavior, while hindering the hybridization of  $4f$ - $5d$  orbitals. In particular, this effect is visible only at extremely low temperatures.

At this state, further analysis are necessary. Unfortunately, a direct observation of electrostriction in this condition has not yet carried out and therefore will not be part of this work. However, EXAFS measurements were performed. The data will be soon analyzed and included in the future publication.

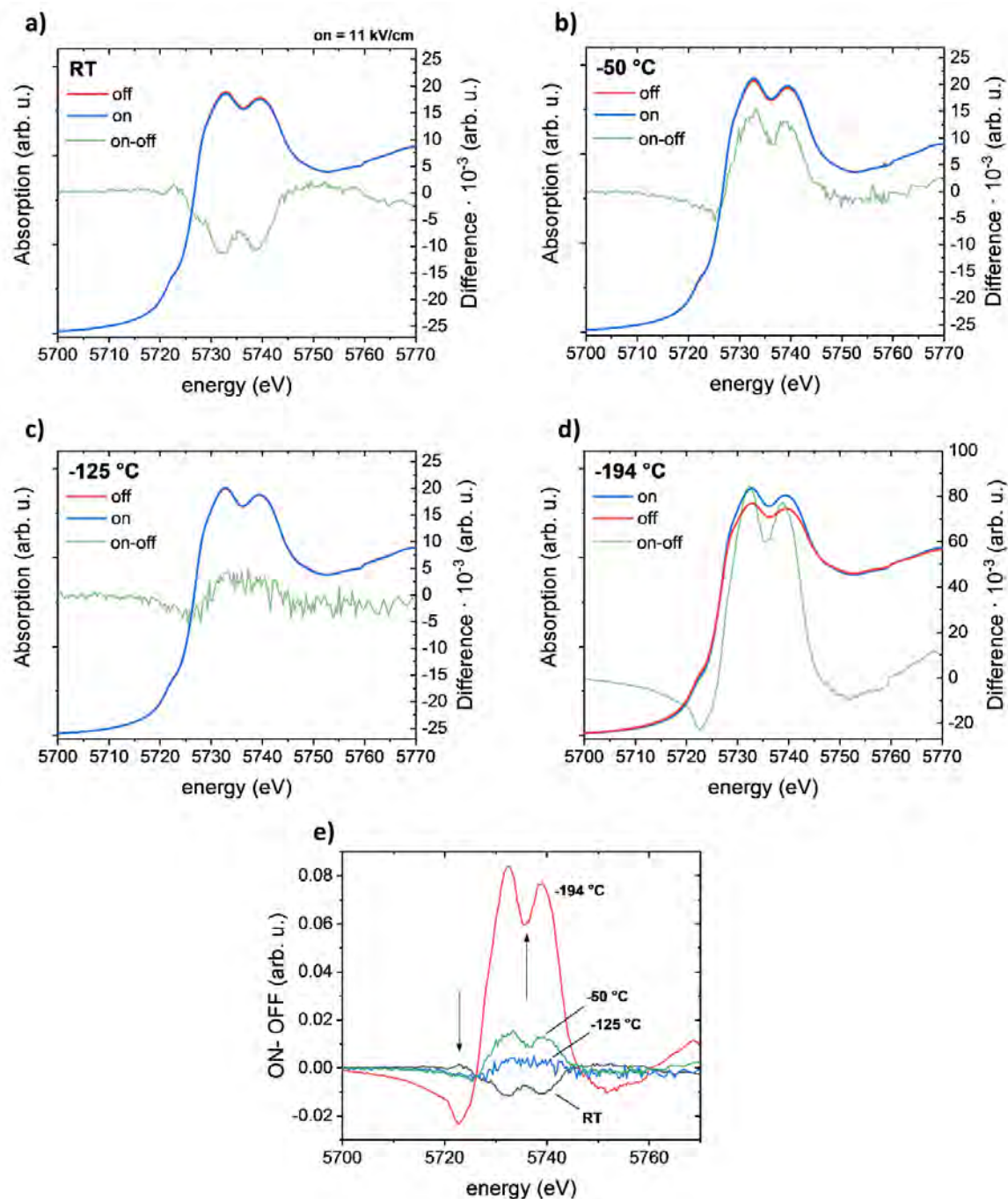


Figure 5-3: XANES spectra at Ce L-III edge for different temperatures. "on" and "off" states are reported as well as differential XANES ("on-off"). a) room temperature. b) -50 °C. c) -125 °C. d) -194 °C. e) Diff XANES for CGO-SC at different temperatures.



### 5.2.1 Electrostriction frequency stability in Ca-doped ceria

This work describes frequency dependent electrostriction properties of calcium doped ceria (CDC or CCO) pellets. Gd-doped ceria shows a quick relaxation of electrostrictive performances at high frequencies<sup>22–25</sup>. However, a higher frequency working regime is mostly unknown in defective oxides electrostrictors, while it is fundamental in many practical fields such as ultrasound imaging and inkjet printing<sup>26–29</sup>.  $\text{Ca}^{2+}$  ion is divalent and, in comparison with  $\text{Gd}^{3+}$ , it has a higher effective charge and higher cation size. Therefore, a stronger columbic interaction of  $\text{Ca}^{2+}-\text{V}_\text{O}^{\bullet\bullet}$  pairs as well as elastic strain are expected<sup>30,31</sup>. The hypothesis here is then that stronger dynamics should improve the electromechanical response of the material for high frequencies.

DiffXANES measurements are taken to characterize the local structure of 5 (CDC-5) and 15 mol% (CDC-15) Ca doped ceria at the SuperXAS beamline. The detection technique is carried out as described earlier, with 4 kV/cm applied during the “on” state. High frequencies measurements are also taken, using QuickEXAFS technique<sup>4</sup>, which allows to perform a scan in few seconds. However, these measurements did not provide sufficient result. Therefore, only static field DiffXANES are reported. Ca edge is not analyzed as the beamline could not supply such low energies  $\approx 4$  keV.

The CDC-5 and CDC-15 samples are obtained by powder by cold pressing with a uniaxial pressure of 200 MPa for 30 seconds and sintering in air at 1450 °C for 10 hours. Squared pellets with 3-4 mm of side and 0.7-0.8 mm thickness are obtained.

The structural characterization of the samples is presented in Figure 5-4. Both samples possess a pure fluorite structure (Figure 5-4a). Figure 5-4b exhibits the SEM cross-section images of the pellets. The grain size ranges from 1-5  $\mu\text{m}$ . The electrical properties of the bulk (data not shown here), are similar in all the samples but are slightly different in the case of grain boundaries.

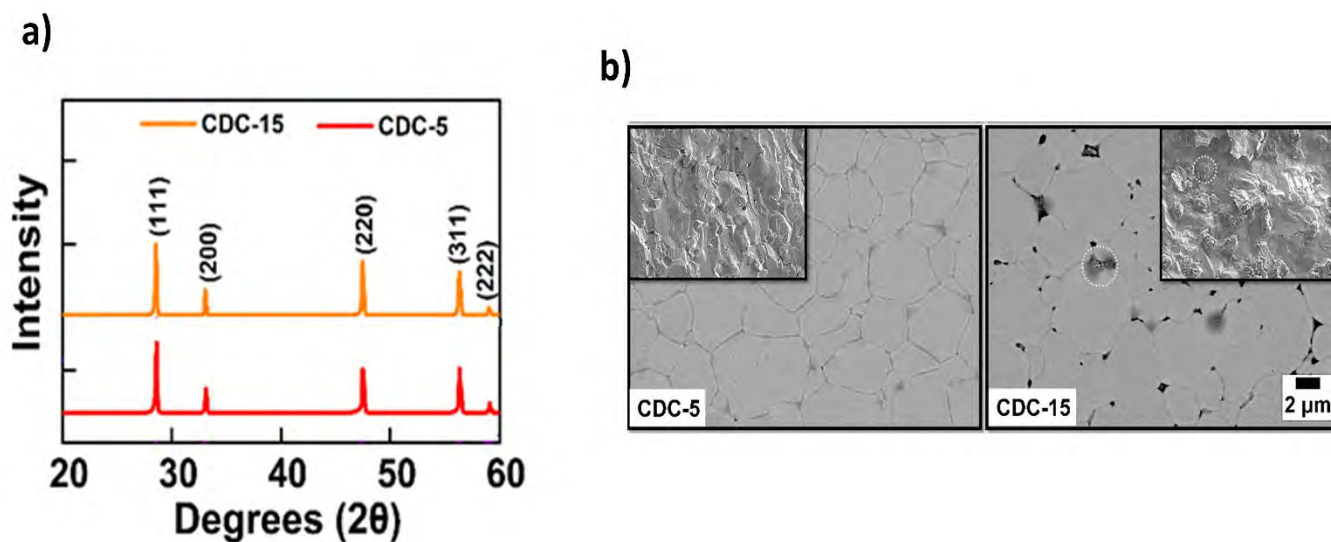


Figure 5-4: a)  $\theta$ - $2\theta$  scans of calcium-doped ceria (CDC) powders and pellets. b) Scanning electron microscopy (SEM) images of the polished cross-section of the CDC pellets. The inset reports the cold-fractured cross-sectional region. The scale bar is 2  $\mu\text{m}$

The XANES measurements are reported in Figure 5-5 for CDC-5 and CDC-15. The results show a slight increase of the edge when the field is applied, indicating an evolution of the local environment and in stronger Ce-O ionic bond<sup>19</sup>. CDC-15 displays a higher differential spectrum (Figure 5-5b) up to  $\approx 1\%$  at the peaks position. As mentioned before, this effect is related to crystal distortion.

As anticipated from the XANES data, both samples display electrostrictive behavior. CDC-5 and CDC-15 show similar electrostriction coefficient at 0.15 Hz, with an effective  $M_{33} \approx 1.7\text{-}3.5 \cdot 10^{-18} \text{ (m}^2\text{V}^{-2}\text{)}$ . Interestingly, both samples display stable performances up to 10 Hz. To further analyze frequency stability, electromechanical measurements are carried out up to 800 Hz in several samples. This is the highest frequency available for reliable measurements both at DTU and Weizmann institute (WIS).

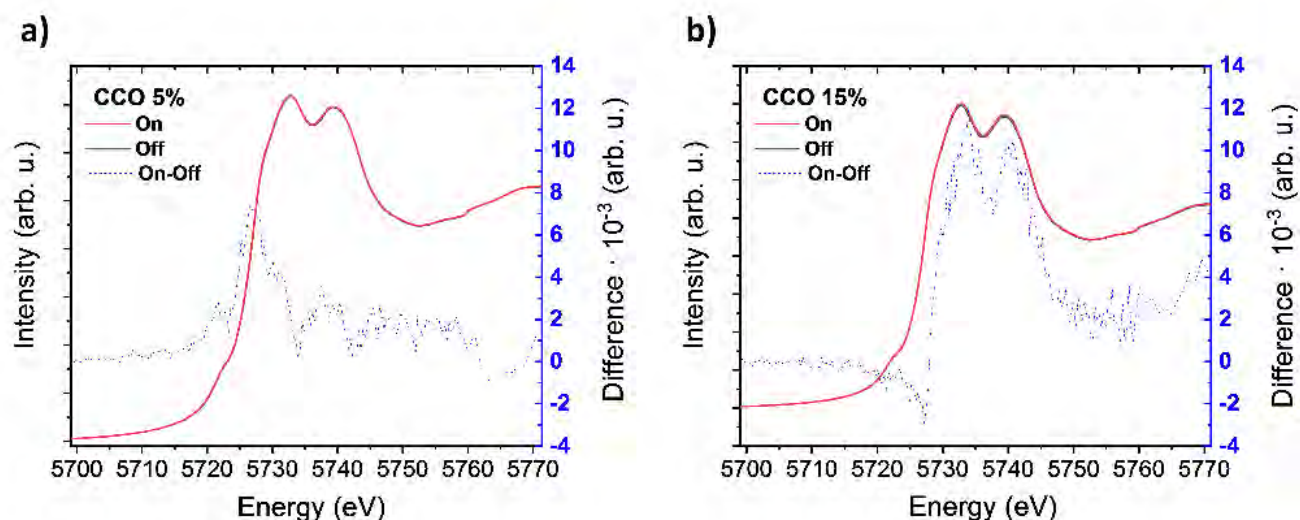


Figure 5-5: XANES spectra at the Ce-L<sub>III</sub> edge edge of CDC-5 (CCO 5%) and CDC-15 (CCO 15%) samples. 4 kV/cm electric field is applied during the field on measurements for about 5h.

The results are summarized in Table 5-2 for various frequencies. Remarkably,  $M_{33}$  does not demonstrate relaxation and vibrate steadily up to 800 Hz. All Ca doped pellets have the same behavior, with slightly different electrostriction coefficients within  $1.2\text{--}3.5 \cdot 10^{-18} \text{ m}^2\text{V}^{-2}$ .

Table 5-2: Electrostriction longitudinal coefficient ( $M_{33}$ ) of CDC pellets at certain frequencies.

$M_{33} \text{ (m}^2\text{V}^{-2}\text{) at}$	0.15 Hz	1 Hz	10 Hz	100 Hz	800 Hz
<b>CDC-5</b>	$3.5 \cdot 10^{-18}$	$3 \cdot 10^{-18}$	$2.5 \cdot 10^{-18}$	$2.9 \cdot 10^{-18}$	$2.4 \cdot 10^{-18}$
<b>CDC-10</b>	$1.7 \cdot 10^{-18}$	$1.5 \cdot 10^{-18}$	$1.3 \cdot 10^{-18}$	$1.4 \cdot 10^{-18}$	$1.2 \cdot 10^{-18}$

These findings suggest that electromechanical response in the ceria-based compound is independent of the amount of doping, and is effectively influenced by a columbic interaction of  $\text{Ca}^{2+}\text{--V}_\text{O}^\bullet$  pairs. The steady behavior of the samples in fact, is not associated with the blocking effect or Ca segregation or secondary phases, as not detected.

DiffXANES confirmed the crystallographic distortion. However, also Ca edge should be analyzed to support its active role in electrostriction.

## 5.3 XANES ANALYSIS FOR INTERFACIAL DISLOCATIONS IN HIGHLY ELECTROSTRICTIVE FILMS.

---

Low dimensional CGO layers have been studied as electrolyte in relation to micro-SOFC application<sup>32–34</sup>. Gd-doped ceria possesses high ionic conductivity at intermediate temperatures<sup>32</sup>, and it can be further increased by strain in STO-buffered films<sup>35</sup> or heterostructures<sup>36,37</sup>. When the substrate induces tensile kind of strain, such in CGO grown on YSZ<sup>36</sup>, the mobility of oxygen vacancies increases. Also, the migration energy barrier is reduced<sup>35,38</sup> and the exchange rate is increased in expanded lattice<sup>39</sup>, resulting in higher ionic conduction. On the other hand, compressive strain raises the activation energy of the carriers, and the diffusion of oxygen vacancies is reduced<sup>40,41</sup>.

The accumulation of stress caused by lattice mismatch can be compensated by the formation of lattice defects and resulting in partial strain relaxation<sup>35,42,43</sup>. Such dislocations accumulate at the interface with the substrate<sup>42</sup>. Crystal defects also affect diffusion and electric properties of ceria films<sup>40</sup>. In particular they are found to reduce the mobility and increase the activation barrier of the carriers, and consequently reduce the vacancies migration<sup>35,40,44,45</sup>. Dislocation also create a local elastic field deviation<sup>46</sup>. Previous studies report a further reduced carrier mobility and higher activation energy in films with low thickness<sup>47</sup>

Overall, by manipulating the configuration of defects of lattice at the interface, one can modify the dynamics of the oxygen vacancies. As  $V_O^{\bullet\bullet}$  represent the primary reason of the electromechanical effect in CGO, electrostriction is expected to depend by strains. In particular, a static configuration of the vacancies is expected to increase the electromechanical effect because in this condition they can induce cells distortion as described in Chapter 4.2. Moving vacancies instead, do not contribute to the distortion.

20 mol% Gd-doped ceria thin films are deposited on  $\text{NGO}_{(110)}$ <sup>35,38,39,48,49</sup>,  $\text{STO}_{(200)}$ <sup>48,50</sup> and  $\text{LAO}_{(100)}$ <sup>36,46,50</sup> substrates. A set of thick samples is also grown with relaxed structure as a comparison. Electrostriction effect is measured and compared. The XAS characterization includes analysis at the Ce M4 and M5 edges, performed at APE beamline of Elettra synchrotron. The measurements give information about

the chemical environment and oxidation state of Ce, in particular the presence of 3+ phase, which induce defects in the lattice and promotes oxygen vacancies formation.

### 5.3.1 APE beamline

This beamline <sup>51</sup> is a versatile facility for both surface and absorption techniques. Part of the experimental apparatus has already been described in Chapter 2.1.2. APE can operate in two modes: low (8-120 eV) and high (150-1600) energy. The low energy setup offers surface-focused techniques such as Angle-resolved photoemission spectroscopy (ARPES), electronic band structure and Fermi surface mapping characterization. High energy techniques include XAS, x-ray magnetic circular and linear dichroism (XMCD, XMLD) and x-ray photoelectron spectroscopy (XPS). The main chamber is kept in high vacuum condition ( $10^{-9}$  mbar). We perform measurements at Ce M4-5 edges ( $\approx 884$  and 900 eV respectively) in fluorescence mode, with  $10^{11}$  photons/sec flux and  $200 \times 70 \mu\text{m}^2$  spot size. XANES spectra showed a merge of several measurements and have been normalized with Athena software.

### 5.3.2 Structural characterization

The samples were deposited by PLD. The size of the substrate were  $5 \times 2.5$  mm and 0.1 mm thick. A laser frequency of 10 Hz and energy 120 mJ were used. The deposition time for the sets of thin and thick films was 12 and 120 minutes, respectively. The fluence was about  $1.8 \text{ J cm}^{-2}$ , and the calculated deposition rate was  $\sim 0.02 \text{ \AA/pulse}$ . The background oxygen pressure is set at  $10^{-3}$  mbar, with a temperature of 600 °C. Au top electrodes with planar configuration are sputtered at room temperature.

Figure 5-6 exhibits the structural characterization of the 17 nm thick samples.  $\theta$ - $2\theta$  scans are depicted in Figure 5-6a. CGO shows a single (200) orientation on all the substrates. The thickness of the samples is calculated through x-ray reflectivity depicted in Figure 5-6b, indicating 17 nm. Figure 5-6c,d,e present the rocking curve scans of (200) peak of the films. High crystallinity is confirmed with FWHM of  $0.17^\circ$ ,  $0.38^\circ$  and  $0.32^\circ$  for CGO/NGO, CGO/LAO and CGO/STO respectively.

The structural characterization of the thick set of samples is reported in Figure 5-7. The  $\theta$ - $2\theta$  scans of the thick samples demonstrate a pure (200) orientation except for CGO/LAO, which also shows a (220)

peak. This is quite unusual and can be due to condition of deposition not optimal. The thickness of samples is calculated from the deposition rate value, obtaining 170 nm.

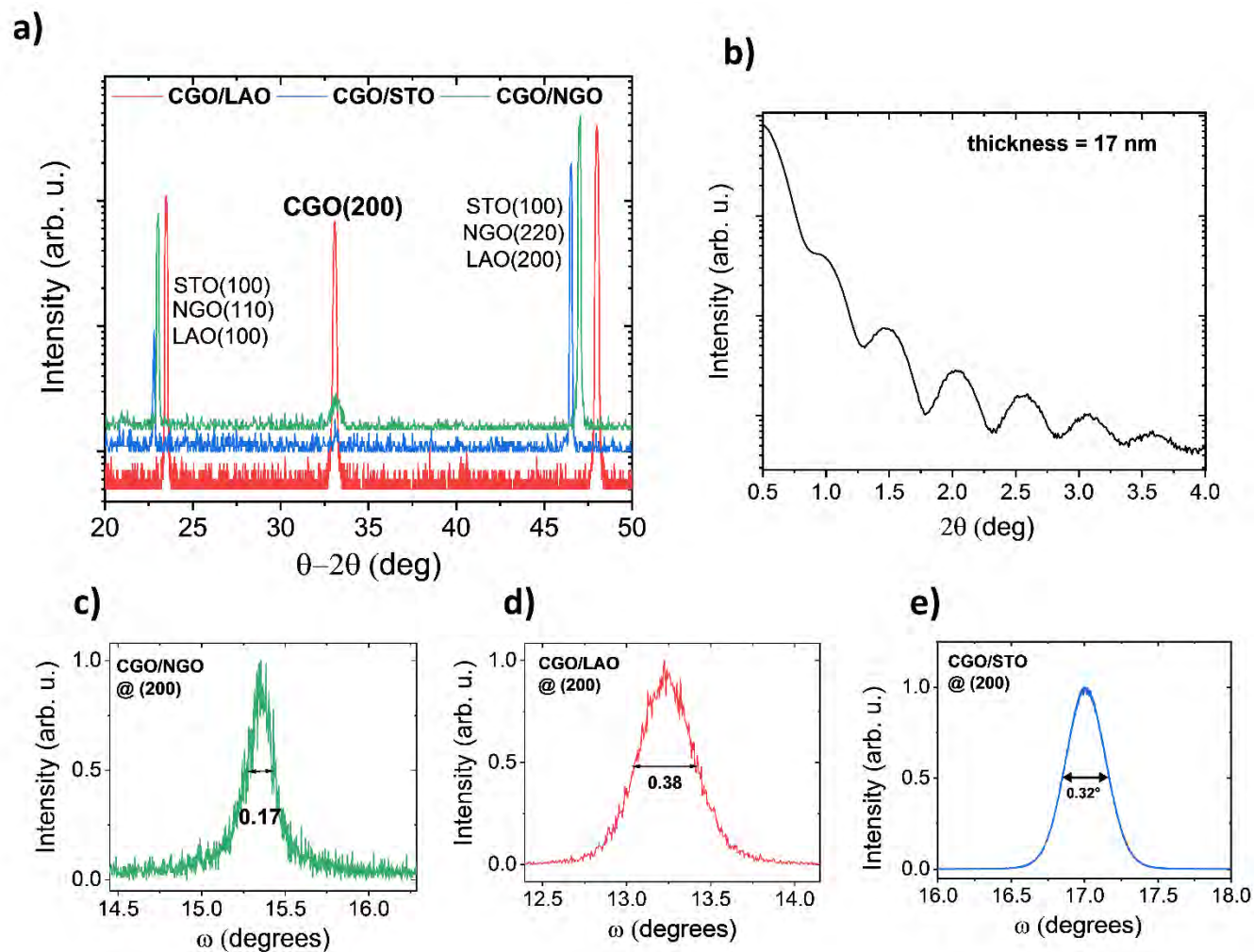


Figure 5-6: Structural characterization of 17 nm thin films by XRD. a)  $\theta$ - $2\theta$  scans of CGO on NGO, STO and LAO substrates. b) X-ray reflectivity of the samples indicating 17 nm of CGO film thickness. c) Rocking curve of CGO/LAO with FWHM of 0.38°. d) Rocking curve of CGO/NGO with FWHM of 0.17°. e) Rocking curve of CGO/STO smoothed. FWHM = 0.32°.

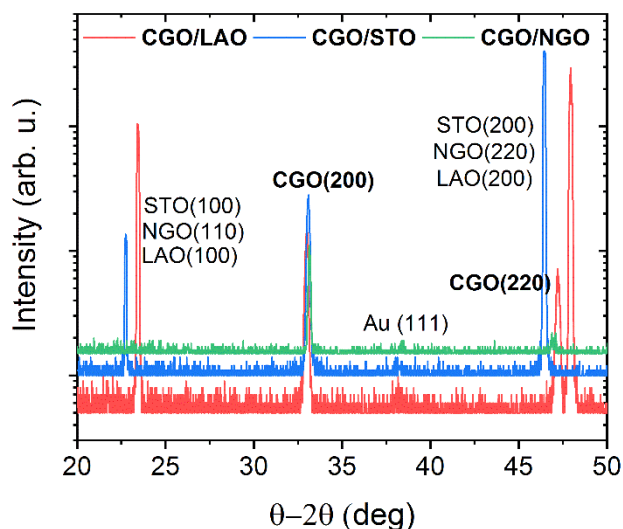


Figure 5-7:  $\theta$ - $2\theta$  scans of 170 nm thick CGO on NGO, STO and LAO substrates with gold top electrodes.

### 5.3.3 Electromechanical performances.

In order to evaluate the electrostriction properties of the samples, the cantilever vibration method described in chapter 2.2 was used on planar electrodes structure (chapter 3.2). The electric field is applied in all the samples along [110] direction at a frequency of 0.5 Hz. Figure 5-8 reports the electrostrictive response of the thin and thick sets of samples. All the films show high electrostriction coefficient around  $\approx 10^{-16} \text{ m}^2\text{V}^{-2}$ .

170 nm thick films demonstrate similar performances regardless of the substrates, as depicted in Figure 5-8a. CGO/NGO has the highest coefficient with  $M_{33} = 4.24 \cdot 10^{-16} \text{ m}^2\text{V}^{-2}$ , followed by CGO/STO and CGO/LAO with a coefficient of  $1.96 \cdot 10^{-16} \text{ m}^2\text{V}^{-2}$  and  $0.82 \cdot 10^{-16} \text{ m}^2\text{V}^{-2}$  respectively. The strain effect in this set of sample is negligible, as the lattice parameter for such thick films is relaxed.

Noticeably, all the samples display stress saturation around 100 MPa, for different electric fields. As the thickness, microstructure and dopant amount are the same in all three samples. The saturation can represent the maximum electrostriction achievable in this condition. Further polarization through the electric field does not traduce into mechanical distortion.



Figure 5-8b displays the electromechanical response of the 17 nm thick set of samples. CGO/NGO and

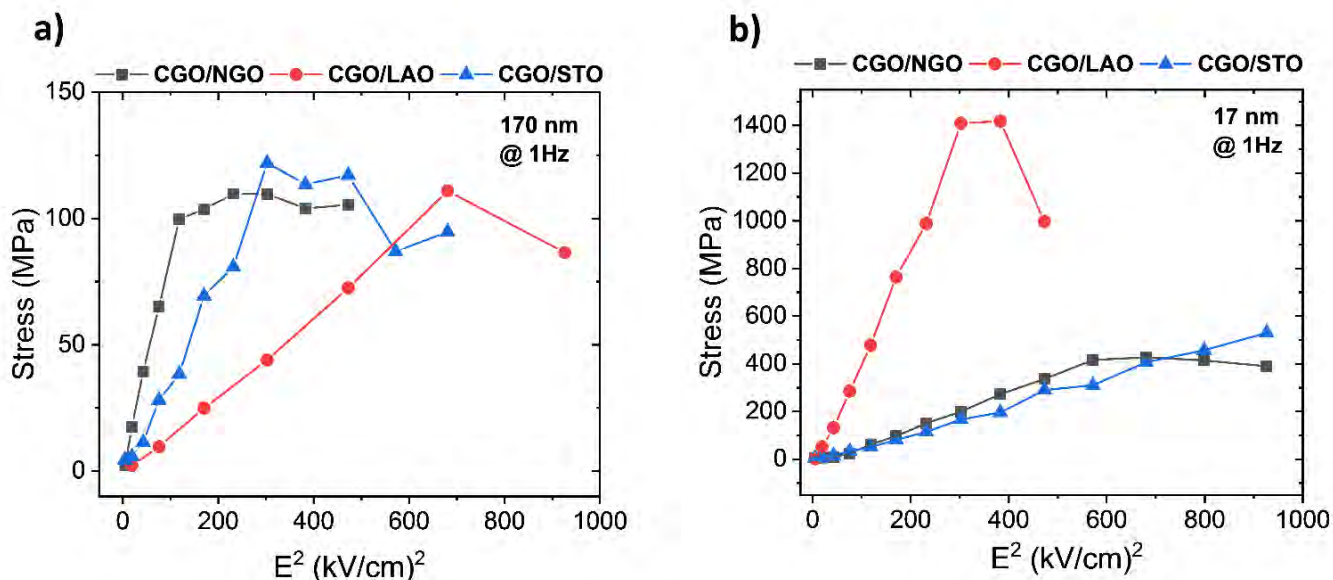


Figure 5-8: electromechanical performances of a) 170 nm and b) 17 nm thick CGO film deposited on NGO (black), LAO (red) and STO (blue).

CGO/STO electrostriction coefficients are  $2.94 \cdot 10^{-16} \text{ m}^2\text{V}^{-2}$  and  $2.94 \cdot 10^{-16} \text{ m}^2\text{V}^{-2}$  respectively. Interestingly, CGO/LAO displays a considerable increase in performances, reaching  $M_{33} = 23.5 \cdot 10^{-16} \text{ m}^2\text{V}^{-2}$ .

By comparing the two sets of samples, CGO/NGO and CGO/STO samples demonstrate a similar electrostriction coefficient for both 17 nm and 170 nm thicknesses. On the other hand, CGO/LAO demonstrates an extreme increase of electrostriction coefficient. LAO is expected to induce a compressive in-plane strain on CGO film and, as a consequence, high activation energy and low mobility of carriers. This results suggest that fixed oxygen vacancies contribute to the lattice distortion to a greater extent. The values of electrostriction coefficients for the thick and thin sample are reported and compared in Table 5-3.

In order to analyze the role of the microscopic configuration of the lattice, we performed XAS analysis described in the next section.



Table 5-3: Electrostriction coefficient for CGO/STO, CGO/NGO and CGO/LAO for 17 nm and 170 nm thick films.

$M_{33}$ ( $m^2V^{-2}$ )	CGO/STO	CGO/NGO	CGO/LAO
170 nm	$1.96 \cdot 10^{-16}$	$4.24 \cdot 10^{-16}$	$0.82 \cdot 10^{-16}$
	$\approx$	$\approx$	$\nearrow \nearrow \nearrow$
17 nm	$2.94 \cdot 10^{-16}$	$3.69 \cdot 10^{-16}$	$23.5 \cdot 10^{-16}$

### 5.3.4 X-ray absorption spectroscopy and discussion.

XANES measurements are taken at the Elettra synchrotron (Trieste), APE beamline. We analyzed Ce M4 and M5 edges. The spectra give information about the oxidation state of Ce species inside the material by recognizing features characteristic of 4+ or 3+ state.

Figure 5-9 shows the spectra of all samples with thick and thin films compared. CGO films grown on STO substrate are depicted in Figure 5-9a. The 170 nm thick film spectrum presents mostly Ce 4+ features: two sharp peaks for each edge <sup>52–54</sup>. A small pre-peak is visible before the M5 peak at 877 eV, indicating a minimal amount of Ce 3+ <sup>52–54</sup>. 17 nm thick CGO/STO on the other hand, develops shoulders before both M4 and M5 edges, suggesting a higher amount of Ce 3+. Also, M4 main peak is shifted by 0.2 eV to lower energy, a further characteristic of a Ce 3+ phase <sup>55</sup>.

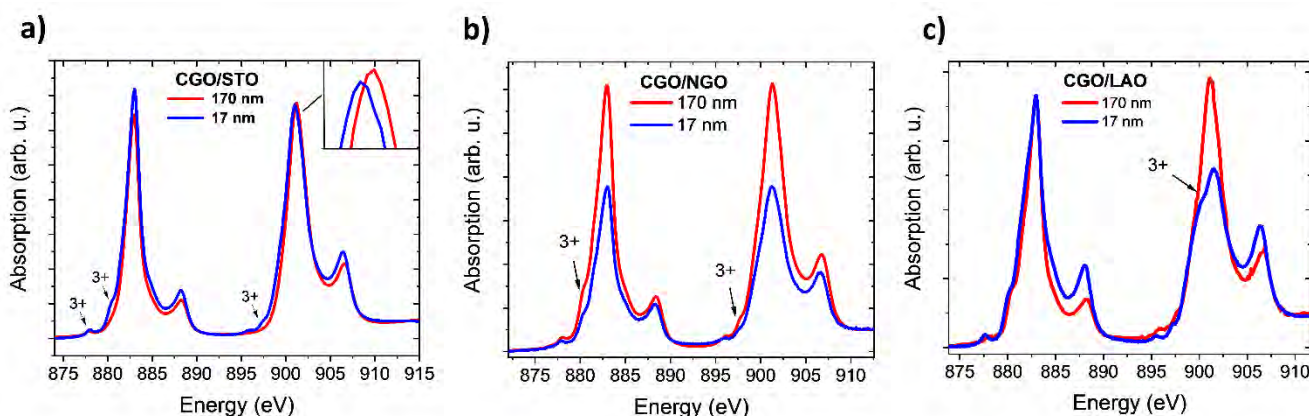


Figure 5-9: XANES of Ce M4 (900 eV) and M5 (882 eV) edges. a) 17 nm and 170 nm CGO/STO. b) 17 nm and 170 nm CGO/NGO. The lower peak intensity of 17 nm samples is not an indication of Ce 3+. c) 17 nm and 170 nm CGO/LAO. The M4 and M5 relative peaks height difference is a 3+ feature.

Figure 5-9b displays CGO/NGO samples. The spectra display 3+ features for samples of both thicknesses, in particular in the peak shoulder areas marked in the figure. 17 nm sample in this case, shows a similar spectrum, with just a slight increase of the shoulders.

CGO/LAO samples are depicted in Figure 5-9c: both possess 3+ features, but the difference between 17 nm and 170 nm thick films is noteworthy. The thinner film M4 edge presents a twin peaks shape, and the relative height respect to M5 is different. These features are characteristic of Ce 3+ spectrum<sup>52-54</sup>.

In general, 17 nm thick films exhibit higher 3+ features respect to the thicker samples, meaning that Ce 3+ phase aggregates at the interface. Trivalent Ce generates oxygen vacancies by redox process, leading to a high amount of defects in 17 nm thin films. CGO/LAO sample shows prominent 3+ phase features, suggesting that LAO substrate induces a high amount of defects if compared with STO and NGO, probably due to a compressive strain in the film lattice.

The exceptionally high electrostriction coefficient in CGO/LAO thin film is caused by two factors. The first is the low mobility of oxygen vacancies and their high activation energy, due to the local defects at the interface. The second reason is the high concentration of vacancies due to high Ce 3+ defects, leading to high amount of distorted cells. This effect takes place close to the film/substrate interface, as suggested by XANES.

This findings demonstrate the presence of an interfacial electrostriction that can be orders of magnitude higher than the bulk effect and can be controlled by the choice of the substrate.

### 5.3.5 XANES on Nd-YAG laser deposited: Sm-doped ceria.

We further deposited Gd and Sm doped ceria thin films with APE group using PLD deposition technique was used with Nd-YAG solid-state laser. This source sends pulses with fixed energy and frequency, resulting in a very stable laser fluency. The frequency of the beam (1064 nm) is not suitable to deposit oxides, as the absorption coefficient for the corresponding wavelength is low<sup>56</sup>. Therefore, oxides are usually deposited using frequency multiplier crystals<sup>57,58</sup> or oxygen reactive atmosphere<sup>59,60</sup>. So far, there are no previous works reporting oxide deposition with Nd:YAG using first harmonic and vacuum condition.

Despite that, with the group of APE beamline pure and doped ceria films are deposited on single-crystal substrate. The deposition condition is 670-700 °C temperature,  $5 \cdot 10^{-4}$  mbar oxygen partial pressure,  $\approx 5$  cm target/substrate distance. The laser settings are 2 Hz of frequency, 1064 nm pulse wavelength with 700 mJ of energy. The dynamics of the deposition are still clear and structural analysis is still going on.

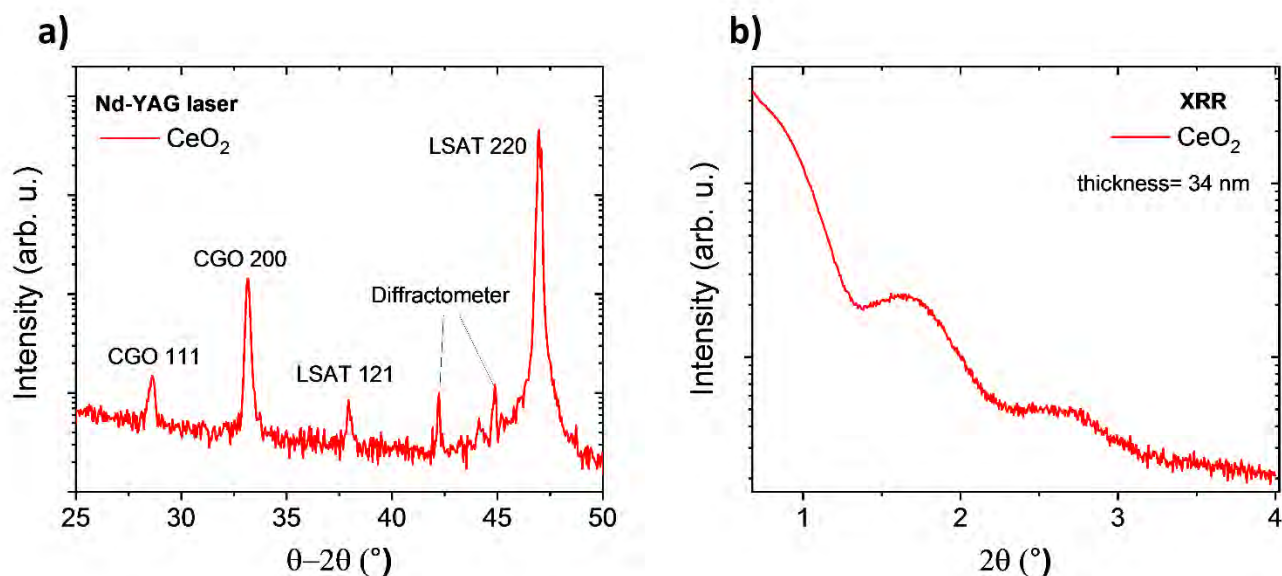


Figure 5-10: Structural characterization of pure ceria deposited with Nd-YAG laser by PLD. a)  $\theta$ - $2\theta$  scan. b) XRR showing a thickness of 34 nm.

Figure 5-10 exhibits the only structural characterization available currently. The sample is a film of pure ceria deposited on (220) oriented  $(\text{LaAlO}_3)_{0.3}(\text{Sr}_2\text{TaAlO}_6)_{0.7}$  (LSAT) substrate deposited for 15 minutes.  $\theta$ - $2\theta$  scan in Figure 5-10a highlights a preferred (200) orientation, with a certain amount of (111) texturing. The measurements presents some ghost peak caused by the multiple wavelength of the x-ray source. Figure 5-10b instead presents x-ray reflectivity of the sample. The thickness calculated is 34 nm, then the deposition rate estimated is 0.19 Å/pulse. This high rate is probably due to the high energy used.

In order to continue the analysis of interfacial defects of Ce, we deposited 20% and 40% Gd and Sm doped ceria to study the effect of different dopant element, and then the effect of electrostriction. The deposition took place over 20 minutes long, corresponding to a thickness of  $\approx 45.6$  nm.

Figure 5-11a shows XANES measurements of 20% Gd and Sm doped ceria on STO (200) substrate. The former exhibits the main M5 peak split in two and the peaks at 887 eV with reduced intensity, indicating a high amount of 3+ defects. Besides, Figure 5-11b displays 20% and 40% Sm doped ceria grown on NGO (110) substrate. Highly doped thin films display higher 3+ features. According to the results

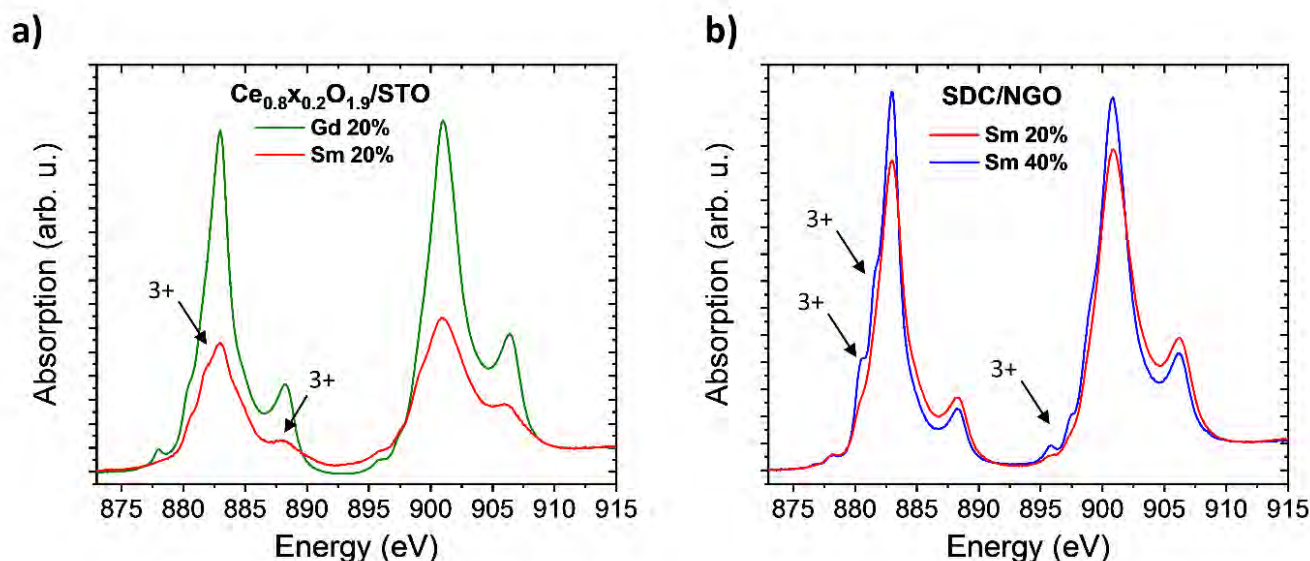


Figure 5-11: XANES spectra of thin films deposited by PLD with Nd-YAG laser. a) Comparison of 20% Gd or Sm doped ceria. b) comparison of 20% and 40% Sm doped thin films.

described in the previous section on strained thin films, 3+ phase should enhance electrostriction. Although these results are encouraging, further analysis is necessary to characterize the microstructure and electrostriction properties.

## 5.4 REFERENCES

<sup>1</sup><https://www.Cells.Es/En/Beamlines/BI22-Claess>

<sup>2</sup><https://www.Psi.Ch/En/SIs/Superxas>

- <sup>3</sup> L. Simonelli, C. Marini, W. Olszewski, M. Ávila Pérez, N. Ramanan, G. Guilera, V. Cuartero, and K. Klementiev, *Cogent Phys.* **3**, (2016).
- <sup>4</sup> O. Müller, M. Nachtegaal, J. Just, D. Lützenkirchen-Hecht, and R. Frahm, *J. Synchrotron Radiat.* **23**, 260 (2016).
- <sup>5</sup> R. Korobko, A. Patlolla, A. Kossoy, E. Wachtel, H.L. Tuller, A.I. Frenkel, and I. Lubomirsky, *Adv. Mater.* **24**, 5857 (2012).
- <sup>6</sup> R. Korobko, A. Lerner, Y. Li, E. Wachtel, A.I. Frenkel, and I. Lubomirsky, *Appl. Phys. Lett.* **106**, 042904 (2015).
- <sup>7</sup> Y. Li, O. Kraynis, J. Kas, T.C. Weng, D. Sokaras, R. Zacharowicz, I. Lubomirsky, and A.I. Frenkel, *AIP Adv.* **6**, (2016).
- <sup>8</sup> B. Ravel and M. Newville, *J. Synchrotron Radiat.* **12**, 537 (2005).
- <sup>9</sup> B. Ravel and M. Newville, *Phys. Scr. T* **T115**, 1007 (2005).
- <sup>10</sup> C. Marini, R. Boada, J. Prieto Burgos, N. Ramanan, I. García Domínguez, J. Zhao, T.T. Xiao, and L. Simonelli, *Nucl. Instruments Methods Phys. Res. Sect. A Accel. Spectrometers, Detect. Assoc. Equip.* **908**, 333 (2018).
- <sup>11</sup> M. Povia, J. Herranz, T. Binninger, M. Nachtegaal, A. Diaz, J. Kohlbrecher, D.F. Abbott, B.J. Kim, and T.J. Schmidt, *ACS Catal.* **8**, 7000 (2018).
- <sup>12</sup> A.D. Ushakov, E. Mishuk, E. Makagon, D.O. Alikin, A.A. Esin, I.S. Baturin, A. Tselev, V.Y. Shur, I. Lubomirsky, and A.L. Kholkin, *Appl. Phys. Lett.* **110**, 142902 (2017).
- <sup>13</sup> E. Mishuk, A.D. Ushakov, S.R. Cohen, V.Y. Shur, A.L. Kholkin, and I. Lubomirsky, *Solid State Ionics* **327**, 47 (2018).
- <sup>14</sup> S. Berendts and M. Lerch, *J. Cryst. Growth* **336**, 106 (2011).
- <sup>15</sup> J.J. Neumeier, M.T. Elm, B. Luerßen, and J. Janek, *Phys. Chem. Chem. Phys.* **20**, 8294 (2018).

- <sup>16</sup> J.P. Eufinger, M. Daniels, K. Schmale, S. Berendts, G. Ulbrich, M. Lerch, H.D. Wiemhöfer, and J. Janek, *Phys. Chem. Chem. Phys.* **16**, 25583 (2014).
- <sup>17</sup> K. Michel, J.P. Eufinger, G. Ulbrich, M. Lerch, J. Janek, and M.T. Elm, *Phys. Chem. Chem. Phys.* **19**, 17661 (2017).
- <sup>18</sup> K. Neuhaus, F. Schulze-Küppers, S. Baumann, G. Ulbrich, M. Lerch, and H.D. Wiemhöfer, *Solid State Ionics* **288**, 325 (2016).
- <sup>19</sup> F. Zhang, P. Wang, J. Koberstein, S. Khalid, and S.W. Chan, *Surf. Sci.* **563**, 74 (2004).
- <sup>20</sup> A.M. Shahin, F. Grandjean, G.J. Long, and T.P. Schuman, *Chem. Mater.* **17**, 315 (2005).
- <sup>21</sup> J.C. Kuang, *Adv. Mater. Res.* **1022**, 72 (2014).
- <sup>22</sup> E. Mishuk, E. Makagon, E. Wachtel, S.R. Cohen, R. Popovitz-Biro, and I. Lubomirsky, *Sensors Actuators, A Phys.* **264**, 333 (2017).
- <sup>23</sup> M. Hadad, H. Ashraf, G. Mohanty, C. Sandu, and P. Murali, *Acta Mater.* **118**, 1 (2016).
- <sup>24</sup> N. Yavo, O. Yeheskel, E. Wachtel, D. Ehre, A.I. Frenkel, and I. Lubomirsky, *Acta Mater.* **144**, 411 (2018).
- <sup>25</sup> R. Korobko, E. Wachtel, and I. Lubomirsky, *Sensors Actuators, A Phys.* **201**, 73 (2013).
- <sup>26</sup> H. Wijshoff, *Phys. Rep.* **491**, 77 (2010).
- <sup>27</sup> T.A. Ritter, T.R. Shrout, R. Tutwiler, and K.K. Shung, *IEEE Trans. Ultrason. Ferroelectr. Freq. Control* **49**, 217 (2002).
- <sup>28</sup> R. Abdolvand, H.M. Lavasani, G.K. Ho, and F. Ayazi, *IEEE Trans. Ultrason. Ferroelectr. Freq. Control* **55**, 2596 (2008).
- <sup>29</sup> N.N.G. Jones T.B., *Electromechanics and MEMS* (Cambridge University Press, 2013).
- <sup>30</sup> X. Guo and R. Waser, *Prog. Mater. Sci.* **51**, 151 (2006).
- <sup>31</sup> S. Kim, J. Fleig, and J. Maier, *Phys. Chem. Chem. Phys.* **5**, 2268 (2003).

- <sup>32</sup> J.L.M. Rupp and L.J. Gauckler, *Solid State Ionics* **177**, 2513 (2006).
- <sup>33</sup> A. Infortuna, A.S. Harvey, and L.J. Gauckler, *Adv. Funct. Mater.* **18**, 127 (2008).
- <sup>34</sup> N. Pryds, K. Rodrigo, S. Linderöth, and J. Schou, *Appl. Surf. Sci.* **255**, 5232 (2009).
- <sup>35</sup> K. Mohan Kant, V. Esposito, and N. Pryds, *Appl. Phys. Lett.* **100**, (2012).
- <sup>36</sup> S. Sanna, V. Esposito, A. Tebano, S. Licoccia, E. Traversa, and G. Balestrino, *Small* **6**, 1863 (2010).
- <sup>37</sup> D. Pergolesi, E. Gilardi, E. Fabbri, V. Roddatis, G.F. Harrington, T. Lippert, J.A. Kilner, and E. Traversa, *ACS Appl. Mater. Interfaces* **10**, 14160 (2018).
- <sup>38</sup> G.F. Harrington, L. Sun, B. Yildiz, K. Sasaki, N.H. Perry, H.L. Tuller, B. Yildiz, L. Sun, N.H. Perry, B. Yildiz, K. Sasaki, N.H. Perry, and H.L. Tuller, *Acta Mater.* **166**, 447 (2019).
- <sup>39</sup> N. Yang, P. Orgiani, E. Di Bartolomeo, V. Foglietti, P. Torelli, A. V. Ievlev, G. Rossi, S. Licoccia, G. Balestrino, S. V. Kalinin, and C. Aruta, *J. Phys. Chem. C* **121**, 8841 (2017).
- <sup>40</sup> Y. Shi, S.C. Lee, M. Monti, C. Wang, Z.A. Feng, W.D. Nix, M.F. Toney, R. Sinclair, and W.C. Chueh, *ACS Nano* **10**, 9938 (2016).
- <sup>41</sup> J.L.M. Rupp, E. Fabbri, D. Marrocchelli, J.W. Han, D. Chen, E. Traversa, H.L. Tuller, and B. Yildiz, *Adv. Funct. Mater.* **24**, 1562 (2014).
- <sup>42</sup> B.H. Rainwater, N. Velisavljevic, C. Park, H. Sun, G.H. Waller, G.M. Tsoi, Y.K. Vohra, and M. Liu, *Solid State Ionics* **292**, 59 (2016).
- <sup>43</sup> R. Sinclair, S.C. Lee, Y. Shi, and W.C. Chueh, *Ultramicroscopy* **175**, 25 (2017).
- <sup>44</sup> L. Ma, N. Doudin, S. Surnev, G. Barcaro, L. Sementa, A. Fortunelli, and F.P. Netzer, *J. Phys. Chem. Lett.* **7**, 1303 (2016).
- <sup>45</sup> L. Sun, D. Marrocchelli, and B. Yildiz, *Nat. Commun.* **6**, 1 (2015).
- <sup>46</sup> D.X. Huang, C.L. Chen, L. Chen, and A.J. Jacobson, *Appl. Phys. Lett.* **84**, 708 (2004).
- <sup>47</sup> K. Rodrigo, S. Heiroth, M. Lundberg, N. Bonanos, K. Mohan Kant, N. Pryds, L. Theil Kuhn, V. Esposito,

- S. Linderoth, J. Schou, and T. Lippert, Appl. Phys. A Mater. Sci. Process. **101**, 601 (2010).
- <sup>48</sup> S. Sanna, V. Esposito, D. Pergolesi, A. Orsini, A. Tebano, S. Licoccia, G. Balestrino, and E. Traversa, Adv. Funct. Mater. **19**, 1713 (2009).
- <sup>49</sup> L. Chen, C.L. Chen, D.X. Huang, Y. Lin, X. Chen, and A.J. Jacobson, Solid State Ionics **175**, 103 (2004).
- <sup>50</sup> N. Pryds and V. Esposito, J. Electroceramics **38**, 1 (2017).
- <sup>51</sup> [Http://www.Elettra.Trieste.It/Elettra-Beamlines/Ape.Html](http://www.Elettra.Trieste.It/Elettra-Beamlines/Ape.Html)
- <sup>52</sup> L. Howald, E. Stilp, P.D. De Réotier, A. Yaouanc, S. Raymond, C. Piamonteze, G. Lapertot, C. Baines, and H. Keller, Sci. Rep. **5**, (2015).
- <sup>53</sup> D. Hou, W. Zhou, C. Wu, P. Dorenbos, H. Liang, T.K. Sham, B. Zhang, Y. Huang, and Y. Tao, Phys. Chem. Chem. Phys. **17**, 22035 (2015).
- <sup>54</sup> S.O. Kucheyev, B.J. Clapsaddle, Y.M. Wang, T. Van Buuren, and A. V. Hamza, Phys. Rev. B - Condens. Matter Mater. Phys. **76**, 1 (2007).
- <sup>55</sup> P. Eriksson, A.A. Tal, A. Skallberg, C. Brommesson, Z. Hu, R.D. Boyd, W. Olovsson, N. Fairley, I.A. Abrikosov, X. Zhang, and K. Uvdal, Sci. Rep. **8**, 1 (2018).
- <sup>56</sup> R. Eason, *Pulsed Laser Deposition of Thin Films* (2007).
- <sup>57</sup> R. Shimizu, I. Sugiyama, N. Nakamura, S. Kobayashi, and T. Hitosugi, AIP Adv. **8**, 1 (2018).
- <sup>58</sup> Y.Y. Villanueva, D.R. Liu, and P.T. Cheng, Thin Solid Films **501**, 366 (2006).
- <sup>59</sup> R.A. Ismail, B.G. Rasheed, E.T. Salm, and M. Al-Hadethy, J. Mater. Sci. Mater. Electron. **18**, 1027 (2007).
- <sup>60</sup> X.M. Fan, J.S. Lian, Z.X. Guo, and H.J. Lu, Appl. Surf. Sci. **239**, 176 (2005).



# 6 CONCLUSION AND FUTURE PERSPECTIVE

---

In this thesis, a detailed characterization of non-classical electrostriction in doped ceria has been studied. The steps in my project have been divided into developing an experimental setup for sub-nano displacement evaluation, improving stability and performances of the devices and extending to the structure/property relationship.

To do this, I have created a measurement set-up at DTU Energy which enable the measurements of electrostriction. I investigated Gd-doped ceria thin films, grown by PLD in a polycrystalline phase and evaluating performances by electric field-induced vibration. The integration of CGO with TiN electrodes and Si substrate demonstrated superior operative condition and strength, improving the stability of CGO based electrostrictive devices. This represents a step forward for practical applications, due to the enhanced reliability but also thanks to the compatibility with TiN and Si, widely used in microelectronics and other technologies.

CGO thin films with different crystallographic directions have been grown with high-coherency on various single crystal substrates. With a planar electrode configuration, applying electric field along specific crystallographic direction was realized. I found that, electrical fields along [001] induce the highest electrostriction coefficient, followed by [110] and then by [111]. Based on these results, I proposed a new model to interpret the atomic mechanism for giant electrostriction in this class of material. More importantly, the electrostriction coefficient was improved by one order of magnitude through controlling of CGO film orientation.

Low-temperature Ce chemical environment was characterized by *in-situ* XANES without and upon applying of electric field. The bonding properties of Ce showed to evolve significantly due to the applied

voltage, with a more substantial effect at low temperature. In particular, the hybridization of  $f$  and  $d$  orbitals seems to decrease dramatically. Consequently, electrostriction properties should be improved as a consequence of cell elastic field rearrangement. This result encourages further low-temperature studies of CGO electrostriction.

During this project, the role of oxygen vacancies has been further determined in low dimensional strained thin films. Ultrathin epitaxial CGO films were (17 nm) grown on substrates with different lattice parameter, and were compared with thick films (170 nm). Electrostriction coefficient was increased dramatically in thin films with compressive strain. In the same system, oxygen vacancies acquire a fixed configuration and as a consequence contributes to the lattice distortion. XANES measurements highlighted Ce 3+ impurities at the interface with a compressive strain inducing substrate, therefore inducing further vacancies. This mix of such factors caused the electrostriction coefficient to reach values  $\approx 10^{-15} \text{ m}^2\text{V}^{-2}$ , never achieved before.

Future development of this research should address in two parallel ways: (1) The description of the structure/property relationship and (2) the development of devices suitable to bring these materials into a real application. For the former, it is crucial to find other defective oxides showing the same electrostrictive behavior. That should bring a more formal description of the effect and encourage the scientific community to join this new field. New systems should be studied, such as heterostructures. CGO multilayer systems, in particular with YSZ or  $\text{Bi}_2\text{O}_3$  that are widely studied for SOFC applications, and drastic change in both materials properties has been already demonstrated.

However, a step towards real application should be also done. Promising results have been presented in both bulk and membranes. Electrostriction relaxation at high frequency is a severe hindering factor. Future work should focus also on the adaption of operative high-frequency condition.

# APPENDICES

## A. LIST OF PAPERS INCLUDED ON THE THESIS

---

- I. **Simone Santucci**, Haiwu Zhang, Simone Sanna, Nini Pryds, Vincenzo Esposito.  
*“Enhanced electro-mechanical coupling of TiN/Ce<sub>0.8</sub>Gd<sub>0.2</sub>O<sub>1.9</sub> thin film electrostrictor”*, APL Mater. 7, 071104 (2019).  
Published  
Contribution: Film growing, structural characterization, electromechanical characterization, experimental planning and writing of the article.
- II. Ahsanul Kabir, **Simone Santucci**, Ngo Van Nong, Maxim Varenik, Igor Lubomirsky, Robin Nigon, Paul Murali, Vincenzo Esposito.  
*“Effect of Oxygen Defects Blocking Barriers on Gadolinium Doped Ceria (GDC) Electro-Chemo-Mechanical Properties”*, Acta Mater. 174, 53 (2019).  
Published  
Contribution: experimental part of impedance spectroscopy.
- III. **Simone Santucci**, Haiwu Zhang, Simone Sanna, Nini Pryds, Vincenzo Esposito.  
*“Electrostriction in ceria through controlled orientation”*  
Submitted to Acta Materialia  
Contribution: Film growing, structural characterization, electromechanical characterization, experimental planning, microscopic model development and writing of the article

- IV. **Simone Santucci**, Haiwu Zhang, Sandeep Chavuladi, Simone Sanna, Pasquale Orgiani, Nini Pryds, Vincenzo Esposito  
*“Interfacial electromechanical effect tuned by strain in Gd-doped ceria thin films”*  
 In preparation  
 Contribution: film growing, structural characterization, X-ray absorption spectroscopy analysis, experimental planning and writing of the article
- V. Ahsanul Kabir, **Simone Santucci**, Karl Tor Sune Thyden, Maxim Varenik, Igor Lubomirsky, Eugenio Paris, Vincenzo Esposito  
*“Steady Electrostriction Properties in Calcium Doped Cerium Oxide”*.  
 In preparation  
 Contribution: Experimental part of impedance spectroscopy
- VI. **Simone Santucci**, Ahsanul Kabir, Haiwu Zhang, Jin Kyu Han, Simone Sanna, Nini Pryds, Vincenzo Esposito  
*“Low temperature in-situ EXAFS on electrostrictor doped ceria”*  
 In preparation  
 Contribution: X-ray absorption spectroscopy analysis, experimental planning and writing of the article.
- VII. **Simone Santucci**, Vincenzo Esposito.  
*“Electrostrictive Ceramics and their applications”* Book chapter, included in *“Encyclopedia of Materials: Technical Ceramics and Glasses”*, Elsevier (2020)  
 Accepted  
 Contribution: writing of the article.

## B. LIST OF CONFERENCES CONTRIBUTION

---

- 1- Sustain 2017, DTU, Denmark. 6-12-2017/6-12/2017.  
Poster: "Giant Electrostriction in highly defective oxides: The next generation of electromechanical materials." Santucci, S., Esposito, V. & Pryds, N.
  
- 2- 2018 Material Research Society (MRS), Boston, USA. 25-11-2018/30-11-2018.  
Oral Presentation: "Defective Metal Oxides—New Generation of Electrostrictor Materials", Santucci, S., Sanna, S., Pryds, N. & Esposito, V.
  
- 3- XVI Conference and exhibition of the European Ceramic Society (ECerS), Turin, Italy. 16-06-2019/20-06-2019.  
Oral Presentation: "*Defective ceria actuator: the influence of electrodes*", Santucci, S., Zhang, H., Sanna, S., Pryds, N. & Esposito, V.

## C. ARTICLES AND MANUSCRIPT

---

# Enhanced electro-mechanical coupling of $\text{TiN}/\text{Ce}_{0.8}\text{Gd}_{0.2}\text{O}_{1.9}$ thin film electrostrictor

Cite as: APL Mater. 7, 071104 (2019); <https://doi.org/10.1063/1.5091735>

Submitted: 05 February 2019 . Accepted: 23 June 2019 . Published Online: 10 July 2019

Simone Santucci , Haiwu Zhang , Simone Sanna , Nini Pryds , and Vincenzo Esposito 



View Online



Export Citation



CrossMark

## ARTICLES YOU MAY BE INTERESTED IN

**Large-area cost-effective lithography-free infrared metasurface absorbers for molecular detection**

APL Materials **7**, 071102 (2019); <https://doi.org/10.1063/1.5102106>

**Self-assembly and properties of domain walls in  $\text{BiFeO}_3$  layers grown via molecular-beam epitaxy**

APL Materials **7**, 071101 (2019); <https://doi.org/10.1063/1.5103244>

**Direct observation of delithiation as the origin of analog memristance in  $\text{Li}_x\text{NbO}_2$**

APL Materials **7**, 071103 (2019); <https://doi.org/10.1063/1.5108525>



**AMERICAN ELEMENTS**  
THE ADVANCED MATERIALS MANUFACTURER®

**Now Invent.™**  
The Next Generation of Material Science Catalogs

[www.americanelements.com](http://www.americanelements.com)

American Elements opens up a world of possibilities so you can **Now Invent!**

Over 15,000 certified high purity laboratory chemicals, metals, & advanced materials and a state-of-the-art Research Center. Printable GHS-compliant Safety Data Sheets. Thousands of new products. And much more. All on a secure multi-language "Mobile Responsive" platform.

# Enhanced electro-mechanical coupling of TiN/Ce<sub>0.8</sub>Gd<sub>0.2</sub>O<sub>1.9</sub> thin film electrostrictor

Cite as: APL Mater. 7, 071104 (2019); doi: 10.1063/1.5091735

Submitted: 5 February 2019 • Accepted: 23 June 2019 •

Published Online: 10 July 2019



Simone Santucci,<sup>a)</sup> Haiwu Zhang, Simone Sanna, Nini Pryds, and Vincenzo Esposito<sup>a)</sup>

## AFFILIATIONS

Department of Energy Conversion and Storage, Technical University of Denmark, Frederiksborgvej 399 Roskilde, Denmark

<sup>a)</sup> Authors to whom correspondence should be addressed: [sisan@dtu.dk](mailto:sisan@dtu.dk) and [vies@dtu.dk](mailto:vies@dtu.dk)

## ABSTRACT

Gadolinium doped ceria, Gd:CeO<sub>2</sub> (CGO), have recently been shown to possess an exceptional high electrostriction coefficient ( $Q$ ), which is at the least three orders of magnitude larger than the best performing lead-based electrostrictors, e.g. Pb(Mn<sub>1/3</sub>Nb<sub>2/3</sub>)O<sub>3</sub>. Herein, we show that CGO thin films fabricated by a pulsed laser deposition method can be directly integrated onto the Si substrate by using TiN films of few nanometers as functional electrodes. The exceptional good coupling between TiN and Ce<sub>0.8</sub>Gd<sub>0.2</sub>O<sub>1.9</sub> yields a high electrostriction coefficient of  $Q_e = 40 \text{ m}^4 \text{ C}^{-2}$  and a superior electrochemomechanical stability with respect to the metal electrodes.

© 2019 Author(s). All article content, except where otherwise noted, is licensed under a Creative Commons Attribution (CC BY) license (<http://creativecommons.org/licenses/by/4.0/>). <https://doi.org/10.1063/1.5091735>

Electrostrictive materials respond with mechanical strain when subjected to external electric fields. They are deployed as actuators or transducers in a wide field of applications, including electronics, robotics, and ultrasound imaging.<sup>1–3</sup>

Nowadays, the widely used electrostrictor materials are piezoelectric materials such as Pb(Mn<sub>1/3</sub>Nb<sub>2/3</sub>)O<sub>3</sub> (PMN) which are toxic and are being banned to be used due to environmental concerns. This limits their future applications in new highly relevant fields such as electronic, medical, and biocompatible applications. Meanwhile, Pb is highly diffusive and is prone to react with the silicon.<sup>4,5</sup> Pb-based piezoelectrics are thus difficult to be integrated with silicon technology, e.g., for MEMS, NMES, and CMOS technology.<sup>5,6</sup> To overcome such issues, complex architectures with chemical barrier layers and crystallization seed layers at the support have been fabricated to avoid chemical interaction between the Si and the film.<sup>7,8</sup>

On an alternative path, recent studies disclosed an exceptional high electrostriction response in Pb-free defective metal oxides, in particular, in Gd-doped Ceria (CGO).<sup>9–13</sup> CGO not only is environmental friendly<sup>14</sup> but also it showed gigantic electrostriction with  $Q_e$  values above  $17 \text{ m}^4 \text{ C}^{-2}$ , or field electrostrictive coefficient of  $M_e \approx 10^{-18} \text{ m}^2/\text{V}^2$ <sup>15</sup> that does not depend on the polarization of the sample [both values are usually reported; see Eq. (4) for conversion]. These values are higher or at least comparable with the best State-of-the-Art materials such as PMN ( $Q = 0.002 \text{ m}^4 \text{ C}^{-2}$

and  $M_e = 2 \times 10^{-18} \text{ m}^2/\text{V}^2$ ),<sup>16</sup> BaBi<sub>2</sub>Nb<sub>2</sub>O<sub>9</sub> ( $Q = 0.038 \text{ m}^4 \text{ C}^{-2}$  and  $M_e = 4.9 \times 10^{-19} \text{ m}^2/\text{V}^2$ ),<sup>17</sup> or Na<sub>0.5</sub>Bi<sub>0.5</sub>TiO<sub>3</sub> ( $Q = 0.022 \text{ m}^4 \text{ C}^{-2}$  and  $M_e = 1.51 \times 10^{-19} \text{ m}^2/\text{V}^2$ ).<sup>18,19</sup> Unlike such classic electrostrictors, CGO based materials do not follow Newnham's law<sup>20,21</sup> that relates both dielectric and mechanical properties with the electrostriction coefficient.

Therefore, a different electromechanical mechanism is in play for oxygen defective metal oxides as compared with the standard electrostriction. CeO<sub>2–δ</sub> has a centrosymmetric fluorite structure, where a central cerium cation is surrounded by eight oxygen anions and oxygen vacancies. Acceptor dopants, such as Gd<sup>3+</sup>, promote the formation of oxygen vacancies ( $V_{\text{O}}^{\bullet}$ ) in the lattice, e.g., 20 mol. % Gd doping (Ce<sub>0.8</sub>Gd<sub>0.2</sub>O<sub>2–δ</sub>) corresponds to 5 mol. % oxygen vacancies ( $\delta = 0.1$ ).<sup>9,12,22</sup> According to Lubomirsky *et al.*,<sup>9,12,23</sup> oxygen vacancies trigger the giant electrostrictions by reducing the Ce–O bond length of the local Ce-coordination shell and increasing the Ce– $V_{\text{O}}^{\bullet}$  pair distance.<sup>11</sup> Under these conditions, electromechanically active  $V_{\text{O}}^{\bullet}$ -cation complexes are formed in the lattice and these induce a significant local distortion under the application of moderate electrical fields. In a thin film cantilever configuration, these properties are manifested by the generation of an exceptional in-plane high stress, up to 500 MPa, between the CGO thin film and the substrate.<sup>9</sup> This process is thought to be rather slow, as its magnitude decreases readily with the frequency.<sup>10,11</sup>



Evidence of such electromechanical performances has been confirmed recently by Hadad *et al.*,<sup>24</sup> by depositing CGO thin films on Si with different metal electrodes (Si/x/CGO/x, x = Al, Pt, Cr). They found that the electromechanical performances and stability of the CGO thin films depend critically on the electrodes used, making a rigorous characterization of the film itself difficult. CGO electrostrictive thin films deposited on metal electrodes often show mechanical decoupling during operation due to poor adhesion at the ceramic-metallic interface.<sup>11,24–26</sup>

Furthermore, cerium oxide is a refractory material, and conversely to Pb-based materials that need chemical barrier layers, it does not react with Si/SiO<sub>2</sub> substrates and is compatible with many materials for both low and high temperature uses.<sup>27–29</sup>

In this study, in order to overcome these limitations, we included Ce<sub>0.8</sub>Gd<sub>0.2</sub>O<sub>1.9</sub> thin films with titanium nitride (TiN) electrodes (TiN/CGO/TiN configuration) by Pulsed Laser Deposition (PLD). TiN has a rock-salt (NaCl) structure and shows excellent mechanical and electrical properties, such as low resistance ( $\sigma \approx 200$  S/cm at room temperature) and high chemical stability.<sup>30,31</sup> Therefore, TiN is an ideal candidate for Si integrated technologies and microelectronics such as electrodes, diffusion barriers, gates, or Schottky barrier contacts.<sup>32–35</sup> Coupling CGO with TiN can significantly simplify the integration procedures of these electrostrictors with Si-based technologies and microelectronics. Moreover, as a ceramic material, TiN is expected to provide superior crystallographic transport matches to CGO and chemical stability. As for a comparison, CGO thin films with a Au/CGO/TiN configuration were also fabricated to analyze stability and degradation behavior.

The Ce<sub>0.8</sub>Gd<sub>0.2</sub>O<sub>1.9</sub> target for the deposition was fabricated by synthesized Ce<sub>0.8</sub>Gd<sub>0.2</sub>O<sub>1.9</sub> powder following by uniaxial cold-pressing at 140 MPa and then sintered at 1723 K for 10 h. A high pure fluorite phase was observed for the as prepared targets.

CGO films with thicknesses of 800 and 1400 nm were deposited by PLD on a commercial [90 nm TiN/525  $\mu$ m Si] substrate (*Prime Wafers*). The wavelength of the excimer laser is 248 nm, with a 20 Hz repetition rate, an output energy of 200 mJ, and a fluence of 3 J cm<sup>-2</sup> (growth rate of 0.05 Å/pulse).<sup>28</sup> The deposition temperature was set to be 400 °C, and the target-substrate distance was fixed at ~72 mm. In order to avoid possible oxidation of TiN, the

first 15 min of deposition was carried out with nitrogen flow at 10<sup>-3</sup> mbar, after which it was switched to oxygen at 10<sup>-3</sup> mbar. Then, for films with the TiN/CGO/TiN configuration, TiN was grown by PLD with a temperature of 600 °C and N<sub>2</sub> flow at 10<sup>-3</sup> mbar. For films with the Au/CGO/TiN configuration, the Au top electrode was sputtered at room temperature with a Bal-Tec SCD 005 Sputter Coater. The samples were cut in beam shape: 7–8 mm wide and 15 mm long.

XRD analyses were performed with a Bruker D8 on deposited films. No secondary phases in the as deposited thin films were observed within the resolution limit of the instrument. Microstructure investigation and thickness measurement were carried out with the Zeiss Gemini-Merlin FE-SEM on the cross section of the samples.

For electromechanical characterization, one end of the beam sized samples was clamped and the other end was free to move [see Fig. 1(c)]. Vertical displacement at the free end was measured with a nanovibration analyzer with a single-beam laser interferometer (SIOS NA Analyzer). A sinusoidal electric field was applied with an Aim-TTI TGP 3100 function generator at frequency  $f = 100$  mHz, and the contacts were made with tungsten tips. Based on the vertical displacements of the free end, the change in stress was calculated, and subsequently, the electrostriction coefficient was obtained. As the measured displacement  $d$  is much smaller than the beam length  $L$  (i.e.,  $d \ll L$ ), the change in curvature  $\Delta k$  is

$$\Delta k = \frac{2d}{L^2}. \quad (1)$$

Using this value, the in plane stress  $\Delta\sigma$  was calculated using the Stoney formula

$$\Delta\sigma = \frac{Y_s}{1-\nu_s} \frac{t_s^2}{6t_f} \Delta k, \quad (2)$$

where  $Y_s$  and  $\nu_s$  are Young's modulus and the Poisson ratio of the substrate and are 130 GPa and 0.28, respectively, for Si.<sup>36</sup>  $t_s$  and  $t_f$  are the thickness of the substrate and film, respectively. The field electrostriction coefficient  $M_e$  is then obtained with the equation

$$\Delta\sigma = Y_f * M_e * E^2, \quad (3)$$

where  $E$  is the external electric field applied and  $Y_s$  is Young's modulus of CGO ( $\approx 200$  GPa).<sup>9</sup> In order to isolate harmonics

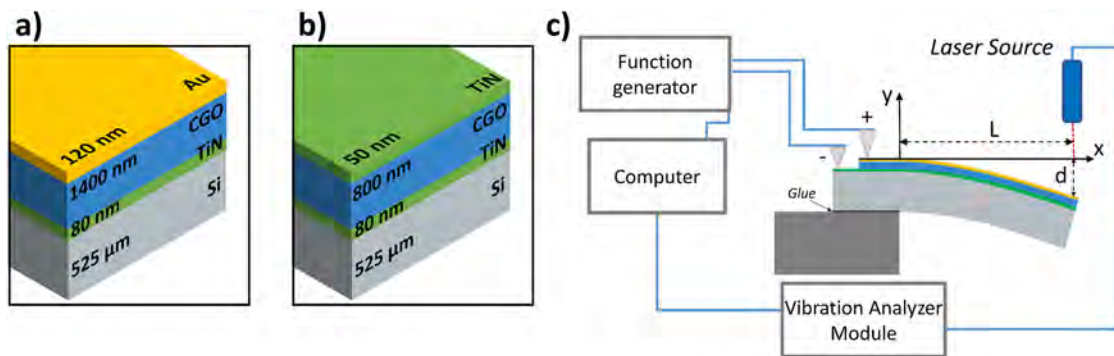


**FIG. 1.** Schematic illustration of the CGO thin films with (a) Au/CGO/TiN and (b) TiN/CGO/TiN configurations. (c) Schematic of the setup for beam deflection measurement. The dimension of the beam shaped samples is 7–8 mm × 15 mm.

oscillation, the signal was smoothed and the mechanical drift of the interferometer removed with a linear fit of the background.

Although the polarization electrostriction coefficient ( $Q_e$ ) is generally used to describe the classic electrostrictors, the field electrostriction coefficient ( $M_e$ ) is preferably used in the experimental procedure, as it is related to the electric field instead of polarization.  $M_e$  and  $Q_e$  coefficients are related by the equation

$$M_e = Q_e \{\epsilon_0(\epsilon_r - 1)\}^2, \quad (4)$$

where  $\epsilon_0$  is the vacuum permittivity and  $\epsilon_r$  is the relative dielectric constant of CGO ( $\approx 28$ ).<sup>9,12,37,38</sup> During the experiment, we tracked potential temperature variation with a FLIR SC5000 thermal camera with a waveband of 2.5–5.1  $\mu\text{m}$  and 20 mK sensitivity.

The film quality is generally improved by increasing the temperature at the substrate ( $T_s$ ) above 400 °C and by reducing the oxygen partial pressure ( $p\text{O}_2$ ) within the PLD deposition chamber.<sup>28,39,40</sup> The substrate temperature ( $T_s$ ) during PLD is a particularly important parameter to achieve high density of the CGO thin films, ensuring mechanical continuity of the electrostrictive film.<sup>41</sup> High crystallographic order is achieved, as CGO is deposited on structurally similar substrates with similar lattice parameters.<sup>41,42</sup> On the other hand, Infortuna *et al.*<sup>39</sup> found that  $p\text{O}_2 < 5 \times 10^{-2}$  mbar promotes a dense columnar structure in CGO, above which disordered and porous microstructures were observed. The top TiN electrode was deposited at 600 °C to increase conductivity,<sup>43</sup> avoiding residual strain.<sup>44</sup> During the deposition,  $\text{N}_2$  flow was used to avoid oxygen inclusion<sup>43</sup> and the variation of the stoichiometry of TiN. The correct stoichiometry was confirmed by XRD (Fig. S1 of the supplementary material).

Figures 1(a) and 1(b) schematically illustrate the configurations of Au/CGO/TiN and TiN/CGO/TiN, respectively. Structural and microstructural analyses reveal that the thickness of the bottom TiN electrode is 80 nm and the thickness of  $\text{Ce}_{0.8}\text{Gd}_{0.2}\text{O}_{1.9}$  within Au/CGO/TiN and TiN/CGO/TiN thin films are 800 and 1400 nm, respectively (Fig. S2 of the supplementary material). The top electrode in the former (Au) and the latter (TiN) is 120 and 50 nm, respectively. The CGO layers exhibit a preferred (111) orientation (Fig. S1 of the supplementary material), as consistent with that prepared by RF sputtering,<sup>10,24</sup> and show a columnar structure with no detectable porosity. The electromechanical characterization with a cantilever vibration setup is shown in Fig. 1(c).

Figure 2 shows the oscillating response of the Au/CGO/TiN and TiN/CGO/TiN under the application of alternating electric fields (25 and 27 kV/cm) at  $f_E = 100$  mHz. The measurements indicate that the films expand perpendicularly to the electric field, developing in-plane stress. As already highlighted in previous works,<sup>9–11,24</sup> the in-plane expansion is a peculiar behavior in  $\text{CeO}_2$ -based electrostrictive materials, as the characteristic second harmonic oscillation,<sup>21</sup> found at a frequency of  $2f_E = 200$  mHz. Electrostriction in other materials is usually attributed to possible Maxwell-tensor and/or thermal Joule effects.<sup>45</sup> For the Maxwell tensor effect, these are observed in polymers and it is generally negligible in hard inorganic materials,<sup>46</sup> and thus, its contribution to the in-plane stress resulting by the out-of-plane electric field is surely null.<sup>45</sup> On the other hand, the Joule effect due to the thermal expansion-driven bending is difficult to be distinguished and isolated from electromechanical oscillation. Both thermal expansion and electrostriction in CGO develop tensile in-plane stress and quadratic

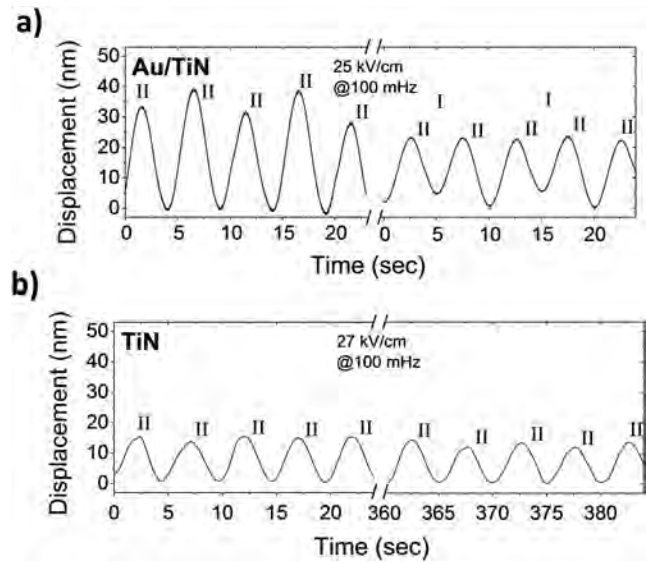


**FIG. 2.** Cantilever vertical displacement at the free end with 100 mHz applied electric field. II and I indicate the contribution from the second harmonic (200 mHz) and the first harmonic (100 mHz), respectively. (a) Displacements of Au/CGO/TiN at 25 kV/cm at the initial condition (left) and after consecutive measurements (right). (b) Displacements of TiN/CGO/TiN at 27 kV/cm as a function of measuring time.

dependence with respect to the electric field. In our case, however, the thermal contribution to the total displacement is negligible as its calculated value was found to be low ( $\sim 0.1$  nm for Au/CGO/TiN and  $\sim 0.5$  nm for TiN/CGO/TiN) and no temperature increase was detected with the thermal camera. The contribution of the mechanical resonance can also be excluded due to the higher resonance frequency than that of oscillation ( $> 1$  kHz vs 200 mHz).

At the initial stage of the experiments, the electrostriction coefficients of the Au/CGO/TiN and the TiN/CGO/TiN are similar, with the field electrostriction coefficient being  $M_e = 2.3 \pm 0.3 \times 10^{-18} \text{ m}^2/\text{V}^2$  and  $M_e = 1.5 \pm 0.2 \times 10^{-18} \text{ m}^2/\text{V}^2$ , respectively. These values are very high and fully consistent with the other values reported for this class of materials.<sup>9–12,24</sup>

In order to evaluate the stability of the performances of the samples, we included the oscillation in the late part of the experiment, after several repeating and measuring times. Figure 2(a) shows that continuous voltage stress causes a decrease in the oscillation of Au/CGO/TiN thin films, which displays a double first and second harmonics oscillation. The double harmonics behavior should rise only in samples subjected to AC ( $E_{ac}$ ) and DC ( $E_{dc}$ ) electric fields simultaneously. Under this condition, the harmonic evolution of stress is proportional to two periodic terms,<sup>9</sup>

$$\sigma \propto \{E_{ac} \cos(\omega t) + E_{dc}\}^2 = E_{dc}^2 + \frac{E_{ac}^2}{2} + 2E_{ac}E_{dc} \cos(\omega t) + \frac{E_{ac}^2}{2} \cos(2\omega t), \quad (5)$$

with  $\omega = 2\pi f$  being the angular frequency of applied field. The first harmonic behavior has been ascribed to an internal bias ( $E_{int}$ ) in the sample, which is generally attributed to the different quality of

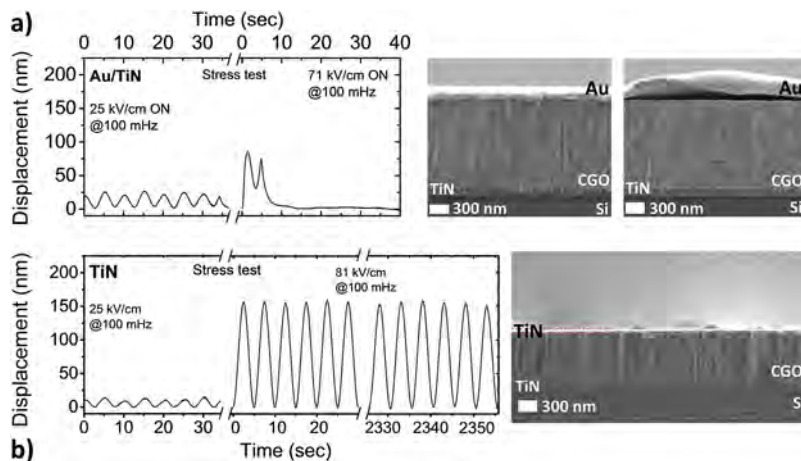


**FIG. 3.** (a) Stress test on a TiN/CGO/Au thin film: (left) beam displacement at 25 kV/cm, displaying the failure at 71 kV/cm; (middle) FE-SEM cross section images with the Au top electrode still adherent to the film; (right) postmortem cross section showing top electrode detachment caused by voltage stress. (b) Stress test of the TiN/CGO/TiN thin film; (left) beam displacement at 25 kV/cm and 81 kV/cm over 40 min showing high stability; (right) FE-SEM cross section image after stress test, showing TiN electrodes still perfectly adhered to the CGO film.

the two electrodes.<sup>26</sup> Figure 2(a) also shows that at the early stage of the measurements, only the second harmonic contribution was detected. This suggests a development of internal bias contribution  $E_{\text{int}}$  caused by continuous electric field stress. A possible reason for the appearance of the internal electric field and decreased oscillation magnitude can thus be ascribed to the possible degradation of the electrode and CGO/electrode interfaces. The decrease in the oscillations yields to a decreased electrostriction coefficient, i.e.,  $M_e = 1.50 \pm 0.03 \times 10^{-18} \text{ m}^2/\text{V}^2$ , which is still comparable with the early values. On the other hand, TiN/CGO/TiN thin films did not show any sign of degradation over a long period of time, as demonstrated by their displacements as a function of time [Fig. 2(b)]. The oscillation is stable in the amplitude and is only the II harmonic dependent, which excludes the degradation of the electrodes or the development of internal bias, demonstrating the reliability of TiN electrodes as a function of time.

In order to investigate the film stability, under high voltage stress, we applied an alternating electric field of 71 kV/cm and 81 kV/cm ( $f = 100 \text{ MHz}$  for both cases) to Au/CGO/TiN and TiN/CGO/TiN thin films, respectively. Figure 3(a) (left) shows that as soon as the higher voltage was applied, the sample displayed a high oscillation over a very short time after which no mechanical response was detected. The resistance of the sample increased to 100–200 M $\Omega$  and it did not recover over time, which may indicate mechanical damage in the structure involving the film, the electrodes, or the interfaces. Postmortem SEM analysis on the sample [Fig. 3(a) on the right] shows no cracks in the CGO film. This was expected as others reported even higher operating electric fields.<sup>10,24</sup> The TiN bottom electrodes did not show visible degradation while a clear failure was observed at the Au top electrode, which should be responsible for the deterioration of performances. The stability of the TiN electrodes is further confirmed by the outcome of the stress test for the TiN/CGO/TiN sample: Figure 3(b) shows an exceptional stability at a high field, 81 kV/cm. No visible degradation of the displacements was observed over a rather long measuring time (e.g., 40 min). SEM cross section observations confirm that the films and interfaces remained intact, indicating an exceptional good coupling between the CGO and TiN and points out to the direction of integrating the CGO with Si technology using TiN electrodes.

In summary, the effects of ceramic electrodes on the electrostrictive response and stability of CGO films were investigated using a hybrid metal-ceramics configuration, using Au/TiN as electrodes, and a full ceramic device (TiN/TiN). Electromechanical properties were studied using beam deflection technique, and an active response was observed for both Au/CGO/TiN and TiN/CGO/TiN samples, with electrostriction coefficients of  $M_e = 2.3 \times 10^{-18} \text{ m}^2 \text{ V}^{-2}$  and  $M_e = 1.5 \times 10^{-18} \text{ m}^2 \text{ V}^{-2}$ , respectively. Our study shows a decrease in the performances and internal stability of the sample with the metal electrode. TiN/CGO/TiN on the other hand displayed good durability. On an electromechanical stress-test, we show a critical failure of Au/CGO/TiN caused by the detachment of the metal electrode at 71 kV/cm. On the other hand, TiN/CGO/TiN was stable up to 81 kV/cm, with no signs of degradation or mechanical failures. Our results indicated excellent mechanical integrity between the TiN electrodes and the CGO film. TiN is found to be a very promising electrode on Si and, therefore, is of particular interest for further investigation as a platform for growing CGO thin films.

See [supplementary material](#) for structural characterization by X-ray diffraction and SEM cross section.

This research was supported by the Danish Council for Independent Research Technology and Production Sciences for the DFF-Research Project 2 (Grant No. 48293) and the BioWings project funded by the European Union's Horizon 2020, Future and Emerging Technologies (FET) programme (Grant No. 801267).

## REFERENCES

- S. H. Baek, J. Park, D. M. Kim, V. A. Aksyuk, and R. R. Das, *Science* **334**, 958 (2011).
- G. H. Haertling, *J. Am. Ceram. Soc.* **82**, 797 (1999).
- A. L. Kholkin, E. K. Akdogan, A. Safari, P. F. Chauvy, and N. Setter, *J. Appl. Phys.* **89**, 8066 (2001).
- N. Ledermann, P. Murali, J. Baborowski, S. Gentil, K. Mukati, M. Cantoni, A. Seifert, and N. Setter, *Sens. Actuators, A* **105**, 162 (2003).
- R. A. Dorey and R. W. Whatmore, *J. Electroceram.* **12**, 19 (2004).
- A. Schatz, D. Pantel, and T. Hanemann, *J. Appl. Phys.* **122**, 114502 (2017).
- D. Isarakorn, A. Sambri, P. Janphuang, D. Briand, and S. Gariglio, *J. Micromech. Microeng.* **20**, 055008 (2010).

- <sup>8</sup>M. D. Nguyen, H. Yuan, E. P. Houwman, M. Dekkers, G. Koster, J. E. ten Elshof, and G. Rijnders, *ACS Appl. Mater. Interfaces* **8**, 31120 (2016).
- <sup>9</sup>R. Korobko, A. Patlolla, A. Kosoy, E. Wachtel, H. L. Tuller, A. I. Frenkel, and I. Lubomirsky, *Adv. Mater.* **24**, 5857 (2012).
- <sup>10</sup>R. Korobko, E. Wachtel, and I. Lubomirsky, *Sens. Actuators, A* **201**, 73 (2013).
- <sup>11</sup>A. D. Ushakov, N. Yavo, E. Mishuk, I. Lubomirsky, V. Y. Shur, and A. L. Kholkin, *KnE Mater. Sci.* **1**, 177 (2016).
- <sup>12</sup>R. Korobko, A. Lerner, Y. Li, E. Wachtel, A. I. Frenkel, and I. Lubomirsky, *Appl. Phys. Lett.* **106**, 042904 (2015).
- <sup>13</sup>A. Kabir, S. Santucci, N. Van Nong, M. Varenik, I. Lubomirsky, R. Nigon, P. Mural, and V. Esposito, *Acta Mater.* **174**, 53 (2019).
- <sup>14</sup>C. Sun, H. Li, and L. Chen, *Energy Environ. Sci.* **5**, 8475 (2012).
- <sup>15</sup>A. Kosoy, Q. Wang, R. Korobko, V. Grover, Y. Feldman, E. Wachtel, A. K. Tyagi, A. I. Frenkel, and I. Lubomirsky, *Phys. Rev. B* **87**, 054101 (2013).
- <sup>16</sup>R. E. N. V. Sundar, J.-F. Li, and D. Viehland, *Mater. Res. Bull.* **31**, 555 (1996).
- <sup>17</sup>F. Li, L. Jin, Z. Xu, and S. Zhang, *Appl. Phys. Rev.* **1**, 011103 (2014).
- <sup>18</sup>A. You, M. A. Y. Be, and I. In, *202902*, 0 (2017).
- <sup>19</sup>A. Hussain, A. Maqbool, R. A. Malik, M. H. Kim, T. K. Song, and W. J. Kim, *IOP Conf. Ser.: Mater. Sci. Eng.* **146**, 012006 (2016).
- <sup>20</sup>N. Yavo, A. D. Smith, O. Yehekel, S. Cohen, R. Korobko, E. Wachtel, P. R. Slater, and I. Lubomirsky, *Adv. Funct. Mater.* **26**, 1138 (2016).
- <sup>21</sup>R. E. Newnham, V. Sundar, R. Yimnirun, J. Su, and Q. M. Zhang, *J. Phys. Chem. B* **101**, 10141 (1997).
- <sup>22</sup>E. Wachtel and I. Lubomirsky, *Scr. Mater.* **65**, 112 (2011).
- <sup>23</sup>Y. Li, O. Kraynis, J. Kas, T. C. Weng, D. Sokaras, R. Zacharowicz, I. Lubomirsky, and A. I. Frenkel, *AIP Adv.* **6**, 055320 (2016).
- <sup>24</sup>M. Hadad, H. Ashraf, G. Mohanty, C. Sandu, and P. Mural, *Acta Mater.* **118**, 1 (2016).
- <sup>25</sup>E. Mishuk, E. Makagon, E. Wachtel, S. R. Cohen, R. Popovitz-Biro, and I. Lubomirsky, *Sens. Actuators, A* **264**, 333 (2017).
- <sup>26</sup>A. D. Ushakov, E. Mishuk, E. Makagon, D. O. Alikin, A. A. Esin, I. S. Baturin, A. Tselev, V. Y. Shur, I. Lubomirsky, and A. L. Kholkin, *Appl. Phys. Lett.* **110**, 142902 (2017).
- <sup>27</sup>A. Bieberle-Hütter, J. L. Hertz, and H. L. Tuller, *Acta Mater.* **56**, 177 (2008).
- <sup>28</sup>N. Pryds, K. Rodrigo, S. Linderorth, and J. Schou, *Appl. Surf. Sci.* **255**, 5232 (2009).
- <sup>29</sup>V. Esposito, D. W. Ni, S. Sanna, F. Gualandris, and N. Pryds, *RSC Adv.* **7**, 13784 (2017).
- <sup>30</sup>J. E. Sundgren, *Thin Solid Films* **128**, 21 (1985).
- <sup>31</sup>N. K. Ponon, D. J. R. Appleby, E. Arac, P. J. King, S. Ganti, K. S. K. Kwa, and A. O. Neill, *Thin Solid Films* **578**, 31 (2015).
- <sup>32</sup>R. H. Dauskardt, M. Lane, Q. Ma, and N. Krishna, *Eng. Fract. Mech.* **61**, 141 (1998).
- <sup>33</sup>M. C. Lemme, J. K. Efavi, T. Mollenhauer, M. Schmidt, H. D. B. Gottlob, T. Wahlbrink, and H. Kurz, *Microelectron. Eng.* **83**, 1551 (2006).
- <sup>34</sup>M. Lukosius, C. Walczyk, M. Fraschke, D. Wolansky, H. Richter, and C. Wenger, *Thin Solid Films* **518**, 4380 (2010).
- <sup>35</sup>C. N. Kirchner, H. Hallmeier, R. Szargan, T. Raschke, and C. Radehaus, *Electroanalysis* **19**, 1023 (2007).
- <sup>36</sup>M. A. Hopcroft, W. D. Nix, and T. W. Kenny, *J. Microelectromech. Syst.* **19**, 229 (2010).
- <sup>37</sup>V. Shelukhin, I. Zon, E. Wachtel, Y. Feldman, and I. Lubomirsky, *Solid State Ionics* **211**, 12 (2012).
- <sup>38</sup>S. Kim and J. Maier, *J. Electrochem. Soc.* **149**, J73 (2002).
- <sup>39</sup>A. Infortuna, A. S. Harvey, and L. J. Gauckler, *Adv. Funct. Mater.* **18**, 127 (2008).
- <sup>40</sup>J. Schou, *Appl. Surf. Sci.* **255**, 5191 (2009).
- <sup>41</sup>S. Sanna, V. Esposito, D. Pergolesi, A. Orsini, A. Tebano, S. Licoccia, G. Balestrino, and E. Traversa, *Adv. Funct. Mater.* **19**, 1713 (2009).
- <sup>42</sup>K. Rodrigo, S. Heiroth, M. Lundberg, N. Bonanos, K. Mohan Kant, N. Pryds, L. Theil Kuhn, V. Esposito, S. Linderorth, J. Schou, and T. Lippert, *Appl. Phys. A* **101**, 601 (2010).
- <sup>43</sup>R. Chowdhury, R. D. Vispute, K. Jagannadham, and J. Narayan, *J. Mater. Res.* **11**, 1458 (1996).
- <sup>44</sup>D. Rasic, R. Sachan, M. F. Chisholm, J. Prater, and J. Narayan, *Cryst. Growth Des.* **17**, 6634 (2017).
- <sup>45</sup>Y. M. Shkel and D. J. Klingenberg, *J. Appl. Phys.* **80**, 4566 (1996).
- <sup>46</sup>L. Liu and P. Sharma, *J. Mech. Phys. Solids* **112**, 1 (2018).





## Full length article

## Effect of oxygen defects blocking barriers on gadolinium doped ceria (GDC) electro-chemo-mechanical properties

Ahsanul Kabir <sup>a, c, \*</sup>, Simone Santucci <sup>a</sup>, Ngo Van Nong <sup>a</sup>, Maxim Varenik <sup>b</sup>, Igor Lubomirsky <sup>b</sup>, Robin Nigon <sup>c</sup>, Paul Murali <sup>c</sup>, Vincenzo Esposito <sup>a, \*\*</sup>

<sup>a</sup> Department of Energy Conversion and Storage, Technical University of Denmark, Frederiksborgvej 399, Roskilde, 4000, Denmark

<sup>b</sup> Department of Materials and Interfaces, Weizmann Institute of Science, Rehovot, 76100, Israel

<sup>c</sup> Ceramics Laboratory, Department of Materials, Swiss Federal Institute of Technology, Lausanne, 1015, Switzerland

## ARTICLE INFO

## Article history:

Received 15 February 2019

Received in revised form

24 April 2019

Accepted 5 May 2019

Available online 10 May 2019

## Keywords:

Electrostriction

Vacancies

Gadolinium-doped ceria

Sintering

## ABSTRACT

Some oxygen defective metal oxides, such as cerium and bismuth oxides, have recently shown exceptional electrostrictive properties that are even superior to the best performing lead-based electrostrictors, e.g. lead-magnesium-niobates (PMN). Compared to piezoelectric ceramics, electromechanical mechanisms of such materials do not depend on crystalline symmetry but on the concentration of oxygen vacancy ( $V_{\text{O}}^{\bullet\bullet}$ ) in the lattice. In this work, we investigate for the first time the role of oxygen defects configuration on the electro-chemo-mechanical properties. This is achieved by tuning the oxygen defects blocking barrier density in polycrystalline gadolinium doped ceria with known oxygen vacancy concentration,  $\text{Ce}_{0.9}\text{Gd}_{0.1}\text{O}_{2-\delta}$ ,  $\delta = 0.05$ . Nanometric starting powders of ca. ~12 nm are sintered in different conditions, including field assisted spark plasma sintering (SPS), fast firing and conventional method at high temperatures. These approaches allow controlling grain size and Gd-dopant diffusion, i.e. via thermally driven solute drag mechanism. By correlating the electro-chemo-mechanical properties, we show that oxygen vacancy distribution in the materials plays a key role in ceria electrostriction, overcoming the expected contributions from grain size and dopant concentration.

© 2019 Acta Materialia Inc. Published by Elsevier Ltd. All rights reserved.

## 1. Introduction

Cerium oxide ( $\text{CeO}_2$ ) has been comprehensively investigated in the last few decades due to its multifold applications, more specifically in electro-ceramics and catalysts [1–4]. It has a centrosymmetric fluorite structure with a pronounced oxygen defectivity, i.e. oxygen vacancies ( $V_{\text{O}}^{\bullet\bullet}$ ). This feature makes ceria an excellent ionic conductor, especially suitable for solid-state electrolytes at high temperatures [5], where acceptor dopants are used to enhance oxygen defects concentration,  $[V_{\text{O}}^{\bullet\bullet}]$ , in the lattice [6,7]. In cerium oxide,  $\text{Ce}^{4+}$  cation can also be reduced to  $\text{Ce}^{3+}$  under low oxygen partial pressure ( $P_{\text{O}_2}$ ) at high temperatures, creating both *quasi*-free localized electrons, i.e. small polarons and oxygen vacancies [8], resulting in mixed ionic-electronic

conductivity (MIEC) [5,9]. Besides these properties, ceria exhibits non-classical giant electrostriction at room temperatures [10–12], both in thin films and bulk materials. Remarkably, ceria thin film expands perpendicular to applied field direction, with large compressive stress ( $\approx 500$  MPa) [10]. The average electrostriction coefficient ( $M_e$ ) is reported as  $\approx 6.5 \cdot 10^{-18}$  (m/V)<sup>2</sup> for  $[V_{\text{O}}^{\bullet\bullet}] = 5\%$ , i.e. 20 mol% Gd-doped ceria [10]. Such value is high for a material with low dielectric constant ( $\epsilon_r^{\text{GDC}} \approx 30$ ) [13], even higher compared to relaxor ferroelectric metal oxides, e.g. Ca-doped PMN ( $\text{Pb,MgNbO}_3$  ( $\epsilon_r^{\text{Ca-PMN}} \approx 4000$ )) [14]. Yavo et al. also verified this type of electromechanical properties in bulk gadolinium doped ceria and another oxygen defective fluorite oxide ( $\text{Bi}_2\text{O}_3$ ), which exhibit similar results, thus representing to a new class of electroactive materials [12,15]. The atomistic model proposed by Lubomirsky et al. based on XANES/EXAFS measurements [16] comprehensively explains the underlying phenomena of this unusual behavior, further suggested that the presence of oxygen vacancy makes distorted  $\text{CeCe}-7\text{O}-V_{\text{O}}^{\bullet\bullet}$  units: consisting of contracted  $\text{Ce}-\text{O}$  and expanded  $\text{Ce}-V_{\text{O}}^{\bullet\bullet}$  bond, compared to  $\text{Ce}-\text{O}$  bond in  $\text{Ce}-8\text{O}$  unit [10,16]. As a result, asymmetric charge

\* Corresponding author. Department of Energy Conversion and Storage, Technical University of Denmark, Frederiksborgvej 399, Roskilde, 4000, Denmark.

\*\* Corresponding author.

E-mail addresses: [ahsk@dtu.dk](mailto:ahsk@dtu.dk) (A. Kabir), [vies@dtu.dk](mailto:vies@dtu.dk) (V. Esposito).

distribution and anisotropic local dipolar elastic field are developed in the fluorite lattice [17]. Under the applied electric field, distorted  $\text{Ce}_{\text{Ce}}-7\text{O}_0-\text{V}_\text{O}^\bullet$  complexes conform to more fluorite-like structure and subsequently, local atomic displacement produces giant electromechanical effect [16]. Despite intriguing, some questions about the role of oxygen vacancies and microstructure on electrostriction still remain unexplored [12]. Besides, Lubomirsky and co-workers suggested a power-law dependence of  $I-V$  relationship in grain boundary blocking behavior based on space charge mechanisms [18,19] and demonstrated that an increase of grain boundary resistance leads to a decrease in the portion of applied voltage drop in the bulk, decreasing electromechanical properties [20].

As ionic conductor at high temperatures, bulk properties of ceria-based compounds are controlled by process parameters, i.e. morphology of initial powders, sintering kinetics/thermal history, densification, final microstructure, etc. For sintering and consolidation, mass diffusion mechanisms are especially dominated by solute drag phenomena, which, depends on both dopant size and valence. These can influence ionic configurations at the grain boundary, for instance, by trapping vacancies in disorder and/or in vacancies-ions complexes with low mobility [21,22]. This is described by the so-called “brick model” that is observed for highly defective ceria where fast ionic migration mechanisms are activated, thus reducing cations trapping effects at the grain boundaries [23–26]. Solute drag phenomena create specific grain boundary configurations and non-stoichiometry, which acts as blocking barriers to migrate charge species in the material, significantly affect intrinsic properties [21]. Moreover, Shibata et al. experimentally showed that the long-range electric interaction is the governing factor in controlling the local charge distribution at the crystal interface [27].

Based on previously published reports, designing the microstructure at nano-scale is also expected to create more significant differences between oxygen migration effects, revealing dissimilar physical and chemical properties than a grain of micron sizes. In addition, decreasing the grain size leads to increase grain boundary effect on the material, as well as increasing the density of the blocking barrier [28]. On the other hand, Esposito et al. proposed that grain boundary blocking factor is not necessarily a geometrical factor [3]: at a fixed oxygen vacancy concentration, different grain boundary blocking effects are encountered, depending on the entity of solute drag effect, controlled by sintering conditions [3]. The grain boundary blocking effect is explained both theoretically and experimentally by the distribution of defects by space charge layer model [29–35]. Other techniques also can disrupt the solute drag effect, even maintaining the polycrystalline in the nanoscale. This occurs by field assisted sintering techniques (FASTs), such as spark plasma sintering (SPS) [36]. FASTs use three important parameters (i) pulsed electric field, (ii) high heating rates and (iii) high pressure to preserve ultra-fine grains [37,38].

In the present work, we use nanometric 10 mol % gadolinium doped ceria (GDC10) to produce polycrystalline samples with different oxygen vacancy configuration. This is done by sintering the nano-powders by field assisted (SPS), fast firing and conventional method, which yields dense polycrystalline samples with tuned oxygen ions blocking barriers. A commercial high-density tape cast sample with minimized grain boundary is also used for comparison. The influence of oxygen vacancy configuration on electro-chemo-mechanical properties of GDC was investigated, comparing the electrochemical properties from low to intermediate temperatures (ca. 300–575 °C) with the electromechanical properties at room temperatures, expecting unchanged oxygen vacancy configuration in the materials.

## 2. Experimental procedure

### 2.1. Powder synthesis

Nano size gadolinium doped ceria (GDC10) powders were prepared by co-precipitation method using diamine in aqueous solution [3]. Cerium nitrate hexahydrate (Sigma-Aldrich, USA) and gadolinium nitrate hexahydrate (Sigma-Aldrich, USA) salts were mixed together in stoichiometric proportions to prepare 0.1 M solution in deionized water. Then MDEA (N-methyl-diethanolamine) was added dropwise. The molar ratio between total cations and MDEA was 1:3. The resulting precipitates were kept overnight under mild stirring. Afterward, the precipitates were centrifuged and washed several times with ethanol. The resulting gel was dried at 120 °C followed by calcination at 500 °C for 2 h. After the calcination, hard agglomerated powders were ball-milled in ethanol with 2 mm zirconia balls for 10–12 h at 50 rpm, followed by drying at 120 °C for 10 h. Finally, the powders were softly crushed by mortar and pestle and sieved using a 150 µm mesh.

### 2.2. Pellet preparation

The SPS sample was consolidated by field assisted spark plasma sintering (SPS) (Dr. Sinter Lab 515S, Japan) under high vacuum ( $\leq 6 \cdot 10^{-6}$  Torr) at 980 °C, uniaxial pressure of 70 MPa with 5 min dwelling. To minimize the chemical reduction that may occur by FAST treatments, the sample was re-oxidized by post-heating at 700 °C for 1 h. For the conventional sample, powders were uniaxially cold pressed at 200 MPa for 30 s, followed by sintering at 1450 °C in air for 10 h. To achieve high density in the pellets independently by the powders packing [39], the fast-fired sample was pre-densified by SPS at 900 °C and then thermally treated at 1450 °C for 0.1 h with 20 °C/min heating and cooling rate. Commercial tape (Kerafol Germany) was sintered at 1450 °C for 2.5 h.

### 2.3. Materials characterization

The density of the samples was measured in water using Archimedes method. The particle size and phase composition of the samples were analyzed by transmission electron microscope (TEM) (JEOL 2100, USA) and X-ray diffraction technique (XRD) (Bruker D8, Germany), respectively. The microstructure was investigated by a high-resolution scanning electron microscope (SEM) (Zeiss Merlin, Germany). The grain sizes were calculated by the linear intercept method using a minimum of 100 grains, multiplying with correction factor 1.57 [40]. The electrochemical impedance spectroscopy (EIS) was performed at 300–575 °C in air using Solarton 1260 (UK), in a frequency range of 0.01 Hz–1 MHz with a 100 mV alternate signal. The samples have bar-like geometry. Gold-silver mixture electrodes pastes were coated on top of the sample and dried at 600 °C for 15 min. Symmetric configuration using gold as electrodes, silver as current collectors and platinum wire as current leads were used. The EIS data were plotted using Real  $Z'$  and Imaginary  $Z''$  of the impedance normalized by the geometrical cell parameter  $k$  of each sample, where  $k = A/t$ ,  $A$  is the electrode area and  $t$  is the thickness. The resulting geometry normalized EIS plots are thus expressed as geometrically normalized Nyquist plots, i.e.  $\rho'$  vs  $\rho''$  (Cole-Cole plots), and as  $\rho''$  vs frequency plots (similar to Bode-plot). The latter related the relative dielectric constant,  $\epsilon_r = \frac{1}{-2 \cdot \pi \cdot f \cdot \rho''}$ , as a function of the AC electric field frequency ( $f$ ). The data were fitted by equivalent circuit and analyzed by ZView software shareware version. The electromechanical measurement was performed using a proximity sensor (Capacitance, Lion) based system with a lock-in detection, as previously reported in Refs. [12,15]. Prior to measurement, the system was calibrated with

PZT (Shenzhen Yuije Electronics Co. Ltd. China). The sample was pressed between two metal electrodes using a spring. A pushrod is used to transfer displacement from the electrodes to a proximity sensor. The signal from the proximity sensor is captured using a lock-in amplifier. Longitudinal electrostrictive strain (parallel to the applied electric field) is calculated as a ratio between the displacement and the original thickness of the ceramic pellets.

### 3. Results and discussion

Use of nano-powder in ceramic processing allows fine control of the microstructural features in final bulk materials. The morphology and structure of the starting nano-powder used in this work are shown in Fig. 1. TEM analysis revealed that particles have a spherical shape and are loosely agglomerated. The nano-powders have a narrow range of size distribution with an average particle size ranging between 10–15 nm. Electron diffraction pattern shows fluorite symmetry of ceria. Crystallography was further confirmed by X-Ray diffraction technique.

Fig. 2 illustrates the XRD pattern of GDC powder and sintered samples. Within the detection threshold of the technique, the patterns reveal no secondary phases. The reflection peaks of the pattern perfectly fit with the theoretical pattern (ICSD code 251473). Average crystallite size by Scherrer and lattice parameter for the starting powders are estimated as  $\approx 12$  nm and 0.540 nm, respectively. Results are consistent with the TEM analysis in Fig. 1. For the sintered samples, XRD patterns in Fig. 2 also display identical results. Narrow peaks imply an increase of particle size during sintering, according to the Scherrer formula [41].

The microstructures of sintered GDC samples are presented in Fig. 3. The micrographs indicate that grains are highly dense with negligible intra-granular porosity. The outcome is consistent with the experimental density of the pellets, which is above  $\geq 96\%$ , for all samples. Grain size analysis shows that both the SPS and fast firing sample have a significantly smaller grain size (around 150–200 nm) than conventionally sintered materials. They exhibit typical polygonal grains with nearly homogeneous size distribution. Furthermore, they show no surface relaxation at the grain boundary. Plapcianu et al. found similar results in SPS sintering of GDC [37]. These authors stated that restricted grain growth in this type of non-conventional sintering is attributed to fast heating rates especially in the initial stage of sintering, where grain-

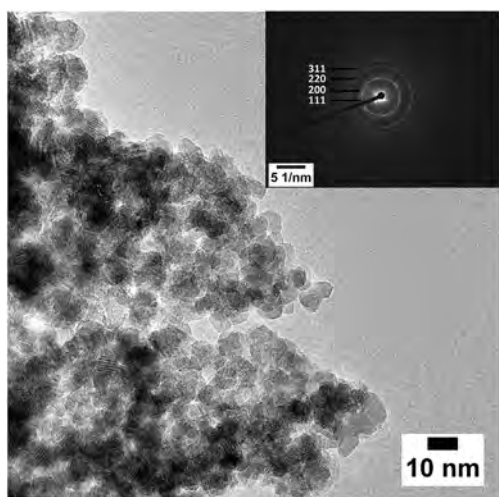


Fig. 1. Bright field TEM images of GDC powder, calcined at 500 °C for 2 h. Inset shows the selective area electron diffraction (SAED) pattern of it.

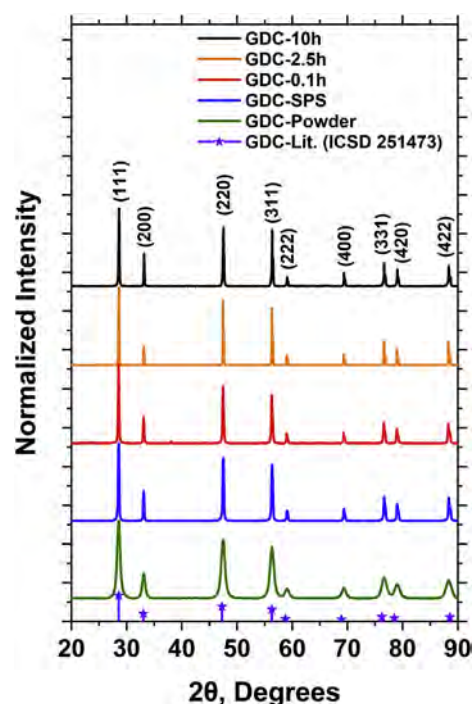


Fig. 2. XRD pattern of gadolinium doped ceria (GDC) powder and sintered pellets.

coarsening mechanism dominates. However, GDC-10 h and GDC-2.5 h materials show a high degree of grain growth with an average grain size of  $2.0 \pm 0.3 \mu\text{m}$  and  $1.5 \pm 0.2 \mu\text{m}$ , respectively. Nearly all grains have equilibrium shape at the triple point (red lines in Fig. 3c, 3d) with fully relaxed and residual small grain boundary curvature (see black arrows in Fig. 3c, 3d).

Fig. 4a and Fig. 4b illustrates the geometry normalized Nyquist plots ( $\rho'$  vs  $\rho''$ ) at 300 °C. The geometrical normalization is carried out for the total volume of the samples, to have a direct comparison between the materials, and it does not take into account the actual volume fraction of the grain boundary in the sample. These Nyquist spectra were fitted by using parallel equivalent circuits of RQ element. R is denoted as resistor and Q is termed as constant phase element, as  $C = (R^{1-n}Q)^{1/n}$ , where C is the capacitance and n is the fitting parameter. At this temperature, as evident from Fig. 4a, only one semicircle is observed in both the nanostructured GDC-SPS and GDC-0.1 h samples, which correspond to strongly overlapped bulk and grain boundary contribution, with capacitance representing the bulk value (see Table 1). Similar features were previously reported in other studies on nanocrystalline ceria materials, suggesting superimposed semicircle is predominated by grain boundary impedance [42,43]. Tuller et al. stated that such overlapping behavior is due to the similar order of magnitude between the space charge width and grain size [44]. Since deconvolution of bulk and grain boundary contribution from these samples is not possible and due to the typical frequency response, the single semicircle is attributed to the grain boundary. On the other hand, conventionally sintered microcrystalline GDC-10 h and GDC-2.5 h samples display two well-defined semi-circles (see Fig. 4b) that according to brick layer model, refer to the high and intermediate frequency associated bulk and grain boundary impedance, respectively [45]. The low frequency arc attributes to the electrode/material interface polarization mechanisms that are not relevant for this discussion [46]. Both GDC-10 h and GDC-2.5h samples exhibit a comparable bulk resistance, however, distinct grain boundary resistance is measured. The effect of grain boundary



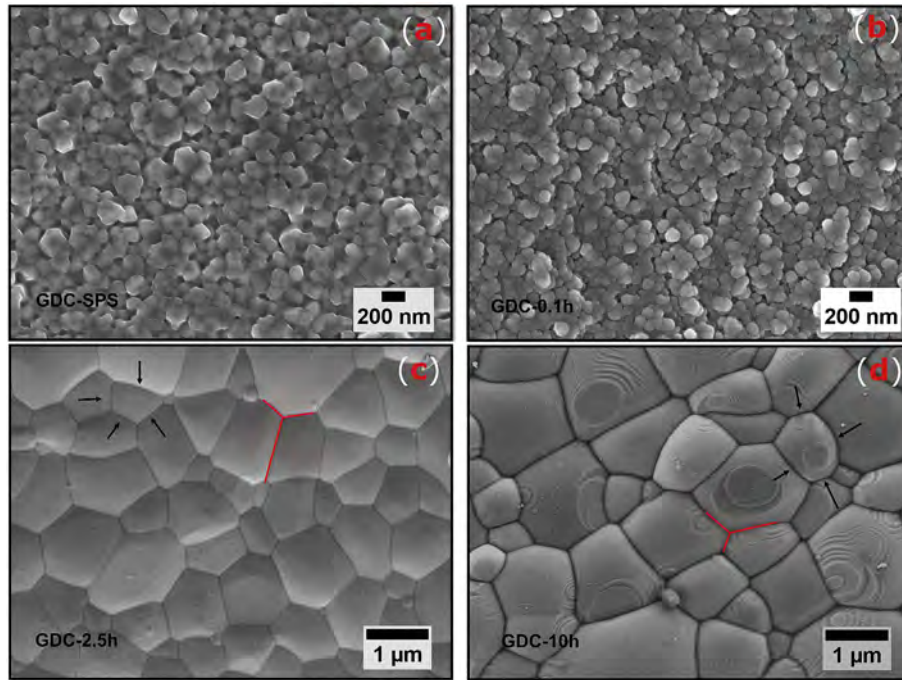


Fig. 3. SEM images of four different GDC samples, sintered in (a) SPS at 980 °C, 70 MPa (b) air at 1450 °C, for 0.1 h (c) air at 1450 °C, for 2.5 h (d) air at 1450 °C, for 10 h.

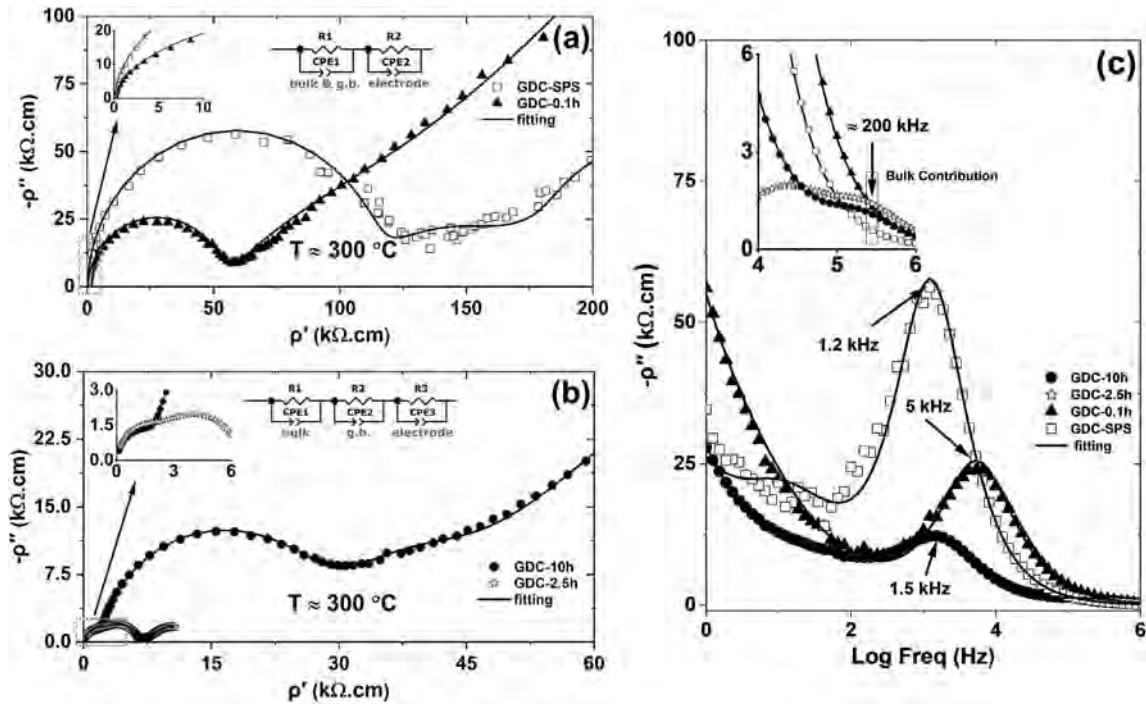


Fig. 4. Geometry normalized (a) Nyquist plot ( $p'$  vs  $p''$ ) of GDC-SPS and GDC-0.1 h samples, (b) Nyquist plot ( $p'$  vs  $p''$ ) of GDC-10 h and GDC-2.5 h samples, (c) imaginary  $p''$  vs log frequency (f) plots of all the GDC samples, measured at 300 °C.

resistance is characterized by the grain boundary blocking factor ( $\alpha_{gb}$ ), which is defined as the ratio of grain boundary resistance to the total resistance ( $\alpha_{gb} = \frac{R_{gb}}{R_{bulk} + R_{gb}}$ ) [47]. The grain boundary blocking factor ( $\alpha_{gb}$ ) is estimated as  $\approx 0.65$  and  $\approx 0.9$  for GDC-2.5 h and GDC-10 h at 300 °C, respectively. Comparing the microstructure, such behavior is unexpected as GDC-10 h has larger grain size, i.e. lower gb/grain geometrical ratio, than GDC-2.5 h sample.

Similar results were previously reported, where long-term thermal treatment, i.e. 36 h, possesses a detrimental effect on the blocking factors for low dopant concentration, e.g. for the conventional sintering for 10 h [3]. Furthermore, a significantly higher resistance in GDC-SPS compared to GDC-10 h indicates a field assisted trapping of oxygen vacancies in the lattice during SPS. High electric fields in SPS can result in a frozen non-equilibrium dopant



distribution, which could decrease the possible vacancy mobility in the nanometric polycrystalline materials. Moreover, one report suggests that the chemical reducing condition occurring during the SPS can also create a large number of  $\text{Ce}^{3+}$  species that remain confined at the grain boundary, even after long time re-oxidation [36], resulting in an increment of grain boundary space charge potential. As mentioned before, nanostructures in SPS create a high density of grain boundaries, which act as a high blocking barrier to charge migration [48,49]. Although having similar nanostructure like GDC-SPS, fast firing sample, i.e. GDC-0.1 h presents an intermediary behavior between GDC-SPS and GDC-10 h. To sum up, all the samples possess similar density and exactly same dopant concentration, however, they develop quite different grain boundary resistance (blocking barrier), an effect that is ascribed to dissimilar oxygen vacancy configurations. In a broader sense, various sintering mechanisms lead to govern unlike oxygen vacancy configurations in the material, as well as dissimilar ordering of vacancies and defect hopping probabilities, which could be attributed to the nature of solute drag effect due to various thermal treatments.

In Fig. 4c,  $\rho''$  vs frequency plots elucidate the distribution of charge transport by means of its relaxation frequency. Both GDC-10 h and GDC-2.5 h expose a bulk relaxation frequency around ~200 kHz, while, grain boundary relaxation frequency exhibits around 1.5 kHz and 20 kHz (data not shown here), respectively. Such a low grain boundary frequency response is attributed to high blocking barrier effect in the GDC-10 h compound. GDC-SPS and GDC-0.1 h show an overlapped relaxation frequency at 1.2 kHz and 5 kHz, respectively. This overlay behavior is ascribed to different charge transport mechanism, as resulting from unrelaxed microstructure and non-equilibrium fast thermal treatment. Above all, comparative analysis of high frequency response (see inset Fig. 4c) suggests that possible bulk relaxation behavior of GDC-0.1 h is equivalent to GDC-10 h sample, while GDC-SPS show very limited response.

Table 1 summarizes the capacitance, relaxation frequency values of the samples at 300 °C, along with average grain size. These values are calculated from the constant phase element with the 1/RC relationship from the fitted plots.

The temperature dependence of the total electrical conductivities ( $\sigma = 1/\rho'$ ), i.e. bulk plus grain boundary is illustrated with an Arrhenius plot in Fig. 5a. As anticipated and observed, conventionally sintered microcrystalline samples display superior electrical conductivity than non-conventional nanocrystalline materials. Additionally, it is worth mentioning that at high doping content such as 10 mol% Gd, electronic conductivity is negligible at atmospheric pressure [50], therefore it can be assumed that total electrical conductivity (bulk and grain boundary) in air is solely controlled by the migration/mobility of  $\text{V}_\text{O}^\bullet$ . GDC-2.5 h displays highest electrical conductivity among all of them, whereas, GDC-SPS reveals the minimum, which is directly interlinked with activation energy values. The high activation energy in GDC-SPS is also consistent with the existence of a large density of blocking barrier illustrated in Fig. 4, an effect conceivably caused by vacancy

trapping or/and vacancy clustering mechanisms. The minimum activation energy observed in GDC-2.5 h could be of different grain boundary composition (uniform dopant distribution) due to short thermal treatment. GDC-0.1 h shows similar conductivity of previous work (see Fig. 5a), however, as expected, GDC-10 h sample displays much higher conductivity than GDC-36 h [3]. At the same time, Fig. 5b distinguishes between bulk and grain boundary conductivity for GDC-10 h and GDC-2.5 h samples. In this case, the resistivity of the two contributions is normalized by the actual volume of bulk and grain boundaries, as reported in Ref. [50]. According to expectations, microcrystalline samples show a similar trend in bulk conductivity. A significant difference is determined in grain boundary conductivity value, which is linked to the grain boundary blocking factor. Low grain boundary conductivity in GDC-10 h also confirms that oxygen vacancy at the grain boundary is less mobile than GDC-2.5 h sample. The most substantial result is that measured ionic conductivity of GDC-0.1 h lies in between grain boundary conductivity of GDC-10 h and GDC-2.5 h samples, at these temperatures range. This outcome further presupposes that grain boundary blocking factor ( $\alpha_\text{gb}$ ) in GDC-0.1 h sample might be in between 0.65 and 0.9. Additionally, it supports the hypothesize that the conduction mechanism in nanocrystalline ceria is ruled by grain boundary blocking factors.

The electrostrictive strain as a function of applied electric field square is presented in Fig. 6. All the compounds exhibit negative longitudinal strain that agrees with previous reports of GDC thin films and bulk materials [10,12]. They respond at the second harmonic of the applied electric field with different frequency within the applied range, further confirming its electrostriction behavior. Besides, the graph explains the following trends i.e. at low frequency, the strain saturates with increasing electric field amplitude, whereas with increasing frequency magnitude of strain value declines dramatically. The strain saturation behavior empirically fits the following equation:

$$u(E^2) = M_{33} \cdot E_{\text{sat}}^2 \cdot \left[ 1 - \exp\left(-E^2/E_{\text{sat}}^2\right) \right] \quad (1)$$

Where  $M_{33}$  is the electrostriction 3-3 strain coefficient and  $E_{\text{sat}}$  is the saturation electric field. Beyond the saturation point, the linear relationship between electrostriction strain vs  $E^2$  is no longer valid. At certain electric field and frequency, GDC-10 h shows maximum electrostrictive strain among all the samples, which has a high bulk and low grain boundary relaxation frequency (see Fig. 4c). Surprisingly, GDC-2.5 h, with low blocking barriers, exhibits  $M_{33}$  value much smaller than GDC-10 h. Furthermore, it does not show any strain saturation behavior, and strain linearly increases with  $E^2$ . The reason for this effect could be of high grain boundary conductivity, which leads to a marginal voltage drop at bulk grain. On the other hand, being nanostructured and having higher blocking effect compared to GDC-2.5 h sample, GDC-0.1 h generates much higher electrostriction than counterpart does. The most surprising result is observed with GDC-SPS sample. The electromechanical response of this sample is significantly lower compared to others, for instance, electrostrictive strain coefficient ( $M_{33}$ ) value being one order of magnitude lower than GDC-10 h. The small value of the former is not due to its unrelaxed grain size but connected to trapped ionic/electronic defects-cation association and its interaction with the electric field. These defect-complexes are neutral and do not respond at low electric fields, suggesting super blocking behavior at the grain boundary.

This significantly highlights the flexibility of the blocking barrier in tuning the electrostrictive strain. For high electrostriction, the barriers should block oxygen vacancy migration without meaningfully decreasing the potential drop and vacancy should resonate

**Table 1**  
Grain size, capacitance and relaxation frequency response of the samples.

Sample ID	$C_{\text{total}}$ (F)	$f_{\text{total}}$ (Hz)	Grain Size (nm)		
GDC-SPS	$2.0 \times 10^{-11}$	$1.2 \times 10^3$	$200 \pm 25$		
GDC-0.1 h	$3.5 \times 10^{-11}$	$5.0 \times 10^3$	$170 \pm 20$		
	$C_{\text{Bulk}}$ (F)	$C_{\text{G.B.}}$ (F)	$f_{\text{Bulk}}$ (Hz)	$f_{\text{G.B.}}$ (Hz)	Grain Size ( $\mu\text{m}$ )
GDC-10 h	$1.2 \times 10^{-11}$	$3.0 \times 10^{-10}$	$2.0 \times 10^5$	$1.5 \times 10^3$	$2.0 \pm 0.3$
GDC-2.5 h	$2.9 \times 10^{-11}$	$4.0 \times 10^{-10}$	$2.0 \times 10^5$	$2.0 \times 10^4$	$1.5 \pm 0.2$

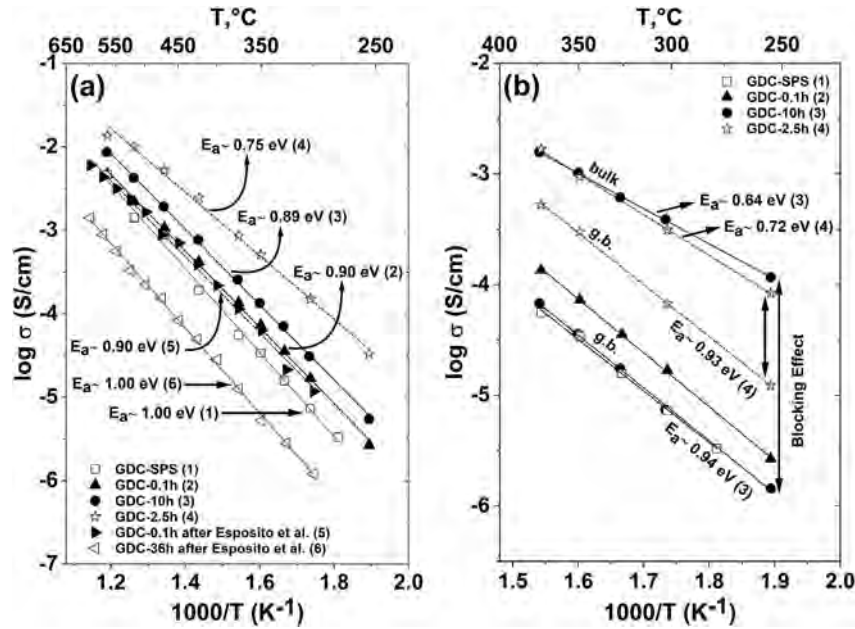


Fig. 5. Arrhenius plot (a) for the estimation of total electrical conductivities of the samples, results are compared with the literature [3], (b) for the bulk and grain boundary conductivities of conventionally sintered GDC-10 h and GDC-2.5 h samples; entire experiments are carried out in air.

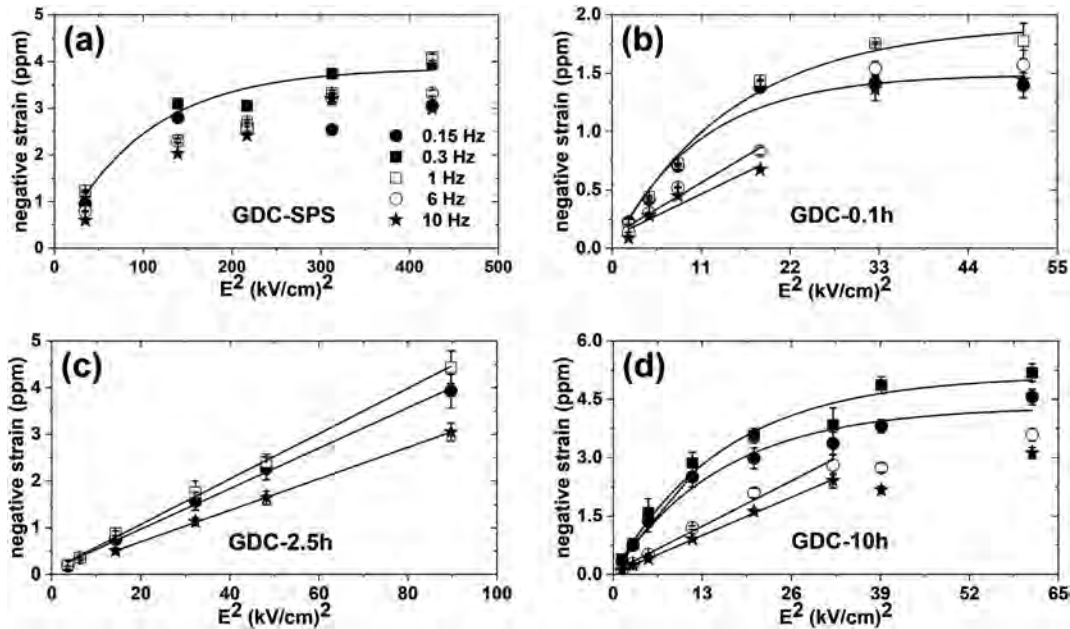


Fig. 6. Electrostrictive negative strain as a function of applied electric field square at frequencies 0.15–10 Hz, showing strain saturation behavior at a lower frequency.

within the lattice, as per the model described by Lubomirsky et al. [16].

Fig. 7 demonstrates the declining trend of electrostrictive strain coefficient ( $M_{33}$ ) with increasing frequency. This type of electrostriction relaxation with frequency can be fitted by (non-ideal-Debye) following function:

$$M_{33}(f) = \frac{M_{33}^0}{\sqrt{1 + (\tau \cdot f)^{2+\alpha}}} + M_{33}^\infty \quad (2)$$

Here,  $M_{33}^0$  and  $M_{33}^\infty$  are frequency independent electrostriction coefficient,  $\tau$  is the relaxation time and  $\alpha$  is denoted as a non-

ideality factor. Both the saturation and relaxation phenomena are observed in the recent publication of Yavo et al. [12], specifying that both mechanisms are intrinsic properties of electromechanical behavior of gadolinium doped ceria. Moreover,  $M_{33}$  values are approximately in order of  $\geq 10^{-18}$  (m/V)<sup>2</sup> at 10 Hz for all the samples, which are still one order of magnitude higher than the classical electrostriction model.

Table 2 describes the comparative analysis of grain boundary resistivity and electrostriction coefficient among the samples. Finally, by correlating experimental findings, it can be concluded that electrostriction in GDC materials increases with grain boundary blocking factor up to a certain level (below super blocking

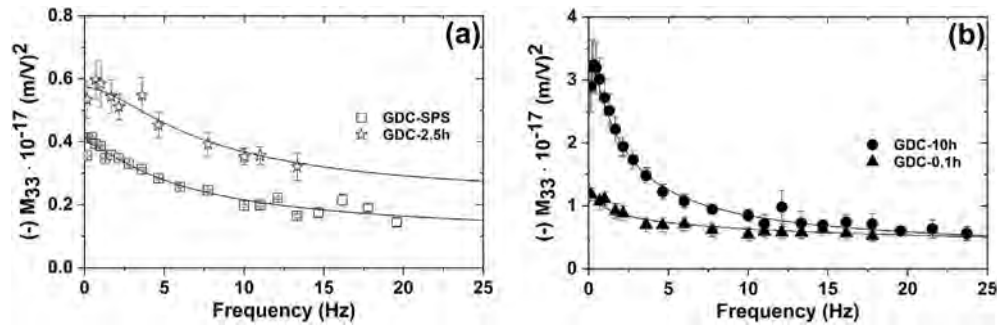


Fig. 7. Frequency dependent relaxation of electrostriction strain coefficient ( $M_{33}$ ), for conventional and non-conventional sintered samples, for frequencies  $0 < f < 25$  Hz.

Table 2

Comparative analysis of grain boundary resistivity and electrostriction coefficient between samples.

Material Properties	Nano size grain		Micron size grain	
	GDC-SPS	GDC-0.1 h	GDC-10 h	GDC-2.5 h
G.B. Resistivity ( $\approx 300$ °C) [ $\Omega\cdot\text{cm}$ ]	$\sim 100000$	$\sim 50000$	$\sim 30000$	$\sim 3500$
Electrostriction ( $\approx 1$ Hz) ( $\text{m}/\text{V}^2$ )	$0.4 \times 10^{-17}$	$1.0 \times 10^{-17}$	$2.8 \times 10^{-17}$	$0.6 \times 10^{-17}$

**Nano size grain**

Highly blocking

GDC-SPS

**Micron size grain**

Intermediate blocking

GDC-0.1h   GDC-10h

Nominally blocking

GDC-2.5h

region) and then decreases dramatically. The effect of blocking in electrostriction is also schematically presented in Table 2. The blocking diagram and the data strongly suggest that electrostriction is not dependent on the geometrical ratio between bulk and grain boundary. Microstructure does not necessarily influence the electromechanical properties. Additionally, it also confirms that the nominal oxygen vacancy concentration is not a true parameter that controls electrostriction. In conclusion, it is the blocking barrier at the grain boundaries, which regulates the electrostrictive properties. The blocking barrier is tuned by the configuration of oxygen vacancy within the grain boundary. Despite more uniform oxygen vacancy distribution, both GDC-SPS and GDC-0.1 h materials show considerably limited electromechanical activity compared to GDC-10 h with a low density of large blocking barriers. These results finally conclude the dominant distribution of oxygen defect configuration to the electromechanical properties.

#### 4. Conclusion

In this work, highly dense GDC ceramic pellets were fabricated by both non-conventional and conventional sintering methods. Non-conventional sintering was performed by SPS and fast firing to achieve similar nanometric microstructures with tuned oxygen vacancy configurations, with the same nominal oxygen vacancy concentration. The resulting polycrystalline materials exhibit unrelaxed microstructure with nano-grains, while the samples sintered in conventional method exhibits equilibrium grain of micron size. Surprisingly, electro-chemo-mechanical properties of the samples did not follow a mere geometrical grain size dependency. They show a strict dependency on ionic migration blocking barriers

built in the materials by the different sintering processes. Furthermore, all the compounds show non-classical giant electrostriction with a strong dependency on the frequency and electric field amplitude. Above all, it was observed that sample with high bulk and low grain boundary relaxation frequency exhibits large electrostrictive coefficient, which is further related to the distribution of oxygen vacancies. In summary, the oxygen defects configuration rather than their nominal concentration in the bulk controls the electromechanical behavior in Gd-doped ceria.

#### Acknowledgements

This research was supported by DFF-Research project grants from the Danish Council for Independent Research, Technology and Production Sciences, June 2016, grant number 48293 (GIANT-E) and the European H2020-FETOPEN-2016-2017 project BioWings, grant number 801267. The authors would like to thank Massimo Rosa for assistance in TEM.

#### References

- [1] H.L. Tuller, A.S. Nowick, Doped ceria as a solid oxide electrolyte, *J. Electrochem. Soc.* 122 (1975) 255–259.
- [2] H. Inaba, H. Tagawa, Ceria-based solid electrolytes, *Solid State Ionics* 83 (1996) 1–16.
- [3] V. Esposito, E. Traversa, Design of electroceramics for solid oxides fuel cell applications: playing with ceria, *J. Am. Ceram. Soc.* 91 (2008) 1037–1051.
- [4] M. Mogensen, N.M. Sammes, G.A. Tompsett, Physical, chemical and electrochemical properties of pure and doped ceria, *Solid State Ionics* 129 (2000) 63–94.
- [5] S.R. Bishop, T.S. Stefanik, H.L. Tuller, “Electrical conductivity and defect equilibria of  $\text{Pr}_{0.1}\text{Ce}_{0.9}\text{O}_{2-\delta}$ ”, *Phys. Chem. Chem. Phys.* 13 (2011) 10165–10173.
- [6] D. Pérez-Coll, D. Marrero-López, P. Núñez, S. Piñol, J.R. Frade, Grain boundary

- conductivity of  $\text{Ce}_{0.8}\text{Ln}_{0.2}\text{O}_{2-\delta}$  ceramics (Ln = Y, La, Gd, Sm) with and without Co-doping, *Electrochim. Acta* 51 (2006) 6463–6469.
- [7] A. Arabaci, Effect of Sm and Gd dopants on structural characteristics and ionic conductivity of ceria, *Ceram. Int.* 41 (2015) 5836–5842.
  - [8] H.L. Tuller, A.S. Nowick, Small polaron electron transport in reduced  $\text{CeO}_2$  single crystals, *J. Phys. Chem. Solids* 38 (1977) 859–867.
  - [9] T.S. Stefanik, H.L. Tuller, Nonstoichiometry and defect chemistry in praseodymium-cerium oxide, *J. Electroceram.* 13 (2004) 799–803.
  - [10] R. Korobko, A. Patlolla, A. Kossoy, E. Wachtel, H.L. Tuller, A.I. Frenkel, I. Lubomirsky, Giant electrostriction in Gd-doped ceria, *Adv. Mater.* 24 (2012) 5857–5861.
  - [11] M. Hadad, H. Ashraf, G. Mohanty, C. Sandu, P. Muralt, Key-features in processing and microstructure for achieving giant electrostriction in gadolinium doped ceria thin films, *Acta Mater.* 118 (2016) 1–7.
  - [12] N. Yavo, O. Yehekel, E. Wachtel, D. Ehre, A.I. Frenkel, I. Lubomirsky, Relaxation and saturation of electrostriction in 10 mol% Gd-doped ceria ceramics, *Acta Mater.* 144 (2018) 411–418.
  - [13] V. Shelukhin, I. Zon, E. Wachtel, Y. Feldman, I. Lubomirsky, Low temperature dielectric properties of  $\text{Ce}_{0.8}\text{Gd}_{0.2}\text{O}_{1.9}$  films, *Solid State Ionics* 211 (2012) 12–19.
  - [14] R.E. Newnham, V. Sundar, R. Yimnirun, J. Su, Q.M. Zhang, “Electrostriction, Nonlinear electromechanical coupling in solid dielectrics, *J. Phys. Chem. B* 101 (1997) 10141–10150.
  - [15] N. Yavo, A.D. Smith, O. Yehekel, S. Cohen, R. Korobko, E. Eachtel, P.R. Slater, I. Lubomirsky, Large nonclassical electrostriction in (Y, Nb)-stabilized  $\delta\text{-Bi}_2\text{O}_3$ , *Adv. Funct. Mater.* 26 (2016) 1138–1142.
  - [16] Y. Li, O. Kraynis, J. Kas, T. Weng, D. Sokaras, R. Zacharowich, I. Lubomirsky, A.I. Frenkel, Geometry of electromechanically active structures in Gadolinium - doped Cerium oxides, *AIP Adv.* 6 (2016), 055320–7.
  - [17] A.S. Nowick, B.S. Berry, J.L. Katz, Anelastic relaxation in crystalline solids, *J. Appl. Mech.* 42 (1975) 750.
  - [18] S.K. Kim, S. Khodorov, C.T. Chen, S. Kim, I. Lubomirsky, How to interpret current-voltage relationships of blocking grain boundaries in oxygen ionic conductors, *Phys. Chem. Chem. Phys.* 15 (2013) 8716–8721.
  - [19] S. Kim, S.K. Kim, S. Khodorov, J. Maier, I. Lubomirsky, On determining the height of the potential barrier at grain boundaries in ion-conducting oxides, *Phys. Chem. Chem. Phys.* 18 (2016) 3023–3031.
  - [20] A.D. Ushakov, E. Mishuk, E. Makagon, D.O. Alikin, A.A. Esin, I.S. Baturin, A. Tselev, V.Y. Shur, I. Lubomirsky, A.L. Kholkin, Electromechanical properties of electrostrictive  $\text{CeO}_2\text{:Gd}$  membranes: effects of frequency and temperature, *Appl. Phys. Lett.* 110 (2017) 142902–142904.
  - [21] P.L. Chen, I.W. Chen, Grain growth in  $\text{CeO}_2$ : dopant effects, defect mechanism, and solute drag, *J. Am. Ceram. Soc.* 79 (1996) 1793–1800.
  - [22] P.L. Chen, I.W. Chen, Role of defect interaction in boundary mobility and cation diffusivity of  $\text{CeO}_2$ , *J. Am. Ceram. Soc.* 77 (1994) 2289–2297.
  - [23] V. Esposito, D.W. Ni, Z. He, W. Zhang, A.S. Prasad, J.A. Glasscock, C. Chatzichristodoulou, S. Ramousse, A. Kaier, Enhanced mass diffusion phenomena in highly defective doped ceria, *Acta Mater.* 61 (2013) 6290–6300.
  - [24] D.W. Ni, D.Z. de Florio, D. Marani, A. Kaiser, V.B. Tinti, V. Esposito, Effect of chemical redox on Gd-doped ceria mass diffusion, *J. Mater. Chem.* 3 (2015) 18835–18838.
  - [25] F. Teocoli, D.W. Ni, S. Sanna, K. Thyden, F.C. Fonseca, V. Esposito, Fast mass interdiffusion in ceria/alumina composite, *J. Mater. Chem.* 3 (2015) 17135–17143.
  - [26] D.W. Ni, J.A. Glasscock, A. Pons, W. Zhang, A. Prasad, S. Sanna, N. Pryds, V. Esposito, Densification of highly defective ceria by high temperature controlled re-oxidation, *J. Electrochem. Soc.* 161 (2014), F3072–F3078.
  - [27] B. Feng, N.R. Lugg, A. Kumamoto, Y. Ikuhara, N. Shibata, Direct observation of oxygen vacancy distribution across Yttria-Stabilized Zirconia grain boundaries, *ACS Nano* 11 (2017) 11376–11382.
  - [28] D.V. Quach, S. Kim, R.A. De Souza, M. Martin, Z.A. Munir, Grain size effect in the electrical properties of nanostructured functional oxides through pressure modification of the spark plasma sintering method, *Key Eng. Mater.* 484 (2011) 107–116.
  - [29] X. Guo, R. Waser, Electrical properties of the grain boundaries of oxygen ion conductors: acceptor-doped zirconia and ceria, *Prog. Mater. Sci.* 51 (2016) 151–210.
  - [30] X. Guo, J. Maier, Grain boundary blocking effect in zirconia: a Schottky barrier analysis, *J. Electrochem. Soc.* 148 (2001) E121.
  - [31] S. Kim, J. Fleig, J. Maier, Space charge conduction: simple analytical solutions for ionic and mixed conductors and application to nanocrystalline ceria, *Phys. Chem. Chem. Phys.* 5 (2003) 2268–2273.
  - [32] J. Maier, Ionic conduction in space charge regions, *Prog. Solid State Chem.* 23 (1995) 171–263.
  - [33] X. Guo, W. Sigle, J.U. Fleig, J. Maier, Role of space charge in the grain boundary blocking effect in doped zirconia, *Solid State Ionics* 154–155 (2002) 555–561.
  - [34] S. Kim, J. Fleig, J. Maier, Space charge conduction: simple analytical solutions for ionic and mixed conductors and application to nanocrystalline ceria, *Phys. Chem. Chem. Phys.* 5 (2003) 2268–2273.
  - [35] J. Fleig, The grain boundary impedance of random microstructures: numerical simulations and implications for the analysis of experimental data, *Solid State Ionics* 150 (2002) 181–193.
  - [36] U. Anselmi-Tamburini, F. Magila, G. Chiodelli, A. Tacca, G. Spinolo, P. Riello, S. Bucella, Z.A. Munir, Nanoscale effects on the ionic conductivity of highly doped bulk nanometric cerium oxide, *Adv. Funct. Mater.* 16 (2006) 2363–2368.
  - [37] C. Plapcianu, C. Valsangiacom, J.E. Schaffer, A. Wieg, J. Garay, L. Stanciu, Spark plasma sintering studies of nanosize lanthanidoped ceria obtained by sol-gel method, *J. Optoelectron. Adv. Mater.* 13 (2011) 1101–1108.
  - [38] O. Guillon, J.G. Julian, B. Dargatz, T. Kessel, G. Schiering, J. Raethel, M. Herrmann, Field-assisted sintering technology/spark plasma sintering: mechanisms, materials, and technology developments, *Adv. Eng. Mater.* 16 (2014) 830–849.
  - [39] J.A. Glasscock, V. Esposito, S.P.V. Foghmoes, T. Stegk, D. Matuschek, M.W.H. Ley, S. Ramousse, The effect of forming stresses on the sintering of ultra-fine  $\text{Ce}_{0.9}\text{Gd}_{0.1}\text{O}_{2-\delta}$  powders, *J. Eur. Ceram. Soc.* 33 (2013) 1289–1296.
  - [40] M.I. Mendelson, Average grain size in polycrystalline ceramics, *J. Am. Ceram. Soc.* 52 (1969) 443–446.
  - [41] A.L. Patterson, The scherrer formula for X-ray particle size determination, *Phys. Rev.* 56 (1939) 978–982.
  - [42] M.C. Göbel, G. Gregori, J. Maier, Electronically blocking grain boundaries in donor doped cerium dioxide, *Solid State Ionics* 215 (2012) 45–51.
  - [43] G. Gregori, B. Rahmati, W. Sigle, P.A. Van Aken, J. Maier, Electric conduction properties of boron-doped ceria, *Solid State Ionics* 192 (2011) 65–69.
  - [44] H.L. Tuller, Ionic conduction in nanocrystalline materials, *Solid State Ionics* 131 (2000) 143–157.
  - [45] X. Guo, S. Mi, R. Waser, Nonlinear electrical properties of grain boundaries in oxygen ion conductors: acceptor-doped ceria, *Electrochem. Solid State Lett.* 8 (2004) J1.
  - [46] D.Z. de Florio, R. Muccillo, V. Esposito, E. Di Bartolomeo, E. Traversa, Preparation and electrochemical characterization of Perovskite/YSZ ceramic films, *J. Electrochem. Soc.* 152 (2004) A88.
  - [47] K. Neuhaus, R. Dolle, H.-D. Wiemhöfer, Assessment of the effect of transition metal oxide addition on the conductivity of commercial Gd-Doped Ceria, *J. Electrochem. Soc.* 165 (2018), F533–F542.
  - [48] A. Hara, Y. Hirata, S. Sameshima, N. Matsunaga, T. Horita, Grain size dependence of electrical properties of Gd-doped ceria, *J. Ceram. Soc. Japan* 116 (2008) 291–297.
  - [49] E.C.C. Souza, W.C. Chueh, W. Jung, E.N.S. Muccillo, S.M. Haile, Ionic and electronic conductivity of nanostructured Samaria-doped ceria, *J. Electrochem. Soc.* 159 (2012) K127.
  - [50] M.G. Bellino, D.G. Lamas, N.E.W. De Reca, Enhanced ionic conductivity in nanostructured heavily doped ceria ceramics, *Adv. Funct. Mater.* 16 (2006) 107–113.



## Electrostriction in ceria through controlled orientation

*Simone Santucci\**, *Haiwu Zhang*, *Simone Sanna*, *Nini Pryds*, *Vincenzo Esposito\**

S. Santucci, Dr. H. Zhang, Dr. S. Sanna, Prof. N. Pryds, Prof. V. Esposito

Department of Energy Conversion and Storage, Technical University of Denmark, Fysikvej, Building 310, 2800 Kgs. Lyngby, Denmark.

E-mail: [sisan@dtu.dk](mailto:sisan@dtu.dk), [vies@dtu.dk](mailto:vies@dtu.dk)

Keywords: electrostriction, cerium oxide, defective oxides, piezoelectricity, MEMS

Gd-doped ceria fluorites (CGO) is one of the most promising materials as new generation electrostrictors, thanks to a *facile* integration on silicon and superior performances to the *state-of-the-art* electrostrictors such as  $\text{Pb}(\text{Mn}_{1/3}\text{Nb}_{2/3})\text{O}_3$ . The current structural model indicates that  $[111]$  direction promotes high atomic distortion and thus results in the largest electrostriction response. For this reason, only out-of-plane electrostriction (i.e.  $M_{13}$ ) in  $(111)$  CGO oriented thin films has been reported so far. The open question is still whether other crystallographic directions show higher electrostriction value. Here, we are able to measure the longitudinal and shear deformations (i.e.  $M_{11}$  and  $M_{12}$ ) of epitaxial  $(100)$ ,  $(110)$  and  $(111)$  oriented CGO thin films for the first time. We present electromechanical performances along with different crystallographic directions and we find an order of magnitude higher electrostrictive coefficient along  $[100]$ . Moreover, a new insight into the mechanism of CGO electrostriction is provided using a new structural model.

## 1. Introduction:

Ceria-based materials have been used in a wide range of applications such as solid oxide fuel cells (SOFCs) [1–3], oxygen sensors [3,4] and storage[5], catalysts [5–7] and memristors [8–10]. Ceria oxide, i.e.  $\text{CeO}_{2-\delta}$ , is capable of accommodating a high amount of oxygen vacancies ( $\text{V}_\text{O}^{\bullet\bullet}$ ) into the lattice, which results in a remarkable versatility as ionic conductor and catalyst [11–13]. At temperatures superior to 1200 °C [14] and low oxygen partial pressure ( $p_{\text{O}_2} \approx 2.5 \times 10^{-3}$  atm) [15], ceria undergoes a chemical reduction of  $\text{Ce}^{4+}$  to  $\text{Ce}^{3+}$  releasing oxygen gas and consequently increasing the defects concentration,  $\delta = [\text{V}_\text{O}^{\bullet\bullet}]$  [5,16]. Acceptor doping, *e.g.* by substitutional rare-earth cations with a 3+ valence state (*i.e.* Gd, Nd, Sm, La), stabilizes the structure and leads to high ionic mobility [2,7,17–21]. At room temperature, doped ceria showed outstanding electromechanical properties due to local distortion in the vicinity of oxygen vacancies [22]. Studies carried out on Gd-doped ceria (CGO) thin films [22–26], bulk [27,28] and membranes [29–31], show an average electrostriction coefficient of  $M_e \approx 6 \cdot 10^{-18}$  ( $\text{m}^2 \text{V}^{-2}$ ) [22], which is comparable to the *state-of-the-art* materials such as  $\text{Pb}(\text{Mn}_{1/3}\text{Nb}_{2/3})\text{O}_3$  ( $M_e = 2 \cdot 10^{-18} \text{ m}^2 \text{V}^{-2}$ ) [32]. For classical electrostrictors, Newnham *et al.* provided a relationship in which the logarithm of performances depends on  $(S/\epsilon)$ , with  $S$  elastic compliance and  $\epsilon$  dielectric constant [33]. However, Yavo *et al.* [34] showed that CGO electromechanical properties are conflicting with Newnham law, as it displays an electrostriction coefficient two-three orders of magnitude higher than similar materials with low dielectric constant ( $\epsilon_{\text{CGO}} \approx 28$ ) [35], meaning that a different electromechanical mechanism is in play. In the same study, they also showed high electrostriction in (Y, Nb)-stabilized  $\text{Bi}_2\text{O}_3$  bulk, suggesting that such features are common to some defective fluorite structures, representing a new family of electromechanical functional materials.

X-ray absorption spectroscopy (XAS) measurements on CGO attribute the electromechanical activity to the lattice distortion in the presence of oxygen vacancies [22,36,37]. Although the dopant has not an active role in the single lattice model [22,36], doping and vacancies association are able to influence the electrostriction in cerium oxide. In polycrystalline CGO, vacancies are mainly controlled by associations at the grain boundaries [38–40], which also act as ionic blocking barriers controlled by the dopant [17,38,41,42]. Under an electric field, if the grain boundaries of the material have high resistivity, the voltage at the materials drops with a consequent decrease of the overall electromechanical response [30]. However, grain size is not directly related to electrostriction performances [27] and our recent work shows that the electrostrictive behavior of polycrystalline CGO ceramics depends on the vacancy configurations within the grain boundaries. For these reasons, a grain boundaries-free (e.g. epitaxial) material is needed to have a clear insight of the sole lattice distortion effect.

To date, only the out-of-plane component of electrostriction i.e.  $M_{13}$  has been measured in thin films [23,43]. Here, we apply a top planar electrodes configuration which allows investigating the other electrostriction directions of the matrix i.e.  $M_{11}$ ,  $M_{12}$ . By varying the crystal orientation of the film, we are able to study the crystal distortion at different crystallographic directions.

**Fig. 1a** shows the structural model that previous studies used to explain the electrostriction mechanism [22,36,37]. When an oxygen vacancy  $V_O^{\bullet\bullet}$  is included in a CGO cell ( $Ce_{ce}7O_O-V_O^{\bullet\bullet}$ ), it causes the distortion of the unit, with a consequent rearrangement of the local elastic field and charge distribution. As formalized in previous works [36,37], the distortion takes place by elongation of the diagonal  $V_O^{\bullet\bullet} - Ce_{Ce} - O_O$  triplet (black vector) along the  $[111]$  direction. As a counter effect, the six oxygen atoms that do not belong to the triplet, i.e.  $6O$ , collapse toward the center (blue vectors). The resulting  $V_O^{\bullet\bullet}-Ce_{Ce}$

and  $Ce_{Ce}-O_O$  pairs along the diagonal have longer bonds and the rest  $Ce_{Ce}-6O_O$  pairs are shorter. Under the influence of electric field, the electroactive  $V_O^{\bullet\bullet}-Ce_{Ce}-O_O$  triplet shrinks and consequently it “squeezes out” the remaining six oxygen atoms in the perpendicular direction, yielding electrostriction. According to this interpretation, a field parallel to the  $[111]$  direction maximizes the electrostriction effect, as the most efficient way to induce strain of the  $V_O^{\bullet\bullet}-Ce_{Ce}-O_O$  triplets and consequently of oxygen atoms [22,26]. However, the current model considers only a single unit, neglecting the surrounding structure. Oxygen atoms in CGO lattice have a coordination number of 4, meaning that a single vacancy produces four  $Ce_{Ce}-7O-V_O^{\bullet\bullet}$  units. Fig. 1b shows a schematic illustration of the resulting complex. Under electric field, all four  $Ce_{Ce}-7O-V_O^{\bullet\bullet}$  units rearrange simultaneously. Particularly, six oxygen atoms (numbered in Fig. 1b) are bonded to two cations each as illustrated for atom 1 and 2 (red lines). With an applied field, the 6O are expected to strongly contribute to the lattice distortion as they withstand the force of two  $V_O^{\bullet\bullet}-Ce_{Ce}-O_O$  triplets at once. Moreover, they are the closest oxygen atoms to the  $V_O^{\bullet\bullet}$  site, which is the center of the local elastic field and the center of the charge distribution distortion. Such a large range arrangement is illustrated in Fig. 1c that also highlights as a model the overall arrangement of the 6O atoms, represented as a regular octahedron centered on the  $V_O^{\bullet\bullet}$  site.

A similar octahedron microscopic structural model was also used to describe the effect of local distortion induced by an electric field in  $ABO_3$  perovskites, where oxygen atoms dispose as an octahedron with a centered B-ion that induces stress [44–46]. For piezoelectric perovskites, Li et al. [45,46] also showed a trend of the distortion magnitude as a function of the electric field with respect to the crystalline directions. Such an analysis shows that an electric field parallel to  $\langle 100 \rangle$  allows oxygen to release the stress imposed by the cation easily along the octahedron axis, favoring atomic distortion. By comparison, the displacement along the  $\langle 110 \rangle$  directions results in an overall counteracting of the



surrounding leading to a decreased electromechanical response. In the same way,  $\langle 111 \rangle$  directions shows an even weaker distortion effect [45,46]. On the other hand, the trend is the opposite for fluorite structures such as  $\text{CaF}_2$  [45].

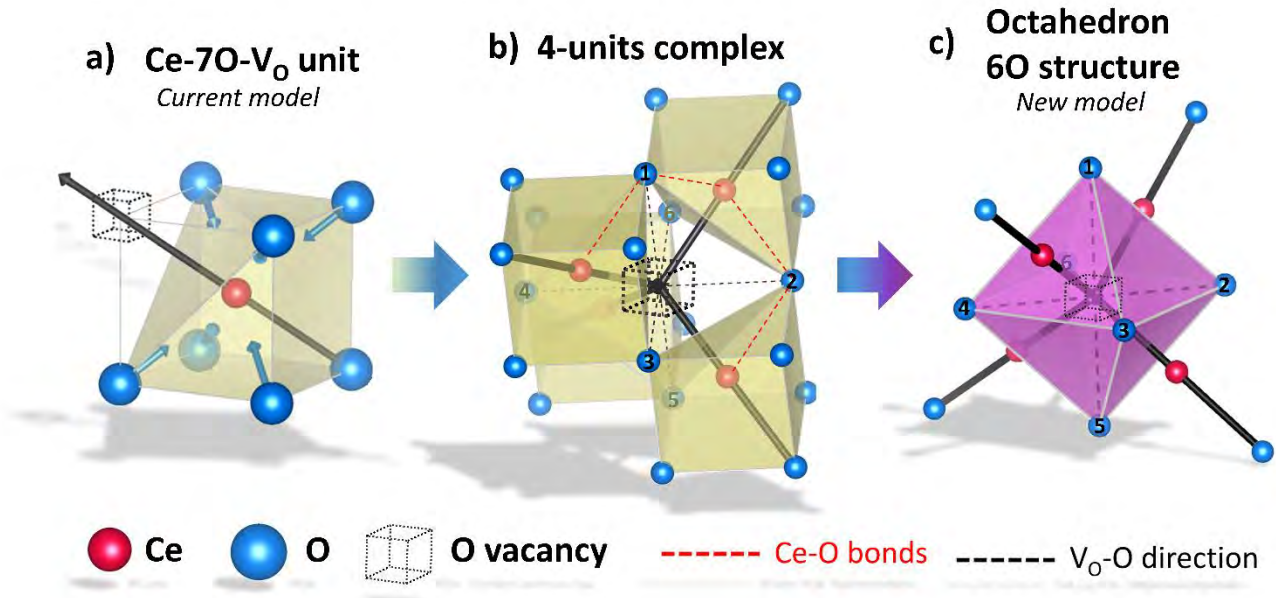


**Fig. 1.** Vacancy neighbor structure of  $\text{CeO}_2$  and related structures. a)  $\text{Ce}_{\text{ce}}\text{-7O-}V_{\text{O}}^{\bullet\bullet}$  unit, structure of the current model for electrostriction in CGO. Black vector:  $V_{\text{O}}^{\bullet\bullet}$  -  $\text{Ce}_{\text{ce}}$  -  $\text{O}_{\text{O}}$  electroactive triplet and distortion direction. Blue vectors: consequent 6O displacement b) 4-units complex composed of four  $\text{Ce}_{\text{ce}}\text{-7O-}V_{\text{O}}^{\bullet\bullet}$  distorted units with central vacancy. Near-empty site oxygen atoms, *i.e.* 6O, are numbered. Red lines highlight the bond direction of Ce atoms with oxygen 1 and 2. c) 6O octahedron structure composed of six near-empty site oxygen atoms, base structure for our new model.

In this work, we use pulsed laser deposition (PLD) technique to grow (100)-, (110)-, and (111)-oriented CGO epitaxial thin films on (100)-oriented  $\text{SrTiO}_3$  (STO) [2,47], (110) YSZ [47,48] and (100)  $\text{NdGaO}_3$  (NGO) [47,49,50] respectively. To study the electrostriction effect we analyze both the longitudinal ( $M_{11}$ ) and the shear ( $M_{12}$ ) responses of the films as a function of the crystallographic orientation and

the direction of the electric field. We then compare the experimental results with the microscopic model based on  $\text{ABO}_3$  octahedron applied to CGO, providing thus a new insight on the electrostrictive mechanics in the defective fluorite structure.

## **2. Experimental:**

### *2.1 Film and electrodes deposition:*

$\text{Ce}_{0.8}\text{Gd}_{0.2}\text{O}_{1.9}$  target is fabricated from powder pressed at 140 MPa and then sintered at 1723 K for 10 h. XRD investigation indicates a pure fluorite phase of the target. 1  $\mu\text{m}$  thick films of  $\text{Ce}_{0.8}\text{Gd}_{0.2}\text{O}_{1.9}$  are grown on  $\text{STO}_{(100)}$ ,  $\text{NGO}_{(100)}$  and  $\text{YSZ}_{(110)}$  substrates by PLD using a KrF the excimer laser ( $\lambda = 248$  nm), at 20 Hz repetition rate, 120 mJ energy and fluency of about  $1.8 \text{ J cm}^{-2}$  (deposition rate was  $\sim 0.07$  Å/pulse). During the deposition, the background oxygen pressure is fixed at  $10^{-3}$  mbar, with a temperature of 600 °C. Au top electrodes are sputtered with a Bal-Tec SCD 005 Sputter Coater at room temperature. The substrates size was 5 x 2.5 mm and 0.1 mm thick.

### *2.2 Structural characterization:*

the crystallographic properties of the grown samples are analyzed using X-ray diffraction with a Rigaku Smartlab diffractometer.  $\theta$ -2 $\theta$  and rocking curve scans are carried out and the crystalline quality of the film was established by evaluating the full-width-half-maximum (FWHM). Grazing incident angle scans with  $\alpha = 1^\circ$  were performed on CGO/NGO to exclude the reflection of the substrate, as (100) NGO and (200) CGO reflection overlap at  $\approx 33^\circ$  and confirm the correct (111) orientation of the film. The cross section of the samples was analyzed with a Zeiss Gemini-Merlin FE-SEM for microstructure and thickness measurements.

### *2.3 Electrostriction setup:*

The electromechanical characterization is carried out on a one-side clamped cantilever, with a single-beam laser interferometer SIOS NA analyzer. The experimental setup is described in detail elsewhere [23]. The instrument resolution is 5 pm, but the background noise is usually higher and it is not possible to observe displacements smaller than 3-4 nm. In order to increase the resolution of the setup, the interferometer is coupled with an Ametek 7230 DSP Lock-in Amplifier. Since lock-in detection spots only periodically signal with a specific set frequency, the measured response is not affected by mechanical drift or external noises. The environmental noise then is reduced to values around 0.1-0.2 nm that are used as error bars in our measurements. An AIM-TTI TGP 3100 function generator connected with a Trek 2220 amplifier, are used to apply a sinusoidal electric field to the samples. The contacts are made with tungsten tips. Oscillation in electrostrictive materials always takes place with double of the frequency of applied field, for this reason the source generator and the lock-in amplifier were set at 0.5 Hz and 1 Hz respectively, so the displacement measured in this work is always related to the II harmonic contribution to the oscillation amplitude.

#### *2.4 Electrostriction coefficients calculation:*

A planar electrodes configuration allows to stimulate the film in the in-plane directions to measure both longitudinal (*i.e.*  $M_{11}$ ) and transverse ( $M_{12}$ ) electrostriction coefficients. The longitudinal electrostriction effect is evaluated by measuring the vertical displacement  $d$  of the cantilever depending on the applied electric field. The curvature  $\Delta k$  and stress are then calculated with the method reported elsewhere [23]. The value of  $M_{11}$  is obtained using a linear fit of stress versus squared field, following the equation:

$$M = \frac{\sigma}{E^2 \cdot Y}$$

where  $Y$  is Young's modulus of CGO (200 GPa) [23]. In order to evaluate shear electrostriction coefficient  $M_{12}$ , the vertical displacement  $d$  is measured along the sample electrode width (see Fig. 2) of about 1-2 mm. A second order polynomial fit is used to obtain the trend. The curvature of the parabolic profile of the displacement is then calculated with the equation:

$$\Delta k = \frac{2a}{(1 + (2ay + b)^2)^{3/2}} \quad 2$$

Considering  $d = ay^2 + by + c$ , with  $z$  vertical displacement and  $y$  width position. The lowest curvature radius in the parabola is considered. Stress is calculated with the procedure previously described [23] and then  $M_{12}$  is obtained through Equation 1.

In order to exclude the thermal contribution to the oscillation, an Optris PI thermal camera with a sensitivity of 0.1 mK is used to detect potential temperature differences. However, no heating is observed. We use the current monitor of Trek voltage amplifier during the application of the electric field. The current is always below the resolution of the instrument ( $< 3\mu\text{A}$ ). High electric fields can cause other effects such as polarization or electrostatic force (*i.e.* Maxwell stress tensor), so the bare substrates were characterized by the same method, followed by subtraction of their contributions. The characterization of substrates is reported in the supplementary information.

The applied electric field is considered constant along the vertical direction as the thickness of the sample is low compared to the in-plane size of the sample. This is a widely accepted approximation in planar impedance spectroscopy experiments [2,12,16,51]. Also, it is not possible to deposit the

electrodes before CGO, as the spread of gold particles on the substrates would decrease dramatically the quality of the epitaxial films.

### 3. Result and discussion:

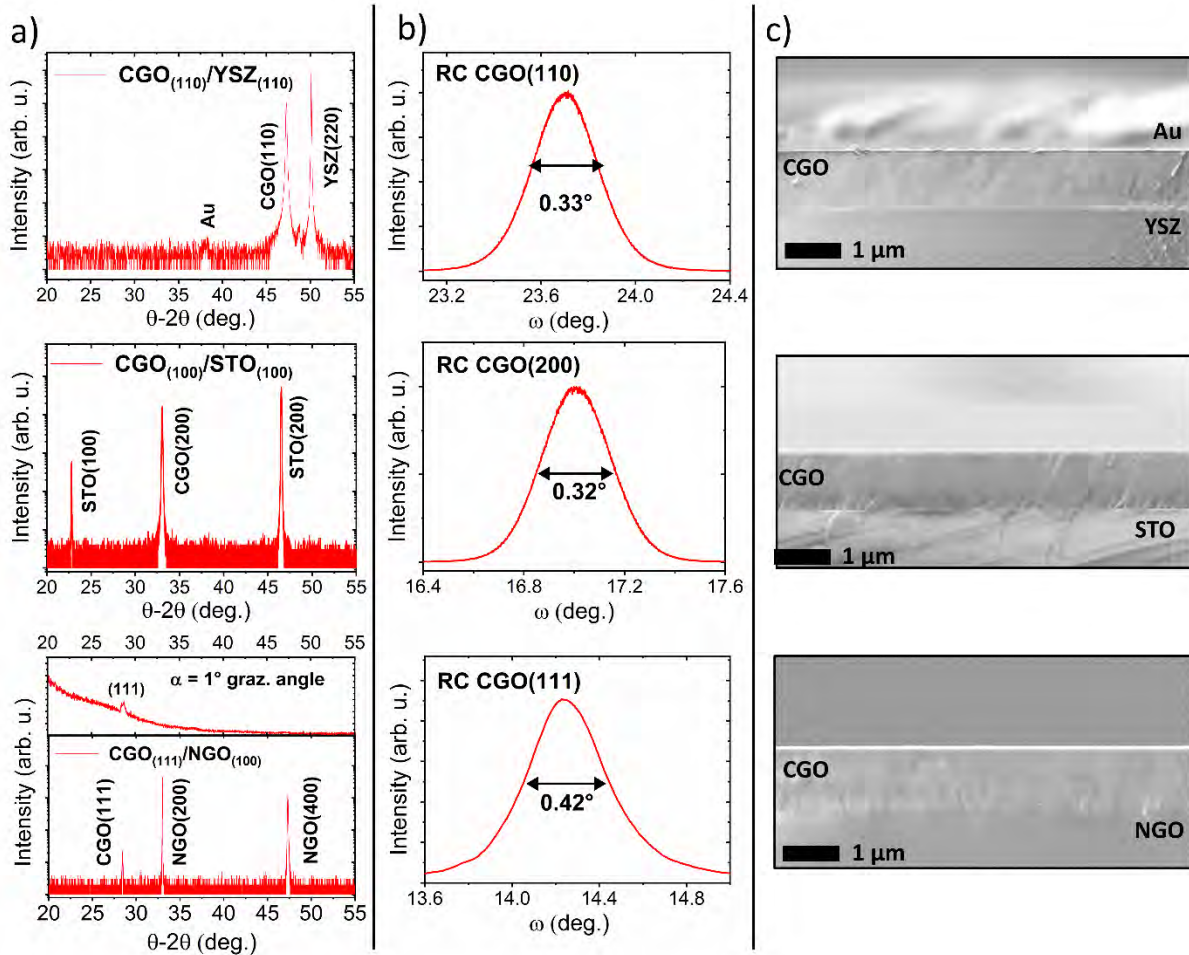


**Fig. 2.** Structural characterization of CGO<sub>(111)</sub>/NGO<sub>(100)</sub>, CGO<sub>(100)</sub>/STO<sub>(100)</sub> and CGO<sub>(110)</sub>/YSZ<sub>(110)</sub> thin films. a)  $\theta$ -2 $\theta$  scans of CGO<sub>(110)</sub>/YSZ<sub>(110)</sub> at the top, CGO<sub>(100)</sub>/STO<sub>(100)</sub> and CGO<sub>(111)</sub>/NGO<sub>(100)</sub> at the bottom. *Inset:*  $\theta$ -2 $\theta$  scan in grazing angle mode. b) rocking curve at (220) peak of CGO on YSZ, (200) peak of CGO on STO and (111) peak of CGO on NGO. c) cross section images by SEM: from the top CGO<sub>(110)</sub>/YSZ<sub>(110)</sub>, CGO<sub>(100)</sub>/STO<sub>(100)</sub> and CGO<sub>(111)</sub>/NGO<sub>(100)</sub>.

Highly coherent CGO thin films are deposited on several single crystal substrates. **Fig. 2** shows the results of both the structural characterization, i.e. XRD pattern in  $\theta$ - $2\theta$  scan mode, rocking curve and the microstructure of the samples thin films by scanning electron microscope (SEM) images. Depending on the orientation of the substrates, the films are grown in a single orientation, i.e. CGO<sub>(110)</sub>/YSZ<sub>(110)</sub>, CGO<sub>(100)</sub>/STO<sub>(100)</sub> and CGO<sub>(111)</sub>/NGO<sub>(100)</sub> (Fig. 2a). The inset of CGO<sub>(111)</sub>/NGO<sub>(100)</sub> plot shows a grazing angle scan to exclude the presence of CGO (200). For the CGO<sub>(200)</sub>/STO<sub>(100)</sub>, the cubic cell aligns along the [110] direction of the STO substrate and grows 45° in-plane tilted (Fig. S2) [2]. Fig. 2b shows the rocking curve scans of CGO<sub>(111)</sub>/NGO<sub>(100)</sub>, CGO<sub>(100)</sub>/STO<sub>(100)</sub> and CGO<sub>(110)</sub>/YSZ<sub>(110)</sub> with FWHM values of 0.42°, 0.32°, and 0.33° respectively. Such low values indicate a high order of crystallinity. The cross section of films (Fig. 2c) also shows a homogenous and continuous microstructure without the signature of vertical grain boundaries, i.e. columnar grains. The samples are grown to a thickness of 1 μm and the lattice parameter of the CGO, as determined from the XRD, indicates that the structures are fully relaxed.

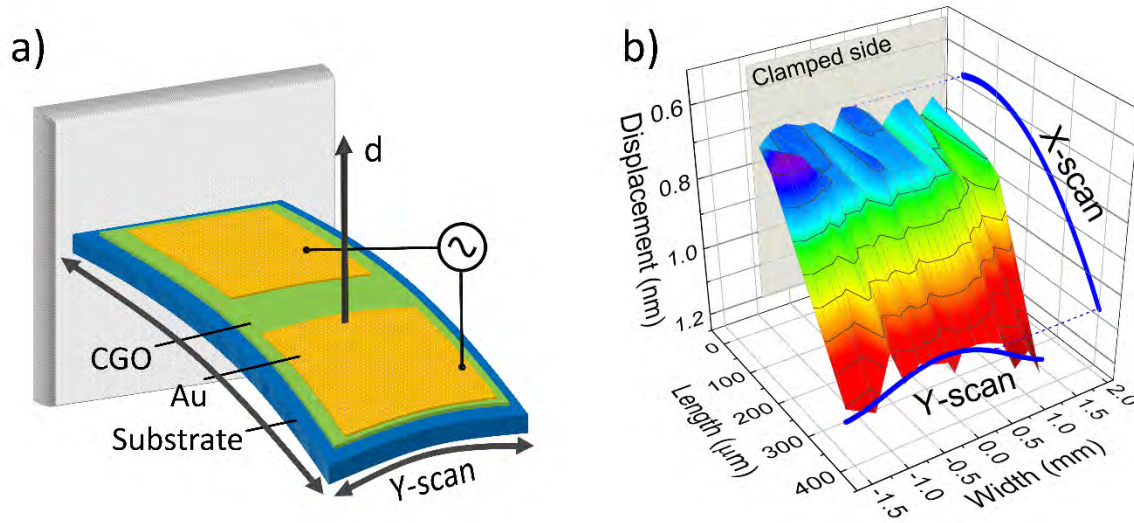


**Fig. 3.** Cantilever beam geometry and operation. *a)* Schematic of the samples. The vertical displacement  $d$  is measured while applying voltage to the planar gold electrodes.  $M_{11}$  is calculated measuring  $d$  while increasing the electric field,  $M_{12}$  is calculated by shear scans along the width of the sample (Y-scan). *b)* Deformation map of CGO film, for 16 kV/cm applied field with 1 Hz frequency. The distortion takes place both along the length (X-scan) and the width (Y-scan).

For the electromechanical performances, we measure the longitudinal  $M_{11}$  and the transverse  $M_{12}$  electrostriction coefficients using cantilever vibration method (described elsewhere) [23] using in-plane top electrodes. **Fig. 3a** shows a schematic illustration of the measurement setup. Note that counter electrodes configuration cannot be used here as metal electrodes at the bottom impair a loss of film coherency. In  $\text{CGO}_{(111)}/\text{NGO}_{(100)}$ , we apply electric field along  $[-211]$  and  $[0-11]$  directions by “tilting” the position of electrodes by  $90^\circ$ . In the same way,  $\text{CGO}_{(110)}/\text{YSZ}_{(110)}$  has  $[001]$  and  $[-223]$  in-plane directions with a  $45^\circ$  angle, as also depicted in the supplementary information, Fig. S1-3. **Fig. 3b** shows a typical map of the 2nd harmonic component of vertical displacement  $d$  in different positions on the sample. The X-scans and Y-scans indicate a distortion both parallel and perpendicular to the electric field, respectively. To measure the longitudinal electrostriction coefficient  $M_{11}$ , we measure the displacement  $d$  in a fixed position for different electric fields. The scans along the width of the sample (Y-scans) allow evaluating the shear component  $M_{12}$  (see the experimental section for details). **Fig. 4** shows the electromechanical response of CGO thin films for both longitudinal and shear directions. The corresponding geometry of 6O octahedron is also displayed with electric field and vertical directions (Fig. 4c, f, i, n). **Fig. 4a** shows the performances of  $\text{CGO}_{(110)}/\text{YSZ}_{(110)}$  in response to electric field along  $[001]$  direction. The longitudinal electrostriction coefficient is found to be  $M_{11} = 4.93 \cdot 10^{-17} \text{ m}^2\text{V}^{-2}$ . **Fig. 4d, 4g** shows the response of  $\text{CGO}_{(100)}/\text{STO}_{(100)}$  and  $\text{CGO}_{(111)}/\text{NGO}_{(100)}$  to the electric field along  $[110]$  direction with a longitudinal electrostriction coefficient of  $2.22 \cdot 10^{-17} \text{ m}^2\text{V}^{-2}$  and  $3.50 \cdot 10^{-18}$

$\text{m}^2\text{V}^{-2}$ , respectively. As illustrated in Fig. 4I, the electric field in  $\text{CGO}_{(111)}/\text{NGO}_{(100)}$  sample with  $90^\circ$  tilted in-plane electrodes is along  $[-211]$  direction with an  $M_{11} = 2.03 \cdot 10^{-18} \text{ m}^2\text{V}^{-2}$ . In  $\text{CGO}_{(110)}/\text{YSZ}_{(110)}$  with  $45^\circ$  tilted electrodes, the electric field is aligned along the  $[-223]$  direction. Interestingly, along such a direction the electrostriction is annihilated and the oscillations are so weak to be comparable with the background noise. Therefore, we cannot calculate the electrostriction coefficient and we report it as noise minimal value  $M_{11} = <6.72 \cdot 10^{-19} \text{ m}^2\text{V}^{-2}$ .



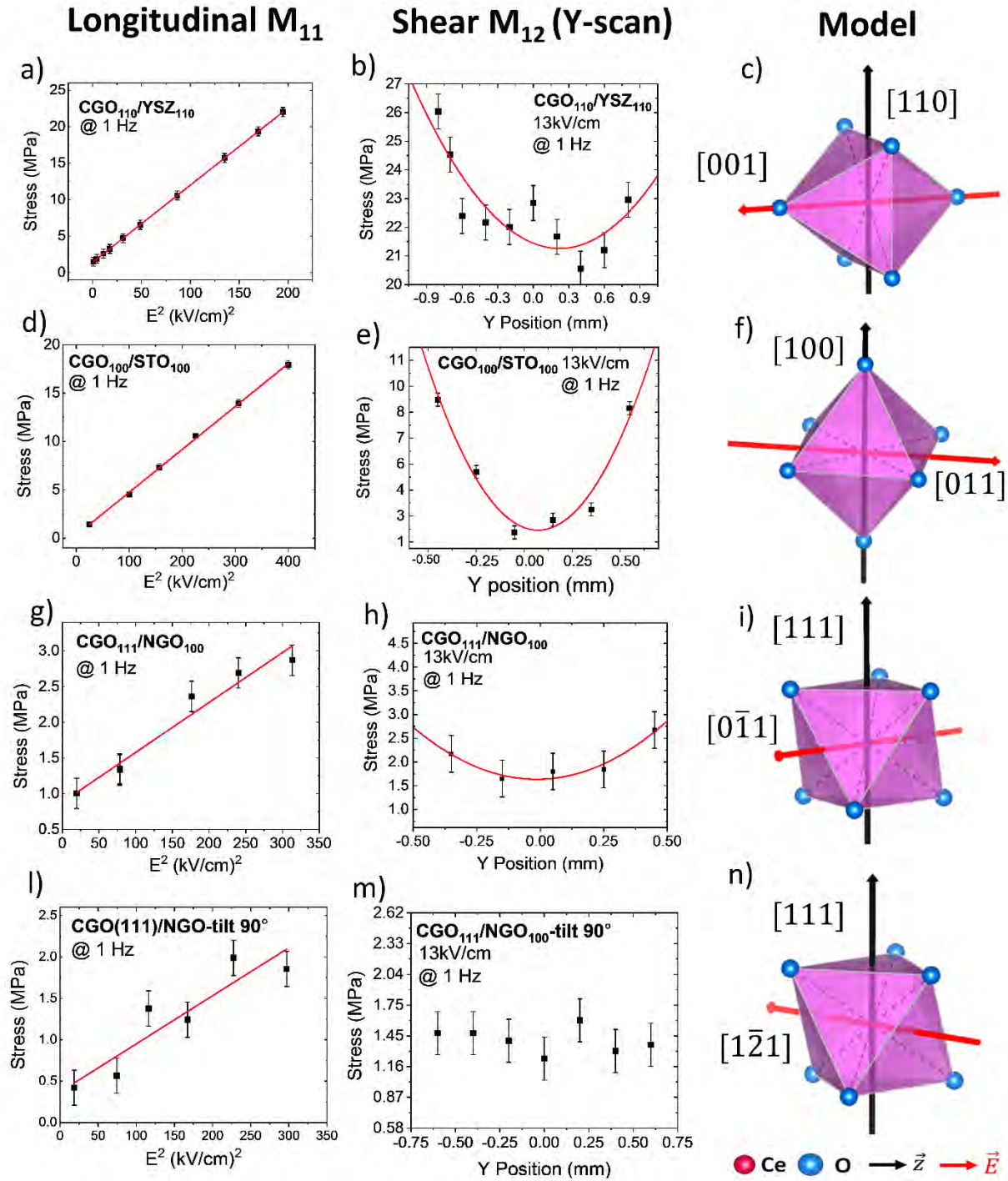


**Fig. 4.** Electromechanical response of CGO thin films for different orientations and electric field direction, II harmonic of oscillation @ 1 Hz. First row: CGO (110) oriented on YSZ with electric field along [001] axis. b) Longitudinal stress vs electric field,  $M_{11}$ , c) Y-scan of displacement. d) Octahedron model geometry with direction of electric field (red arrow) and

crystal orientation (black arrow) displayed. Second row: CGO (100) on STO with  $\vec{E} \parallel [011]$ . *e)* Longitudinal stress, *f)* shear displacement and *g)* octahedron model. Third row: CGO (111) on NGO with  $\vec{E} \parallel [0-11]$ . *h)* Longitudinal stress, *i)* shear displacement and *l)* octahedron model. Fourth row: CGO (111) on NGO with  $\vec{E} \parallel [-211]$ . *m)* Longitudinal stress, *n)* shear displacement and *o)* octahedron model.

Fig. 4b, e, h, m shows the full Y-scans for  $M_{12}$  analysis as result of laser profilometry measurements. The transverse electrostriction coefficient represents the component of stress that is perpendicular with respect to the electric field. As the electrostriction effect takes place at both in- and out- of plane directions, we describe the crystal distortion in terms of vertical and lateral directions. Fig. 4b shows the transverse electrostrictive response of  $\text{CGO}_{(110)}/\text{YSZ}_{(110)}$  with a measured value of  $M_{12} = 0.26 \cdot 10^{-17} \text{ m}^2\text{V}^{-2}$  considering the vertical ( $z$ ) and in-plane ( $y$ ) directions  $[110]_z / [-1-10]_y$ . On other hand, for the  $\text{CGO}_{(100)}/\text{STO}_{(100)}$  sample, the electrostriction coefficient is  $M_{12} = 0.79 \cdot 10^{-17} \text{ m}^2\text{V}^{-2}$  along  $[100]_z / [0-11]_y$  as depicted in Fig. 4e.  $\text{CGO}_{(111)}/\text{NGO}_{(100)}$  shows an electrostriction coefficient of  $M_{12} = 1.9 \cdot 10^{-18}$  for  $[111]_z / [-211]_y$  directions. Finally,  $90^\circ$  tilted  $\text{CGO}_{(111)}/\text{NGO}_{(100)}$  with  $[111]_z / [-101]_y$  perpendicular directions does not show a clear parabolic profile along Y.

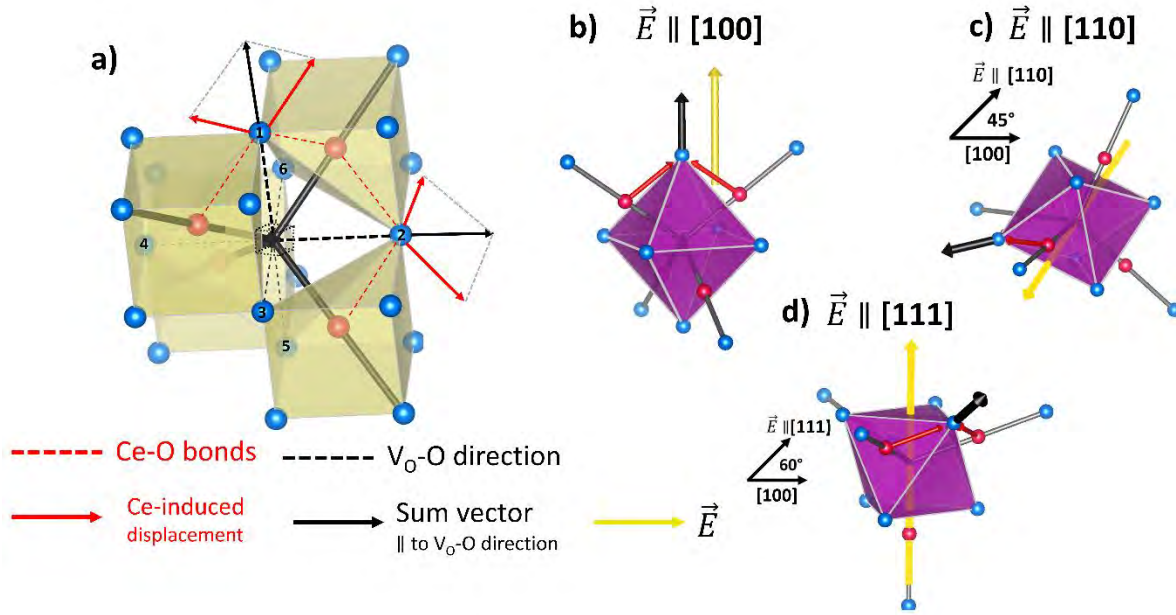


**Fig. 5.** Microscopic interpretation of CGO electrostriction in  $V_O^{\bullet\bullet}$  neighborhood lattice. *a)* 4-units complex with  $V_O^{\bullet\bullet}$  -  $Ce_{Ce}$  -  $O_O$  triplets imposed stress. *b)* Preferred direction in octahedron structure parallel with electric field along [100] direction. *c)* Preferred direction (black line) compared to induced stress with electric field (yellow line) along [110] with an angle of 45°. *d)* Preferred direction with electric field parallel to [111] with a 60° angle.

Our measurements deviate from the current structural model of the single cell described by Yavo *et al.* [22,36,37] which suggests that the distortion is favored if the electric field is along the [111] direction (see Fig. 1a). Conversely, the octahedron model shown in Fig. 1c supports our experimental results. Particularly, **Fig. 5a** shows that in the octahedron structure, each of the 6  $O$  atoms withstands a force imposed by two  $V_O^{\bullet\bullet}$  -  $Ce_{Ce}$  -  $O_O$  triplets along their preferential direction, as depicted for atoms 1 and 2 (red arrows). Considering both forces, the resulting preferred direction is parallel with [100] (black lines), corresponding with the octahedron axis. We approximate the stress to have the same intensity for all triplets. As a result, when an electric field is aligned with the  $\langle 100 \rangle$  directions, the atomic

displacement is maximized because it is parallel to the favored distortion directions (Fig. 5b). When the field is applied along a non-preferential direction, the distortion decreases as the angle respect to the preferred direction increases. In particular,  $\langle 110 \rangle$  and  $\langle 111 \rangle$  directions have an angle  $45^\circ$  and  $60^\circ$  respectively (Fig. 5c, d). Again, the same relation between distortion magnitude and crystal direction is found in the microscopic model for  $\text{ABO}_3$  perovskites [44–46]. In summary, CGO electrostriction can be described by an “*octahedron model*”, *i.e.* distortion of 6O atoms octahedron with central  $\text{V}_\text{O}^{\bullet\bullet}$ , in which the electroactive forces are mediated by the  $\text{V}_\text{O}^{\bullet\bullet} - \text{Ce}_{\text{Ce}} - \text{O}_\text{O}$  triplets. The preferential directions of atomic distortion are along  $\langle 100 \rangle$ , followed by  $\langle 110 \rangle$  and then  $\langle 111 \rangle$ , with the electromechanical performances following this trend. Interestingly, these results suggest that the geometric properties of CGO electrostriction are similar to perovskite structures rather than regular fluorites such as  $\text{CaF}_2$ , which preferred distortion is along  $\langle 111 \rangle$  [45]. As the force applied from each triplet to one oxygen can be different, an asymmetric contribution to the overall distortion could take place. Moreover, a contribution from the oxygen atoms outside the octahedron can play an important role in the resulting electromechanical response. As we use the octahedron model to explain the electromechanical results, the  $M_{11}$  values follow the expected trend, with higher electromechanical performances for electric field along  $\langle 100 \rangle$  in  $\text{CGO}_{(110)}/\text{YSZ}_{(110)}$  sample, intermediate performances for  $\langle 110 \rangle$  directions in  $\text{CGO}_{(100)}/\text{STO}_{(100)}$  and lower performances for diagonal direction  $[-211]$  in  $\text{CGO}_{(111)}/\text{NGO}_{(100)}$ . The  $M_{12}$  values are considerably lower than longitudinal coefficients but, considering both in-plane ( $y$ ) and vertical ( $z$ ) directions, the performances of the samples consistently follow the trend expected from the model. **Tab. 1** summarizes the results for the longitudinal and the transverse electrostriction coefficients at different crystal directions. The  $\text{CGO}_{(100)}/\text{STO}_{(100)}$  sample in particular, despite having lower  $M_{11}$  compared to  $\text{CGO}_{(110)}/\text{YSZ}_{(110)}$ , shows an  $M_{12}$  value of about three times higher. In  $\text{CGO}_{100}/\text{STO}_{100}$  the out-of-plane distortion takes place along  $[100]_z$  which allows to release stress easily

compared to  $[110]_z$  direction in  $\text{CGO}_{110}/\text{YSZ}_{110}$ , resulting thus in a larger electrostriction coefficient. Remarkably, the  $M_{11}$  of the  $\text{CGO}_{(100)}/\text{STO}_{(100)}$  and  $\text{CGO}_{(111)}/\text{NGO}_{(100)}$  samples show a difference despite having the field applied along with directions of the same family:  $[011]$  and  $[0-11]$  respectively (Fig. 4f,h). This can be explained by assuming that the weaker transverse effect of  $\text{CGO}_{(111)}/\text{NGO}_{(100)}$  influences the longitudinal performances.

	ORIENTATION $\parallel \vec{E}$	LONGITUDINAL $M_{11} (m^2/V^2)$	ORIENTATION $\perp \vec{E}$	SHEAR $M_{12} (m^2/V^2)$
<b>CGO<sub>110</sub>/YSZ<sub>110</sub></b>	[001]	$4.93 \cdot 10^{-17}$	<sup>a)</sup> $[110]_z / [-1-10]_y$	$0.26 \cdot 10^{-17}$
<b>CGO<sub>100</sub>/STO<sub>100</sub></b>	[011]	$2.22 \cdot 10^{-17}$	$[100]_z / [01-1]_y$	$0.79 \cdot 10^{-17}$
<b>CGO<sub>111</sub>/NGO<sub>100</sub></b>	[0-11]	$3.50 \cdot 10^{-18}$	$[111]_z / [-211]_y$	$1.9 \cdot 10^{-18}$
<b>CGO<sub>111</sub>/NGO<sub>100</sub>*</b>	[-211]	$2.03 \cdot 10^{-18}$	$[111]_z / [-101]_y$	//
<b>CGO<sub>110</sub>/YSZ<sub>110</sub>**</b>	[-223]	$<6.72 \cdot 10^{-19}$	$[110]_z / [-33-4]_y$	//

\*90° tilted. \*\*45° tilted

**Tab. 1.** Longitudinal ( $M_{11}$ ) and shear ( $M_{12}$ ) electrostriction coefficient of CGO thin films depending on electric field direction and perpendicular orientation. <sup>a)</sup> ( $z$  and  $y$  denote the vertical and lateral orientation of the films, respectively).

#### 4. Conclusion:

In this work, we fabricate epitaxial CGO thin films with (100), (110) and (111) orientation. These films are electromechanical tested using a planar electrodes geometry at different electric field directions for both longitudinal ( $M_{11}$ ) and transverse ( $M_{12}$ ) directions. The electrostrictive performances depend on the crystalline direction of the film, showing a maximum value of  $M_{11} = 4.93 \cdot 10^{-17} \text{ m}^2\text{V}^{-2}$  along  $\langle 100 \rangle$  direction, followed by  $\langle 110 \rangle$  and then  $\langle 111 \rangle$ . To support the experimental results, we propose a microscopic model, based on the octahedron structure of oxygen atoms neighbor of a  $\text{V}_\text{O}^\bullet$  site. By such

an interpretation, we explain the reason for the performances trend in relation to crystal direction, giving a new insight of the microscopic mechanism behind electrostriction in CGO.

## **Supporting Information**

Supporting Information is available from the Wiley Online Library reporting substrate characterization.

## **Acknowledgments**

This research was supported by the Danish Council for Independent Research Technology and Production Sciences for the DFF- Research Project 2 (Grant No. 48293) and the BioWings project funded by the European Union's Horizon 2020, Future and Emerging Technologies (FET) programme (Grant No. 801267).

## **References:**

- [1] V. Esposito, E. Traversa, Design of electroceramics for solid oxides fuel cell applications: Playing with ceria, *J. Am. Ceram. Soc.* 91 (2008) 1037–1051. <https://doi.org/10.1111/j.1551-2916.2008.02347.x>.
- [2] S. Sanna, V. Esposito, D. Pergolesi, A. Orsini, A. Tebano, S. Licoccia, G. Balestrino, E. Traversa, Fabrication and electrochemical properties of epitaxial samarium-doped ceria films on SrTiO<sub>3</sub>-buffered MgO substrates, *Adv. Funct. Mater.* 19 (2009) 1713–1719. <https://doi.org/10.1002/adfm.200801768>.
- [3] C. Sun, H. Li, L. Chen, Nanostructured ceria-based materials: Synthesis, properties, and applications, *Energy Environ. Sci.* 5 (2012) 8475–8505. <https://doi.org/10.1039/c2ee22310d>.

- [4] P. Jasinski, T. Suzuki, H.U. Anderson, Nanocrystalline undoped ceria oxygen sensor, *Sensors Actuators, B Chem.* 95 (2003) 73–77. [https://doi.org/10.1016/S0925-4005\(03\)00407-6](https://doi.org/10.1016/S0925-4005(03)00407-6).
- [5] M. Kuhn, S.R. Bishop, J.L.M. Rupp, H.L. Tuller, Structural characterization and oxygen nonstoichiometry of ceria-zirconia ( $\text{Ce}_{1-x}\text{Zr}_x\text{O}_{2-\delta}$ ) solid solutions, *Acta Mater.* 61 (2013) 4277–4288. <https://doi.org/10.1016/j.actamat.2013.04.001>.
- [6] J. Kas, P. Fornasiero, M. Graziani, Use of  $\text{CeO}_2$ -based oxides in the three-way catalysis, *Catal. Today.* 50 (1999) 285–298. [papers3://publication/uuid/050378FF-922D-4D42-A3A9-DCE4FB80233B](https://doi.org/10.1016/S0925-4005(99)00033-8).
- [7] N. Yang, Y. Shi, S. Schweiger, E. Strelcov, A. Belianinov, V. Foglietti, P. Orgiani, G. Balestrino, S. V. Kalinin, J.L.M. Rupp, C. Aruta, Role of Associated Defects in Oxygen Ion Conduction and Surface Exchange Reaction for Epitaxial Samaria-Doped Ceria Thin Films as Catalytic Coatings, *ACS Appl. Mater. Interfaces.* 8 (2016) 14613–14621. <https://doi.org/10.1021/acsami.6b03909>.
- [8] A. Younis, D. Chu, X. Lin, J. Yi, F. Dang, S. Li, High-performance nanocomposite based memristor with controlled quantum dots as charge traps, *ACS Appl. Mater. Interfaces.* 5 (2013) 2249–2254. <https://doi.org/10.1021/am400168m>.
- [9] S. Schweiger, M. Kubicek, F. Messerschmitt, C. Murer, J.L.M. Rupp, A microdot multilayer oxide device: Let us tune the strain-ionic transport interaction, *ACS Nano.* 8 (2014) 5032–5048. <https://doi.org/10.1021/nn501128y>.
- [10] R. Schmitt, J. Spring, R. Korobko, J.L.M. Rupp, Design of Oxygen Vacancy Configuration for Memristive Systems, *ACS Nano.* 11 (2017) 8881–8891.

<https://doi.org/10.1021/acsnano.7b03116>.

- [11] N. Pryds, V. Esposito, When two become one: An insight into 2D conductive oxide interfaces, *J. Electroceramics*. 38 (2017) 1–23. <https://doi.org/10.1007/s10832-016-0051-0>.
- [12] K. Rodrigo, S. Heiroth, M. Lundberg, N. Bonanos, K. Mohan Kant, N. Pryds, L. Theil Kuhn, V. Esposito, S. Linderorth, J. Schou, T. Lippert, Electrical characterization of gadolinia-doped ceria films grown by pulsed laser deposition, *Appl. Phys. A Mater. Sci. Process.* 101 (2010) 601–607. <https://doi.org/10.1007/s00339-010-5975-7>.
- [13] K.M. Kant, V. Esposito, N. Pryds, Enhanced conductivity in pulsed laser deposited  $\text{Ce}_{0.9}\text{Gd}_{0.1}\text{O}_{2-\delta}/\text{SrTiO}_3$  heterostructures, *Appl. Phys. Lett.* 97 (2010) 5–8. <https://doi.org/10.1063/1.3497294>.
- [14] M. Melchionna, P. Fornasiero, The role of ceria-based nanostructured materials in energy applications, *Mater. Today*. 17 (2014) 349–357. <https://doi.org/10.1016/j.mattod.2014.05.005>.
- [15] S. Ackermann, A. Steinfeld, Diffusion of Oxygen in Ceria at Elevated Temperatures and Its Application to  $\text{H}_2\text{O}/\text{CO}_2$  Splitting Thermochemical Redox Cycles, *J. Phys. Chem.* (2014) 5216–5225. <https://doi.org/10.1021/jp500755t>.
- [16] I. Kosacki, T. Suzuki, V. Petrovsky, H.U. Anderson, Electrical conductivity of nanocrystalline ceria and zirconia thin films, *Solid State Ionics*. 136–137 (2000) 1225–1233. [https://doi.org/10.1016/S0167-2738\(00\)00591-9](https://doi.org/10.1016/S0167-2738(00)00591-9).
- [17] K. Mohan Kant, V. Esposito, N. Pryds, Strain induced ionic conductivity enhancement in epitaxial  $\text{Ce}_{0.9}\text{Gd}_{0.1}\text{O}_{2-\delta}$  thin films, *Appl. Phys. Lett.* 100 (2012). <https://doi.org/10.1063/1.3676659>.



- [18] S. Wang, T. Kobayashi, M. Dokiya, T. Hashimoto, Electrical and Ionic Conductivity of Gd-Doped Ceria, *J. Electrochem. Soc.* 147 (2000) 3606. <https://doi.org/10.1149/1.1393946>.
- [19] G. Baure, R.M. Kasse, N.G. Rudawski, J.C. Nino, Across plane ionic conductivity of highly oriented neodymium doped ceria thin films, *Phys. Chem. Chem. Phys.* 17 (2015) 12259–12264. <https://doi.org/10.1039/c5cp00668f>.
- [20] T.S. Stefanik, H.L. Tuller, Nonstoichiometry and defect chemistry in praseodymium-cerium oxide, *J. Electroceramics*. 13 (2004) 799–803. <https://doi.org/10.1007/s10832-004-5195-7>.
- [21] S.R. Bishop, T.S. Stefanik, H.L. Tuller, Electrical conductivity and defect equilibria of  $\text{Pr}_{0.1}\text{Ce}_{0.9}\text{O}_{2-\delta}$ , *Phys. Chem. Chem. Phys.* 13 (2011) 10165–10173. <https://doi.org/10.1039/c0cp02920c>.
- [22] R. Korobko, A. Patlolla, A. Kossoy, E. Wachtel, H.L. Tuller, A.I. Frenkel, I. Lubomirsky, Giant electrostriction in Gd-doped ceria, *Adv. Mater.* 24 (2012) 5857–5861. <https://doi.org/10.1002/adma.201202270>.
- [23] S. Santucci, H. Zhang, S. Sanna, N. Pryds, V. Esposito, Enhanced electro-mechanical coupling of  $\text{TiN/Ce}_{0.8}\text{Gd}_{0.2}\text{O}_{1.9}$  thin film electrostrictor, *APL Mater.* 7 (2019) 071104. <https://doi.org/10.1063/1.5091735>.
- [24] R. Korobko, E. Wachtel, I. Lubomirsky, Cantilever resonator based on the electrostriction effect in Gd-doped ceria, *Sensors Actuators, A Phys.* 201 (2013) 73–78. <https://doi.org/10.1016/j.sna.2013.06.021>.
- [25] A.D. Ushakov, N. Yavo, E. Mishuk, I. Lubomirsky, V.Y. Shur, A.L. Kholkin, Electromechanical Measurements Of Gd-Doped Ceria Thin Films By Laser Interferometry, *KnE*

Mater. Sci. 1 (2016) 177. <https://doi.org/10.18502/kms.v1i1.582>.

- [26] M. Hadad, H. Ashraf, G. Mohanty, C. Sandu, P. Muralt, Key-features in processing and microstructure for achieving giant electrostriction in gadolinium doped ceria thin films, *Acta Mater.* 118 (2016) 1–7. <https://doi.org/10.1016/j.actamat.2016.07.025>.
- [27] A. Kabir, S. Santucci, N. Van Nong, M. Varenik, I. Lubomirsky, R. Nigon, P. Muralt, V. Esposito, Effect of Oxygen Defects Blocking Barriers on Gadolinium Doped Ceria (GDC) Electro-Chemo-Mechanical Properties, *Acta Mater.* 174 (2019) 53–60. <https://doi.org/10.1016/j.actamat.2019.05.009>.
- [28] N. Yavo, O. Yeheskel, E. Wachtel, D. Ehre, A.I. Frenkel, I. Lubomirsky, Relaxation and saturation of electrostriction in 10 mol% Gd-doped ceria ceramics, *Acta Mater.* 144 (2018) 411–418. <https://doi.org/10.1016/j.actamat.2017.10.056>.
- [29] E. Mishuk, E. Makagon, E. Wachtel, S.R. Cohen, R. Popovitz-Biro, I. Lubomirsky, Self-supported Gd-doped ceria films for electromechanical actuation: Fabrication and testing, *Sensors Actuators, A Phys.* 264 (2017) 333–340. <https://doi.org/10.1016/j.sna.2017.07.047>.
- [30] A.D. Ushakov, E. Mishuk, E. Makagon, D.O. Alikin, A.A. Esin, I.S. Baturin, A. Tselev, V.Y. Shur, I. Lubomirsky, A.L. Kholkin, Electromechanical properties of electrostrictive  $\text{CeO}_2:\text{Gd}$  membranes: Effects of frequency and temperature, *Appl. Phys. Lett.* 110 (2017) 142902. <https://doi.org/10.1063/1.4979642>.
- [31] E. Mishuk, A.D. Ushakov, S.R. Cohen, V.Y. Shur, A.L. Kholkin, I. Lubomirsky, Built-in bias in Gd-doped ceria films and its implication for electromechanical actuation devices, *Solid State Ionics.* 327 (2018) 47–51. <https://doi.org/10.1016/j.ssi.2018.10.012>.

- [32] R.E.N. V. Sundar, J.-F. Li, D. Viehland, INTERFEROMETRIC EVALUATION OF ELECTROSTRICTION COEFFICIENTS, *Mater. Res. Bull.* 31 (1996) 555–563.
- [33] R.E. Newnham, V. Sundar, R. Yimnirun, J. Su, Q.M. Zhang, Electrostriction: Nonlinear Electromechanical Coupling in Solid Dielectrics, *J. Phys. Chem. B.* 101 (1997) 10141–10150. <https://doi.org/10.1021/jp971522c>.
- [34] N. Yavo, A.D. Smith, O. Yeheskel, S. Cohen, R. Korobko, E. Wachtel, P.R. Slater, I. Lubomirsky, Large Nonclassical Electrostriction in (Y, Nb)-Stabilized  $\delta$ -Bi<sub>2</sub>O<sub>3</sub>, *Adv. Funct. Mater.* 26 (2016) 1138–1142. <https://doi.org/10.1002/adfm.201503942>.
- [35] S. Kim, J. Maier, On the Conductivity Mechanism of Nanocrystalline Ceria, *J. Electrochem. Soc.* 149 (2002) J73. <https://doi.org/10.1149/1.1507597>.
- [36] R. Korobko, A. Lerner, Y. Li, E. Wachtel, A.I. Frenkel, I. Lubomirsky, In-situ extended X-ray absorption fine structure study of electrostriction in Gd doped ceria, *Appl. Phys. Lett.* 106 (2015) 042904. <https://doi.org/10.1063/1.4906857>.
- [37] Y. Li, O. Kraynis, J. Kas, T.C. Weng, D. Sokaras, R. Zacharowicz, I. Lubomirsky, A.I. Frenkel, Geometry of electromechanically active structures in Gadolinium - Doped Cerium oxides, *AIP Adv.* 6 (2016). <https://doi.org/10.1063/1.4952645>.
- [38] L. Sun, D. Marrocchelli, B. Yildiz, Edge dislocation slows down oxide ion diffusion in doped CeO<sub>2</sub> by segregation of charged defects, *Nat. Commun.* 6 (2015) 1–10. <https://doi.org/10.1038/ncomms7294>.
- [39] Y. Lei, Y. Ito, N.D. Browning, T.J. Mazanec, Segregation effects at grain boundaries in fluorite-structured ceramics, *J. Am. Ceram. Soc.* 85 (2002) 2359–2363. <https://doi.org/10.1111/j.1151->

2916.2002.tb00460.x.

- [40] S. Kim, P. Jain, H.J. Avila-Paredes, A. Thron, K. Van Benthem, S. Sen, Strong immobilization of charge carriers near the surface of a solid oxide electrolyte, *J. Mater. Chem.* 20 (2010) 3855–3858. <https://doi.org/10.1039/b926664j>.
- [41] Y.L. Kuo, C. Lee, Y.S. Chen, H. Liang, Gadolinia-doped ceria films deposited by RF reactive magnetron sputtering, *Solid State Ionics*. 180 (2009) 1421–1428.  
<https://doi.org/10.1016/j.ssi.2009.08.016>.
- [42] H.J. Avila-Paredes, K. Choi, C.T. Chen, S. Kim, Dopant-concentration dependence of grain-boundary conductivity in ceria: A space-charge analysis, *J. Mater. Chem.* 19 (2009) 4837–4842.  
<https://doi.org/10.1039/b904583j>.
- [43] A. Infortuna, A.S. Harvey, L.J. Gauckler, Microstructures of CGO and YSZ thin films by pulsed laser deposition, *Adv. Funct. Mater.* 18 (2008) 127–135.  
<https://doi.org/10.1002/adfm.200700136>.
- [44] K. Uchino, S. Nomura, L.E. Cross, R.E. Newnham, S.J. Jang, Electrostrictive effect in perovskites and its transducer applications, *J. Mater. Sci.* 16 (1981) 569–578.  
<https://doi.org/10.1007/BF02402772>.
- [45] F. Li, L. Jin, Z. Xu, S. Zhang, Electrostrictive effect in ferroelectrics: An alternative approach to improve piezoelectricity, *Appl. Phys. Rev.* 1 (2014). <https://doi.org/10.1063/1.4861260>.
- [46] F. Li, L. Jin, Z. Xu, D. Wang, S. Zhang, Electrostrictive effect in  $\text{Pb}(\text{Mg}_{1/3}\text{Nb}_{2/3})\text{O}_{3-x}\text{PbTiO}_3$  crystals, *Appl. Phys. Lett.* 102 (2013). <https://doi.org/10.1063/1.4802792>.

- [47] S. Sanna, V. Esposito, A. Tebano, S. Licoccia, E. Traversa, G. Balestrino, Enhancement of ionic conductivity in sm-doped ceria/yttria-stabilized zirconia heteroepitaxial structures, *Small*. 6 (2010) 1863–1867. <https://doi.org/10.1002/sml.200902348>.
- [48] R. Sinclair, S.C. Lee, Y. Shi, W.C. Chueh, Structure and chemistry of epitaxial ceria thin films on yttria-stabilized zirconia substrates, studied by high resolution electron microscopy, *Ultramicroscopy*. 175 (2017) 25–35. <https://doi.org/10.1016/j.ultramic.2016.12.023>.
- [49] L. Chen, C.L. Chen, D.X. Huang, Y. Lin, X. Chen, A.J. Jacobson, High temperature electrical conductivity of epitaxial Gd-doped CeO<sub>2</sub> thin films, *Solid State Ionics*. 175 (2004) 103–106. <https://doi.org/10.1016/j.ssi.2004.09.034>.
- [50] N. Yang, P. Orgiani, E. Di Bartolomeo, V. Foglietti, P. Torelli, A. V. Ievlev, G. Rossi, S. Licoccia, G. Balestrino, S. V. Kalinin, C. Aruta, Effects of Dopant Ionic Radius on Cerium Reduction in Epitaxial Cerium Oxide Thin Films, *J. Phys. Chem. C*. 121 (2017) 8841–8849. <https://doi.org/10.1021/acs.jpcc.7b00386>.
- [51] A. Bieberle-Hütter, J.L. Hertz, H.L. Tuller, Fabrication and electrochemical characterization of planar Pt-CGO microstructures, *Acta Mater*. 56 (2008) 177–187. <https://doi.org/10.1016/j.actamat.2007.09.006>.

# Electrostrictive Ceramics and their applications

*Simone Santucci, Vincenzo Esposito*

*Department of Energy Conversion and Storage, Technical University of Denmark, Fysikvej Building 310  
2800 Kgs. Lyngby.*

Keywords: actuator, cerium oxide, defective oxides, electromechanical, electrostriction, MEMs, Newnham's law, piezoelectricity, polymers, relaxor ferroelectrics, transducer.

## Abstract

Since the discovery of ferroelectric electrostrictive ceramics such as  $\text{Pb}(\text{Mg}_{1/3}\text{Nb}_{2/3})\text{O}_3$  (PMN) in '80 and following inclusion of other kind of materials (linear dielectrics, glass ceramics, defective oxides), electrostriction effect has been focus of much attention of research and industry with a succession of new field of development and commercial application.

While piezoelectricity remains a “competitor”, electrostrictive ceramics set aside a market in low dimensional application such as micro-pumps, positioning and micro-electromechanical systems (MEMSs). Also the heterogeneous variety of electrostrictors materials is a crucial point on the development of lead-free transducer.

In this work, we describe the basics of the electrostriction effect, in both microscopic and macroscopic points of view. We highlight the most relevant applications and we analyze the different families of electrostrictive compounds.

## 1 ELECTROSTRICTION

---

Electrostriction is the ability of all insulator or dielectric materials to develop mechanical deformation if subjected to an electric field. The effect is a consequence of the polarization of the ions inside the

material. For insulators in standard condition, the net charge is macroscopically zero. Anyway at the atomic level, the crystal is composed of positive (cation) and negative (anion) charged ions. When an electric field is applied through the material, cations and anions rearrange their relative position according to the field itself. As a consequence, the macroscopic size of the material changes. The phenomenological equations of the effect report the electrically induced strain ( $\lambda_{ij}$ ) that is proportional to the squared of the applied electric field ( $E$ ) or polarization ( $P$ ). In tensor notation it is expressed as:

$$\lambda_{ij} = M_{ijkl} E_k E_l,$$

or

$$\lambda_{ij} = Q_{ijkl} P_k P_l$$

Where,  $M_{ijkl}$  ( $\text{m}^2\text{V}^{-2}$ ) and  $Q_{ijkl}$  ( $\text{C}^2\text{m}^{-4}$ ) are the so-called electrostriction coefficients and they are elements of a fourth-rank tensor, meaning that electrostriction takes place in all crystal symmetries (Li *et al.*, 2014). The subscripts  $i,j,k,l$  can be abbreviated for material with isotropic or cubic structure, so it is common to use the Voigt notation:  $M_{ij}$  and  $Q_{ij}$  with  $i,j = 1$  to 4. As reported in the equations, the strain depends on the squared of the electric field ( $\propto E_k E_l$ ). As a consequence, the distortion always develops in the same direction, regardless of the sign of  $E$  or  $P$ . Figure 1a shows the parabolic field-induced strain in electrostrictive materials. As depicted in Figure 1b, if the applied field is not static but oscillating with a frequency  $f$  (the case of AC application), the electrostrictor material oscillates with twice the frequency  $2f$  (2<sup>nd</sup> harmonic). The strain can develop either as a contraction ( $M, Q < 0$ ) or an expansion ( $M, Q > 0$ ), depending on the material. When an object withstands a distortion, it generates a related force or stress  $\sigma$  ( $\text{N}\cdot\text{m}^{-2}$ ). According to Hooke's law:

$$\sigma = Y \cdot \lambda$$

Where  $Y$  is Young's modulus, usually reported in MPa. With the same strain, hard materials with high  $Y$  develop higher stress compared to soft materials, such as rubber or polymers.

Electrostriction coefficients  $M$  and  $Q$  are related by the permittivity properties of the material:

$$M_{ijkl} = Q_{ijkl} \{\epsilon_0(\epsilon_r - 1)\}^2$$

With  $\epsilon_0$  is the vacuum permittivity and  $\epsilon_r$  is the dielectric constant of the material. The use of one coefficient or another depends on the type of material. In high permittivity dielectrics that can show nonlinear polarization or hysteresis,  $Q$  is usually preferred. It is worth noticing that for the same  $Q$  value, materials with larger  $\epsilon_r$  deploy larger strain. As electrostriction comes from a fundamental interaction common in all materials, it can change considerably in both magnitude and dynamics depending on the physical properties of the material. Consequently, electrostriction coefficients range across several orders of magnitude depending on the material itself, with a  $Q$  from  $10^{-3} \text{ m}^4\text{C}^{-2}$  for ferroelectrics to  $10^3 \text{ m}^4\text{C}^{-2}$  for polymers (Newnham *et al.*, 2002). Furthermore, while most of electrostrictors such as linear dielectrics, ceramics and perovskites develop a positive strain (expansion), fluorites and polymers can have the opposite behavior (Sundar and Newnham, 1996; Newnham *et al.*, 1997; Zhang, Bharti and Zhao, 1998; Li *et al.*, 2014).

In materials that are also piezoelectric, the two effects sum up and the general electromechanical effect is written as:

$$\lambda_{ij} = g_{kij}P_k + Q_{ijkl}P_kP_l$$

With  $g_{kij}$  ( $\text{C}/\text{m}^2$ ) piezoelectric coefficient. Electrostriction can be considered as a second-order contribution of the general electromechanical coupling. Usually, the electrostrictive effect is smaller than the linear contribution by few orders of magnitude. Electrostrictive materials however, show peculiar characteristics such as low hysteresis in the polarization-strain loop and no remnant strain, making them particularly suitable for high accuracy applications (Uchino *et al.*, 1981; Haertling, 1999; Li *et al.*, 2014).



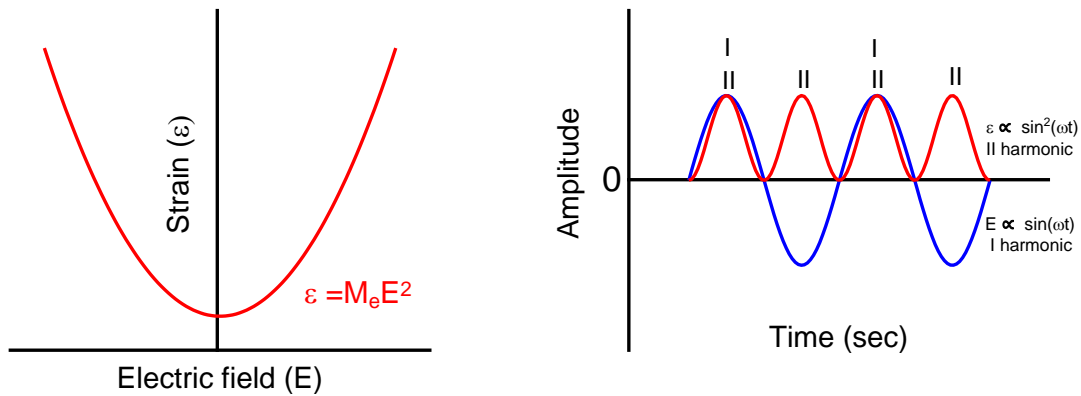


**Figure 1:** a) Strain quadratic response to electric field for electrostrictive materials. b) Electrostriction dynamics under an applied AC field.

## 2 APPLICATION

---

The ability of electrostrictors to convert an electric signal to mechanical distortion has been extensively used in transducing technologies (Meyer *et al.*, 2001; Restagno *et al.*, 2001; Baek *et al.*, 2011; Jones T.B., 2013; Martin *et al.*, 2014). In particular, an actuator is a transducer which function is to displace an object, working as an electrostrictive motor. Actuators are used in devices that need electrical/mechanical signal conversion such as ink-jet printer head, micro-pump and noise cancellation systems. A proper actuator should provide a significant displacement with an electric field as low as possible. Also, the performances should be stable and reproducible, allowing fine control of the actuating process. The average strain of a standard actuator is around  $10^{-3}$ . However, this value can be improved in specific engineered devices such as multilayered actuators, or flexensional actuators (CYMBALs) (Haertling, 1999; Meyer *et al.*, 2001; Uchino, 2008). Transducers can also be used in ultrasound imaging and sensors for diagnostic and sonar devices. An electrostrictive ultrasound device can convert electrical signal in mechanical vibration, generating ultra-acoustic waves with extreme accuracy.

Piezoelectric transducers usually have higher performances. Nonetheless, electrostrictors have many advantages over piezoelectrics, such as high accuracy of the strain-field response (no hysteresis or remnant strain), low creep or aging effects and high speed response ( $<10$  ms) (Newnham *et al.*, 1997). Also, they can perform at high temperature and frequency. Such features are useful in optical systems such as interferometric dilatometers and deformable mirrors.

In recent years, electrostrictor materials have been frequently included in miniaturized devices known as micro-electromechanical systems (MEMS) (Uchino *et al.*, 1981; Uchino, 2008). MEMS applications are several and heterogeneous: robotics, micro-motors and electronics, biomedical devices. The preference for electrostrictors over piezoelectrics has several reasons. As in small sized devices the electric field increases, the quadratic effect becomes the main contribution to the electromechanical activity. This effect was shown in amorphous silica glass ( $10^{-21}$  m<sup>2</sup>V<sup>-2</sup>). In thin films with a thickness lower than 100 Å, electrostriction strain is higher than piezoelectric contribution (Newnham *et al.*, 1997). This effect can be exploited in the design of materials with a zero-electromechanical coefficient, useful in devices potentially damaged by electric fields. In MEMS, the electro-active material is integrated as thin films and coupled with substrates, usually Si. Piezoelectrics are hard to integrate into these devices, because of high temperature processes and poling needed and diffusion effects often showed for lead-based piezoelectrics.

Both piezoelectric and electrostrictive materials have a limited role in pure medical application, as the best performing materials are lead-based (PZT, PMN). Moreover, these materials have been banned by the RoHS compliant of 2006, due to environmental awareness. For this reason, many efforts have been made in recent years to find a lead-free alternative.

Half of the global market of actuators is focused in MEMs application, followed by phone and digital cameras or lenses (42%), fuel injectors (5%) and ink cartridges (3.3%) (Jo *et al.*, 2012). These data are updated to 2012 when the market value was around 12 millions of dollars, the double respect to 2009 (Jo *et al.*, 2012).

### 3 MICROSCOPIC EXPLANATION OF ELECTROSTRICTION

---

When polarized with an electric field, the ions of the material shift from their original position, causing a mechanical strain. The relative displacement of positive and negative ions should erase each other, and the net strain should be null. However, the energy required to compress an ion-pair ( $U_c$ ) is usually higher than the energy needed to enlarge it ( $U_e$ ) (Kittel, 2005; Li *et al.*, 2014). This is clear from the ion-pair potential respect to the equilibrium position showed in **Figure 2**. Consequently, the polarization usually results in increasing of the ion-pair bond length and a positive electrostriction coefficient. Nevertheless, for some materials such as fluorites, polarization shrinks the ions-pair, causing a negative electrostriction coefficient (V. Sundar, J.-F. Li, D. Viehland, 1996; Newnham *et al.*, 2002). Also, the ion-pair potential varies depending on the material.

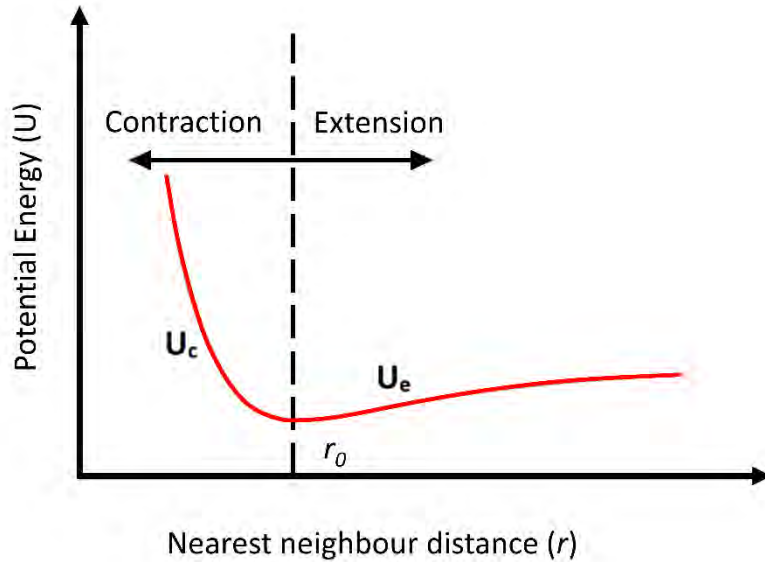


**Figure 2:** Ion-pair potential in ionic crystals,  $r_0$  is the equilibrium distance between positive and negative ions.

Considering a rigid model of  $+q$  and  $-q$  charged ions, the potential energy function can be described as (Uchino *et al.*, 1984; Sundar and Newnham, 1996; Li *et al.*, 2014):

$$\Delta U = U(r) - U(r_0) = f(r - r_0)^2 - g(r - r_0)^3$$

Where  $r$  is the relative distance of positive and negative ions and  $r_0$  is the equilibrium position.  $f$  and  $g$  represent the harmonic and anharmonic contribution of the energy. Under an electric field, the strain and polarization can be calculated (Uchino *et al.*, 1984; Sundar and Newnham, 1996; Li *et al.*, 2014):

$$\varepsilon_1 = (3gq^2/4f^3r_0)E_1^2$$

$$P_1 = (q^2/4fr_0^3)E_1$$

As well as the electrostriction coefficient:

$$Q_{11} = 12gr_0^5/fq^2$$

$g/f$  represents the ration between anharmonic and harmonic energy contribution to the overall ion-pair potential. Therefore, high anharmonic component corresponds to high electrostriction coefficient.  $f$  and  $g$  are associated with the material microscopic properties such as ionic radius and charge, crystal structure and symmetry. Consequently, compounds with similar microscopic environment show a similar electrostriction magnitude (Warner, Onoe and Coquin, 1967; Yamada, 1972; Sundar and Newnham, 1996; Sundar, Li, Viehland, 1996; Newnham *et al.*, 2002; Wang *et al.*, 2010; Li *et al.*, 2014).

## 4 THERMAL EXPANSION, NEWNHAM'S LAW AND MATERIALS

---

In order to describe materials with different anisotropic properties, it is useful to define the hydrostatic electrostriction coefficient  $Q_h$ , as the variation of electrical susceptibility with applied hydrostatic pressure. For isotropic or cubic materials,  $Q_h$  can be written as:

$$Q_h = 0.5 (d\chi/dp) \approx Q_{11} + 2Q_{12}$$

Where  $Q_{11}$  and  $Q_{12}$  are the longitudinal and transverse electrostriction coefficients, respectively. Newnham carried out several studies finding an empirical relationship between macroscopic physical properties and electrostriction coefficients for several kinds of materials (Uchino *et al.*, 1981; Newnham *et al.*, 2002; Li *et al.*, 2014). Electrostriction and thermal expansion both originate from ion-

pair potential anharmonicity (Uchino *et al.*, 1981). The thermal expansion coefficient can in fact be written as:

$$\alpha = \frac{3gk_b}{4f^2r_0}$$

With  $k_b$  is the Boltzmann's constant and  $r_0$  is the cation-anion distance at equilibrium. Similarly to electrostriction, thermal expansion coefficient  $\alpha$  is zero when the anharmonic factor  $g$  is 0. Based on Newnham results:

$$\alpha = 4.2 \cdot 10^{-5} Q_h^{0.5}$$

Thermal expansion and  $Q_h$  are related, as both are related to anharmonic ions potential.

Newnham also reported a connection between  $Q_h$  and elastic/dielectric effects. As a result, the vast majority of electrostrictive materials follow an empirical relationship:

$$|Q_h| \approx 2.37 \cdot (S/\epsilon_0\epsilon_r)^{0.59}$$

Where  $S$  is the elastic constant, inverse of Young's modulus. Figure 3 shows the logarithm of the electrostriction coefficient, that depends almost linearly on  $\log(S/\epsilon_0\epsilon_r)$ . Most of the materials

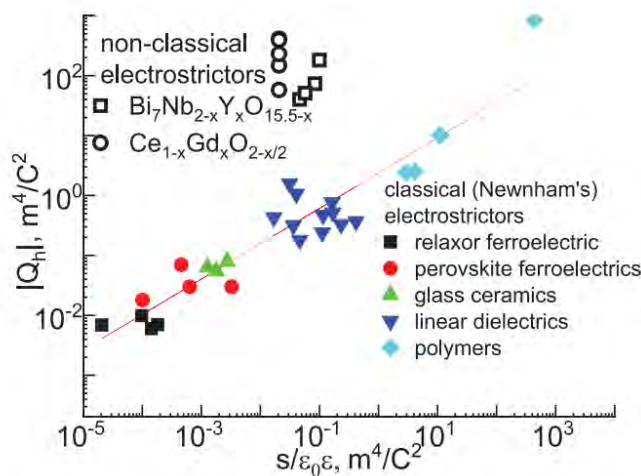


**Figure 3:** Hydrostatic electrostriction coefficient for Newnham's and non-classical electrostrictors. Red line: Newnham's law. Reported with permission from (Wachtel, Frenkel and Lubomirsky, 2018)

Copyright 2018, Wiley-VCH.

follow this relationship, even if they show very different properties. We split the plot into four areas to better group the families of materials. The center of the plot represents materials with high stiffness but low dielectric constant such as linear dielectrics and glass ceramics. The left side includes materials with high dielectric constants such as ferroelectrics and relaxors. On the right side there are polymers, with low permittivity and low stiffness. On the top, defective oxides that share the same properties of linear dielectrics, do not follow Newnham's law and show two orders of magnitude higher electrostriction.

#### **4.1 LINEAR DIELECTRICS AND GLASSES CERAMICS**

Linear dielectrics are materials which polarization depends linearly on the electric field. They can be single crystals, glasses or ceramics (Newnham *et al.*, 1997; Yimnirun *et al.*, 2002; Li *et al.*, 2014). These materials usually have low dielectric constant ( $\epsilon < 10$ ) and Young's modulus around  $Y \approx 10^2$  GPa. Some examples are  $\text{CaF}_2$  single crystal or AlN and ceramics, with  $Q_h = 0.47$  and  $0.3 \text{ m}^4\text{C}^{-2}$  respectively (Newnham *et al.*, 1997; Yimnirun *et al.*, 2002). Some ceramics, such as  $\text{BaBi}_2\text{Nb}_2\text{O}_9$  reach high permittivity:  $\epsilon \approx 400$  (Ujma and Pawe, 2006) and  $Q_h = 0.038$  (Li *et al.*, 2014).

#### **4.2 PEROVSKITE FERROELECTRICS AND RELAXOR FERROELECTRICS**

Ferroelectrics are materials with domains that are microscopically polarized in random directions. Like piezoelectrics, it is possible to pole ferroelectrics to enhance their performances. Perovskite ferroelectrics show higher dielectric constant respect to linear dielectrics such as  $\text{SrTiO}_3$  ( $\epsilon = 450$ ),  $\text{PbTiO}_3$  ( $\epsilon = 270$ ) and  $\text{BaTiO}_3$  ( $\epsilon = 1070$ ) but similar Young's modulus. The electrostriction coefficients are  $Q \approx 0.04 \text{ m}^4\text{C}^{-2}$ .

Relaxors is a family of ferroelectrics with diffuse phase transition. They show a high dielectric constant ( $\epsilon \approx 10^3$ ) that depends strongly on both temperature and frequency. (Moulson and Herbert, 2003; Heywang W., Lubitz and Wersing, 2008; You, Be and In, 2009; Cross and Cross, 2011). Relaxor ferroelectrics are generally lead-based perovskites with  $\text{Pb}(\text{B}_1\text{B}_2)\text{O}_3$  structure, where  $\text{B}_1$  and  $\text{B}_2$  are two different ions. These compounds are frequently used as piezoelectrics, but they also possess high

electrostriction coefficient. The interest of research and industry started in the '80 thanks to the first electrostrictive relaxors:  $\text{Pb}(\text{Mg}_{1/3}\text{Nb}_{2/3})\text{O}_3$  (PMN),  $\text{Pb}(\text{Zn}_{1/3}\text{Nb}_{2/3})\text{O}_3$  (PZN) and  $\text{Pb}(\text{La}_{0.09}\text{Zr}_{0.65}\text{Ti}_{0.35})\text{O}_3$  (PLZT) were studied thanks to the promising performances, with a strain up to 0.3% (Haertling, 1999) (Uchino *et al.*, 1981; Blackwoodt and Ealey, 1993; Haertling, 1999; Moulson and Herbert, 2003; Li *et al.*, 2014). The electrostriction coefficients are about  $Q_h = 0.002 \text{ m}^4\text{C}^{-2}$  and  $M = 2 \cdot 10^{-18} \text{ m}^2\text{V}^{-2}$  for PMN (V. Sundar, J.-F. Li, D. Viehland, 1996). Lead-based piezoelectrics and electrostrictors are used in most of the transducer and actuator devices (Jo *et al.*, 2012) in which a combination of massive displacement and high mechanical reliability is needed (Uchino, 2008). Moreover, most of the relaxors are also piezoelectric, and it is possible to combine the two effects (Haertling, 1999). As said before, many efforts have been made to introduce lead-free electromechanical materials, and some relaxor alternatives examples are bismuth or niobium based systems (Jo *et al.*, 2012).

### 4.3 DEFECTIVE OXIDES

Gd-doped ceria (CGO) and (Y, Nb)-stabilized  $\delta\text{-Bi}_2\text{O}_3$  have been recently reported to possess high electrostrictor behavior, mostly as thin films (Korobko *et al.*, 2012; Korobko, Wachtel and Lubomirsky, 2013; Hadad *et al.*, 2016; Santucci *et al.*, 2019). These two materials are both oxides with fluorite structure and a large amount of defects in the form of oxygen vacancies. Being ceramics, their Young's modulus is high:  $Y_{\text{CGO}} = 200 \text{ GPa}$ ,  $Y_{\text{Bi}_2\text{O}_3} = 85 \text{ GPa}$ . They also have low dielectric constants:  $\epsilon_{\text{CGO}} \approx 28$ ,  $\epsilon_{\text{Bi}_2\text{O}_3} \approx 26\text{-}30$ . The mechanism behind electrostriction in these materials is not the same, and it is related to the local geometry around the oxygen vacancies and their configuration inside grain boundaries (Li *et al.*, 2016; Kabir *et al.*, 2019).

In a pure crystal, one oxygen vacancy forms an octahedron shaped complex with six oxygen atoms. When the field is applied the octahedron withstands a rearrangement including all the oxygen atoms, amplifying the effect. For this reason, the electrostrictive coefficient results particularly high in both materials:  $Q_h = 124 \text{ m}^4\text{C}^{-2}$  for CGO and  $40\text{-}182 \text{ m}^4\text{C}^{-2}$  for  $\delta\text{-Bi}_2\text{O}_3$ . CGO and  $\delta\text{-Bi}_2\text{O}_3$  do not follow the trend of Newnham's electrostrictors. Even though possessing the same mechanical/electrical

properties of linear dielectrics in fact, they place two-three orders of magnitude above similar materials. This is attributed to the particular mechanism involving oxygen vacancies. An extensive analysis of other materials with a high amount of vacancies would bring new insight of the effect, maybe showing a new trend for defective oxides.

Although too early for commercial devices, CGO showed good results as membrane and bulk (Mishuk *et al.*, 2017; Ushakov *et al.*, 2017; Kabir *et al.*, 2019). Being a non-toxic and environmentally friendly material, CGO opens new possibilities in high performance bio-compatible and medical application. CGO is also compatible with Si and ceramic electrodes (Santucci *et al.*, 2019) and does not need pre-processing or poling, making it a promising candidate for a new generation of lead-free MEMs.

#### **4.4 POLYMERS**

Ferroelectric polymers such as polyvinylidene fluoride (PVDF) and its copolymers, show drastically different mechanical properties respect to ceramics and glasses. Polymers are flexible, with a low density and small Young's modulus ( $\approx 10^3$  MPa). They also display a low relative permittivity ( $\epsilon \approx 10$ ) (Newnham *et al.*, 2002). Under an electric field, polymers deploy large strain of the order of 0.25% (Newnham *et al.*, 2002), with resulting electrostriction coefficients around  $Q_h \approx 2 \text{ m}^4\text{C}^{-2}$ . Particular interest has been given to polyurethane, a non-ferroelectric elastomer. Elastomers have usually very low stiffness ( $Y = 40 \text{ MPa}$ ), that allows these polymers to deploy a high strain response with high electrostriction coefficient of  $Q_h \approx 10^3 \text{ m}^4\text{C}^{-2}$ . Other polymer's properties include frequency dependence field induced strain and high Maxwell stress contribution. In terms of displacement, polymers are comparable with the best relaxor electrostrictors (PMN, PZT) (Yimnirun *et al.*, 2002), Polymers do not generate high stress because of the small Young's modulus, making them difficult to integrate with force related applications. They are however cheap and they comply to complex shapes and surfaces. Polymers are frequently used in composite technology coupled with electromechanical ceramics (Moulson and Herbert, 2003). The properties of the devices are usually engineered to the specific application, and the connectivity between the two materials has a significant role. Composites materials offer advantages in sonar and medical ultrasonic imaging, in which the polymer usually faces soft tissues (Moulson and Herbert, 2003).



## 5 SUMMARY

---

Electrostriction effect is a mechanism that all materials possess and it consists of a mechanical displacement as a response to an electric field. As the strain-field relationship is squared, electrostriction distortion does not depend on the direction of the electric field and happens with twice its frequency. While usually smaller than the piezoelectric effect, electrostriction has some peculiar characteristic useful in applications such as high temperature and frequency operation. Also, electrostrictor materials do not need poling or pre-process to be fully operational. Electrostrictors are particularly suitable for MEMs devices. For low dimension devices, a higher electric field goes through the material, exploiting electrostrictive behavior more than piezoelectric. Also, electrostriction related strain is highly reproducible and without strain-field hysteresis. That makes electrostrictors valuable in high precision actuators.

Microscopically, electrostriction is due to the anharmonicity of ion pair potential. When the field is applied, the ions rearrange their relative position and are set apart. The species of ion and crystal structure have a major role in the magnitude of electrostriction. Elastic/dielectric properties are also related to the electromechanical activity. In particular,  $\log(Q_h)$  depends almost linearly on  $\log(S/\epsilon_0\epsilon_r)$ . Most of the electrostrictive materials follow this trend. The most performing materials are lead-based relaxor ferroelectrics, which possess high permittivity and Young's modulus. Polymers are also suitable for particular application thanks to high field induced strain that unfortunately cannot be converted in stress because polymers low Young's modulus. Defective oxides are found not to follow this trend: while having mechanical and electrical properties similar to linear dielectrics, they show two-three order of magnitude higher electrostriction coefficient. This is due to a peculiar effect involving oxygen vacancies and a field induced local rearrangement, that amplifies the performances.

## 6 REFERENCES

---

- Baek, S. H. *et al.* (2011) 'Giant Piezoelectricity on Si for', *Science*, 334(November), pp. 958–961.
- Blackwoodt, G. H. and Ealey, M. A. (1993) 'Electrostrictive behavior in lead magnesium niobate (PMN) actuators. Part I: Materials perspective', *Smart Materials and Structures*, 2(2), pp. 124–133. doi: 10.1088/0964-1726/2/2/008.
- Cross, L. E. and Cross, L. E. (2011) 'Relaxor ferroelectrics', 0193(1987), pp. 241–267. doi: 10.1080/00150198708016945.
- Hadad, M. *et al.* (2016) 'Key-features in processing and microstructure for achieving giant electrostriction in gadolinium doped ceria thin films', *Acta Materialia*. Elsevier Ltd, 118, pp. 1–7. doi: 10.1016/j.actamat.2016.07.025.
- Haertling, G. H. (1999) 'Ferroelectric ceramics: History and technology', *Journal of the American Ceramic Society*, 82(4), pp. 797–818. doi: 10.1111/j.1151-2916.1999.tb01840.x.
- Heywang W., Lubitz, K. and Wersing, W. (2008) *Piezoelectricity*.
- Jo, W. *et al.* (2012) 'Giant electric-field-induced strains in lead-free ceramics for actuator applications - Status and perspective', *Journal of Electroceramics*, 29(1), pp. 71–93. doi: 10.1007/s10832-012-9742-3.
- Jones T.B., N. N. G. (2013) *Electromechanics and MEMS*. Cambridge University Press.
- Kabir, A. *et al.* (2019) 'Effect of Oxygen Defects Blocking Barriers on Gadolinium Doped Ceria (GDC) Electro-Chemo-Mechanical Properties', *Acta Materialia*. Elsevier Ltd, 174, pp. 53–60. doi: 10.1016/j.actamat.2019.05.009.
- Kittel, C. (2005). *Introduction to Solid State Physics*. John Wiley & Sons, Inc.
- Korobko, R. *et al.* (2012) 'Giant electrostriction in Gd-doped ceria', *Advanced Materials*, 24(43), pp. 5857–5861. doi: 10.1002/adma.201202270.

- Korobko, R., Wachtel, E. and Lubomirsky, I. (2013) 'Cantilever resonator based on the electrostriction effect in Gd-doped ceria', *Sensors and Actuators, A: Physical*. Elsevier B.V., 201, pp. 73–78. doi: 10.1016/j.sna.2013.06.021.
- Li, F. *et al.* (2014) 'Electrostrictive effect in ferroelectrics: An alternative approach to improve piezoelectricity', *Applied Physics Reviews*, 1(1). doi: 10.1063/1.4861260.
- Li, Y. *et al.* (2016) 'Geometry of electromechanically active structures in Gadolinium - Doped Cerium oxides', *AIP Advances*, 6(5). doi: 10.1063/1.4952645.
- Martin, K. *et al.* (2014) 'Dual-Frequency Piezoelectric Transducers for Contrast Enhanced Ultrasound Imaging', *Sensors*, 14(11), pp. 20825–20842. doi: 10.3390/s141120825.
- Meyer, R. J. *et al.* (2001) 'Displacement amplification of electroactive materials using the cymbal flextensional transducer', *Sensors and Actuators, A: Physical*, 87(3), pp. 157–162. doi: 10.1016/S0924-4247(00)00489-1.
- Mishuk, E. *et al.* (2017) 'Self-supported Gd-doped ceria films for electromechanical actuation: Fabrication and testing', *Sensors and Actuators, A: Physical*. Elsevier B.V., 264, pp. 333–340. doi: 10.1016/j.sna.2017.07.047.
- Moulson, A. J. and Herbert, J. M. (2003) 'Electroceramics', *Wiley*, pp. 339–409. doi: 10.1002/0470867965.
- Newnham, R. E. *et al.* (1997) 'Electrostriction: Nonlinear Electromechanical Coupling in Solid Dielectrics', *The Journal of Physical Chemistry B*, 101(48), pp. 10141–10150. doi: 10.1021/jp971522c.
- Newnham, R. E. *et al.* (2002) 'Electrostriction: Nonlinear Electromechanical Coupling in Solid Dielectrics', *The Journal of Physical Chemistry B*, 101(48), pp. 10141–10150. doi: 10.1021/jp971522c.
- Restagno, F. *et al.* (2001) 'A new capacitive sensor for displacement measurement in a surface force apparatus', *Measurement Science and Technology*, 12(Umr 5672), pp. 16–22. doi: 10.1088/0957-0233/12/1/302.

Santucci, S. *et al.* (2019) 'Enhanced electro-mechanical coupling of TiN/Ce<sub>0.8</sub>Gd<sub>0.2</sub>O<sub>1.9</sub> thin film electrostrictor', *APL Materials*, 7(7), p. 071104. doi: 10.1063/1.5091735.

V. Sundar, J.-F. Li, D. Viehland, R. E. N. (1996) 'Interferometric evaluation of electrostriction coefficients', *Materials Research Bulletin*, 31(5), pp. 555–563.

Sundar, V. and Newnham, R. E. (1996) 'Converse method measurements of electrostriction coefficients in low-K dielectrics', *Materials Research Bulletin*, 31(5), pp. 545–554. doi: 10.1016/S0025-5408(96)00035-9.

Uchino, K. *et al.* (1981) 'Electrostrictive effect in perovskites and its transducer applications', *Journal of Materials Science*, 16(3), pp. 569–578. doi: 10.1007/BF02402772.

Uchino, K. *et al.* (1984) 'Pressure dependence of the refractive index and dielectric constant in a fluoroperovskite, KMgF<sub>3</sub>', *Physical Review B*, 29(12), pp. 6921–6925. doi: 10.1103/PhysRevB.29.6921.

Uchino, K. (2008) 'Piezoelectric Actuators 2006', *J Electroceram*, 20, pp. 301–311. doi: 10.1007/s10832-007-9196-1.

Ujma, M. A. Æ. Z. and Pawe, Æ. M. (2006) 'Dielectric properties of BaBi<sub>2</sub>Nb<sub>2</sub>O<sub>9</sub> ceramics', pp. 5317–5322. doi: 10.1007/s10853-006-0300-8.

Ushakov, A. D. *et al.* (2017) 'Electromechanical properties of electrostrictive CeO<sub>2</sub>:Gd membranes: Effects of frequency and temperature', *Applied Physics Letters*, 110(14), p. 142902. doi: 10.1063/1.4979642.

Wachtel, E., Frenkel, A. I. and Lubomirsky, I. (2018) 'Anelastic and Electromechanical Properties of Doped and Reduced Ceria', *Advanced Materials*, 30(41), pp. 1–17. doi: 10.1002/adma.201707455.

Wang, J. J. *et al.* (2010) 'Lattice, elastic, polarization, and electrostrictive properties of BaTiO<sub>3</sub> from first-principles', *Journal of Applied Physics*, 108(3). doi: 10.1063/1.3462441.

Warner, A. W., Onoe, M. and Coquin, G. A. (1967) 'Determination of Elastic and Piezoelectric Constants for Crystals in Class (3 m)', *The Journal of the Acoustical Society of America*, 42(6), pp.

1223–1231. doi: 10.1121/1.1910709.

Yamada, T. (1972) 'Electromechanical properties of oxygen-octahedra ferroelectric crystals', *Journal of Applied Physics*, 43(2), pp. 328–338. doi: 10.1063/1.1661117.

Yimnirun, R. *et al.* (2002) 'Electrostrictive strain in low-permittivity dielectrics', *Journal of Electroceramics*, 8(2), pp. 87–98. doi: 10.1023/A:1020543610685.

You, A., Be, M. A. Y. and In, I. (2009) 'Investigation of the electrocaloric effect in a  $\text{PbMg}_{2/3}\text{Nb}_{1/3}\text{O}_3$ - $\text{PbTiO}_3$  relaxor thin film', : *Appl. Phys. Lett.* 95, 95(182904), pp. 1–4. doi: 10.1063/1.3257695.

Zhang, Q. M., Bharti, V. and Zhao, X. (1998) 'Giant electrostriction and relaxor ferroelectric behavior in electron- irradiated poly(vinylidene fluoride-trifluoroethylene) copolymer', *Science*, 280(5372), pp. 2101–2104. doi: 10.1126/science.280.5372.2101.